Regulating Bulk and Surface Charge Behaviour of Photoanodes for Enhanced Solar Water Oxidation Efficiency

Peng Luan

Master of Science

A thesis submitted for the degree of *Doctor of Philosophy* at

Monash University in 2020

School of Chemistry

Copyright notice

Content

Abstract

Continuous efforts have been made in developing renewable energy resources to alleviate the upcoming energy crises in this century. Solar energy has been considered as one of the most promising energy sources, since it is clean, sustainable, and abundant. Among various techniques of solar energy conversion, photoelectrochemical (PEC) water splitting to produce hydrogen could potentially provide a cost-effective, eco-friendly and convenient solution by taking advantage of thousands TW-scale of radiation that continually strikes the earth's surface, which can successfully achieve the goal of the economics with zero-carbon emission in the future. Significantly, designing and fabricating highly advanced photoelectrodes plays a critical role in determining solar energy conversion efficiency. There exist mainly four photophysical process in a typical photoelectrode, photon absorption, bulk charge separation, charge transport and surface charge transfer. In this Thesis, I will focus on the development of new methods for photoelectrodes design and fabrication to achieve a better charge separation efficiency both in bulk and on surface for solar water splitting:

Chapter 1. *Background introduction.* A comprehensive literature review of fundamental and rational photoelectrodes design for solar water splitting.

Chapter 2. *Bismuth Vanadate with Electrostatically Anchored 3D Carbon Nitride Nano-networks as Efficient Photoanodes for Water Oxidation.* In this chapter, protonated 3-dimensional (3D) carbon nitride nano-networks/bismuth vanadate (C_3N_4/$BiVO_4$) heterojunctional photoanode was constructed via electrostatic interaction strategy to improve bulk charge separation. This electrostatic self-assembly can initiate and contribute to an intimate contact at the interfaces, leading to an enhanced photoelectrochemical activity and stability compared with that fabricated by non-electrostatic assembly counterpart.

Chapter 3. *Dual Quantum Dot-Decorated Bismuth Vanadate Photoanodes for Highly Efficient Solar Water Oxidation.* In this chapter, dual carbon quantum dots (CQDs) and $BiVO_4$ quantum dots (BQDs) are introduced on the surface of as-prepared $BiVO_4$, in which CQDs can widen photon absorption range from 540 to over 700 nm. More significantly, lattice-matched homojunction construction can enable more efficient bulk interfacial charge separation.

Chapter 4. *Unique Layer-Doping-Induced Regulation of Charge Behaviour in Metal-Free Carbon Nitride Photoanodes for Enhanced Performance.* In this chapter, phosphorus and boron atoms are uniquely layer-doped into the C_3N_4-film photoanode based on different polymerization routes of precursors. This layer-doping fabrication strategy effectively contributes to the formation of dual junctions that optimizing the bulk charge separation efficiency.

Chapter 5. *Polymeric Carbon Nitride Photoanodes Decorated with Atomically Dispersed Ruthenium Cocatalysts for Efficient Solar Water Oxidation.* In this chapter, a novel atomically dispersed ruthenium species are successfully designed and fabricated as cocatalysts on polymeric C_3N_4 photoanode to improve surface reaction kinetics. The integration of RuOP sites into the C_3N_4 frameworks effectively suppress the charge recombination on the photoanode/cocatalyst interface, which enables an enhancement of photocurrent density for polymeric C_3N_4-abased photoanodes from micro-ampere to milli-ampere scale.

Chapter 6. *Summary and outlook.* A brief summary of the thesis and several possible future directions of photoelectrochemical water splitting are proposed.

Declaration

This thesis is an original work of my research and contains no material which has been accepted for the award of any other degree or diploma at any university or equivalent institution and that, to the best of my knowledge and belief, this thesis contains no material previously published or written by another person, except where due reference is made in the text of the thesis.

Signature: …. *Peng Luan*

Print Name: **Peng Luan…**……………….

Date: ……31/08/2020…………………….

Publications during enrolment

1. <u>Peng Luan</u>, Qingqiang Meng, Jing Wu, Qinye Li, Xiaolong Zhang, Ying Zhang, Luke A. O'Dell, Sonia R. Raga, Jennifer M. Pringle, James C. Griffith, Chenghua Sun, Udo Bach, and Jie Zhang*,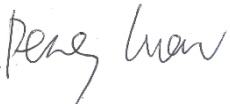 *Unique Layer-Doping-Induced Regulation of Charge Behaviour in Metal-Free Carbon Nitride Photoanodes for Enhanced Performance.* **ChemSusChem** 2020, 13, 328-333.

2. <u>Peng Luan</u>, Xiaolong Zhang, Ying Zhang, Zhijun Li, Udo Bach, and Jie Zhang*, *Dual Quantum Dot-Decorated Bismuth Vanadate Photoanodes for Highly Efficient Solar Water Oxidation.* **ChemSusChem** 2019, 12, 1240-1245.

3. <u>Peng Luan</u>, Ying Zhang, Xiaolong Zhang, Zhijun Li, Ragesh Prathapan, and Jie Zhang*, *Bismuth Vanadate with Electrostatically Anchored 3D Carbon Nitride Nano-networks as Efficient Photoanodes for Water Oxidation.* **ChemSusChem** 2018, 11, 2510-2516.

4. <u>Peng Luan</u> and Jie Zhang*, *Stepping towards Solar Water Splitting: Recent Progress in Bismuth Vanadate Photoanodes.* **ChemElectroChem** 2019, 6, 3227-3243. *(Review)*

5. <u>Peng Luan</u> *et al. Polymeric Carbon Nitride Photoanodes Decorated with Atomically Dispersed Ruthenium Cocatalysts for Efficient Solar Water Oxidation. **To be submitted***

Thesis including published works declaration

I hereby declare that this thesis contains no material which has been accepted for the award of any other degree or diploma at any university or equivalent institution and that, to the best of my knowledge and belief, this thesis contains no material previously published or written by another person, except where due reference is made in the text of the thesis.

This thesis includes *4* original papers published in peer reviewed journals and *1* submitted publications. The core theme of the thesis is *catalysts design for photoelectrochemical water oxidation*. The ideas, development and writing up of all the papers in the thesis were the principal responsibility of myself, the student, working within the *School of Chemistry* under the supervision of *Assoc. Prof. Jie Zhang* and *Prof. Udo Bach*.

The inclusion of co-authors reflects the fact that the work came from active collaboration between researchers and acknowledges input into team-based research.

In the case of *chapter 2-5* my contribution to the work involved the following:

Thesis Chapter	Publication Title	Status (published, in press, accepted or returned for revision, submitted)	Nature and % of student contribution	Co-author name(s) Nature and % of Co-author's contribution*	Co-author(s), Monash student Y/N*
2	*Bismuth Vanadate with Electrostatically Anchored 3D Carbon Nitride Nano-networks as Efficient Photoanodes for Water Oxidation*	*Published*	80%. Concept and collecting data and writing first draft	1. *Y. Zhang, collecting data 5 %* 2. *X. Zhang, collecting data 3 %* 3. *Z. Li, collecting data 3 %* 4. *R. Prathapan, collecting data 2 %* 5. *U. Bach, supervision 2 %* 6. *J. Zhang, supervision and manuscript revision 5 %*	*Yes* *Yes* *No* *Yes* *Yes* *Yes*
3	*Dual Quantum Dot-Decorated Bismuth Vanadate Photoanodes for Highly Efficient Solar Water Oxidation*	*Published*	80%. Concept and collecting data and writing first draft	1. *X. Zhang, collecting data 5 %* 2. *Y. Zhang, collecting data 5%* 3. *Z. Li, collecting data 3%* 4. *U. Bach, supervision 2 %* 5. *J. Zhang, supervision and manuscript revision 5 %*	*Yes* *Yes* *No* *Yes* *Yes*
4	*Unique Layer-Doping-Induced Regulation of Charge Behaviour in Metal-Free*	*Published*	60%. Concept and collecting data and writing first draft	1. *Q. Meng, collecting data 5 %* 2. *J. Wu, collecting data 3 %* 3. *Q. Li, theoretical simulation 1 %*	*No* *No* *Yes* *Yes* *Yes* *No*

	Carbon Nitride Photoanodes for Enhanced Performance			4. *X. Zhang, collecting data 3 %* 5. *Y. Zhang, collecting data 3 %* 6. *L. A. O'Dell, collecting data 2 %* 7. *S. R. Raga, collecting data 5%* 8. *J. Pringle, collecting data 1 %* 9. *J. Griffith, collecting data 5 %* 10.*C. Sun, theoretical simulation 5 %* 11.*U. Bach, supervision 2 %* 12.*J. Zhang, supervision and manuscript revision 5 %*	*Yes* *No* *Yes* *No* *Yes* *Yes*
5	*Polymeric Carbon Nitride Photoanodes Decorated with Atomically Dispersed Ruthenium Cocatalysts for Efficient Solar Water Oxidation*	*Not submitted*	*70% Concept and collecting data and writing first draft*	1. *Liang Huang 10 %* 2. *Bernt Johannessen 10 %* 3. *Jie Zhang 10 %*	*No* *No* *Yes*

I have / have not renumbered sections of submitted or published papers in order to generate a consistent presentation within the thesis.

Student name: Peng Luan

Student signature: <Peng Luan>   -   **Date: 31/08/2020**

I hereby certify that the above declaration correctly reflects the nature and extent of the student's and co-authors' contributions to this work. In instances where I am not the responsible author I have consulted with the responsible author to agree on the respective contributions of the authors.

Main Supervisor name: Jie Zhang

Main Supervisor signature: **Date: 31/08/2020**

Acknowledgements

I would like to express my gratitude to both of my supervisors Assoc. Prof. Jie Zhang and Prof. Udo Bach for giving the opportunity to study and work at Monash University. Particularly, I would thank them for sharing their vision and thoughts which always guide my PhD journey. Besides my supervisors, I would like to thank my panel members: Prof. Douglas Macfarlane, Dr. Toby Bell and Dr. David Turner for not only their insightful comments and hard questions, but also the great encouragement to continue my research career, they are more than advisors but mentors. And many thanks to the financial support from MGS and MIRPS for my PhD study.

I also thank my colleagues in lab, Dr. Xiaolong Zhang, Dr. Fengwang Li, Dr. Ying Zhang, Dr. Jiezhen Li, Dr. Anisur Rahman. Dr. Si-Xuan Guo, Dr. Atul Sharma, Mr. Peng Zhou, Mr. Linbo Li, and Mr. Siram Venkata Mosali, for their very kind help and support on my work. Their sagacity pushes me for striving all the way and I've learned so much from them. And I am so happy to meet them at Monash University and so grateful to become life-long friends with them. Meanwhile, I would like to acknowledge Mr James Griffith and Ms Yvonne Hora for XPS training and measurement, Dr. Finlay Shanks for TGA training, Dr. Peter Nichols for NMR measurement, Mr Phillip Holt for GC training, Dr. Craig Forsyth for XRD training, Dr. Johannessen Bernt and Dr. Qinfen Gu from ANSTO for XAS discussion and measurement, Sonia Ruiz Raga for IMPS training and measurement, as well as the use of facilities within the Monash Centre for Electron Microscopy, the Monash X-Ray Platform, and access for use of Chemical Engineering School labs. Also many thanks to Dr. Zhijun Li, Dr. Qingqiang Meng, Ms Jing Wu's for helpful discussion.

Of course, none of this would have been possible at all without the love and bottomless support of my family, which has always been a guiding influence in my life. And I have to save the most special person for last, my girlfriend Yanyan Feng who has done as much for me as any person could ask for, and then done more. Her endless love and support have made all the difference.

Chapter 1. Fundamental Principles and Rational Design of Photoelectrodes for Solar Water Splitting

Background introduction

Owing to the rapid depletion of traditional fossil fuels and the consequent increased emission of greenhouse gas CO_2, energy and environmental issues are becoming a big challenge for the entire humankind in the 21st century.[1-4] Therefore, it is highly essential to create new industry and energy resources to achieve the goal of zero-carbon emission economics. Harvesting energy directly from sunlight offers a desirable solution toward fulfilling, with minimal environmental impact, the need for clean and sustainable energy.[5-8] Solar energy is a decentralized and inexhaustible natural resource, with the magnitude of 10^5 terawatts (TW) striking the surface of earth (**Figure 1**), which far exceeds the 20~40 TW of global power consumption expected by 2050.[9]
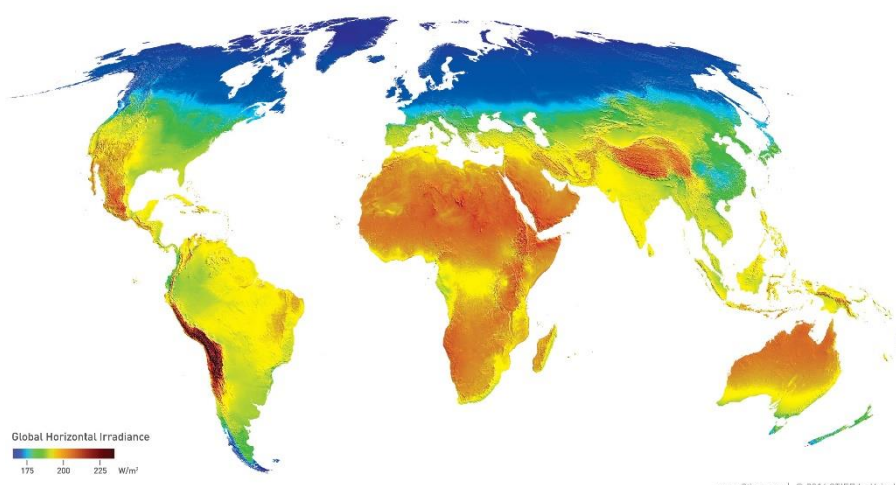
Figure 1. Worldwide mean solar irradiance variation. Reprinted with permission. Copyright (2014) Vaisala Inc. (Source: https://www.3tier.com/static/ttcms/us/images/support/maps/3tier_solar_irradiance.jpg.)

In terms of solar energy utilization, nature has offered us the best-case scenario where photosynthesis can effectively convert and store sunlight in the form of carbohydrate molecules as demonstrated in **Figure 2**. The key processes of natural photosynthesis can be divided into three main steps: (1) initial dual light-harvesting process in photosystem II (PS II) and photosystem I (PS I); (2) spatial charge separation through electron transfer between redox cofactors, and (3) carbohydrate and oxygen

molecule formation at active sites.[7, 10] In order to mimic these biological processes to exploit solar energy, artificial photosynthetic routes need to be well designed and launched.[11-12]
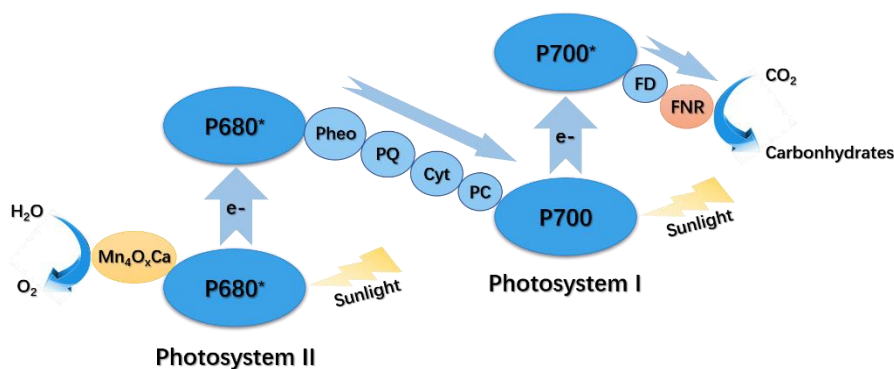
Figure 2. A brief Z-Scheme of natural photosynthesis.

Efficiently splitting water into usable hydrogen could become a new industrial photosynthesis process that would provide clean and carbon-free fuel whose only waste product upon utilization is water. The "Holy Grail" of solar energy conversion and storage, proposed by Allen Bard and Marye Fox in 1995, lies in photoelectrochemical (PEC) water splitting using semiconductor-based photoelectrodes as both light absorber and energy converter to store solar energy in the simplest chemical bond associated with hydrogen (H_2).[13] Since Fujishima's and Honda first report on PEC water using a TiO_2 photoelectrode in 1972,[14] the approaches to address the water splitting problem have been focused on understanding the basic photophysical and photochemical charge behaviour,[15-19] synthesizing novel photoelectrode materials for both anodic/cathodic processes,[20-24] and developing efficient configurations for device assembly.[8, 25-28]
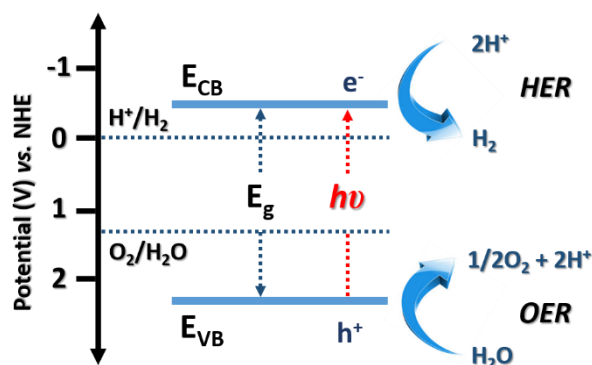
Figure 3. OER and HER for overall solar water splitting.

Basic principles of PEC water splitting

Photoelectrochemistry is an optoelectronic effect that occurs at the interface of a semiconductor photoelectrode and a liquid electrolyte. As seen in **Figure 3**, once upon the illumination, the semiconductor can be excited by the photons with the energy higher than its bandgap (E_g), and the electron-hole pairs can be generated and separated, where the photo-induced electrons exist on the bottom of conduction band position (E_{CB}) while the photo-induced holes are on the top of valence band position (E_{VB}).[29-30] Thermodynamically, water splitting reaction is an uphill reaction in which standard free energy change for the conversion of one molecule of H_2O to H_2 and 1/2 O_2 is $\Delta G^o =$ 237 kJ/mol.[31] Consequently, an ideal semiconductor must have a E_{CB} and E_{VB} that straddle the thermodynamic potentials (E_0) of 0 V *vs.* NHE for H^+/H_2 and 1.23 V *vs.* NHE for O_2/H_2O to meet the requirements of driving hydrogen evolution reaction (HER) and oxygen evolution reaction (OER), respectively (**Equation 1**).[22, 31] However, in order to carry out water splitting reaction, the energy required is frequently reported as 1.6-2.4 eV per electron-hole pair generated to account for these losses of concentration and kinetic overpotentials of HER and OER.[18] Of the two water-splitting half reactions, OER is more kinetically demanding because it requires the coupling of four electrons to four protons in the cleavage of four O-H bonds and formation of two O-O bonds.[32-33]

12

$$H_2O + 2h^+ \rightleftharpoons \frac{1}{2}O_2 + 2H^+ \qquad (OER)$$

$$2H^+ + 2e^- \rightleftharpoons H_2 \qquad (HER)$$

$$H_2O \rightleftharpoons \frac{1}{2}O_2 + H_2 \qquad \qquad \textbf{\textit{Equation 1}}$$
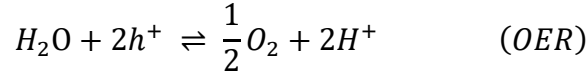
In principle, PEC system consists of a photoelectrode (photoanode or photocathode) as the working electrode for water redox reaction, a current collector as substrate for semiconducting photoelectrode materials, and a counter electrode as the platform for the other half water splitting reaction.[2, 4] Generally, semiconductor-electrolyte interface should be extensively investigated to optimize the PEC performance. Theoretically, the structure of the semiconductor-electrolyte interface is comprised of a space charge layer of semiconductor photoelectrode, a Helmholtz layer (the compact or inner layer), and a Gouy layer (the outer diffuse layer). The thickness of the Helmholtz layer is 0.3-0.5 nm, which is independent of the nature of the photoelectrode. However, the thicknesses of the space charge layer (depletion layer) and Gouy layer decrease with increasing concentrations of charge carriers in the photoelectrode and electrolyte, respectively. For example, the thickness range of the Gouy layer is between 10 and 100 nm in aqueous ionic solutions with low ion concentrations, while it decreases to about a mono-molecular layer in 1 M concentrated ionic solutions.[34]
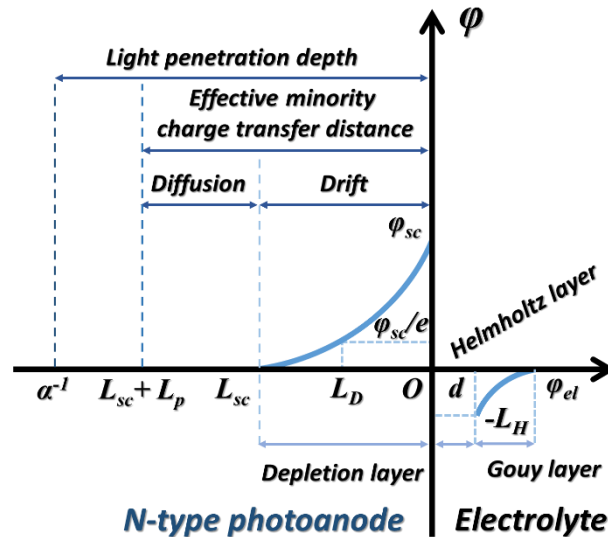
Figure 4. The typical n-type photoanode-electrolyte interface. Reprinted with permission.[34] Copyright (2013) Royal Society of Chemistry.

A more specific typical n-type photoanode/electrolyte interface is illustrated in **Figure 4**. For a film-based n-type photoanode, the effective minority charge (holes) transfer distance ($L_{sc} + L_p$), including the length of diffusion (L_{sc}) and drift (L_p), is within the light penetration depth (α^{-1}) which is determined by the intrinsic absorption coefficients (α), a property of semiconductors. L_D is the Debye length that can be regarded as the characteristic length of potential attenuation. Usually, the space charge layers can be classified into three types: (i) the accumulation layer where mobile majority charge carriers are accumulated; (ii) the depletion layer where mobile majority carriers are depleted and an excess space charge is carried by immobile ionized donors or acceptors; and (iii) the inversion layer where mobile minority charge carriers are accumulated.[35] For the depletion layer, $L_{sc} > L_D$, while $L_{sc} < L_D$ for accumulation layer or inversion layer. And for a typical n-type photoanode, the depletion layer is the most common and important type of the space charge layer.

In the PEC system, an external applied bias is usually required for running the overall water splitting reaction (except the unbiased PEC tandem device), the polarization potential (φ_{sc}) drops on the photoelectrode side is within the depletion layer to tune the level of band bending and the thickness of depletion layer in order to change the property of charge carrier transfer towards to the surface. When the photoelectrode is polarized by a potentiostat at the so-called flat band potential (E_{fb}), the conduction band and valence band are flat throughout the photoelectrode, hence there is no photocurrent flow. In order to generate a redox photocurrent, an external applied bias is moved cathodically (more negative) or anodically (more positive), the E_{CB} and E_{VB} move along with the vacuum level, but the energy levels at the surface stay fixed. It contributes to the formation of band bending and construction of space charge layer so that drives photo-induced holes and electrons separation and migration to achieve the splitting of H_2O.
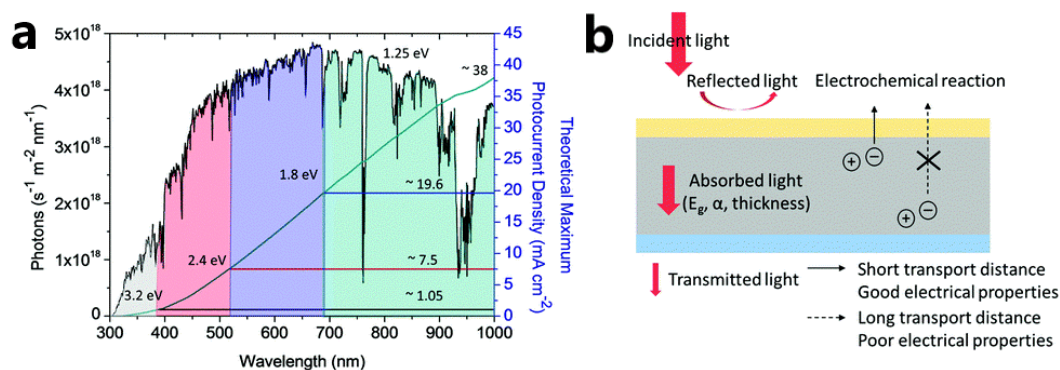
Figure 5. (a) Theoretical maximum photocurrent density depending on the bandgap of semiconductors calculated by assuming all absorbed photons converted to electrons under AM 1.5G solar irradiation, (b) Possible photocurrent loss mechanisms in a real photoelectrode. Reprinted with permission.[36] Copyright (2019) Royal Society of Chemistry.

General considerations for a PEC cell

Performance indicators

In the development of water-splitting photoelectrodes, their performance needs to be evaluated and compared to achieve optimal results. In order to evaluate the PEC performance of a photoelectrode, the most common indicator is the photocurrent density (J) measured in a three-electrode configuration under 1 sun AM 1.5 G illumination (100 mW/cm^2), because the resulting photocurrent is theoretically proportional to H$_2$ or O$_2$ production rate. The photocurrent density presented by photoelectrodes is primarily determined by E_g of the semiconductor, which governs the total amount of photons in the solar flux can be absorbed and converted to electron flows (photocurrent). In **Figure 5a**. the theoretical maximum photocurrent density (J_{max}) can be calculated by integrating the solar flux (Air Mass 1.5 Global) over the photo-active range of wavelengths for a specific photoelectrode.[37-38] Therefore, one facile way to increase J of one photoelectrode towards its J_{max} is to reduce E_g of the semiconductor. **Figure 5b** depicts several factors of photocurrent loss, the very first loss is from the the reflection of the incident light at the photoelectrode surface without absorption, and then

15

transmission is another loss due to incomplete light absorption, resulted from the small E_g, and the

mismatch between α and the thickness of the photoelectrode. The most loss of photocurrent is

originated form the properties of photoelectrode itself, namely electrical loss due to the unfavourable

charge behaviour.
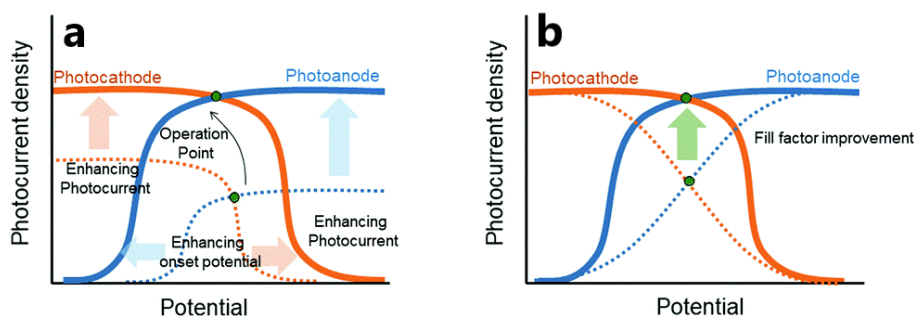
Figure 6. (a) *J-E* curves of a photocathode and photoanode, showing enhancement in V_{oc} and *J*. (b) *J-E* curves of a photocathode and photoanode, showing improvement in *ff*. Reprinted with permission.[36] Copyright (2019) Royal Society of Chemistry.

Similar to photovoltaic (PV) cells, photovoltage (V_{oc}) is a critical property of photoelectrodes, which

corresponds to the maximum driving force available for solar water splitting.[39-40] Basically, V_{oc} is

generated by the Fermi level (E_F) splitting upon the light illumination , where the E_F will split into

the electron quasi-Fermi level ($E_{F,n}$) and hole quasi-Fermi level ($E_{F,p}$). Therefore, any factors, such

as surface states and mismatched band alignment, narrowing the splitting of E_F should be eliminated

in order to increase the output V_{oc}. In the PEC system, together with flat-band potential (E_{fb}), it

determines the onset potential (E_{onset}) range of the photoelectrode. The E_{fb} can define the cathodic

limit of onset potential, but is not very useful in cases of visible light-absorbing photoanodes because

the V_{oc} are generally not enough to drive the water oxidation at an applied bias equal to E_{fb}.[31, 41] **Figure**

6 depicts *J-E* curves of a paired photoanode and photocathode for unassisted water splitting. It is

shown that the optimized trend of *J* and V_{oc} curves from undesired (dot lines) to desired (solid lines)

in **Figure 6a**, in which the intersect current-matching point (operational points) can be enhanced by

increasing J and V_{oc}. Besides V_{oc}, fill factor (*ff*), defined as the maximum power output divided by the V_{oc} and short-circuit current density (J_{sc}), can reflect the trend of how fast the saturated photocurrent can be reached under the anodic or cathodic polarization.[42] **Figure 6b** depicts two photoelectrodes with the same J and V_{oc} (E_{onset}) achieving different efficiencies due to different *ff*, in which a higher *ff* contributes to a saturated photocurrent at a lower potential, and thus a higher operational efficiency.

Critical efficiencies

The efficiency of a photoelectrode is theoretically determined by the energy that can be extracted from the photo-induced electron-hole pairs. In principle, the maximum internal energy that can be extracted from these pairs is given by the difference between E_{CB} and electrochemical redox potential ($-qE$) of H_2O, that is, the barrier height ($q\varphi_b$). To optimize performance of a photoelectrode/electrolyte interface, this difference should be as large as possible. Besides that, some critical efficiencies are also needed to be considered and calculated to evaluate the final solar energy conversion efficiency.
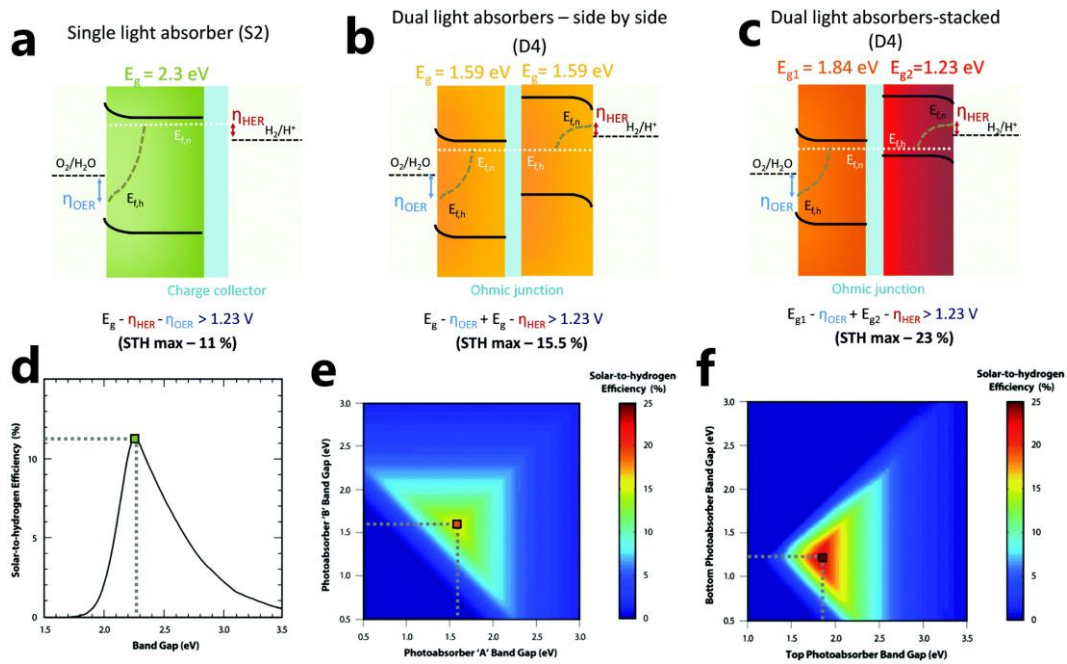
Figure 7. (a) Single light absorber system (S2) configuration, (b) Side-by-side dual light absorber system (D4) configuration, (c) Stacked D4 configuration, (d) Maximum theoretical η_{STH} of S2 configuration as a function of the bandgap. (e) Maximum theoretical η_{STH} of side-by-side D4 configuration. (f) maximum theoretical η_{STH} of stacked D4 configuration. Reprinted with permission.[2] Copyright (2013) Royal Society of Chemistry.

The primary quantified metric for solar water splitting is the solar-to-hydrogen conversion efficiency (η_{STH}), which gives the fraction of the incident solar power that is stored in the H_2 with no external applied bias, and it can be calculated using **Equation 2**:[38]

$$\eta_{STH} = \frac{1.23 \times J_{PEC}}{P_{in}} \times \eta_{O_2/H_2} \qquad \qquad \textbf{\textit{Equation 2}}$$

where J_{PEC} is the measured photocurrent density (mA/cm^2), P_{in} is the incident light intensity (mW/cm^2), η is the Faraday efficiency of O_2 or H_2. In this scenario, O_2 and H_2 gas must be separated to ensure that the reverse reactions are suppressed, such as oxidation of H_2 and reduction of O_2. The maximum η_{STH} and optimal E_g of light absorbers for PEC tandem systems with three configurations are shown: a single light absorber (S2) system in **Figure 7a**, a side-by-side dual light absorber (D4) system in **Figure 7b**, and a stacked dual light absorber (D4) system in **Figure 7c**. The maximum theoretical η_{STH} for S2 system is 11.2 % for a photoelectrode with Eg of 2.26 eV (**Figure 7d**). It is noted that this value falls far short of the thermodynamic limit of ~30% according to previous work,[43] suggesting a significant loss associated with unfavourable charge behaviour in S2 system. By contrast, the maximum η_{STH} is 15.5 % for side-by-side D4 system with the same band gap of 1.59 eV (**Figure 7e**), in which side-by-side D4 system provides more available free energy to meet the requirement of water splitting. Furtherly, the maximum η_{STH} for stacked D4 system can reach 22.8 % (**Figure 7f**), where the photoanode works as the top light absorber (E_g value of 1.84 eV) and photocathode as bottom light absorber (E_g value of 1.23 eV). This enhancement compared to side-by-side system is originated from utilization of more photons in solar spectral range. These theoretical values provide a baseline of reasonable device efficiencies to guide the PEC cell design and fabrication. By far, the

highest η_{STH} reported by Jia *et al.* has achieved as high as 30 % but using a PV-EC system that consists of a triple-junction solar cell (InGaP/GaAs/GaInNAs) and two polymer electrolyte membrane (PEM) electrolysers connected in series.[44] However, the η_{STH} of metal oxide-based PEC and PEC-PV tandem device systems are still low with a value of under 10 %.[45-48]

Generally, most reports are focusing on the evaluation of a single photoanode or photocathode with an external applied potential (E_{app}), so that the applied bias photon-to-current conversion efficiency (η_{ABPE}) is always employed to reveal the conversion efficiency under polarization. Moreover, other critical efficiencies need to be precisely measured and calculated to estimate the PEC performance.[37-38] For instance, incident photon to current conversion efficiency (η_{IPCE}) can reveal the percentage of incident photons those are converted into electrons collected by the PEC cell as a function of the wavelength of the illuminating light; Faradaic efficiency (η_F) can demonstrate the ratio between the charge used for the evolution of H_2/O_2 and the overall charge flow through the external circuit, which can reveal that the generated photocurrent is either from photoelectrode self-oxidation/reduction or water redox reaction. Others like charge separation efficiency (η_{CSE}) and charge injection efficiency (η_{CIE}) can be also investigated in some particular cases to study charge behaviour in the bulk and on the surface of a photoelectrode.[49-52]
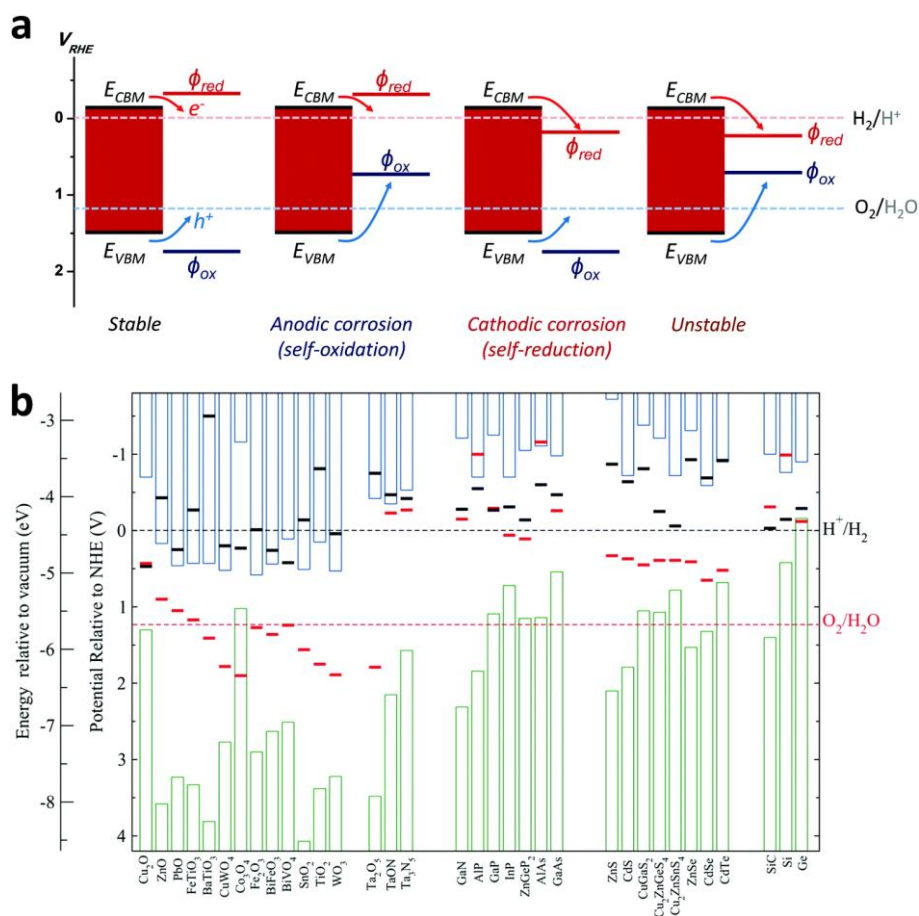
Figure 8. (a) Chemical stability of a photoelectrode without any bias in view of thermodynamics. Reprinted with permission.[34] Copyright (2013) Royal Society of Chemistry. (b) Calculated oxidation potential ϕ_{ox} (red bars) and reduction potential ϕ_{re} (black bars) relative to the NHE and vacuum level for a series of semiconductors in solution of pH = 0, the ambient temperature of 298.15 K, and pressure of 1 bar. The water redox potentials $\varphi(O_2/H_2O)$ and $\varphi(H^+/H_2)$ (dashed lines) and the valence (green columns) and conduction (blue columns) band edge positions at pH = 0 are also plotted. Reprinted with permission.[53] Copyright (2012) American Chemical Society.

Operational stability

Stability is one of the biggest challenges for the commercialization of PEC water splitting cells, which significantly impacts on the cost of producing H_2.[2, 54] Whereas commercial solar cells exhibit an operational stability for over 20 years,

making high stability in PEC cells is a daunting task. Generally, most semiconducting photoelectrodes are thermodynamically unstable for water splitting, including Si, III-V group compounds, and (oxy)nitrides, because their calculated semiconductor oxidation potentials are above the theoretical

20

water oxidation or reduction potential.[55-56] As shown in **Figure 8a**, the semiconductors whose E_{VB} is less negative than water oxidation and E_{CB} is less than water reduction suffer from the anodic self-oxidation and cathodic self-reduction, respectively. A highly efficient, low band gap material that is also stable at the same time is yet to be found since photoelectrodes have to act as both solar light absorber and energy converter. Moreover, high-valence metal oxides can be kinetically stable at high oxidative potentials or in extreme pH electrolytes, while non-oxide semiconductors or low-valence metal oxides can be kinetically stable to the reduction of photo-induced electrons (**Figure 8b**).[53, 57] Besides the intrinsic corrosion, thermodynamically stable metal-oxide semiconductors are also potentially susceptible to generated H_2O_2 corrosion. For instance, WO_3 photoanodes suffer from dissolution due to H_2O_2 production rather than O_2 evolution, because the surface-active sites tend to a two-electron path catalysis than the four-electron route.[58] The same case can also be found for $BiVO_4$ photoanodes.[59-60]

Although extensive investigations have been conducted to design stable photo-response materials or introduce a protection layer on surface of photoelectrodes, intrinsic limited properties are not easy to be improved.[61-63] Zhou *et al.* coated a thin ~ 50 nm film of cobalt oxide (CoO_x) n-type crystalline silicon photoanode,[61] in which CoO_x thin film can form a heterojunction with the silicon so that provided a V_{oc} of 575 mV, and stabilize the unstable silicon photoanode operated in aqueous alkaline electrolytes. Moreover, CoO_x can act as a cocatalyst for water oxidation by reducing the kinetic overpotential, which is highly sluggish for barely silicon photoanode. This silicon/CoO_x photoanode exhibited a continuously operational stability over 2500 h (100 days), which is the longest operation reported so far. Recently, a *in situ* compensation mechanism is proposed for maintaining the operational stability of photoelectrodes.[64] Taking a bismuth vanadate photoanode as a phototype, Lee and Choi demonstrated a strategy of tuning composition of electrolyte with excessive V^{5+} to suppress the loss of V^{5+} from bismuth vanadate itself,[65] and thus decreasing the photocorrosion and enhancing the long-term stability for nearly 500 h. Similarly, Kuang *et al.* utilized an *in situ* compensation

strategy to enhance the self-generation and regeneration of NiFe-based cocatalyst, showing a stable PEC O_2 evolution for > 1100 h at a potential as low as 0.4 V *vs.* RHE, longest operational stability for metal-oxide based photoelectrodes.
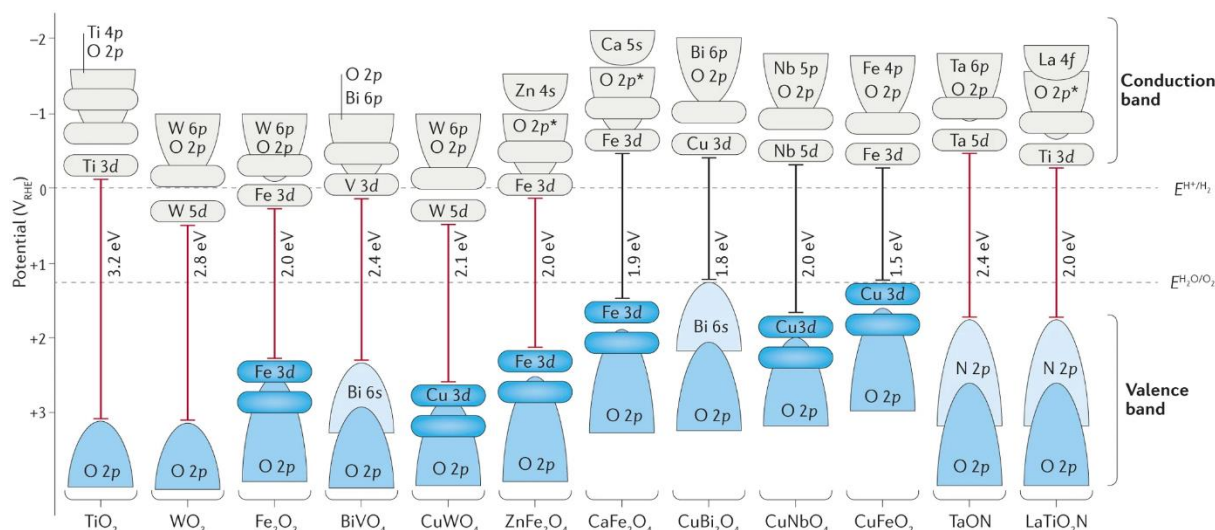
Figure 9. Bandgap structure and selected crystal structures of metal oxide and oxynitride semiconductors for PEC applications. Contribution of metal cation and oxygen anion states to E_{CB} and E_{VB}. The bandgap energy (red for n-type, black for p-type) is shown with respect to RHE and the water redox energy levels (assuming Nernstian behaviour for the band-edge energies with respect to electrolyte pH). Reprinted with permission.[66] Copyright (2016) Nature Publishing Group.

Emerging photoelectrodes

In this section, a literature review of emerging photoelectrode materials, including metal oxides, metal chalcogenides, silicon and polymeric carbon nitride, is demonstrated and summarized in terms of basic electronic and chemical structure. Particularly, the aim of this section is to highlight the key issues associated with each class of materials.

Metal oxides

Semiconducting transition metal oxides are attractive photoanodes for solar water oxidation, because the high electronegativity of oxygen results in the formation of stable compounds based on O^{2-} anions.

The band and crystal structures of some common metal oxides and oxynitride are shown in **Figure 9**.[20, 67] The binary metal oxides, whose metal cations possess empty d bands (d^0) such as Ti^{4+} and W^{6+}, usually have a E_{VB} strongly determined by the O *2p* levels (*e.g.,* TiO_2 and WO_3), showing a high stability towards solar water oxidation. And due to the high ionic character, these binary metal oxides always exhibit a large separation between the band edges, and thus a large E_g value. As a result, in order to utilize more photons in the solar spectrum, doping or introducing mid-gap defect states are required to tune the charge excitation process to enhance the PEC performance.[68-69] Metal oxides containing metal cations with d^n electronic configurations, such as Fe_2O_3, often have smaller E_g due to the great influence of metal-metal *d-d* transitions, and hence are good visible light absorbers.[23] However, charge carrier transport is often limited due to the low polaron conductivity.[70-71] Another promising photoanode material is ternary oxide $BiVO_4$ with a proper E_g of 2.4 eV and suitable E_{VB} edge location for solar water oxidation.[72-73] However, recent studies unveiled that poor electron transport due to limited overlap between V *3d*-V *3d* and V *3d*-Bi *6p* orbitals in the conduction band limits the photocurrent. Although the reported experimental photocurrent density for $BiVO_4$ is approaching its theoretical 7.5 mA/cm^2,[74] further efforts should be still made in the improvement of E_{onset} and *ff*.

By contrast, Cu-based binary and ternary oxides are investigated as photocathodes as the hybridization of Cu *3d*-O *2p* in the E_{VB} of Cu_2O yields a small ionic character,[75] which can promote an increased E_{VB} dispersion, and thereby resulting in favorable p-type semiconductor conductivity.[76] Despite Cu_2O is a promising photocathode candidate, it is intrinsically vulnerable to self-redox photocorrosion and H_2O chemical corrosion during PEC operation. Surface protection layers can be introduced in order to maintain the long-term operational stability.[63, 77] Moreover, the minority charge carrier (electron) diffusion length is approximately 200 nm or less.[78] Efficient nanostructuring that favors for charge carriers transport is highly desired as well.
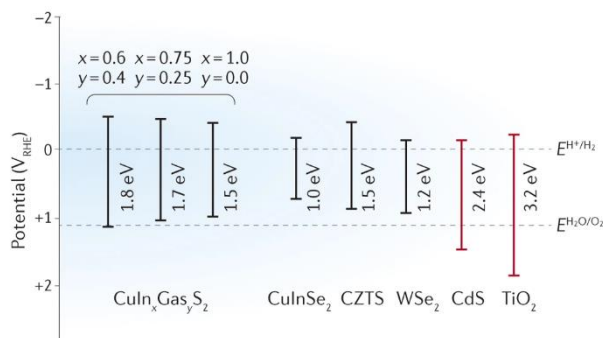
Figure 10. Bandgaps of selected mental chalcogenides with respect to RHE (pH 7), with the exception of WSe_2 which is given at pH 0 because the E_{FB} exhibits a strong variation with pH and is below the water reduction potential at pH 7. Reprinted with permission.[66] Copyright (2016) Nature Publishing Group.

Metal chalcogenides

Sulfur and selenium have higher lying p-band energy levels than oxygen, and can be used to achieve smaller bandgaps compared with oxides.[66] Therefore, metal sulfides and selenides can be used as photocathodes for solar water splitting, such as layered Sb_2Se_3, chalcopyrite $Cu(In,Ga)S(Se)_2$, and kieserite $Cu_2ZnSnS(Se)_4$.[79-81] In fact, these materials have received considerable attention for PV cells attributed to high extinction coefficients, long charge-transport characteristics, and tunable bandgaps (1.0-2.4 eV). Although metal chalcogenides exhibit excellent photophysical properties, they suffer from a major drawback of low chemical stability. Efforts have been made in introducing various protection layers (*e.g.,* TiO_2 and SnO_2) to stabilize the photocathode as well as minimizing undesirable bulk and surface defects.

Another challenge in commercial application of metal chalcogenides is the high cost associated with photocathodes and cocatalysts. For instance, despite recent advance of developing $Cu(In,Ga)S(Se)_2$ (CIGS) photocathode enabling a photocurrent density as high as 25 mA/cm^2 at 0 V *vs.* RHE,[82] the cost of In and Ga is still high. By replacing expensive trivalent cations (*i.e.*, In^{3+} and Ga^{3+}) with cheap di- and tetravalent cations (*i.e.*, Zn^{2+} and Sn^{4+}), kieserite $Cu_2ZnSnS(Se)_4$ (CZTS or CZTS) is emerging

24

as one of low-cost photocathode candidates for solar water splitting.[81] Meanwhile, most reports on

fabricating photocathodes are still using noble metals (*i.e.*, Pt) as cocatalysts to promote the HER

process. Therefore, efficient earth abundant transitional metal-based cocatalysts that can improve the

J, *ff*, and E_{onset} of metal chalcogenide photocathodes are highly desirable.[83-86]
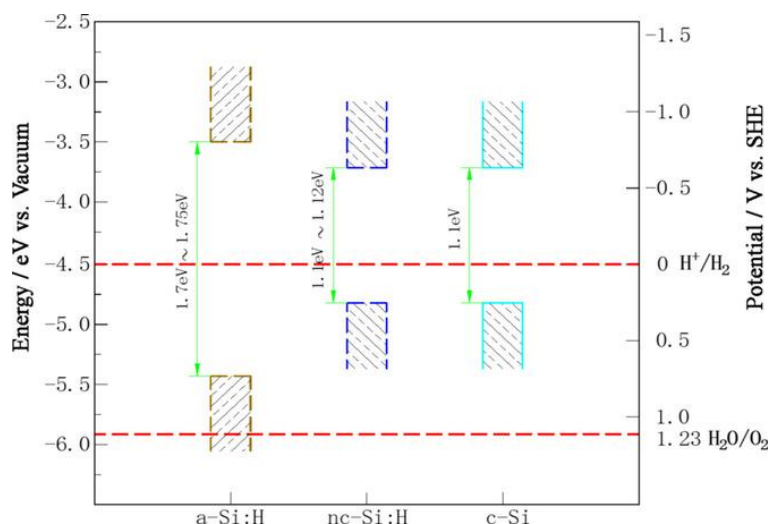
Figure 11. The energy band diagrams of a-Si, mc-Si, and c-Si. Reprinted with permission.[87] Copyright (2017)
Wiley-VCH Verlag GmbH & Co. KGaA.

Silicon

As the most fundamental component of silicon-based PV cells, semiconducting silicon (Si) materials

with various structures have been developed, including crystalline Si (c-Si), nano-crystalline Si (nc-

Si), micro-crystalline Si (mc-Si) and amorphous (a-Si).[87-89] In principle, intrinsic c-Si can be doped

with elements in different valence states to form n-type or p-type semiconductors, enabling c-Si can

be used as photoanodes and photocathodes for solar water oxidation and reduction.[21] The c-Si, with

E_g of about 1.1 eV that could utilize a large portion of the solar spectrum (**Figure 11**) and a theoretical

maximum photocurrent density of 43 mA/cm^2 (without correcting surface reflection), is emerging as

a suitable candidate for a photoelectrode material for solar water splitting.[90] As the charge carrier

mobility of c-Si is 1400 cm^2/V·s for electrons and 450 cm^2/V·s for holes, the maximum diffusion length of carrier in c-Si can reach approximately to millimetres. Therefore, the c-Si photoelectrodes are often fabricated with a thickness of larger than 400 μm, and the light transmission loss is almost negligible in light harvesting.[21] Based on the above analysis, nanostructured silicon, such as nanowires[9], nanopillar arrays[91], and nanocone arrays[92], can be employed to improve photons scattering and interference, and thus enhance light harvesting efficiency. In principle, V_{oc} of c-Si is relatively small for driving solar water splitting due to its small E_g and unfavourable band position compared to the metal oxides. As a result, buried p-n junction should be built in order to increase the V_{oc}.[89, 93] Besides the tuning the properties in bulk, surface condition should be considered as well. Theoretically, Si crystals are formed with four covalent bonds in tetrahedral coordination. When a Si crystal is shrunk into the nanoscale, some covalent bonds should be broken to leave dangling bonds on surface.[94] Although the surface dangling bonds provide an opportunity for surface modifications, these exposed unsaturated bonds dramatically decrease the reactivity and stability. As a result, a protection layer (*e.g.,* intrinsic SiO$_2$, and TiO$_2$)[95-96] or cocatalyst layer (*e.g.,* NiOOH/FeOOH and CoP)[86, 97] need to be deposited and passivate the surface.
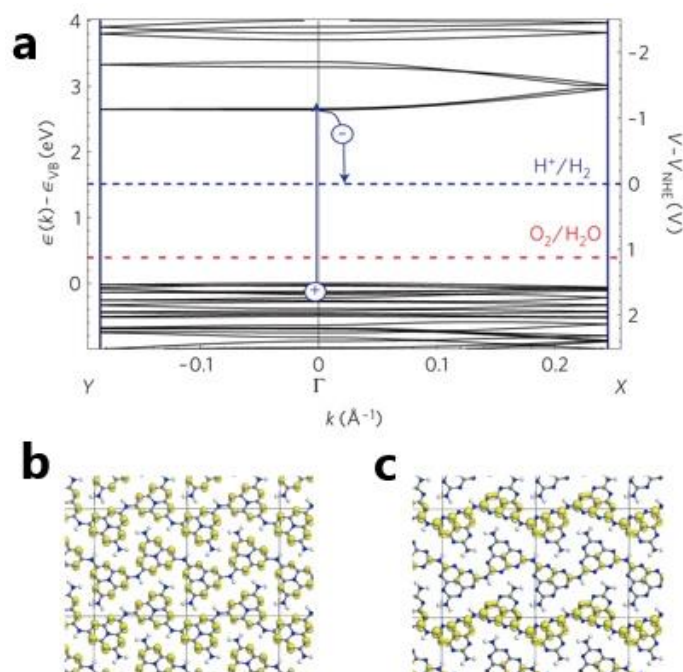
Figure 12. Electronic structure of polymeric melon. (a) Density-functional-theory band structure for polymeric melon calculated along the chain (Γ–X direction) and perpendicular to the chain (Υ–Γ direction). The position of the reduction level for H^+/H_2 is indicated by the dashed blue line and the oxidation potential of H_2O/O_2 is indicated by the red dashed line just above the valence band, (b) the Kohn-Sham orbitals for E_{VB} of polymeric melon, (c) the corresponding E_{CB}. The carbon atoms are grey, nitrogen atoms are blue and the hydrogen atoms are white. The isodensity surfaces are drawn for a charge density of $0:01q_e$ Å^{-3}. Reprinted with permission.[98] Copyright (2009) Nature Publishing Group.

Carbon nitride

Graphitic carbon nitride (g-C$_3$N$_4$) has emerged as a promising heterogeneous catalyst for solar energy conversion attributed to tunable electronic band structure, high stability under harsh chemical conditions, and earth abandunce.[99-100] **Figure 12a** demonstrated that the band structure of polymeric melon structure has a non-isotropic band structure with a direct bandgap at the Γ point and only dispersion along the Γ–X direction parallel to the chain. The wavefunction of the valence band in **Figure 12b** is a combination of the HOMO level of the melem monomer, which is derived from nitrogen p_z orbitals. The conduction band can similarly be connected to the LUMO of the melem monomer, which consists predominantly of carbon p_z orbitals (**Figure 12c**).[98] Despite the fact that suspension-based g-C$_3$N$_4$ photocatalysts have shown some success in water splitting,[101-102] PEC

application of g-C$_3$N$_4$ is still on early stage and less reported. This is partially due to poor crystallinity, low conductivity, and difficulties in fabricating high-quality g-C$_3$N$_4$ layer on substrates.[103-105]

Polymeric g-C$_3$N$_4$ is often synthesized with a low crystallinity compared to metal oxides and Si, as a result, its trap state density is relatively high.[106] Although long-lived charge carriers can be observed due to these deep trap states, it does not ensure a good PEC performance. Efficient engineering to eliminate the deep trap states can contribute to a longer charge diffusion length, and thus a higher PEC performance.[107] The conductivity is not a key factor in suspension-based photocatalysis system, because the charge transport can reach the surface from any direction. However, in the film-based PEC system, the direction of charge transport needs to be controlled, with minority charge moving to the surface while majority charge to the current collector. Therefore, using doping or coupling conductive species to enhance the conductivity is crucial for enhancing PEC performance.[108-109] Finally, the photoelectrode fabrication is important as well to enable a strong adhesion to the substrate. Various strategies like thermal vapor deposition,[110] doctor blading,[105] and electrophoretic deposition,[111] are employed to fabricate a stable g-C$_3$N$_4$ film on conductive substrates.

Based on the above literature overview, although many kinds of semiconductors have been investigated as photoelectrodes for solar water splitting, no single semiconductor has yet satisfied all the basic requirements for manufacturing a practical photoelectrode, including low cost, high efficiency and stability under real operation conditions. Therefore, mechanistic insights into the photo-induced charge behaviour on bulk transfer and surface reaction is crucial for improving the PEC performance and benefitting for scaling up from a laboratory bench scale to an industrial solar farm scale.

Photophysical and photochemical behaviour of charge carriers in PEC water splitting

Fundamental understanding in semiconductor-electrolyte interfacial energetics, and corresponding photophysical/photochemical behaviour of charge carriers in a photoelectrode is the key for

constructing efficient PEC systems. In principle, when a semiconductor is brought into contact with a liquid that contains a redox couple (A/A^-) possessing an energy level of $-qE$, where E is the Nernstian potential of A/A^-, electrons will flow between the semiconductor and the liquid until equilibrium is established. In the case of a PEC system, the redox couples are the H^+/H_2 for a p-type semiconductor photocathode, and the H_2O/O_2 for an n-type semiconductor photoanode. And interfacial electron flow will lead to the reconstruction of the electric field to balance the initial difference between the E_F of photoelectrode and $-qE$ of H_2O. At equilibration, the E_F and $-qE$ are the same everywhere.
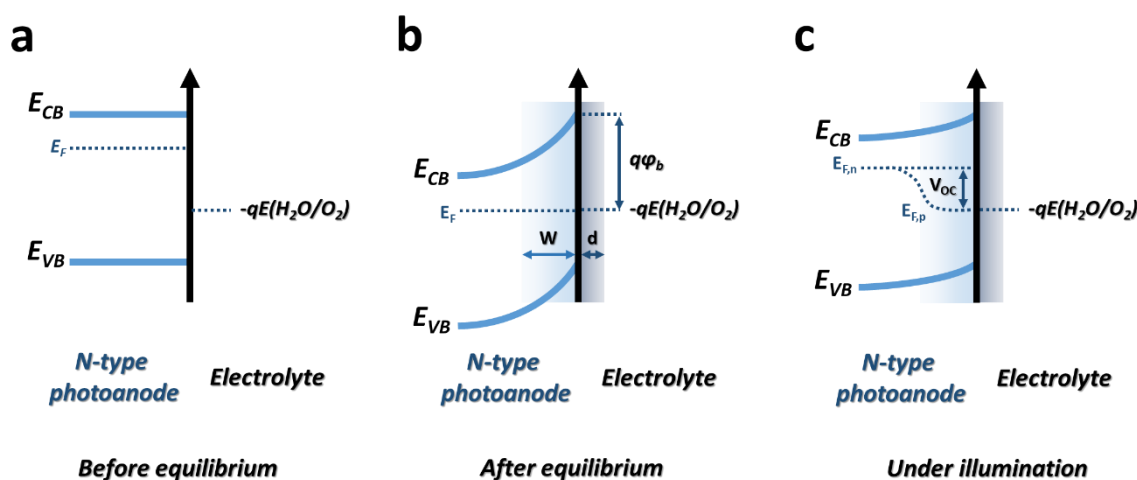
Figure 13. Band energetics on a typical n-type photoanode/electrolyte interface (a) before equilibration, (b) after equilibration in dark, and (c) in quasi-static equilibrium under steady state illumination. Reprinted with permission.[6] Copyright (2010) American Chemical Society.

Taking an n-type photoanode as an example (**Figure 13a**), the excess positive charges in the photoanode will contribute to a more positive E_F than $-qE$ of H_2O/O_2 before equilibrium, arising from the dopant atoms with more valence electrons than the host atoms. When the photoanode is in contact with water, the E_F and $-qE$ tend to be equal due to the interfacial electrons flow (**Figure 13b**). As the energetics of the surface in photoanode keep the same due to the pinning effect, the surface band bending is formed. The positive charge is spread out over the depletion zone of a certain width (W), whereas the negative charge is spread over the Helmholtz layer (d) in water. Under illumination, the

E_F of the semiconductor photoanode will split into two energy states, the $E_{F,n}$ and $E_{F,p}$ as shown in

Figures 13c. The difference between these two energy states under the condition with no net current

flow is referred to as the open-circuit voltage (V_{oc}). It is notable that whether the overall water splitting

can be achieved is determined by $E_{F,n}$, $E_{F,p}$, and V_{oc}, rather than the inherent band edge positions of

the semiconductor photoelectrodes in the real conditions. The p-type semiconductor photocathodes

behave in an analogous manner, except that the ionized dopants are negatively charged and the

electrolyte ion is positively charged. Therefore, p-type semiconductor photocathodes favour electron

flow into the positively charged acceptor species (H^+/H_2) at the interface.
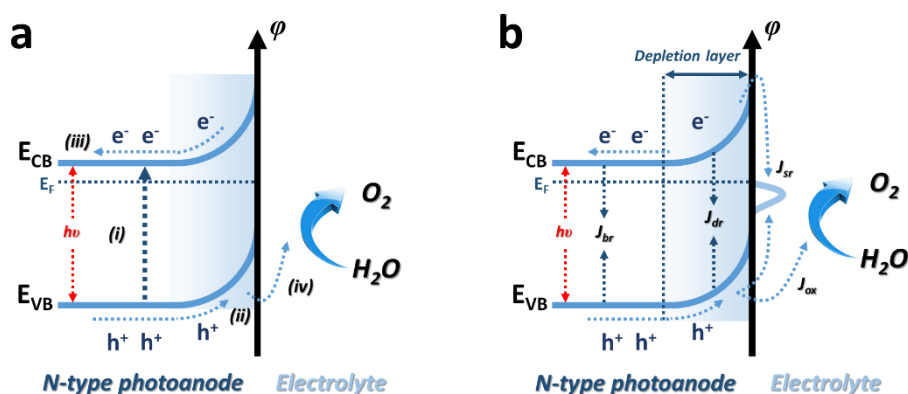
Figure 14. (a) Photophysical and photochemical process of a typical n-type photoanode for PEC water oxidation, and (b) potential recombination pathways for photo-induced holes and electrons, including bulk recombination (J_{br}), depletion region recombination (J_{dr}), and surface recombination (J_{sr}). Reprinted with permission.[6] Copyright (2010) American Chemical Society.

Based on this model, the corresponding photophysical and photochemical process of charge carriers

in a photoanode is given in **Figure 14a**, involving four major steps: (i) photon absorption to generate

electron-hole pairs, (ii) photo-induced hole migration to the surface of the photoanode, (iii) photo-

induced electron transport via external circuit to the counter electrode, and (iv) surface water-

oxidation catalysis.[19, 31] Therefore, an effective photo-induced charge regulation and utilization

strategy that can suppress unfavourable charge recombination plays a significant role in achieving a

high PEC solar energy conversion efficiency. Potential charge recombination pathways of photo-induced hole-electron pairs are illustrated in **Figure 14b**: (i) bulk charge recombination (J_{br}) occurring outside the depletion layer, where the distance to the solid-electrolyte interface is shorter than the penetration depth of the light but longer than the effective minority holes transport distance, (ii) depletion region charge recombination (J_{dr}) occurring inside the depletion layer, where the charge recombination in this region is very low due to a large electric field in the semiconductor ($\sim 10^5$ V/cm) caused by the band bending, (iii) surface charge recombination (J_{sr}) occurring on the photoanode/electrolyte interface due to the presence of intrinsic surface states and slow surface reaction kinetics.[6] As mentioned above, the semiconductor-based PEC water splitting is realized by such complex photo- and electro- chemical processes. Therefore, in order to enhance PEC performance, it is highly desirable to utilize efficient strategies to simultaneously promote the generation and migration of charge carriers during the reactions.

Recent advances in regulating charge behavior in bulk

In this section, it is comprehensively summarized recent advances in regulating charge behavior in bulk by morphological control, heteroatom/defect doping, crystal facet engineering, and junction fabrication, and thereby favoring for the light harvesting, charge transport and charge separation in bulk.

Morphological control

Physical and chemical properties for materials are critically determined by their structure, especially, when the size of materials is reduced to nanoscale dimension. Therefore, design and fabrication of advanced photoelectrodes with well-defined one dimension (1D), two dimension (2D), and three dimension (3D) nanostructures that are beneficial for light trapping, surface area enlargement, charge transport and mass transport, is an effective approach to enhance overall PEC performance.[9, 112-114]
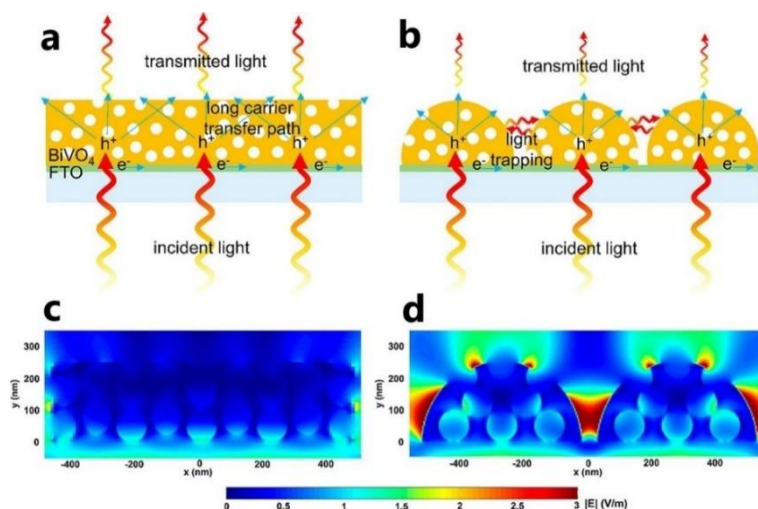
Figure 15. Schematic illustration of the optical absorption and charge carrier transport of thin-film-based BiVO$_4$ photoanode with porous structures: (a) flat BiVO$_4$ film and (b) hierarchical BiVO$_4$ nanostructured film composed of sphere arrays. Comparison of simulated cross-sectional electric field intensity distribution of the electromagnetic wave at 420 nm in (c) flat BiVO$_4$ film and (d) hierarchical BiVO$_4$ film, respectively. The thickness of BiVO$_4$ film and the void diameter are set to 250 and 100 nm, respectively, in the simulation. Reprinted with permission.[115] Copyright (2017) American Chemical Society.

A unique highly oriented and ordered nanostructured platform can provide a gradient of refractive index at the interface between the liquid and semiconductors, dubbed as the light-trapping effect, in which this suitable antireflection layer can suppresses reflection and enhance nondirectional scattering of incident light.[112, 116] For instance, Zhou *et al.* developed a 3D ordered hierarchical BiVO$_4$ nanosphere arrays (NAs) photoanode composed of small nanoparticles and sufficient voids (**Figure 15a** and **b**).[115] This unique nanostructure induced efficient light harvesting by rendering a high capability of multiple light scattering in the sphere arrays and voids along with the large effective thickness of the BiVO$_4$ photoanode. Meanwhile, cross-sectional electric field intensity distributions of the electromagnetic wave plotted in **Figure 15c** and **d** show that the incident light is scattered and trapped in hierarchical BiVO$_4$ NAs as the distance between nanosphere arrays approaches the wavelength of incident light. By contrast, the electric field intensity was evenly distributed in the bulk counterpart. The areas between adjacent NAs exhibited an intensified electric field, corresponding to light trapping in these areas. Shi *et al.* fabricated a helical WO$_3$ arrays photoanode by oblique angle

deposition.[117] Theoretical simulations and analyses suggested that this unique helical arrays scatter light effectively with an electric field distribution of ~ 3-fold higher compared to other nanostructures (such as stack of nanoparticles, nanorods, and thin films) due to their greater cross-sectional light-scattering.
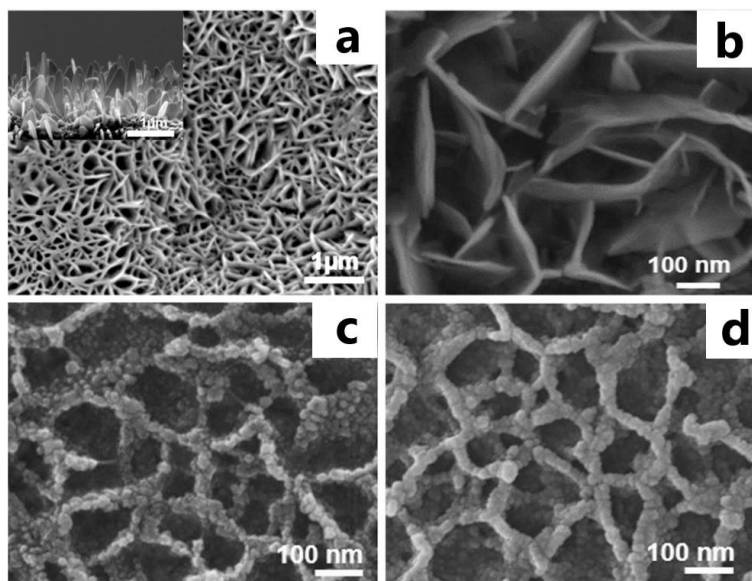
Figure 16. (a) and (b) FESEM surface views of vertically aligned Fe_2O_3 nanosheet films, (c) Ag NPs/Fe_2O_3, (d) CoPi/Ag/Fe_2O_3. Reprinted with permission.[118] Copyright (2016) Wiley-VCH Verlag GmbH & Co. KGaA.

Nanostructured photoelectrodes, such as 2D nanosheets, always exhibit a larger surface area or surface atoms compared to the bulk counterpart.[119-121] Therefore, they can provide more reaction active sites and promote charge migration across both semiconductor/electrolyte and semiconductor/cocatalyst interface, enabling a redox half-reaction of H_2O to proceed at a sufficiently high rate of turnover. The high surface area of nanostructured photoelectrodes will reduce the required overpotentials and flux density for the charge transfer of half reactions, and thus outcompeting the possibility of surface recombination and increase the values of *ff*, E_{onset}, and the eventual energy efficiency.[122] For instance, Peerakiatkhajohn *et al.* synthesized the vertically aligned Fe_2O_3 nanosheets on Fe foil substrates by anodization method (**Figure 16a** and **b**).[118] Due to the well-

defined nanosheet structure, vertically aligned Fe_2O_3 nanosheets effectively provide a large surface area to react with H_2O and a stable substrate for hosting surface plasmon resonance Ag nanoparticles (**Figure 16c**) and CoPi cocatalysts (**Figure 16d**). Meanwhile, as the Fe_2O_3 was synthesized in situ on the Fe foil by the anodization process, an intimate connect is constructed between photocurrent generator (Fe_2O_3) and collector (Fe foil). Zhou *et al.* successfully synthesized an ordered macro-porous $BiVO_4$ photoanode with controllable dual porosity by a modified colloidal crystal templating method.[123] It is notably that the PEC performance shows strong dependence on the relative size of the two pores, in which the optimized periodically ordered macro-porous architectures feature on photo-induced charge migration and mass transport for PEC water splitting.
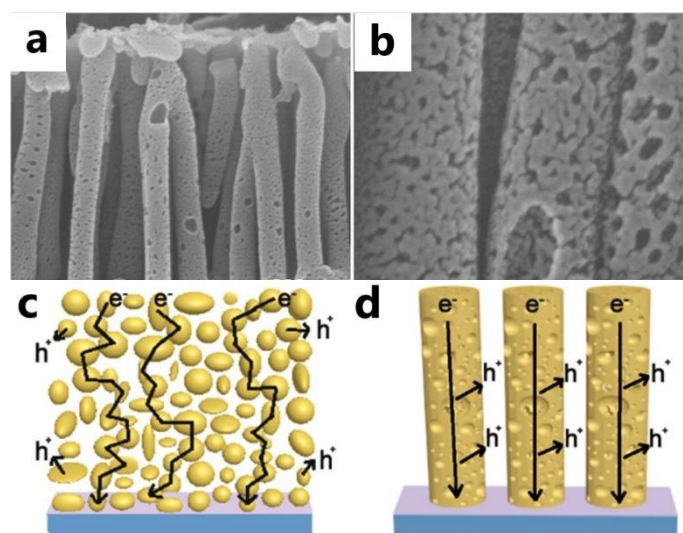
Figure 17. Morphology and structure characterization of the C_3N_4 photoanode. (a) Cross-sectional SEM image, (b) magnified view of the cross section. Schematic diagrams showing the transport pathway of electrons in (e) nanoparticle film (NPF) and (f) porous nanorods (PNR) of C_3N_4. Reprinted with permission.[124] Copyright (2018) American Chemical Society.

Generally, efficient transport of majority charge carriers in nanoparticle-based photoelectrodes is regarded as one of critical steps during solar energy conversion.[113, 125-126] Rational nano-engineering of photoelectrodes to generate charge transport favoring nanostructure, such as 1D nanorods, is essential to improve the PEC performance. For instance, Guo *et al.* reported a novel photoanode based

on a vertically aligned C_3N_4 porous nanorod arrays (**Figure 17a** and **b**) prepared in situ, using a thermal polycondensation approach, with anodic aluminium oxide as the template.[124] In the case of C_3N_4 nanoparticle film, it is obviously seen that the photo-induced electron transport is characterized by slow diffusion through interparticle pathways to reach the charge collector (**Figure 17c**). Particular, thermally activated hopping of electrons via multiple trapping and detrapping can occur at the interparticle boundaries, which increase the probability of charge recombination and back reactions. In contrast, the vertical aligned nanorod arrays of C_3N_4 with decreased interfacial boundaries are beneficial to the smooth migration of photo-induced electrons to the back contact (**Figure 17d**), accelerating electron transport and thus lowering the recombination probability of charge carriers.
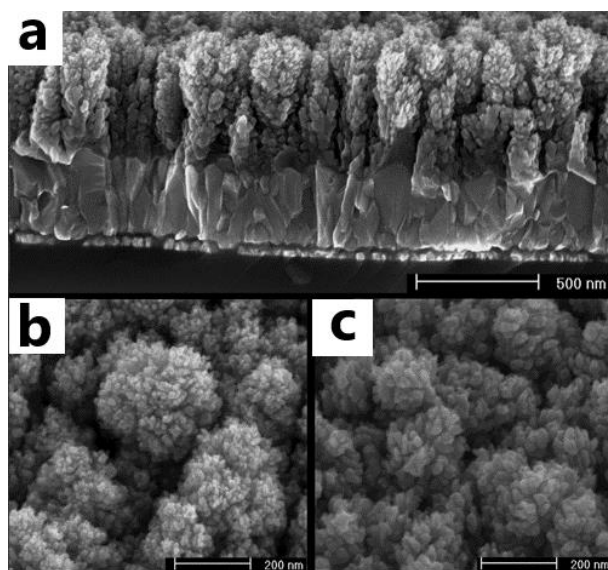
Figure 18. High-resolution images of Fe_2O_3 films grown by APCVD on FTO. (a) Cross-section of 500 nm thick mesoporous Si-doped Fe_2O_3 on 400 nm thick compact FTO. (b) Top view (45° tilted) of the Si-doped Fe_2O_3 film. (c) Top view (45° tilted) of an undoped Fe_2O_3 film. Reprinted with permission.[127] Copyright (2006) American Chemical Society.

Similarly, in the case of Fe_2O_3 photoelectrodes, a thickness of 500 ~ 600 nm is always needed in order to sufficiently absorb sunlight when considering its relatively poor absorptivity.[23, 128] However, the extremely short hole diffusion length (2 ~ 4 nm) and the width of depletion layer (10 ~ 20 nm) make it a great challenge for charge transport across a nearly micrometer-scale distance. Kay *et al.*

utilized an atmospheric pressure chemical vapor deposition (APCVD) method with $Fe(CO)_5$ and tetraethoxysilane (TEOS) as precursors to synthesize a nano-branched Si-doped Fe_2O_3 photoanode with the thickness of 500 nm and a minimum feature size of 5-10 nm on each aggregate (**Figure 18**). [127] Using this method of fabrication, the best Fe_2O_3 film produced a photocurrent density of 2.2 mA/cm^2 at 1.23 *vs.* RHE under standard illumination in 1 M NaOH. This unprecedented high efficiency is in part attributed to the nano-branched structure which simultaneously minimizes the diffusion distance of photo-induced holes to reach the photoanode/electrolyte interface while still allowing efficient light absorption. Additionally, it is found that an increase in the carrier-gas flow rate from 2 to 6 L/min (2L-Fe_2O_3 and 6L-Fe_2O_3) greatly enhanced charge transport of Fe_2O_3 and thus the PEC performance, with little change of the film's morphology (**Figure 19a** and **f**). A shorter gas residence time resulted from higher carrier-gas flow rate contributes to a better adhesion between each particle during the growth of the film.[129]
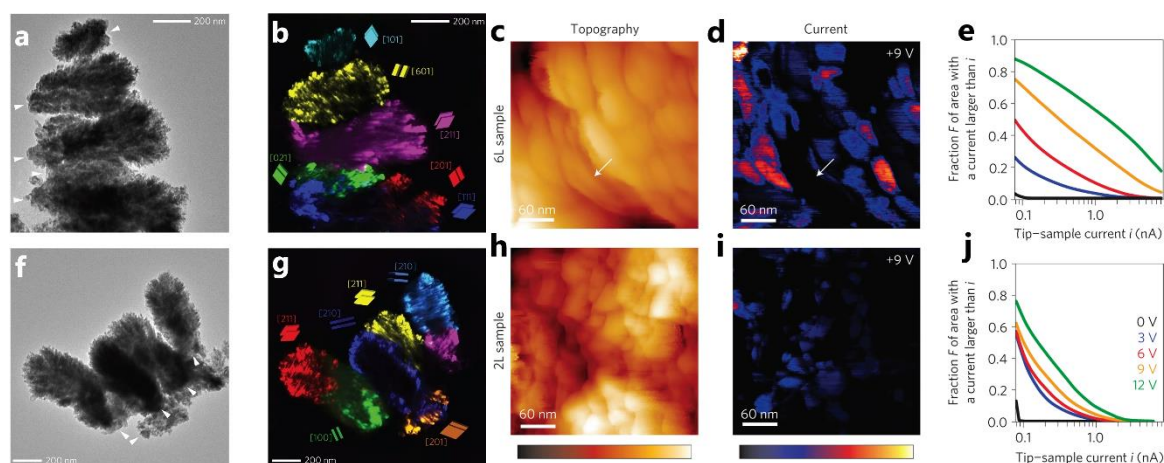
Figure 19. Nanostructured hematite aggregates whose charge transport properties are affected by high-angle grain boundaries: (a-e) for 6L-Fe_2O_3 and (f-j) for 2L-Fe_2O_3. (a) and (f) bright field TEM images, (b) and (g) dark field TEM images, (c) and (h) C-AFM topography, (d) and (i) related current maps at a tip–sample voltage of 9 V, (e) and (j) Statistical analyses of the current maps: the curves represent the fraction F of the area exhibiting a current larger than the current *i* shown on the horizontal axis. Each curve shows these results for a different applied voltage. Reprinted with permission.[130] Copyright (2013) Nature Publishing Group.

In a followed up research by the same group, in order to identify this champion nano-branched Fe_2O_3 by correlating nano-branched structure and charge transport, an approach was developed to correlate the spatial distribution of crystalline and current-carrying domains in entire nanoparticle aggregates by crystal-by-crystal imaging of entire nanocrystal aggregates using dark-field transmission electron microscopy (DF-TEM) and conducting atomic force microscopy (C-AFM). In detail, bright-field TEM (BF-TEM) images presented the branched aggregates consisting of small nanoparticles for both 2L-Fe_2O_3 and 6L-Fe_2O_3 photoelectrodes (**Figure 19a** and **f**), and the related regions with the same colour in DF-TEM imaging represent mosaics of nanocrystals with similar but not identical orientations (**Figure 19b** and **g**). It is clearly observed that each of the upper three aggregates ([101], [601], and [211])shows just one colour for the case of 6L-Fe_2O_3, suggesting that most aggregates of 6L-Fe_2O_3 have a single principal crystallographic orientation (**Figure 19b**). However, multiple crystal orientations are found in one aggregate of 2L-Fe_2O_3 (**Figure 19g**), forming many high-angle grain boundaries. These grain boundaries can generate a potential barrier that blocks majority carrier charge (electrons for n-type Fe_2O_3) transport between adjacent crystals. In addition, the potential drop at high-angle grain boundary barriers decreases the potential that falls at the photoelectrode/electrolyte interface. The vertical charge transport properties of individual nanoparticle aggregates grown on FTO was probed by C-AFM (**Figure 19c-e** and **h-j**), where the size of the current-carrying regions and the magnitude of current passing through them could correlate with the structural features, reflecting potential barriers in these electrodes created by high-angle grain boundaries. The size of regions with similar current for 6L-Fe_2O_3 (60-200 nm) is larger than that of the 2L-Fe_2O_3 ($<$ 60 nm). These sizes are similar to those of the nanocrystalline mosaics in each sample (**Figure 19b** and **g**), implying that majority carrier transport is limited primarily by the potential barriers formed at high-angle grain boundaries. In addition, statistical analyses of the current maps at different applied voltage show that charge transport in the 2L-Fe_2O_3 is significantly slower than the 6L-Fe_2O_3 (**Figure 19e** and **j**). Hence, the facile vertical charge transport toward the substrate with

few high-angle grain boundaries is the key to high PEC performance for nanostructured Fe_2O_3 photoanodes, especially those with a substantial film thickness.

Heteroatom/Defect doping

Doping is one of the most fundamental strategies to tune the properties of a photoelectrode, which can effectively (1) increase the intrinsic electronic conductivity by changing the crystal symmetry and introducing polarons, both of which would benefit a higher charge carrier concentration,[71, 131-132] (2) improve photo-induced charge migration to reduce the charge recombination during drift and diffusion processes,[133-135] (3) narrow the bandgap energy or change the band edge position by forming a new donor energy level/defect level to enhance the photon absorption,[136-138] (4) create intrinsic vacancies properly as the trapping centres to enhance bulk photo-induced charge separation.[139-141]
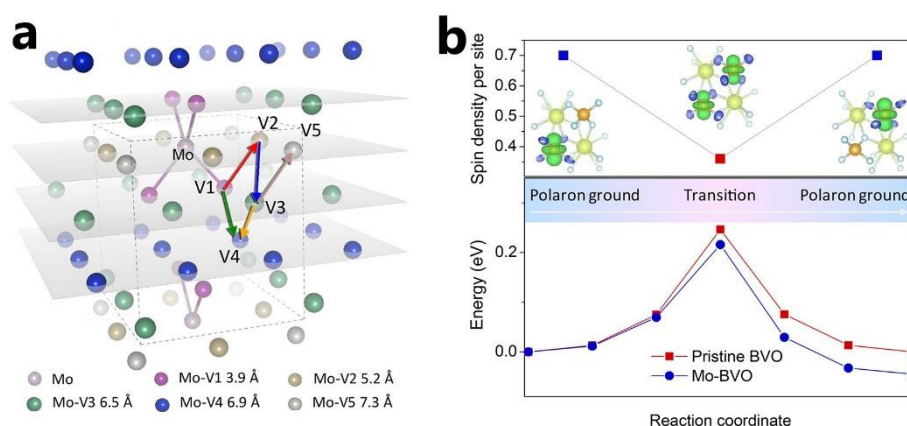
Figure 20. (a) Schematic small polaron hopping paths in Mo-BiVO$_4$ for DFT calculations. Only Mo and V atoms are shown in the schematic structure model. V1-V5 are V positions with different distances to the nearest Mo atom, as listed in the legends. (b) Spin density and average hopping energy barriers in Mo-BiVO$_4$ along the reaction coordination representing one entire small polaron hopping event. The initial state energy of each curve is set to zero. Insets in (b) show the spin-density isosurfaces at an isovalue of 0.002 e/Å^3 near the polaron of initial, transition state, and final states along the reaction coordination. The yellow ball denotes Bi ions, orange is for V, and cyan is for O. Reprinted with permission.[131] Copyright (2018) American Chemical Society.

Small polaron hopping determines carrier transport and limits the ground-state mobility in metal oxides, such as BiVO$_4$ and Fe_2O_3.[70, 142] In principle, small polarons are highly localized and thus

require a large activation energy to hop to the neighboring atoms, leading to a low carrier mobility. High-valence n-type doping is an effective approach to improve the bulk charge transport properties in terms of optimizing polaron hopping mode, increasing carrier concentration and hence the conductivity of metal oxides.[131, 143-144] Generally, hexavalent metals molybdenum (Mo) and tungsten (W) have been extensively investigated as the metallic dopants for $BiVO_4$ photoanodes.[145] For instance, Zhang *et al.* reported an unconventional carrier transport relation induced by extrinsic Mo doping of $BiVO_4$ photoanodes.[131] It is identified that Mo doping significantly condenses the optimal regime between carrier transport and photon collection by substituting V sites, resulting slight tetragonal distortion to the parent monoclinic lattice structure, which simultaneously increases the donor density and lowers the small polaron hopping barrier. **Figure 20a** depicts the comparison of several possible inequivalent hopping paths between the nearest neighbours in multiple directions. The hopping barriers for all paths in Mo-$BiVO_4$ are smaller than those in the pristine $BiVO_4$, with the lowest barrier of 202 m eV for the V^{3+}-V^{5+} hopping route. Meanwhile, according to DFT calculation results (**Figure 20b**), it is stated that V-O bond stretching in the transition state implies strong electron-phonon coupling in this small polaron hopping process while the interaction between polaron and Mo dopants results in dominant photo-induced electron transport and provides a lower barrier for electrons to hop away from Mo dopants. Zhou *et al.* synthesized a Mo-doped $BiVO_4$ photoanode with an inverse opals architecture.[137] The Mo doping effectively optimized photo-induced charge behaviour in two ways: (1) the electron mobility was enhanced by substitution of V^{5+} (tetrahedral ionic radius of 0.35 Å) with a larger Mo^{6+} (tetrahedral ionic radius of 0.41 Å), which could extend the c-axis and promote free electron hopping between internally unconnected VO_4 tetrahedra, where the E_{CB} of $BiVO_4$ mainly consists of V 3d orbitals; (2) the charge carrier density was increased because Mo with one more valence electron than V host atoms can serve as electron donors to increase the charge carrier densities. This strategy can be also applied for Fe_2O_3 photoelectrodes using quadrivalent Ti^{4+} and Sn^{4+} in terms of magnitude enhancement in charge carrier density.[143, 146-148]

Defect engineering, such as introduction of disorder and oxygen vacancies (O_v), can also be considered as a kind of self-doping, which has been intensively studied in energy conversion applications.[149-151] A typical case of defect doping, reported by Chen *et al*, is the hydrogenated treatment of TiO_2 to expand the photon absorption range from ultra-violet to near infrared by creating a disordered surface and O_v.[152] Generally, efficient defect engineering to create O_v can improve the charge carrier density and conductivity in the bulk.[108, 135] For instance, Wang *et al.* first demonstrated hydrogen treatment as a simple and effective strategy to fundamentally improve the PEC performance of TiO_2 nanowires.[153] It is observed that hydrogen treatment increases the donor density of TiO_2 nanowires by 3 orders of magnitude via creating a high density of oxygen vacancies that serve as electron donors.
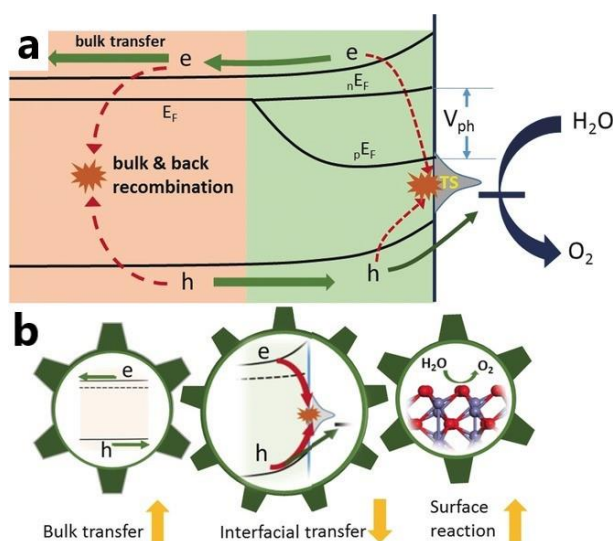
Figure 21. (a) Schematic band structure at the semiconductor-electrolyte interface and the charge transfer (green arrows) and recombination (red arrows) processes. (b) The three key steps for charge transfer, namely bulk transfer, photoelectrode/electrolyte interfacial transfer, and surface reaction. The influence of O_v is indicated with yellow arrows. Reprinted with permission.[139] Copyright (2019) Wiley-VCH Verlag GmbH & Co. KGaA.

Besides the frequently reported improvements in bulk conductivity and charge carrier density, Wang *et al.* found that the role of O_v in PEC process was more complicated based on the study of a Fe_2O_3 photoanode.[139] In the presence of Fermi level pinning by surface trapping states (**Figure 21a**), severe

charge recombination takes place at the photoanode/electrolyte interface. The hole quasi-Fermi level ($E_{F,p}$) will be more reluctant to moving downwards to meet the thermodynamic requirement for water oxidation, and thereby causing sluggish interfacial charge transfer even the surface reaction property can be enhanced by proper intensity of O_v. And once the overpotential is sufficiently large, the E_F pinning at photoanode/electrolyte interface is minimized. High conductivity can accelerate bulk charge transfer and facilitate charge collection, so that bulk recombination by the back-transferred electron-hole pairs and the crystals or particles boundary can be suppressed. Moreover, improved conductivity can lead to a smaller potential drop in the bulk part of Fe_2O_3 photoanode, and thus a greater potential will be applied at the photoanode/electrolyte interface to provide a stronger driving force for surface reactions. This finding suggests that O_v has both positive and negative impacts on PEC performance. The improved bulk conductivity and surface catalysis are beneficial for bulk charge transfer and surface charge consumption while interfacial charge transfer deteriorates because of recombination through O_v-induced trap states at photoanode/electrolyte interface (**Figure 21b**).
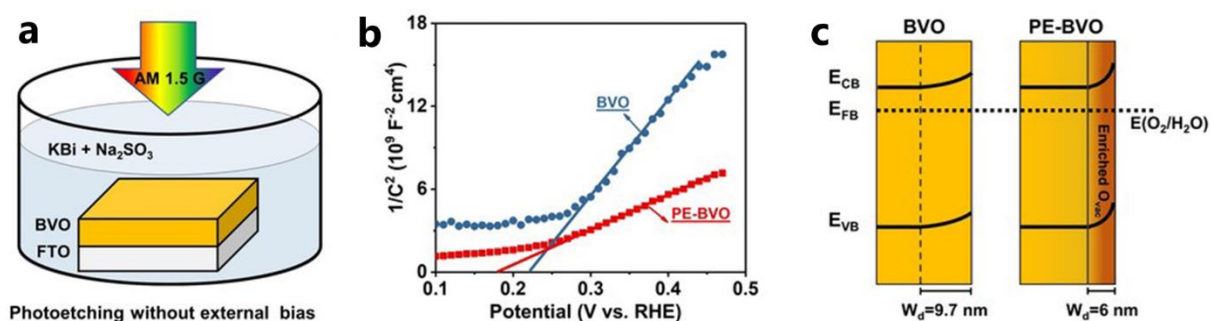
Figure 22. (a) Photoetching for the $BiVO_4$ photoanode without external bias, (b) Mott-Schottky plots measurement of $BiVO_4$ and PE-$BiVO_4$ in the dark, and (c) The band diagrams of $BiVO_4$ and PE-$BiVO_4$ in the dark. Reprinted with permission.[135] Copyright (2020) Wiley-VCH Verlag GmbH & Co. KGaA.

In the contrast to promote bulk charge transport by properly defect engineering, high intensity of O_v in bulk will lead to a poor charge transport efficiency owing to the drag of O_v bound polarons. In order to overcome the negative effect of bulk O_v in photoelectrodes, Qiu *et al.* utilized highly

oxidative 2D bismuth oxyiodate (BiOIO$_3$) as precursor to synthesize BiVO$_4$ photoanodes with reduced bulk O$_v$.[132] As the O$_v$ in bulk was drastically reduced, the released bound polarons enabled a fast charge transport inside BiVO$_4$. Consequently, the performance in tandem devices based on the O$_v$-eliminated BiVO$_4$ was. Apart from selecting propers precursor for photoelectrode fabrication, other methods of defect engineering can also be used to ensure that O$_v$ is only formed on the surface of photoelectrodes. For instance, Feng *et al.* utilized a facile photoetching approach to alleviate the negative effects from bulk defects by confining O$_v$ at the surface of BiVO$_4$ photoanode. A photocurrent density of 3.0 mA/cm^2 at 0.6 V *vs.* RHE was among the highest obtained so far with defect-doped BiVO$_4$ photoanodes.[135] As demonstrated in **Figure 22a**, the photoetching is performed on the as-prepared BiVO$_4$ film in the absence of an external bias by immersing in 1 M potassium borate electrolyte containing 0.2 M Na$_2$SO$_3$ with 10-minute illumination from the solar simulator. A possible mechanism is proposed by the authors, which involves the formation of photo-induced holes in BiVO$_4$ film. These holes can oxidize O$_{lattice}^{2-}$ (lattice oxygen) and release O$_2$ resulting in the formation of O$_v$ according to the reaction equation $2O_{lattice}^{2-} + 4h^+ = O_2 + O_v$. Na$_2SO_3$ is used as a scavenger to remove O$_2$ in order to minimize the reverse reaction between O$_2$ and O$_v$, which could otherwise hinder the formation of O$_v$. Based on the results obtained from the Mott-Schottky plots (**Figure 22b**), the E_{CB} edge remains unchanged upon photoetching while the charge carrier density is significantly increased from 2.71×10^{19} to 8.21×10^{19} cm^{-3}. The enhanced charge carrier density can shorten the depletion width (W$_d$) and enhance the band bending for hole collection (**Figure 22c**), which can accelerate the hole drift and suppress the charge recombination.
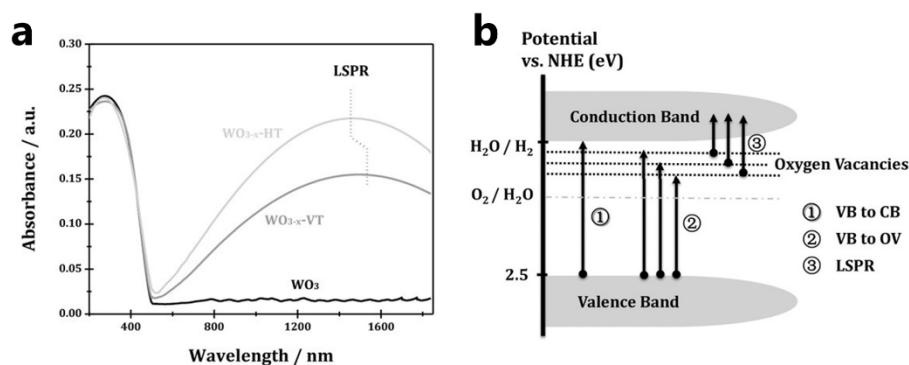
Figure 23. (a) UV-vis -NIR spectra of WO_3, WO_{3-x}-VT (WO_3 obtained by vacuum thermal treatment), and WO_{3-x}-HT (WO_3 obtained by H_2 thermal treatment) nanosheets, and (b) band level arrangements of WO_{3-x}-HT. Reprinted with permission.[69] Copyright (2015) Wiley-VCH Verlag GmbH & Co. KGaA.

Theoretically, there exist three different approaches for solar light harvesting: (1) electrons excited from top of E_{VB} to bottom of E_{CB}; (2) electrons excited from top of E_{VB} to O_v level below the bottom of E_{CB}; and (3) electrons excited by localized surface plasmon resonance (LSPR). Efficient O_v defect engineering can also improve the optical property of photoelectrodes by tuning O_v level and LSPR. For instance, Yan *et al.* successfully synthesized single crystal WO_3 nanosheets from the exfoliation of layered tungstic acid and post thermal treatment, showing dramatically enhanced performance in PEC water oxidation.[69] Post thermal treatment in both vacuum and H_2 can significantly change the electronic structure by forming O_v, which are predominantly located at the outer surface of nanosheets to form a disorder layer. As shown in the diffuse reflectance UV-vis-NIR spectra in **Figure 23a**, WO_3, WO_{3-x}-VT and WO_{3-x}-HT showed similar intrinsic absorption up to 480 nm, consistent with the indirect bandgap absorption edge of pristine WO_3 at 2.6 eV. Significantly, for WO_{3-x}-VT and WO_{3-x}-HT, optical absorption beyond the band edge could be observed in the spectral range of 480-700 nm, which should be due to the new discrete energy bands below the conduction band created by the introduction of anionic vacancies as shown in **Figure 23b**. Moreover, typical LSPR peaks centered at around 1520 and 1450 nm are observed for WO_{3-x}-VT and WO_{3-x}-HT, respectively, which is induced by collective oscillations of surface free electrons. Therefore, the introduction of O_v into

43

single crystal WO_3 nanosheets can induce LSPR effect, which not only creates the light harvesting via LSPR in the near-infrared region but also promotes the light harvesting in the ultraviolet and visible region.
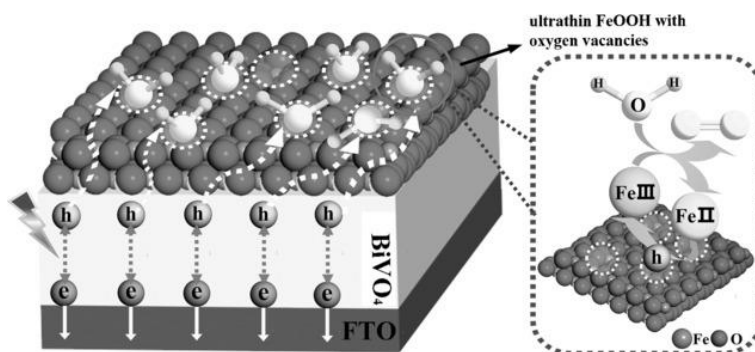

Figure 24. Illustration of the charge transfer on O_v-FeOOH/$BiVO_4$ photoanode. Reprinted with permission.[154] Copyright (2016) Wiley-VCH Verlag GmbH & Co. KGaA.

Besides the photoelectrode itself, the OER co-catalysts can be also tuned by defect engineering for surface charge transfer properties. For instance, Zhang *et al.* developed a facile solution impregnation method for growing an ultrathin high crystalline FeOOH nanolayer with abundant O_v on a $BiVO_4$ photoanode.[154] This O_v-FeOOH can effectively induce the outward driving forces for hole trapping and drive hole migration to alleviate energy loss on the intrinsic potential barrier at the $BiVO_4$/electrolyte interface. Specifically, as shown in **Figure 24**, the created O_v is more favourable for the formation of low-coordination Fe^{2+} sites, leading to a decreased hindrance for the adsorption of H_2O on the surface since Fe^{2+} centre is more active towards the adsorption of H_2O. Owing to the holes with high oxidation capacity and the defects in the ultrathin FeOOH layer, the Fe^{2+} sites could be converted into a higher state (Fe^{3+}) by hole oxidation. And then Fe^{3+} state is reduced to the Fe^{2+} state by getting the electron from the water (produce oxygen). Therefore, it is apparent that the ultrathin O_v-FeOOH not only be served as the hole transport layer to promote charge separation but also the active sites for the water oxidation.

As discussed above, although doping brings significant regulation of electronic structure of a bulk material in some cases, the effect of doping may not be always favourable due to the induced electron-hole recombination due to the presence of more trapping centres, impeded charge transport by providing scattering centres, and the decrease in the thickness of the depletion layer.[73] Therefore, incorporating hetero-atom dopants or defects into semiconductor crystal lattice should be controlled precisely and properly, taking into consideration various factors, such as the absorption coefficient and minority carrier diffusion length.

Crystal facet engineering

Owing to the different atomic arrangements in various facets, semiconductor crystals exhibit facet-dependent anisotropic properties, such as surface electronic structures, redox reaction sites, surface built-in electric fields, molecular adsorption, photoreaction activity, photo-corrosion resistance, and anisotropic electrical conductivity.[24] Usually, exposed facets can be generated by selectively controlling the nucleation and growth rates in different directions during the growth of semiconductor crystals. According to the Gibbs-Wulff theorem, the facets with higher surface energies always grow rapidly and usually account for a very small fraction of the surface or even vanish from the final crystals, whereas the facets with lower surface energies grow slowly and are preserved, constructing the shape of the final crystals.[24, 155] Therefore, advanced technology and efficient capping agents are required to selectively cover the facets with higher surface energies and reduce the surface energies of the corresponding adsorbed facets.[50, 156-158]
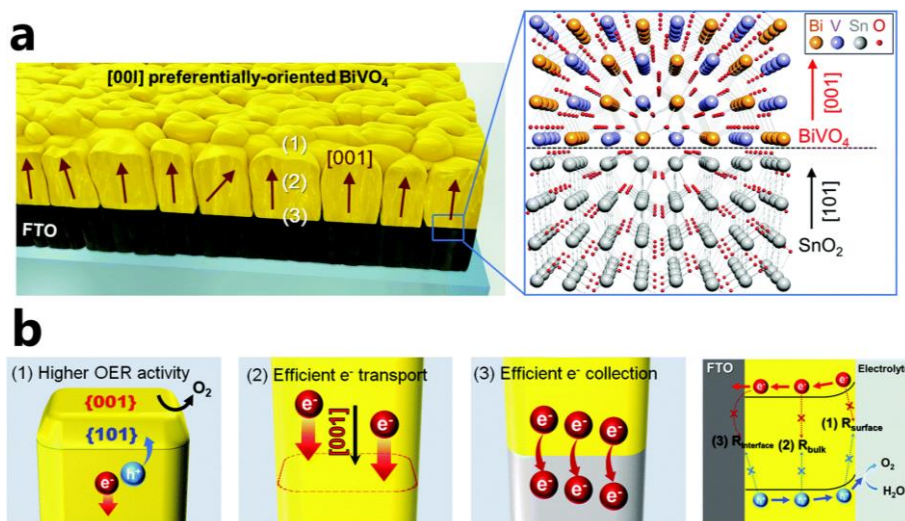
Figure 25. Growth orientation and facet design of a pristine BiVO$_4$ photoanode and their impact on PEC performance. (a) Growth morphology and hetero-epitaxial alignment of a monoclinic BiVO$_4$ film on rutile SnO$_2$. (b) The use of preferentially [001]-oriented BiVO$_4$ to circumvent inherent limitations (sluggish oxygen evolution reaction kinetics and poor charge transport and collection) by reducing surface, bulk, and interfacial charge recombination. Reprinted with permission.[159] Copyright (2018) Royal Society of Chemistry.

Theoretical studies have indicated that [001]-oriented growth of BiVO$_4$ is expected to be better in charge transport properties, while (001) facet of BiVO$_4$ is also suggested exhibit higher OER activity than other facets due to the favourable surface electronic properties and surface atomic structure.[145, 160-161] For instance, Han *et al.* fabricated the pristine BiVO$_4$ photoanode with a preferential [001] growth orientation and exposed (001) facets by a laser ablation assisted epitaxial method on FTO substrates (**Figure 25a**).[159] In **Figure 25b**, it is strikingly presented (1) superior surface reaction, (2) bulk charge transport, and (3) backside charge collection. Correspondingly, (1) the exposed (001) surface facets possess a higher solar water oxidation performance compared to the (101), (2) the charge transport along [001] orientation is more efficient compared to the random growth orientation, and (3) the backside electron collection is more efficient on the lattice-matching BiVO$_4$[001] || SnO$_2$[101] interface. The excellent intrinsic charge transport property and surface reactivity of preferentially [001]-oriented BiVO$_4$ contributes to a 16-times higher photocurrent density compared to the random oriented counterpart, which is the highest value among pristine BiVO$_4$-based photoanodes for solar water oxidation.
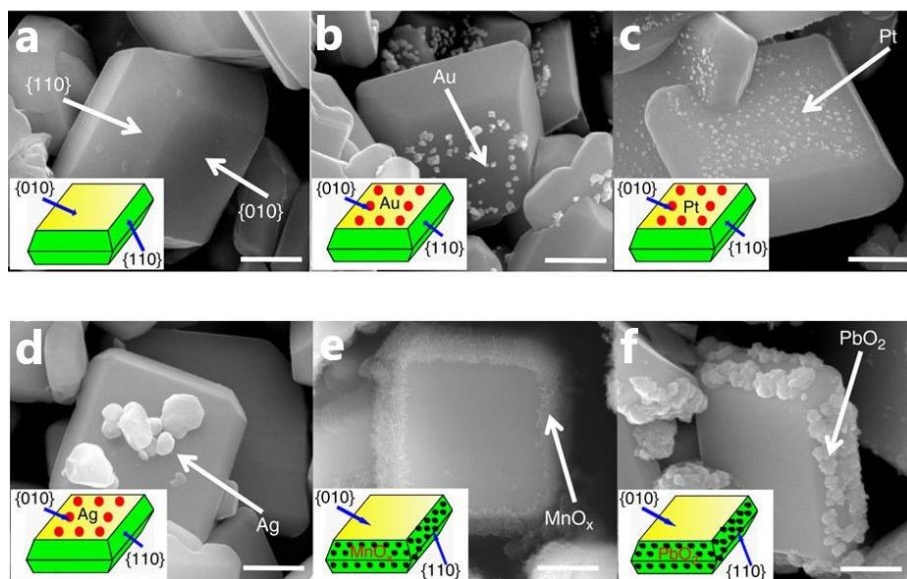
Figure 26. SEM images of BiVO$_4$ with and without single metal/oxide deposited. (a) BiVO$_4$; (b) Au/BiVO$_4$; (c) Pt/BiVO$_4$; (d) Ag/BiVO$_4$; (e) MnO$_x$/BiVO$_4$ and (f) PbO$_2$/BiVO$_4$. Reprinted with permission.[162] Copyright (2013) Nature Publishing Group.

The anisotropic charge transport property in photoelectrodes also tends to induce crystallographic-orientation-dependent photoinduced charge separation.[158, 163-164] For instance, Li *et al.* observed that efficient charge separation can be achieved on different crystal facets using BiVO$_4$ as a model photoelectrode (**Figure 26a**),[162] based on the evidence that reduction reaction with photo-induced electrons and oxidation reaction with photo-induced holes occurred separately on the (010) and (110) facets under illumination. In particular, Ag, Au and Pt particles were all solely deposited on the (010) facets (**Figure 26b-d**), implying photo-induced electrons specifically flowed to the (110) facets, while MnO$_x$ and PbO$_2$ particles were solely deposited on (110) facets, demonstrating the transportation of photo-induced holes to (110) facets (**Figure 26e-f**). This unique phenomenon has also been observed on other semiconductors, such as TiO$_2$ and SrTiO$_3$[50, 158]
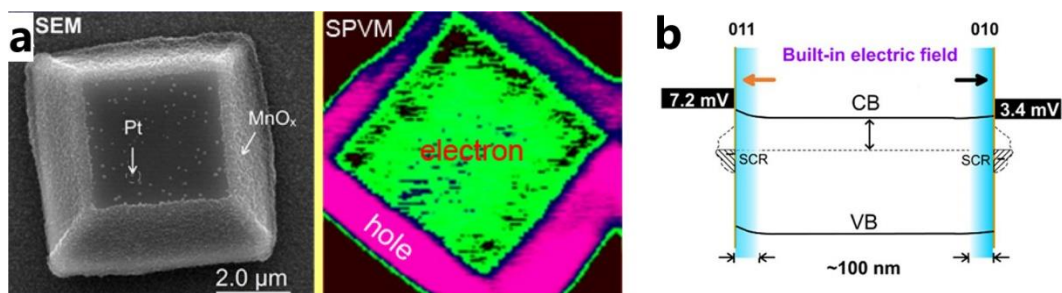
Figure 27. (a) SEM image of and spatial distribution of SPV signals. Pink and green colours correspond to holes and electrons separated toward the external surface, respectively. (b) Schematic band diagrams across the border between the (011) and (010) facets of a bare single $BiVO_4$ photocatalyst particle. Reprinted with permission.[165] Copyright (2017) American Chemical Society.

Although facet-dependent charge transport and surface redox reaction were observed in many reports, the underlying mechanisms are still not well understood. Zhu *et al.* developed a spatially resolved surface photovoltage (SR-SPV) microscopy technique for directly visualizing the local spatial charge separation in single crystal $BiVO_4$ (**Figure 27a**),[165] which provides some insights into the facet-dependent surface charge dynamics. In **Figure 27b**, SR-SPV studies on a single $BiVO_4$ crystal containing (010) and (011) facets revealed that the (011) facet exhibits a much stronger SPV signal intensity than the (010) facet, indicating that the surface band bending in the space charge region of the (011) facet is more significant than that of the (010) facet. Consequently, the surface band bending induced built-in electric fields between these facets are different, leading to the spatial transfer of photo-induced electrons and holes to different facets in a single semiconductor crystal. By increasing the area ratio of (010)/(011), the difference in the SPV signal intensities between the (011) and (010) facets can even reach a factor of 70, suggesting a larger difference in their surface built-in electric fields.

Owing to the unique facet-dependent properties of semiconductor crystals discussed above, it is possible to modify photoelectrodes through crystal facet engineering toward efficient PEC water splitting. Compared to the suspension-based photocatalysis systems, PEC water splitting systems require the efficient loading of photocatalysts on conductive substrates. It is still very challenging to

keep the specific faceted exposing to H_2O and excellent interfacial contact with conductive substrates. To assist the mechanistic understanding of facet-dependent properties of semiconductor, advanced microscopy and spectroscopy techniques should be developed for directly imaging and probing the surface and interface charge transfer dynamics.[163-164, 166]
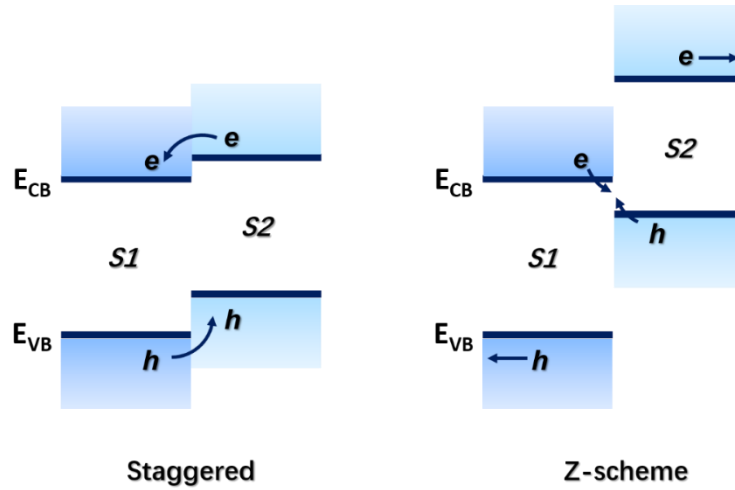
Figure 28. Band structure of two kinds of heterojunction. a) Staggered junction. b) Z-scheme junction.

Hetero/Homo-junction fabrication

Rational design and fabrication of a junction is one of most effective and facile ways to promote the bulk charge separation and transport.[36, 128, 167] From the point of semiconductor materials, junctions can be formed by two different semiconductor materials with a suitable band alignment or the same semiconductor material with different electronic structure or phase. The former is called heterojunction, while the latter is called homojunction. Fundamentally, there exist two kinds of junctions based on the band energy level alignment of the semiconductor pair: staggered junction and Z-scheme junction as shown in **Figure 28**. In a typical staggered band alignment, both E_{CB} and E_{VB} positions of semiconductor 2 (*S2*) are slightly higher than that of semiconductor 1 (*S1*). After intimate contact and band bending formation, a built-in field is constructed that drives the photo-induced

electrons from *S2* to *S1*, and photo-induced holes from *S1* to *S2*, leading to a spatial charge separation of the electron-hole pairs on two sides of heterojunction interface. For Z-scheme junction, as E_{CB} of *S1* is close to E_{VB} of *S2*, the interfacial photo-induced electrons from *S1* and holes from *S2* recombine, enabling forward current flow. The photovoltage is the sum of the photovoltage of *S1* and *S2*. It is clearly seen that, in staggered junction system, two photons can generate two electron-hole pairs for redox reactions, whereas in Z-scheme system only one of the two electron-hole pairs generated by two photons is used for redox reactions due to recombination of one electron-hole pair, which reduces quantum efficiency to half.
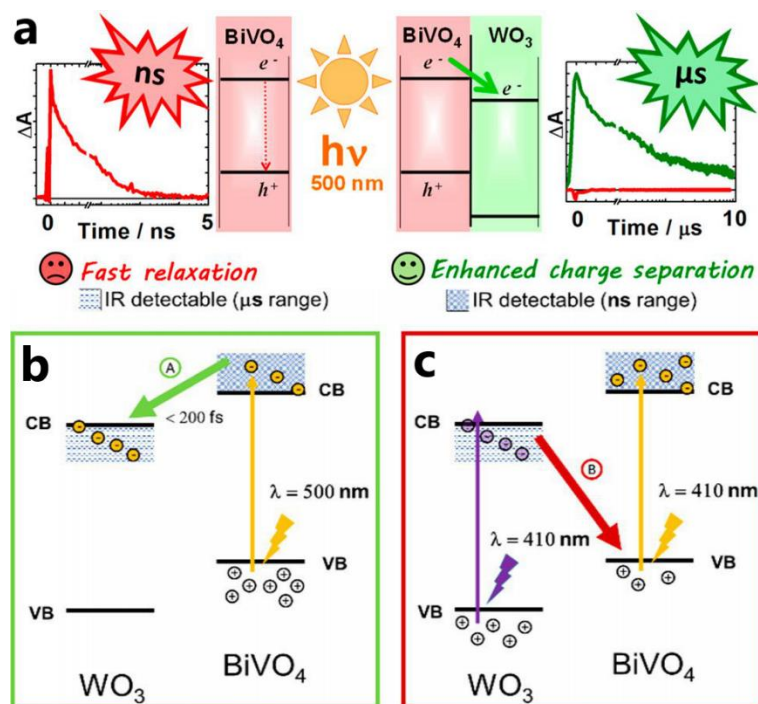
Figure 29. Infrared nanosecond TA traces recorded at 2050 cm^{-1} with BiVO$_4$ and WO$_3$/BiVO$_4$ heterojunction. Reprinted with permission.[168] Copyright (2018) American Chemical Society.

WO$_3$/BiVO$_4$ is one of the best heterojunction pairs for water splitting, because WO$_3$ is a reasonably stable n-type semiconductor with a E_{CB} value of 0.4 V *vs.* NHE allowing facile photo-induced electron injection from the conduction band of BiVO$_4$ with a E_{CB} value of 0.2 V *vs.* NHE. Various nanostructured WO$_3$/BiVO$_4$ heterojunction were designed and fabricated in the past decade for

enhancing the bulk charge separation.[169-172] For instance, Shi *et al.* fabricated a helical WO_3 array on FTO by oblique angle deposition, followed by coating with amorphous (W, Mo)-$BiVO_4$,[117] which exhibited a photocurrent density of as high as ~ 5.35 mA/cm^2 and a IPCE value of over 90 % at 1.23 V *vs.* RHE. Rao *et al.* synthesized WO_3/$BiVO_4$ core/shell nanowire photoanode in which $BiVO_4$ is the primary light-absorber and WO_3 acts as a photo-induced electron conductor,[173] showing a photocurrent density of 3.1 mA/cm^2 and IPCE value of 60 %. In these cases, effective photo-induced charge transfer can occur on the WO_3/$BiVO_4$ interface, and superior nanostructured WO_3 is beneficial for the consequent photo-induced electrons transport. In order to provide a deeper insight of photo-induced charge transfer dynamics, Grigioni *et al.* directly probed the WO_3/$BiVO_4$ heterojunction photoelectrode by transient absorption (TA) midinfrared (mid-IR) spectroscopy on the picosecond to microsecond time scale.[168] It was found that photo-induced electrons in $BiVO_4$ decayed within nanosecond scale, whereas WO_3/$BiVO_4$ heterojunction showed a long-lived IR signal to microsecond scale, as shown in **Figure 29a**. Selective excitation of $BiVO_4$ at 500 nm in WO_3/$BiVO_4$ generates a long-lived IR signal (**Figure 29b**), which provided conclusive evidence that photo-induced electrons from E_{CB} position of $BiVO_4$ promptly move to that of WO_3. Interestingly, a decreased IR signal was observed at the excitation wavelength of 410 nm, indicating that a potential undesirable recombination pathway is present between photo-induced electrons in the conduction band of WO_3 and photo-induced holes in the valence band of $BiVO_4$ upon simultaneous excitation of both oxides (**Figure 29c**). Therefore, in optimized heterojunctions, care should be taken to avoid this parasitic process of wavelength-dependent charge dynamics in the heterojunction system.
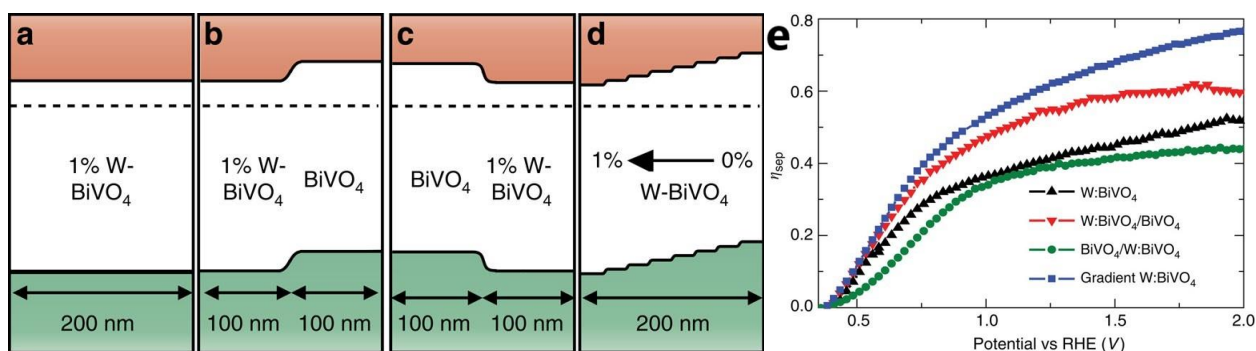
Figure 30. Band diagram schematic of BiVO$_4$ samples. (a) W-BiVO$_4$, (b) W-BiVO$_4$ homojunction, (c) W-BiVO$_4$ reverse homojunction and (d) gradient-doped W-BiVO$_4$. In all cases, the light enters from the right-hand side (through the electrolyte), and the FTO back contact is situated on the left. (e) Carrier-separation efficiency (η_{sep}) as a function of applied potential. Reprinted with permission.[117] Copyright (2013) Nature Publishing Group.

Different from heterojunction, homojunction is composed of same semiconductors but with different electronic structures or phase, such as typically anatase and rutile TiO$_2$. As discussed in **Section 1.5.3**, band position can be effectively tuned by doping method, and thus creating a different electronic structure from the bulk. Abdi *et al.* reported a gradient W dopant concentration in BiVO$_4$ film, thereby creating a distributed n$^+$-n homojunction to enhance the bulk charge separation.[138] By comparing band diagram of pristine W-BiVO$_4$, (**Figure 30a**) and W-BiVO$_4$/BiVO$_4$ (**Figure 30b**), it is found an enhanced bulk charge separation by forming homojunction architecture. To fully leverage this effect, the BiVO$_4$ photoanode with a 10-step in gradient W doping (**Figure 30d**) was fabricated, starting from 1% W at the interface with the back contact to 0% W at the semiconductor/electrolyte interface. This photoanode shows a charge separation efficiency of over 60% (**Figure 30e**). To confirm the cascade charge transfer from BiVO$_4$ to W-BiVO$_4$, a reverse homojunction was fabricated in which the W-BiVO$_4$ side is closest to the electrolyte (**Figure 30c**). It is clearly shown that the charge separation efficiency is decreased as the band bending is present in the opposite direction to act as a barrier for carrier separation. Similarly, Ruan *et al.* synthesized a metal-free photoanode nanojunction architecture, composed of B-doped C$_3$N$_4$ (top layer with a depth of 100 nm) and bulk C$_3$N$_4$ (bottom layer with a depth of 900 nm), by one-step thermal vapour deposition.[108] The B-C$_3$N$_4$/C$_3$N$_4$

nanojunction photoanode produces a 10-fold higher photocurrent density than pristine bulk C_3N_4 photoanode due to the enhanced conductivity and presence of mitigated deep trap states.
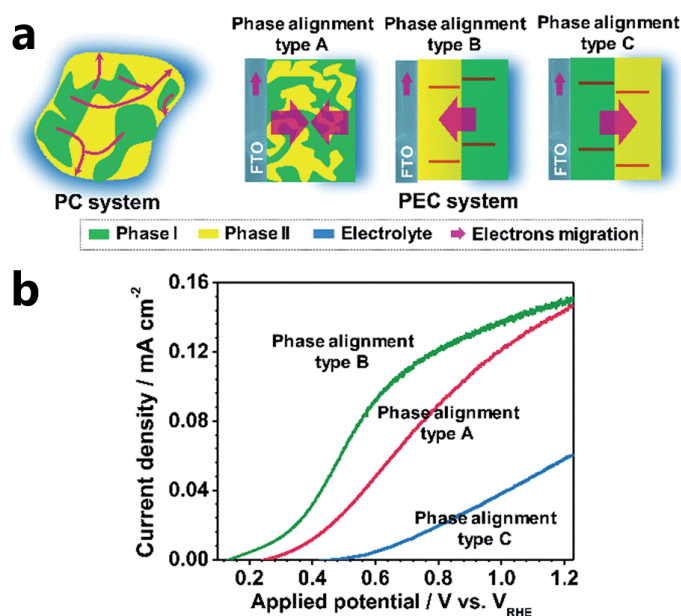
Figure 31. (a) Schematic diagrams showing the phase junction effects on charge separation and transfer in photocatalysis system and PEC system. Type A is the electrode with random phase alignment. Type B and type C are the electrodes with phase alignments for forward and reverse electron migration, respectively. (b) *J-E* curves of TiO_2 electrodes with type A (red), type B (green) and type C (blue) phase alignments. Reprinted with permission.[174] Copyright (2016) Royal Society of Chemistry.

Introducing phase homojunction is also an effective way to promote bulk charge separation.[175-177] Because of the similar crystal structure between the two phases, a phase junction can be more easily formed. In the phase junction, the band alignment between the different phases critically determines the interfacial charge transfer directions thermodynamically then the charge separation. For instance, Li *et al.* utilized typical TiO_2 anatase-rutile phase junction as a model to reveal that appropriate bandgap alignment is essential for unidirectional charge separation and transfer.[174] In photocatalysis system, electron-hole pairs separated across the phase junction can readily react with water (**Figure 31a**). However, different from photocatalysis system, photo-induced charges need to transport in the desired direction in PEC system. Both the random phase junction (type A) and the junction with an

incorrect band energy alignment that causes undesired reverse charge transfer (type C) exhibit a relatively low PEC performance (**Figure 31b**). In contrast, type B phase junction produces a favoured unidirectional photo-induced holes transfer from bulk side to electrolyte side, resulting in the highest PEC water oxidation performance (**Figure b**). Generally, the bandgap of different phases are quite similar due to the same chemical composition, which makes it hard to identify the E_{CB} and E_{VB} of different phases. Moreover, the band alignment is very sensitive to the interfacial structure, the gas atmosphere, or the electrolyte, *etc*. Thus, more efforts are required to clarify the band alignment theoretically or experimentally.

Recent advances in regulating charge behaviour on surface

In this section, recent advances in regulating charge behaviour on surface are presented by introducing various passivation layer and cocatalysts, and thereby enhancing the chemical stability and surface reaction kinetics.

Interface passivation

Passivation layers are applied to the photoelectrode/electrolyte and current collector/photoelectrode interface using various materials (Al_2O_3, SiO_2, ZrO_2, SnO_2, TiO_2)[57, 62, 96, 178] and technologies (atomic layer deposition, electrodeposition)[96, 179], mainly aiming at (1) reducing chemical or photochemical corrosion induced by aqueous electrolyte or detrimental side reaction, (2) manipulating interfacial energetics to decrease the loss of original photovoltage, (3) preventing surface states trapping of surface-reaching charges, and (4) decreasing the charge accumulation on the back contact.
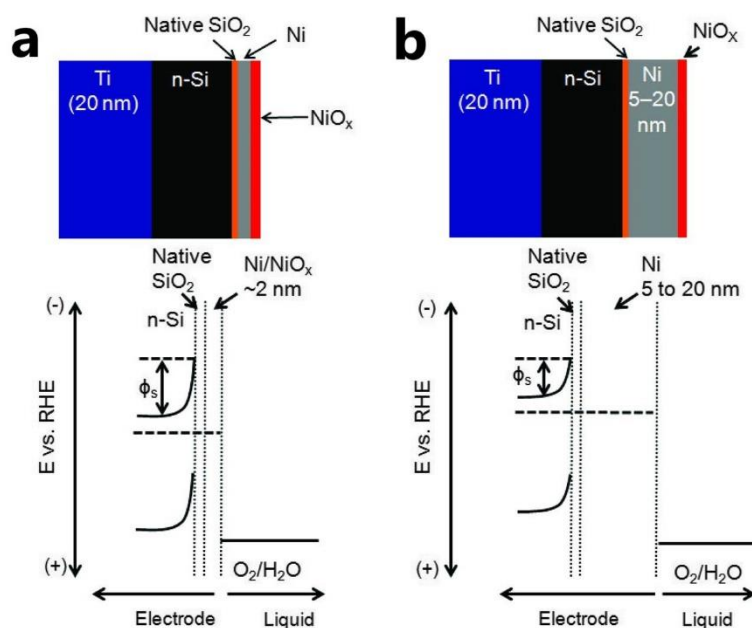
Figure 35. Schematic of Ni/n-Si photoanode. (a) Structure of 2-nm Ni-coated n-Si anode (top) and proposed approximate energy band diagram (bottom). (b) Structure of 5- to 20-nm Ni-coated n-Si anode (top) and a typical Ni/n-Si Schottky barrier formed between 5- to 20-nm Ni and n-Si, with built-in potential φ_s and photovoltage lower than the 2-nm Ni/n-Si case in (a). Reprinted with permission.[180] Copyright (2014) American Association for the Advancement of Science.

Several studies have shown that constructing a metal-insulator-semiconductor (MIS) interface as the surface passivation layer to manipulate interfacial energetics in order to maximum the photovoltage can offer a feasible way to enhance the solar-conversion efficiency. Generally, taking an n-type Si photoanode as an example, the electron quasi-Fermi level falls close to the valence band at the interface, and thus creating a potential barrier that repels the majority carriers when being in contact with a high work function metal or transition-metal-oxide. This barrier height should be closely associated with the work function of the metal relative to the electron affinity of Si according to the Schottky-Mott rule.[96, 181] In order to obtain a high photovoltage, the metal must have a high work function value and the insulator layer must have a proper thickness. For instance, Kenney *et al* reported an MIS interface system using an n-type Si photoanode with its native SiO_2 insulator layer and ~ 2-nanometer high work function nickel metal layer (**Figure 35**), showing an enhanced PEC

water oxidation in both aqueous potassium hydroxide (pH = 14) and aqueous borate buffer (pH = 9.5) solutions. It is demonstrated that the ultrathin Ni/NiO$_x$ and the electrolyte form an effective layer interfacing with Si, affording a high built-in potential (φ_s) and V_{oc}, while φ_s and V_{oc} became lower as the thickness increased from 5 to 20 nm. Similarly, Yao *et al.* manipulated the interfacial energetics of n-type silicon photoanodes by building an n-Si/TiO$_x$/ITO Schottky junction, which exhibited a highly efficient charge transport and a barrier height of 0.95 eV (close to the theoretical optimum for n-Si/ITO Schottky contact).[181] Specifically, the donor-like defects at the n-Si/ITO interface and reverse effects of the defects on charge transfer were eliminated by introducing a thin layer TiO$_x$, while the barrier height and holes extraction efficiency of the optimized n-Si/TiO$_x$/ITO junction can be further enhanced through enlarging the work function of the surface layer.
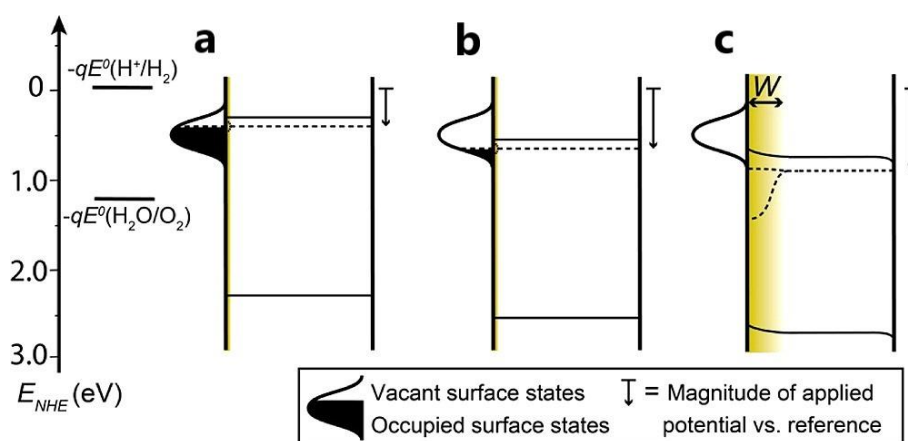
Figure 36. Electron energy scheme of an n-type semiconductor photoanode under polarization using a potentiostat at different potentials and with the presence of surface states that cause Fermi level pinning. (a) Electrode at E_{fb}. (b) An anodic potential empties the surface states but does not induce band bending. Band bending commences at (c) when the surface states are emptied. Reprinted with permission.[18] Copyright (2013) American Chemical Society.

Finally, the effective surface passivation can be also employed to suppress the high density of surface states (or so-called Fermi level pining) caused by defects or oxygen vacancies in polycrystalline metal-oxide photoelectrodes, and thus decreasing surface charge recombination.[18, 179, 182] As seen in **Figure 36**, in principle, the applied bias does not contribute to band bending but instead result in emptying the surface states. And the potential drop occurs over the Helmholtz layer instead of in the

photoelectrode itself, and as a result, space charge field is not present to separate photo-induced charges. It is not until the surface states are emptied that the photoelectrode can lead to surface band bending and a space charge field to generate anodic photocurrent. In other words, these surface states act as trapping centres of photo-induced holes, which is deleterious surface charge injection kinetics. One of the most widely investigated photoelectrodes in surface state passivation is Fe_2O_3 photoanode. There exist mainly two strategies to optimize the surface state to enhance water splitting efficiency. The facile way is thermal treatment under high temperature to improve the crystallinity. Zandi *et al.* utilized the annealing strategy to treat Fe_2O_3 thin film prepared by atomic layer deposition (ALD), which is shown to remove one of two surface states identified to reduce surface photo-induced charge recombination and Fermi level pinning.[182] However, high-temp calcination usually tend to destruct the desirable nanostructure. Li *et al.* synthesized a ZrO_2-induced Fe_2O_3 nanotube photoanode that can be survived over 750 °C.[183] By introducing a ZrO_2 shell on hydrothermal FeOOH nanorods by ALD method, subsequent high-temperature solid-state reaction converts ZrO_2-FeOOH nanorods to ZrO_2-induced Fe_2O_3 nanotubes showing an exciting PEC water oxidation activity among Fe_2O_3-based photoanodes without co-catalysts.

Although passivation is promising strategy to achieve long-term operational stability and to remove high density of surface states, the properties of materials, such as thickness, permeability, stability, and attaching capability, still need to be carefully controlled. Moreover, the effects of surface passivation, catalytic improvement in interfacial charge transfer kinetics, and chemical stabilization are not necessarily independent. Well-designed solar water-splitting devices have to combine these properties to enhance overall performance.
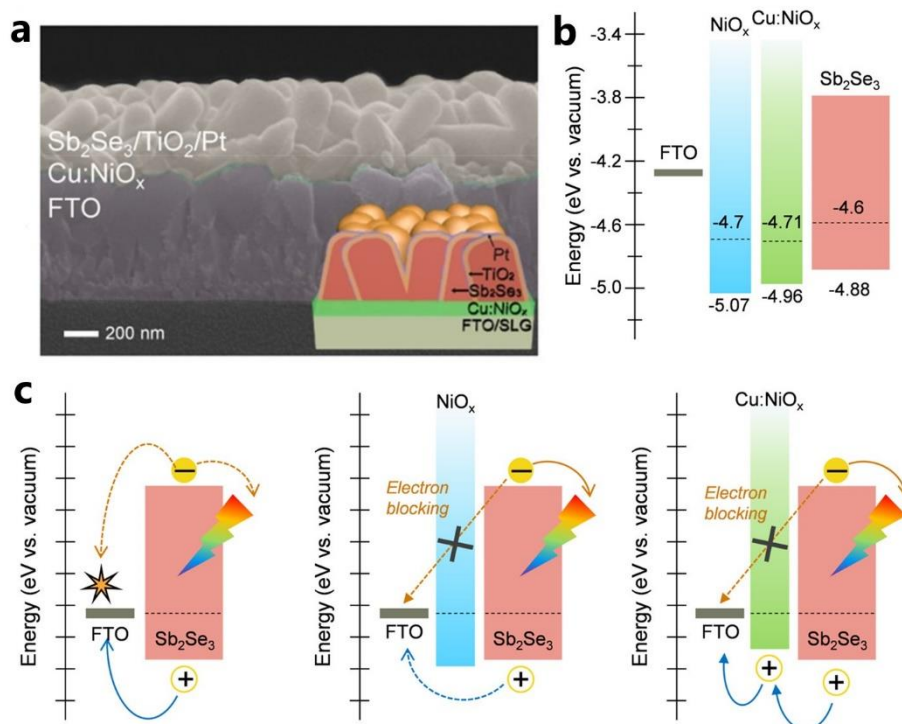
Figure 37. (a) Cross-sectional SEM image of FTO/Cu-NiO$_x$/Sb$_2$Se$_3$/TiO$_2$/Pt photocathode. (b) Schematic band diagram showing the relative energy positions of E_{VB} and E_F for the three different layers with respect to the FTO before equilibrium. Band energy diagram after equilibrium: (d) Without NiO$_x$ layer, (e) NiO$_x$ layer, and (f) Cu-NiO$_x$ layer. Reprinted with permission.[184] Copyright (2019) American Chemical Society.

Besides focusing on the top photoelectrode/electrolyte interface, an effective bottom layer on the current collector/photoelectrode interface is crucial for the back-contact charge transfer as well. In a typical photocathode comprising a p-type semiconductor, the photo-induced electrons should drift to the photocathode/electrolyte interface to drive the HER, while the photo-induced holes are transported to a counter electrode via the back contact and external circuit, followed by the OER process. The slow injection of the photo-induced holes to the back contact is likely to induce charge accumulation and recombination at the back current collector/photoelectrode interface. Lee *et al.* fabricated Cu-doped NiO$_x$ as back contact insertion layer for Sb$_2$Se$_3$ photocathodes (**Figure 37a** and **b**) to block the charge recombination and selectively facilitate photo-induced hole extraction at the back interface.[184] The band alignment between the Sb$_2$Se$_3$ and the back contacts after the E_F

equilibration is further schematically depicted in **Figure 37c**. The photo-induced electrons and holes possibly recombined at the FTO/Sb_2Se_3 interface due to the electron backflow, whereas the fabrication of NiO_x layer between the FTO and Sb_2Se_3 can effectively prevent the photo-induced electron backflow because of the overwhelmingly positive E_{CB} of NiO_x (**Figure 37d**). The hole extraction through NiO_x may have been sluggish because of the undesirable E_{VB} matching. In the case of Cu-NiO_x layer, the photoexcited holes were efficiently extracted through the hole-selective layer because of the more desirable band alignment and the higher electrical conductivity. This result is in good agreement with the literature showing that a small difference in the band offset can result in a significant difference in the performance of semiconductor-based devices.

Co-catalyst deposition

In addition to tuning the physicochemical properties in the bulk of photoelectrodes, surface charge utilization also plays a vital role in solar water splitting, where the kinetics of OER or HER is still relatively sluggish.[11, 16-17, 185] In order to promote the reaction process, typical O_2 and H_2 evolution co-catalysts (OECs and HECs), such as noble and transition metal oxides (RuO_2, IrO_2, CoO_x, MnO_x)[129, 186], oxyhydroxide (NiOOH/FeOOH, FeOOH/CoOOH)[42, 187], transition metal phosphide/phosphate (CoP/CoPi)[86, 188], noble metals (Pt)[82], and enzymes (hydrogenase)[189-190] have been widely studied and employed to deposit on the surface of photoelectrodes. As mentioned above, it is clearly demonstrated that a successful cocatalyst candidate in PEC system must be an efficient electrocatalyst for water splitting. Therefore, inspired by Kanan and Nocera's work on OER catalysed by a CoPi electrocatalyst,[191] the first case of integrating cocatalysts into PEC water splitting was reported by Zhong *et al*. in 2009,[192] in which CoPi was electrodeposited on the nanostructured Fe_2O_3 photoanode resulting in reduction of the overpotential for PEC water oxidation by over 350 mV. Since then, the electrodeposition of sparser CoPi cocatalysts[193] and photo-assisted electrodeposition

of more uniform CoPi cocatalysts[188] have been further developed to enhance the kinetics of the surface reactions of photoelectrodes.
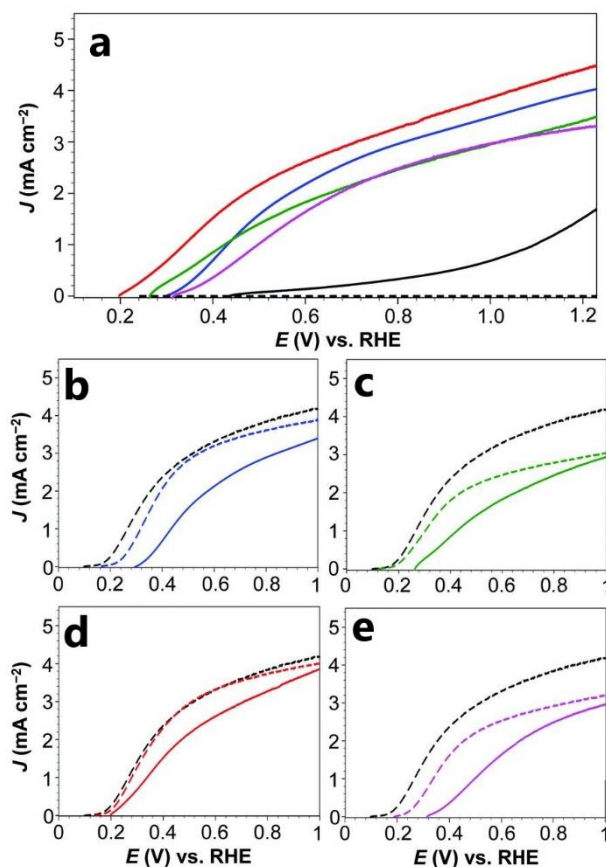
Figure 32. Effect of OECs on photocurrent density for solar water oxidation and Na_2SO_3 oxidation. (a) *J-E* curves of $BiVO_4$ (black solid line), $BiVO_4$/FeOOH (blue), $BiVO_4$/NiOOH (green), $BiVO_4$/FeOOH/NiOOH (red), and $BiVO_4$/NiOOH/FeOOH (pink) for water oxidation measured in a 0.5 M phosphate buffer (pH = 7) under AM 1.5 G illumination. Dark current is shown as a dashed line. *J-E* curves of (b) $BiVO_4$/FeOOH, (c) $BiVO_4$/NiOOH, (d) $BiVO_4$/FeOOH/NiOOH, and (e) $BiVO_4$/NiOOH/FeOOH comparing photocurrent density for Na_2SO_3 oxidation (dashed) and water oxidation (solid) measured with and without the presence of 1.0 M Na_2SO_3 as hole scavenger. Photocurrent for sulfite oxidation by $BiVO_4$ is shown as the black dashed line for comparison. Reprinted with permission.[42] Copyright (2014) American Association for the Advancement of Science.

Considering the crucial role of surface charge utilization in solar water splitting, for the first time, a more efficient dual-layer OER catalyst consisting of FeOOH and NiOOH was fabricated by Kim and Choi on $BiVO_4$ photoanodes.[42] In order to investigate the PEC property of $BiVO_4$ with the implication from poor surface charge utilization, photocurrent density was first examined in the electrolyte

containing Na_2SO_3 as a hole scavenger. A very much lower onset potential of 0.1 V *vs.* RHE, and a much more rapid increase in photocurrent in the potential region of 0.2 V - 0.6 V *vs.* RHE compared to that in the absence of Na_2SO_3. These results illustrate that the majority of the surface-reaching holes recombine because of poor catalytic nature of the $BiVO_4$ surface for water oxidation. By photo-assisted electrodepositing proper amount of a dual layer of FeOOH/NiOOH cocatalyst, a significant reduced overpotential and enhanced photocurrent density were achieved for $BiVO_4$/FeOOH/NiOOH as demonstrated in **Figure 32a**. By comparing the PEC property of $BiVO_4$/FeOOH (**Figure 32b**) and $BiVO_4$/NiOOH (**Figure 32c**) for water oxidation, it is observed that $BiVO_4$/FeOOH generated higher photocurrent density than $BiVO_4$/NiOOH, although $BiVO_4$/NiOOH presented a less positive onset potential, suggesting that the charge recombination at the $BiVO_4$/NiOOH interface is more substantial than that at the $BiVO_4$/FeOOH interface. Moreover, photocurrent density of $BiVO_4$/FeOOH for sulfite oxidation is very close to that for pristine $BiVO_4$, whereas that for $BiVO_4$/NiOOH was considerably lower, which indicated that the charge recombination at the $BiVO_4$/NiOOH interface is indeed more substantial. Therefore, it is demonstrated that the consecutive dual layers of FeOOH/NiOOH simultaneously optimized $BiVO_4$/OEC and OEC/electrolyte interface, in which FeOOH at the $BiVO_4$/OEC junction reduces the interface recombination, while the NiOOH layer at the OEC/electrolyte interface decreases Helmholtz layer potential drop to achieve a more negative E_{fb} for $BiVO_4$ while realizing faster water oxidation kinetics (**Figure 32d**) than if FeOOH was used as the outermost layer (**Figure 32e**).
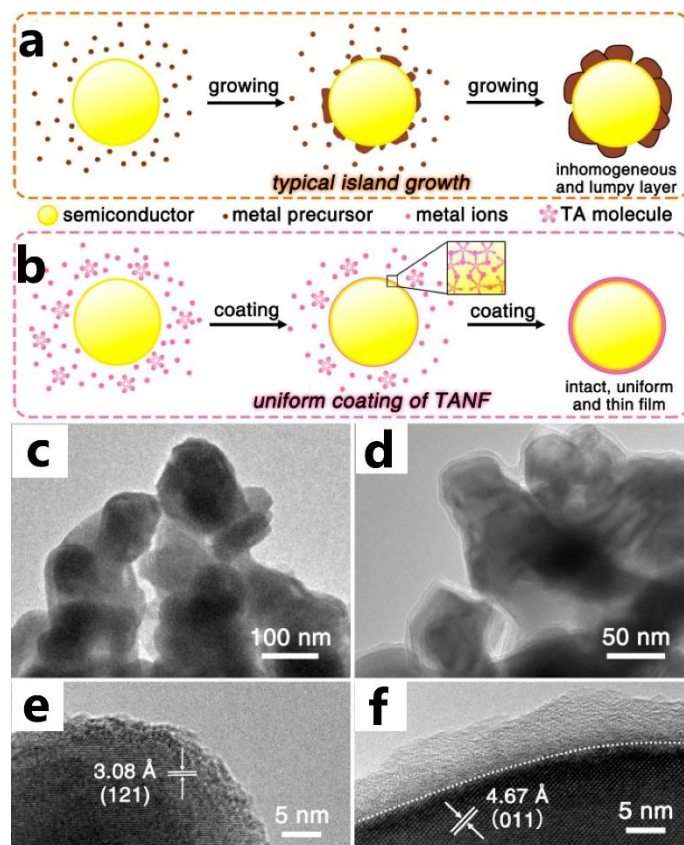
Figure 33. Schematic illustrations of the growth procedure for (a) island growth of traditional CoPi cocatalysts, and (b) coating of TANF on the surface of Mo-BiVO$_4$. TEM images of (c) Mo-BiVO$_4$ and (d) Mo-BiVO$_4$@TANF. HRTEM images of (e) Mo-BiVO$_4$ and (f) Mo-BiVO$_4$@TANF. Reprinted with permission.[194] Copyright (2018) American Chemical Society.

Although the FeOOH/NiOOH cocatalyst is a typical layer double hydroxide (LDH) atomic structure, it often emerged as independent islands instead of a continuous layered nanostructure, making less active sites for surface reaction. Shi *et al.* demonstrated the complex assembly film composed of phenolic ligands (tannic acid) coordinated with Ni and Fe ions (TANF) as a robust and uniform coating on Mo-BiVO$_4$ photoanodes.[194] Different from many traditional cocatalysts with island growth (**Figure 33a**), the TANF exhibits a 2D network structure where tannic acid molecules are connected with metal ions, resulting in a thin layer of an intact and uniform film on the surface of Mo-doped BiVO$_4$ as shown in (**Figure 33b**). This layered TANF cocatalyst could completely cover the surface of Mo-BiVO$_4$ photoanode (**Figure 33c-f**), hence can protect the photoanode from photocorrosion to enhance the operational stability as well as mitigate the surface charge recombination.

Although the overall PEC performance can be improved by introducing the cocatalyst on surface of photoelectrodes, it is still unclear about whether PEC performance is limited by surface charge recombination or surface catalytic reaction. Ye *et al.* systemically compared several OER electrocatalysts of CoPi, IrO$_x$, Pt and Co$_3$O$_4$ on W-BiVO$_4$ photoanodes for PEC and electrochemical water oxidation.[186] It is observed that Pt-modified W-BiVO$_4$ gave the best photocurrent performance followed by CoPi- and Co$_3$O$_4$-modified ones while IrO$_x$ almost showed no enhancement in photocurrent. By contrast, IrO$_x$ exhibited the higher electrochemical OER activity compared to CoPi, Co$_3$O$_4$ and Pt. On basis of these results, it was concluded by the authors that loading OER electrocatalysts on a photoanode could accelerate surface reaction kinetics, but the overall PEC performance was still significantly determined by the nature of the OECs and the semiconductor/OECs interface. This is because the OECs or semiconductor/OECs interface can affect photo-induced charge carrier generation, separation, and recombination in the photoanodes, not just the kinetics of oxygen evolution.
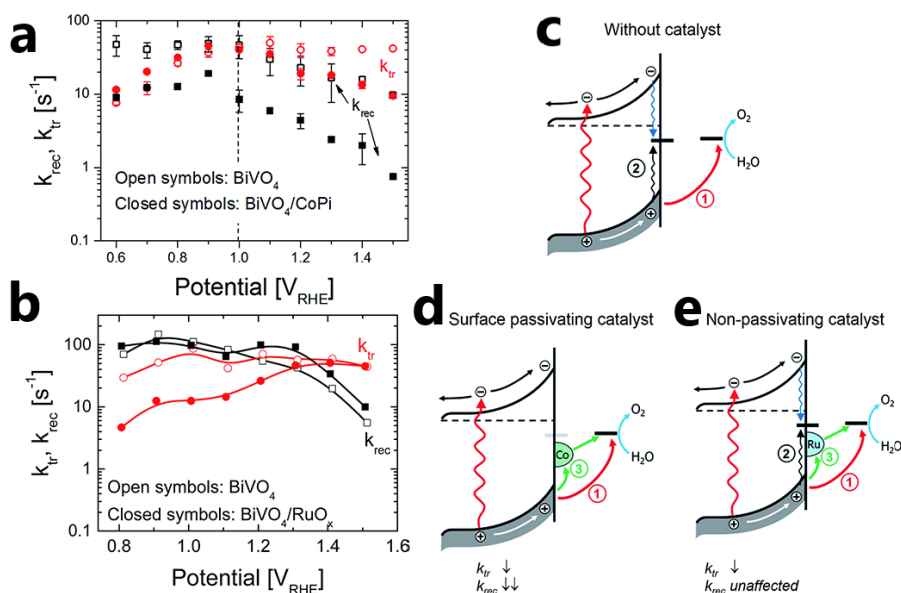
Figure 34. Simplified model of the elementary processes in the BiVO$_4$ photoanode (a) with a surface passivating cocatalyst *(e.g.,* CoPi) and (b) with a non-passivating co-catalyst *(e.g.,* RuO$_x$). Upon illumination, photo-excited carriers move towards the semiconductor-electrolyte interface, (1) direct water oxidation by valence band holes, (2) surface state-mediated recombination, and (3) charge transfer via co-catalyst. Reprinted with permission.[195] Copyright (2017) Royal Society of Chemistry.

Recently, using an intensity modulated photocurrent spectroscopy (IMPS) technique developed by Peter *et al.*,[15] it is possible to determine the reaction rate constants for surface charge recombination and transfer kinetics to the electrolyte. Zachäus *et al.* employed the IMPS technique to investigate the surface charge recombination and transfer kinetics by using a typical BiVO$_4$ photoanode.[195] It is observed that CoPi does not improve the surface charge transfer rate constant (k_t) on the surface of BiVO$_4$, but instead suppresses surface recombination rate constant (k_r) by a factor of 10-20 (**Figure 34a**), leading to an enhanced photocurrent density. In contrast, the photocurrent density of BiVO$_4$ does not improve with the introduction of RuO$_x$, a conventional OER electrocatalyst; instead it decreases, where the k_t is actually smaller than that of the pristine BiVO$_4$, while the k_r is not affected (**Figure 34b**), suggesting that BiVO$_4$ by itself is already thermodynamically active towards water oxidation and RuO$_x$ does not passivate the BiVO$_4$ surface. Therefore, it can be concluded that photocurrent of BiVO$_4$ is limited by surface recombination, not water oxidation kinetics. A more specific scheme in **Figure 34c** show that the photo-induced holes can either directly oxidize water or move to the surface trapping states and recombine with photo-induced electrons. By functionalizing the BiVO$_4$ with a surface passivating "co-catalyst" (CoPi), the surface charge recombination pathway was blocked so that more surface charge can be injected into the electrolyte to directly oxidize water (**Figure 34d**). And a non-passivating co-catalyst (RuO$_x$) on BiVO$_4$ (**Figure 34e**) does not affect the k_r. However, the RuO$_x$ does decrease the k_t compared to pristine BiVO$_4$ due to the lower oxidation power of the holes in RuO$_x$. The similar conclusion that PEC performance is limited by surface recombination rather than surface catalysis is also reached by others using IMPS technique and Fe$_2$O$_3$ as the phototype photoelectrode.[187, 196] It is also note that the same photoelectrode materials prepared by different methods may be limited by various factors. For example, undoped BiVO$_4$ made by magnetron sputtering consistently show lower onset potentials and higher injection efficiencies than sprayed samples.[197] Efforts to improve these sputtered samples by CoPi or RuO$_x$ deposition have

been unsuccessful, most likely because their performance is limited by bulk recombination at sputter induced defects.

Research in this Thesis

My PhD study mainly focused on the development of photoelectrodes for solar water splitting. By utilizing strategies of building junction and fabricating cocatalysts to regulate charge behavior in the bulk and on the surface, respectively, higher PEC performance was achieved in $BiVO_4$ and C_3N_4-based photoelectrodes. And the corresponding mechanism was proposed and investigated for understanding the PEC process. The structure of the Thesis is as follows:

Chapter 2. Bismuth Vanadate with Electrostatically Anchored 3D Carbon Nitride Nano-networks as Efficient Photoanodes for Water Oxidation

Chapter 3. Dual Quantum Dot-Decorated Bismuth Vanadate Photoanodes for Highly Efficient Solar Water Oxidation

Chapter 4. Unique Layer-Doping-Induced Regulation of Charge Behavior in Metal-Free Carbon Nitride Photoanodes for Enhanced Performance

Chapter 5. Atomically Dispersed Ruthenium Cocatalysts on Polymeric Carbon Nitride Photoanodes for Efficient Solar Water Oxidation

Chapter 6. Summary and outlook

Reference

(1).   Lewis, N. S.; Nocera, D. G., Powering the planet: Chemical challenges in solar energy utilization. *Proc. Natl. Acad. Sci.* **2006,** *103*, 15729-15735.

(2).   Pinaud, B. A.; Benck, J. D.; Seitz, L. C.; Forman, A. J.; Chen, Z.; Deutsch, T. G.; James, B. D.; Baum, K. N.; Baum, G. N.; Ardo, S.; Wang, H.; Miller, E.; Jaramillo, T. F., Technical and economic feasibility of centralized facilities for solar hydrogen production via photocatalysis and photoelectrochemistry. *Energy Environ. Sci.* **2013,** *6*, 1983-2002.

(3).   Kim, J. H.; Hansora, D.; Sharma, P.; Jang, J. W.; Lee, J. S., Toward practical solar hydrogen production - an artificial photosynthetic leaf-to-farm challenge. *Chem. Soc. Rev.* **2019,** *48*, 1908-1971.

(4).   Grätzel, M., Photoelectrochemical Cells. *Nature* **2001,** *414*, 338-344.

(5).   Lewis, N. S., Toward cost-effective solar energy use. *Science* **2007,** *315*, 798-801.

(6).   Walter, M. G.; Warren, E. L.; McKone, J. R.; Boettcher, S. W.; Mi, Q.; Santori, E. A.; Lewis, N. S., Solar water splitting cells. *Chem. Rev.* **2010,** *110*, 6446-6473.

(7).   Dogutan, D. K.; Nocera, D. G., Artificial Photosynthesis at Efficiencies Greatly Exceeding That of Natural Photosynthesis. *Acc. Chem. Res.* **2019,** *52*, 3143−3148.

(8).   Jiang, C.; Moniz, S. J. A.; Wang, A.; Zhang, T.; Tang, J., Photoelectrochemical devices for solar water splitting - materials and challenges. *Chem. Soc. Rev.* **2017,** *46*, 4645-4660.

(9).   Deng, J.; Su, Y.; Liu, D.; Yang, P.; Liu, B.; Liu, C., Nanowire Photoelectrochemistry. *Chem. Rev.* **2019,** *119*, 9221-9259.

(10).   Wen, F.; Li, C., Hybrid artificial photosynthetic systems comprising semiconductors as light harvesters and biomimetic complexes as molecular cocatalysts. *Acc. Chem. Res.* **2013,** *46*, 2355-2364.

(11).   Ding, C.; Shi, J.; Wang, Z.; Li, C., Photoelectrocatalytic Water Splitting: Significance of Cocatalysts, Electrolyte, and Interfaces. *ACS Catal.* **2016,** *7*, 675-688.

(12).   Tachibana, Y.; Vayssieres, L.; Durrant, J. R., Artificial photosynthesis for solar water-splitting. *Nat. Photonics* **2012,** *6*, 511-518.

(13).   Bard, A. J.; Fox, M. A., Artificial Photosynthesis: Solar Splitting of Water to Hydrogen and Oxygen. *Acc. Chem. Res.* **1995,** *28*, 141-145.

(14).   Fujishima, A.; Honda, K., Electrochemical Photolysis of Water at a Semiconductor Electrode. *Nature* **1972,** *238*, 37-38.

(15).   Peter, L. M., Dynamic aspects of semiconductor photoelectrochemistry. *Chem. Rev.* **1990,** *90*, 753-769.

(16).   Zhang, P.; Wang, T.; Gong, J., Current Mechanistic Understanding of Surface Reactions over Water-Splitting Photocatalysts. *Chem* **2018,** *4*, 223-245.

(17).   Nellist, M. R.; Laskowski, F. A.; Lin, F.; Mills, T. J.; Boettcher, S. W., Semiconductor-Electrocatalyst Interfaces: Theory, Experiment, and Applications in Photoelectrochemical Water Splitting. *Acc. Chem. Res.* **2016,** *49*, 733-40.

(18).   Sivula, K., Metal Oxide Photoelectrodes for Solar Fuel Production, Surface Traps, and Catalysis. *J. Phys. Chem. Lett.* **2013,** *4*, 1624-1633.

(19).   Zhang, P.; Wang, T.; Chang, X.; Gong, J., Effective Charge Carrier Utilization in Photocatalytic Conversions. *Acc. Chem. Res.* **2016,** *49*, 911-21.

(20).   Yao, T.; An, X.; Han, H.; Chen, J. Q.; Li, C., Photoelectrocatalytic Materials for Solar Water Splitting. *Adv. Energy Mater.* **2018,** *8*, 1800210.

(21).   Luo, Z.; Wang, T.; Gong, J., Single-crystal silicon-based electrodes for unbiased solar water splitting: current status and prospects. *Chem. Soc. Rev.* **2019,** *48*, 2158-2181.

(22).   Luan, P.; Zhang, J., Stepping towards Solar Water Splitting: Recent Progress in Bismuth Vanadate Photoanodes. *ChemElectroChem* **2019,** *6*, 3227-3243.

(23).   Sivula, K.; Le Formal, F.; Gratzel, M., Solar water splitting: progress using hematite a-Fe2O3 photoelectrodes. *ChemSusChem* **2011,** *4*, 432-449.

(24).   Wang, S.; Liu, G.; Wang, L., Crystal Facet Engineering of Photoelectrodes for Photoelectrochemical Water Splitting. *Chem. Rev.* **2019,** *119*, 5192-5247.

(25).   Khaselev, O.; Turner, J. A., A monolithic photovoltaic-photoelectrochemical device for hydrogen production via water splitting. *Science* **1998,** *280*, 425-427.

(26).   Landman, A.; Dotan, H.; Shter, G. E.; Wullenkord, M.; Houaijia, A.; Maljusch, A.; Grader, G. S.; Rothschild, A., Photoelectrochemical water splitting in separate oxygen and hydrogen cells. *Nat. Mater.* **2017,** *16*, 646-651.

(27).   Segev, G.; Beeman, J. W.; Greenblatt, J. B.; Sharp, I. D., Hybrid photoelectrochemical and photovoltaic cells for simultaneous production of chemical fuels and electrical power. *Nat. Mater.* **2018,** *17*, 1115-1121.

(28).   Brillet, J.; Yum, J.-H.; Cornuz, M.; Hisatomi, T.; Solarska, R.; Augustynski, J.; Graetzel, M.; Sivula, K., Highly efficient water splitting by a dual-absorber tandem cell. *Nat. Photonics* **2012,** *6*, 824-828.

(29).   Chen, X.; Shen, S.; Guo, L.; Mao, S. S., Semiconductor-based photocatalytic hydrogen generation. *Chem. Rev.* **2010,** *110*, 6503-6570.

(30).   Ma, Y.; Wang, X.; Jia, Y.; Chen, X.; Han, H.; Li, C., Titanium dioxide-based nanomaterials for photocatalytic fuel generations. *Chem. Rev.* **2014,** *114*, 9987-10043.

(31).   Hisatomi, T.; Kubota, J.; Domen, K., Recent advances in semiconductors for photocatalytic and photoelectrochemical water splitting. *Chem. Soc. Rev.* **2014,** *43*, 7520-35.

(32).   Nocera, D. G., Solar Fuels and Solar Chemicals Industry. *Acc. Chem. Res.* **2017,** *50*, 616-619.

(33).   Huynh, M. H. V.; Meyer, T. J., Proton-coupled electron transfer. *Chem. Rev.* **2007,** *107*, 5004-5064.

(34).   Li, Z.; Luo, W.; Zhang, M.; Feng, J.; Zou, Z., Photoelectrochemical cells for solar hydrogen production: current state of promising photoelectrodes, methods to improve their properties, and outlook. *Energy Environ. Sci.* **2013,** *6*, 347-370.

(35).   Salvador, P., Hole diffusion length in n-TiO2 single crystals and sintered electrodes: Photoelectrochemical determination and comparative analysis. *J. Appl. Phys.* **1984,** *55*, 2977-2985.

(36).   Yang, W.; Prabhakar, R. R.; Tan, J.; Tilley, S. D.; Moon, J., Strategies for enhancing the photocurrent, photovoltage, and stability of photoelectrodes for photoelectrochemical water splitting. *Chem. Soc. Rev.* **2019,** *48*, 4979-5015.

(37).   Govindaraju, G. V.; Wheeler, G. P.; Lee, D.; Choi, K.-S., Methods for Electrochemical Synthesis and Photoelectrochemical Characterization for Photoelectrodes. *Chem. Mater.* **2016,** *29*, 355-370.

(38).   Shi, X.; Cai, L.; Ma, M.; Zheng, X.; Park, J. H., General Characterization Methods for Photoelectrochemical Cells for Solar Water Splitting. *ChemSusChem* **2015,** *8*, 3192-203.

(39).   Lewis, N. S., Mechanistic studies of light-induced charge separation at semiconductor/liquid interfaces. *Aec. Chem. Res.* **1990,** *23*, 176-183.

(40).   Mayer, M. T., Photovoltage at semiconductor–electrolyte junctions. *Curr. Opin. Electrochem.* **2017,** *2*, 104-110.

(41).   Seo, J.; Nishiyama, H.; Yamada, T.; Domen, K., Visible-Light-Responsive Photoanodes for Highly Active, Stable Water Oxidation. *Angew. Chem. Int. Ed.* **2018,** *57*, 8396-8415.

(42).   Kim, T. W.; Choi, K.-S., Nanoporous BiVO4 photoanodes with dual-layer oxygen evolution catalysts for solar water splitting. *Science* **2014,** *343*, 990-994.

(43).   Hu, S.; Xiang, C.; Haussener, S.; Berger, A. D.; Lewis, N. S., An analysis of the optimal band gaps of light absorbers in integrated tandem photoelectrochemical water-splitting systems. *Energy Environ. Sci.* **2013,** *6*, 2984-2993.

(44).   Jia, J.; Seitz, L. C.; Benck, J. D.; Huo, Y.; Chen, Y.; Ng, J. W.; Bilir, T.; Harris, J. S.; Jaramillo, T. F., Solar water splitting by photovoltaic-electrolysis with a solar-to-hydrogen efficiency over 30. *Nat. Commun.* **2016,** *7*, 13237-13242.

(45).   Kim, J. H.; Jo, Y.; Kim, J. H.; Jang, J. W.; Kang, H. J.; Lee, Y. H.; Kim, D. S.; Jun, Y.; Lee, J. S., Wireless solar water splitting device with robust cobalt-catalyzed, dual-doped BiVO4

photoanode and perovskite solar cell in tandem: a dual absorber artificial leaf. *ACS Nano* **2015,** *9*, 11820-11829.

(46).   Shi, X.; Jeong, H.; Oh, S. J.; Ma, M.; Zhang, K.; Kwon, J.; Choi, I. T.; Choi, I. Y.; Kim, H. K.; Kim, J. K.; Park, J. H., Unassisted photoelectrochemical water splitting exceeding 7% solar-to-hydrogen conversion efficiency using photon recycling. *Nat. Commun.* **2016,** *7*, 11943.

(47).   Kim, J. H.; Jang, J. W.; Jo, Y. H.; Abdi, F. F.; Lee, Y. H.; van de Krol, R.; Lee, J. S., Hetero-type dual photoanodes for unbiased solar water splitting with extended light harvesting. *Nat. Commun.* **2016,** *7*, 13380-13388.

(48).   Varadhan, P.; Fu, H. C.; Kao, Y. C.; Horng, R. H.; He, J. H., An efficient and stable photoelectrochemical system with 9% solar-to-hydrogen conversion efficiency via InGaP/GaAs double junction. *Nat. Commun.* **2019,** *10*, 5282.

(49).   Ye, K.-H.; Wang, Z.; Gu, J.; Xiao, S.; Yuan, Y.; Zhu, Y.; Zhang, Y.; Mai, W.; Yang, S., Carbon quantum dots as a visible light sensitizer to significantly increase the solar water splitting performance of bismuth vanadate photoanodes. *Energy Environ. Sci.* **2017,** *10*, 772-779.

(50).   Wang, S.; Chen, P.; Yun, J. H.; Hu, Y.; Wang, L., An Electrochemically Treated $BiVO_4$ Photoanode for Efficient Photoelectrochemical Water Splitting. *Angew. Chem. Int. Ed.* **2017,** *56*, 8500-8504.

(51).   Li, F.; Li, J.; Li, F.; Gao, L.; Long, X.; Hu, Y.; Wang, C.; Wei, S.; Jin, J.; Ma, J., Facile regrowth of $Mg-Fe_2O_3/P-Fe_2O_3$ homojunction photoelectrode for efficient solar water oxidation. *J. Mater. Chem. A* **2018,** *6*, 13412-13418.

(52).   Chang, X.; Wang, T.; Zhang, P.; Zhang, J.; Li, A.; Gong, J., Enhanced Surface Reaction Kinetics and Charge Separation of p-n Heterojunction $Co_3O_4/BiVO_4$ Photoanodes. *J. Am. Chem. Soc.* **2015,** *137*, 8356-8359.

(53).   Chen, S.; Wang, L.-W., Thermodynamic Oxidation and Reduction Potentials of Photocatalytic Semiconductors in Aqueous Solution. *Chem. Mater.* **2012,** *24*, 3659-3666.

(54).   Rongé, J.; Bosserez, T.; Huguenin, L.; Dumortier, M.; Haussener, S.; Martens, J. A., Solar hydrogen reaching maturity. *Oil Gas Sci. Technol.* **2015,** *70*, 863-876.

(55).   Hu, S.; Shaner, M. R.; Beardslee, J. A.; Lichterman, M.; Brunschwig, B. S.; Lewis, N. S., Amorphous TiO2 coatings stabilize Si, GaAs, and GaP photoanodes for efficient water oxidation. *Science* **2014,** *344*, 1005-1009.

(56).   Kuang, Y.; Yamada, T.; Domen, K., Surface and Interface Engineering for Photoelectrochemical Water Oxidation. *Joule* **2017,** *1*, 290-305.

(57).   Liu, R.; Zheng, Z.; Spurgeon, J.; Yang, X., Enhanced photoelectrochemical water-splitting performance of semiconductors by surface passivation layers. *Energy Environ. Sci.* **2014,** *7*, 2504-2517.

(58).   Seabold, J. A.; Choi, K.-S., Effect of a Cobalt-Based Oxygen Evolution Catalyst on the Stability and the Selectivity of Photo-Oxidation Reactions of a WO3Photoanode. *Chem. Mater.* **2011,** *23*, 1105-1112.

(59).   Kuang, Y.; Jia, Q.; Ma, G.; Hisatomi, T.; Minegishi, T.; Nishiyama, H.; Nakabayashi, M.; Shibata, N.; Yamada, T.; Kudo, A.; Domen, K., Ultrastable low-bias water splitting photoanodes via photocorrosion inhibition and in situ catalyst regeneration. *Nat. Energy* **2016,** *2*, 16191-16200.

(60).   Zhang, K.; Liu, J.; Wang, L.; Jin, B.; Yang, X.; Zhang, S.; Park, J. H., Near-Complete Suppression of Oxygen Evolution for Photoelectrochemical H2O Oxidative H2O2 Synthesis. *J. Am. Chem. Soc.* **2020,** *142*, 8641-8648.

(61).   Zhou, X.; Liu, R.; Sun, K.; Papadantonakis, K. M.; Brunschwig, B. S.; Lewis, N. S., 570 mV photovoltage, stabilized n-Si/CoOx heterojunction photoanodes fabricated using atomic layer deposition. *Energy Environ. Sci.* **2016,** *9*, 892-897.

(62).   Le Formal, F.; Tétreault, N.; Cornuz, M.; Moehl, T.; Grätzel, M.; Sivula, K., Passivating surface states on water splitting hematite photoanodes with alumina overlayers. *Chem. Sci.* **2011,** *2*, 737-743.

(63). Pan, L.; Kim, J. H.; Mayer, M. T.; Son, M.-K.; Ummadisingu, A.; Lee, J. S.; Hagfeldt, A.; Luo, J.; Grätzel, M., Boosting the performance of Cu2O photocathodes for unassisted solar water splitting devices. *Nat. Catal.* **2018,** *1*, 412-420.

(64). Gao, R. T.; He, D.; Wu, L.; Hu, K.; Liu, X.; Su, Y.; Wang, L., Towards Long-Term Photostability of Nickel Hydroxide/BiVO4 Photoanodes for Oxygen Evolution Catalysts via In Situ Catalyst Tuning. *Angew. Chem. Int. Ed.* **2020,** *59*, 6213-6218.

(65). Lee, D. K.; Choi, K.-S., Enhancing long-term photostability of BiVO4 photoanodes for solar water splitting by tuning electrolyte composition. *Nat. Energy* **2017,** *3*, 53-60.

(66). Sivula, K.; van de Krol, R., Semiconducting materials for photoelectrochemical energy conversion. *Nat. Rev. Mater.* **2016,** *1*, 15010-15026.

(67). Yang, Y.; Niu, S.; Han, D.; Liu, T.; Wang, G.; Li, Y., Progress in Developing Metal Oxide Nanomaterials for Photoelectrochemical Water Splitting. *Adv. Energy Mater.* **2017,** *7*, 1700555.

(68). Kim, M.; Lee, B.; Ju, H.; Kim, J. Y.; Kim, J.; Lee, S. W., Oxygen-Vacancy-Introduced BaSnO3-δ Photoanodes with Tunable Band Structures for Efficient Solar-Driven Water Splitting. *Adv. Mater.* **2019,** *31*, e1903316.

(69). Yan, J.; Wang, T.; Wu, G.; Dai, W.; Guan, N.; Li, L.; Gong, J., Tungsten oxide single crystal nanosheets for enhanced multichannel solar light harvesting. *Adv. Mater.* **2015,** *27*, 1580-1586.

(70). Carneiro, L. M.; Cushing, S. K.; Liu, C.; Su, Y.; Yang, P.; Alivisatos, A. P.; Leone, S. R., Excitation-wavelength-dependent small polaron trapping of photoexcited carriers in alpha-Fe2O3. *Nat. Mater.* **2017,** *16*, 819-825.

(71). Zhou, Z.; Long, R.; Prezhdo, O. V., Why Silicon Doping Accelerates Electron Polaron Diffusion in Hematite. *J. Am. Chem. Soc.* **2019,** *141*, 20222-20233.

(72). Sayama, K.; Nomura, A.; Arai, T.; Sugita, T.; Abe, R.; Yanagida, M.; Oi, T.; Iwasaki, Y.; Abe, Y.; Sugihara, H., Photoelectrochemical decomposition of water into H2 and O2 on porous

BiVO4 thin-film electrodes under visible light and significant effect of Ag ion treatment. *J. Phys. Chem. B* **2006,** *110*, 11352-11360.

(73). Park, Y.; McDonald, K. J.; Choi, K. S., Progress in bismuth vanadate photoanodes for use in solar water oxidation. *Chem. Soc. Rev.* **2013,** *42*, 2321-2337.

(74). Pihosh, Y.; Turkevych, I.; Mawatari, K.; Uemura, J.; Kazoe, Y.; Kosar, S.; Makita, K.; Sugaya, T.; Matsui, T.; Fujita, D.; Tosa, M.; Kondo, M.; Kitamori, T., Photocatalytic generation of hydrogen by core-shell WO(3)/BiVO(4) nanorods with ultimate water splitting efficiency. *Sci. Rep.* **2015,** *5*, 11141-11150.

(75). Lumley, M. A.; Radmilovic, A.; Jang, Y. J.; Lindberg, A. E.; Choi, K. S., Perspectives on the Development of Oxide-Based Photocathodes for Solar Fuel Production. *J. Am. Chem. Soc.* **2019,** *141*, 18358−18369.

(76). Yang, W.; Moon, J., Recent Advances in Earth-Abundant Photocathodes for Photoelectrochemical Water Splitting. *ChemSusChem* **2019,** *12*, 1889-1899.

(77). Paracchino, A.; Laporte, V.; Sivula, K.; Gratzel, M.; Thimsen, E., Highly active oxide photocathode for photoelectrochemical water reduction. *Nat. Mater.* **2011,** *10*, 456-461.

(78). Paracchino, A.; Brauer, J. C.; Moser, J.-E.; Thimsen, E.; Graetzel, M., Synthesis and Characterization of High-Photoactivity Electrodeposited Cu2O Solar Absorber by Photoelectrochemistry and Ultrafast Spectroscopy. *J. Phys. Chem. C* **2012,** *116*, 7341-7350.

(79). Jian, J.; Jiang, G.; van de Krol, R.; Wei, B.; Wang, H., Recent Advances in Rational Engineering of Multinary Semiconductors for Photoelectrochemical Hydrogen Generation. *Nano Energy* **2018,** *51*, 457-480.

(80). Kobayashi, H.; Sato, N.; Orita, M.; Kuang, Y.; Kaneko, H.; Minegishi, T.; Yamada, T.; Domen, K., Development of highly efficient CuIn0.5Ga0.5Se2-based photocathode and application to overall solar driven water splitting. *Energy Environ. Sci.* **2018,** *11*, 3003-3009.

(81).   Tay, Y. F.; Kaneko, H.; Chiam, S. Y.; Lie, S.; Zheng, Q.; Wu, B.; Hadke, S. S.; Su, Z.; Bassi, P. S.; Bishop, D.; Sum, T. C.; Minegishi, T.; Barber, J.; Domen, K.; Wong, L. H., Solution-Processed Cd-Substituted CZTS Photocathode for Efficient Solar Hydrogen Evolution from Neutral Water. *Joule* **2018,** *2*, 537-548.

(82).   Chen, M.; Liu, Y.; Li, C.; Li, A.; Chang, X.; Liu, W.; Sun, Y.; Wang, T.; Gong, J., Spatial control of cocatalysts and elimination of interfacial defects towards efficient and robust CIGS photocathodes for solar water splitting. *Energy Environ. Sci.* **2018,** *11*, 2025-2034.

(83).   Sun, Y.; Liu, C.; Grauer, D. C.; Yano, J.; Long, J. R.; Yang, P.; Chang, C. J., Electrodeposited cobalt-sulfide catalyst for electrochemical and photoelectrochemical hydrogen generation from water. *J. Am. Chem. Soc.* **2013,** *135*, 17699-17702.

(84).   Creissen, C. E.; Warnan, J.; Antón-García, D.; Farré, Y.; Odobel, F.; Reisner, E., Inverse Opal CuCrO2 Photocathodes for H2 Production Using Organic Dyes and a Molecular Ni Catalyst. *ACS Catal.* **2019,** *9*, 9530-9538.

(85).   Gross, M. A.; Creissen, C. E.; Orchard, K. L.; Reisner, E., Photoelectrochemical hydrogen production in water using a layer-by-layer assembly of a Ru dye and Ni catalyst on NiO. *Chem. Sci.* **2016,** *7*, 5537-5546.

(86).   Thalluri, S. M.; Wei, B.; Welter, K.; Thomas, R.; Smirnov, V.; Qiao, L.; Wang, Z.; Finger, F.; Liu, L., Inverted Pyramid Textured p-Silicon Covered with Co2P as an Efficient and Stable Solar Hydrogen Evolution Photocathode. *ACS Energy Lett.* **2019,** *4*, 1755-1762.

(87).   Recent Advances in Photoelectrochemical Applications of Silicon Materials for Solar-to-Chemicals Conversion. *ChemSusChem* **2017,** *10*, 4324-4341.

(88).   Mayer, M. T.; Du, C.; Wang, D., Hematite/Si nanowire dual-absorber system for photoelectrochemical water splitting at low applied potentials. *J. Am. Chem. Soc.* **2012,** *134*, 12406-12409.

(89).   Wang, H. P.; Sun, K.; Noh, S. Y.; Kargar, A.; Tsai, M. L.; Huang, M. Y.; Wang, D.; He, J. H., High-Performance a-Si/c-Si Heterojunction Photoelectrodes for Photoelectrochemical Oxygen and Hydrogen Evolution. *Nano Lett.* **2015,** *15*, 2817-2824.

(90).   Lee, S. A.; Choi, S.; Kim, C.; Yang, J. W.; Kim, S. Y.; Jang, H. W., Si-Based Water Oxidation Photoanodes Conjugated with Earth-Abundant Transition Metal-Based Catalysts. *ACS Mater. Lett.* **2019,** *2*, 107-126.

(91).   Zhang, H.; Ding, Q.; He, D.; Liu, H.; Liu, W.; Li, Z.; Yang, B.; Zhang, X.; Lei, L.; Jin, S., A p-Si/NiCoSex core/shell nanopillar array photocathode for enhanced photoelectrochemical hydrogen production. *Energy Environ. Sci.* **2016,** *9*, 3113-3119.

(92).   Qiu, Y.; Liu, W.; Chen, W.; Chen, W.; Zhou, G.; Hsu, P.-C.; Zhang, R.; Liang, Z.; Fan, S.; Zhang, Y.; Cui, Y., Efficient solar-driven water splitting by nanocone $BiVO_4$-perovskite tandem cells. *Sci. Adv.* **2016,** *2*, e1501764.

(93).   Guo, B.; Batool, A.; Xie, G.; Boddula, R.; Tian, L.; Jan, S. U.; Gong, J. R., Facile Integration between Si and Catalyst for High-Performance Photoanodes by a Multifunctional Bridging Layer. *Nano Lett.* **2018,** *18*, 1516-1521.

(94).   Neergaard Waltenburg, H.; Yates, J., Surface chemistry of silicon. *Chem. Rev.* **1995,** *95*, 1589-1673.

(95).   Yu, Y.; Zhang, Z.; Yin, X.; Kvit, A.; Liao, Q.; Kang, Z.; Yan, X.; Zhang, Y.; Wang, X., Enhanced photoelectrochemical efficiency and stability using a conformal TiO2 film on a black silicon photoanode. *Nat. Energy* **2017,** *2*, 17045.

(96).   Liu, B.; Feng, S.; Yang, L.; Li, C.; Luo, Z.; Wang, T.; Gong, J., Bifacial passivation of n-silicon metal–insulator–semiconductor photoelectrodes for efficient oxygen and hydrogen evolution reactions. *Energy Environ. Sci.* **2020,** *13*, 221-228.

(97).   Zhao, J.; Cai, L.; Li, H.; Shi, X.; Zheng, X., Stabilizing Silicon Photocathodes by Solution-Deposited Ni–Fe Layered Double Hydroxide for Efficient Hydrogen Evolution in Alkaline Media. *ACS Energy Lett.* **2017,** *2*, 1939-1946.

(98).   Wang, X.; Maeda, K.; Thomas, A.; Takanabe, K.; Xin, G.; Carlsson, J. M.; Domen, K.; Antonietti, M., A metal-free polymeric photocatalyst for hydrogen production from water under visible light. *Nat. Mater.* **2009,** *8*, 76-80.

(99).   Ong, W. J.; Tan, L. L.; Ng, Y. H.; Yong, S. T.; Chai, S. P., Graphitic Carbon Nitride (g-C3N4)-Based Photocatalysts for Artificial Photosynthesis and Environmental Remediation: Are We a Step Closer To Achieving Sustainability? *Chem. Rev.* **2016,** *116*, 7159-7329.

(100).   Wang, H.; Zhang, X.; Xie, Y., Photoresponsive polymeric carbon nitride-based materials: Design and application. *Mater. Today* **2019,** *23*, 72-86.

(101).   Liu, W.; Cao, L.; Cheng, W.; Cao, Y.; Liu, X.; Zhang, W.; Mou, X.; Jin, L.; Zheng, X.; Che, W.; Liu, Q.; Yao, T.; Wei, S., Single-Site Active Cobalt-Based Photocatalyst with a Long Carrier Lifetime for Spontaneous Overall Water Splitting. *Angew. Chem. Int. Ed.* **2017,** *56*, 9312-9317.

(102).   Lin, L.; Yu, Z.; Wang, X., Crystalline Carbon Nitride Semiconductors for Photocatalytic Water Splitting. *Angew. Chem. Int. Ed.* **2019,** *58*, 6164-6175.

(103).   Ruan, Q.; Bayazit, M. K.; Kiran, V.; Xie, J.; Wang, Y.; Tang, J., Key factors affecting photoelectrochemical performance of g-C3N4 polymer films. *Chem. Commun.* **2019,** *55*, 7191-7194.

(104).   Volokh, M.; Peng, G.; Barrio, J.; Shalom, M., Carbon Nitride Materials for Water Splitting Photoelectrochemical Cells. *Angew. Chem. Int. Ed.* **2019,** *58*, 6138-6151.

(105).   Peng, G.; Albero, J.; Garcia, H.; Shalom, M., A Water-Splitting Carbon Nitride Photoelectrochemical Cell with Efficient Charge Separation and Remarkably Low Onset Potential. *Angew. Chem. Int. Ed.* **2018,** *57*, 15807-15811.

(106). Schwinghammer, K.; Mesch, M. B.; Duppel, V.; Ziegler, C.; Senker, J.; Lotsch, B. V., Crystalline carbon nitride nanosheets for improved visible-light hydrogen evolution. *J. Am. Chem. Soc.* **2014,** *136*, 1730-1733.

(107). Noda, Y.; Merschjann, C.; Tarabek, J.; Amsalem, P.; Koch, N.; Bojdys, M. J., Directional Charge Transport in Layered Two-Dimensional Triazine-Based Graphitic Carbon Nitride. *Angew. Chem. Int. Ed.* **2019,** *58*.

(108). Ruan, Q.; Luo, W.; Xie, J.; Wang, Y.; Liu, X.; Bai, Z.; Carmalt, C. J.; Tang, J., A Nanojunction Polymer Photoelectrode for Efficient Charge Transport and Separation. *Angew. Chem. Int. Ed.* **2017,** *56*, 8221-8225.

(109). Peng, G.; Volokh, M.; Tzadikov, J.; Sun, J.; Shalom, M., Carbon Nitride/Reduced Graphene Oxide Film with Enhanced Electron Diffusion Length: An Efficient Photo-Electrochemical Cell for Hydrogen Generation. *Adv. Energy Mater.* **2018,** *8*, 1800566.

(110). Lv, X.; Cao, M.; Shi, W.; Wang, M.; Shen, Y., A new strategy of preparing uniform graphitic carbon nitride films for photoelectrochemical application. *Carbon* **2017,** *117*, 343-350.

(111). Xu, J.; Shalom, M., Electrophoretic Deposition of Carbon Nitride Layers for Photoelectrochemical Applications. *ACS Appl. Mater. Interfaces* **2016,** *8*, 13058-13063.

(112). Tang, S.; Qiu, W.; Xiao, S.; Tong, Y.; Yang, S., Harnessing hierarchical architectures to trap light for efficient photoelectrochemical cells. *Energy Environ. Sci.* **2020,** *13*, 660-684.

(113). Concina, I.; Ibupoto, Z. H.; Vomiero, A., Semiconducting Metal Oxide Nanostructures for Water Splitting and Photovoltaics. *Adv. Energy Mater.* **2017,** *7*, 1700706.

(114). Wang, T.; Luo, Z.; Li, C.; Gong, J., Controllable fabrication of nanostructured materials for photoelectrochemical water splitting via atomic layer deposition. *Chem. Soc. Rev.* **2014,** *43*, 7469-7484.

(115). Zhou, Y.; Zhang, L.; Lin, L.; Wygant, B. R.; Liu, Y.; Zhu, Y.; Zheng, Y.; Mullins, C. B.; Zhao, Y.; Zhang, X.; Yu, G., Highly Efficient Photoelectrochemical Water Splitting from Hierarchical WO3/BiVO4 Nanoporous Sphere Arrays. *Nano Lett.* **2017,** *17*, 8012-8017.

(116). Zhang, P.; Lou, X. W. D., Design of Heterostructured Hollow Photocatalysts for Solar-to-Chemical Energy Conversion. *Adv. Mater.* **2019,** *31*, e1900281.

(117). Shi, X.; Choi, I. Y.; Zhang, K.; Kwon, J.; Kim, D. Y.; Lee, J. K.; Oh, S. H.; Kim, J. K.; Park, J. H., Efficient photoelectrochemical hydrogen production from bismuth vanadate-decorated tungsten trioxide helix nanostructures. *Nat. Commun.* **2014,** *5*, 4775-4782.

(118). Peerakiatkhajohn, P.; Yun, J. H.; Chen, H.; Lyu, M.; Butburee, T.; Wang, L., Stable Hematite Nanosheet Photoanodes for Enhanced Photoelectrochemical Water Splitting. *Adv. Mater.* **2016,** *28*, 6405-10.

(119). Zhou, M.; Lou, X. W.; Xie, Y., Two-dimensional nanosheets for photoelectrochemical water splitting: Possibilities and opportunities. *Nano Today* **2013,** *8*, 598-618.

(120). Faraji, M.; Yousefi, M.; Yousefzadeh, S.; Zirak, M.; Naseri, N.; Jeon, T. H.; Choi, W.; Moshfegh, A. Z., Two-dimensional materials in semiconductor photoelectrocatalytic systems for water splitting. *Energy Environ. Sci.* **2019,** *12*, 59-95.

(121). Hou, Y.; Wen, Z.; Cui, S.; Guo, X.; Chen, J., Constructing 2D porous graphitic C3 N4 nanosheets/nitrogen-doped graphene/layered MoS2 ternary nanojunction with enhanced photoelectrochemical activity. *Adv. Mater.* **2013,** *25*, 6291-6297.

(122). Cho, I. S.; Chen, Z.; Forman, A. J.; Kim, D. R.; Rao, P. M.; Jaramillo, T. F.; Zheng, X., Branched TiO2 nanorods for photoelectrochemical hydrogen production. *Nano Lett.* **2011,** *11*, 4978-84.

(123). Zhou, M.; Wu, H. B.; Bao, J.; Liang, L.; Lou, X. W.; Xie, Y., Ordered macroporous BiVO4 architectures with controllable dual porosity for efficient solar water splitting. *Angew. Chem. Int. Ed.* **2013,** *52*, 8579-8583.

(124). Guo, B.; Tian, L.; Xie, W.; Batool, A.; Xie, G.; Xiang, Q.; Jan, S. U.; Boddula, R.; Gong, J. R., Vertically Aligned Porous Organic Semiconductor Nanorod Array Photoanodes for Efficient Charge Utilization. *Nano Lett.* **2018,** *18*, 5954-5960.

(125). Hou, Y.; Zuo, F.; Dagg, A. P.; Liu, J.; Feng, P., Branched WO3 nanosheet array with layered C3 N4 heterojunctions and CoOx nanoparticles as a flexible photoanode for efficient photoelectrochemical water oxidation. *Adv. Mater.* **2014,** *26*, 5043-5049.

(126). Wang, Y.; Tian, W.; Chen, C.; Xu, W.; Li, L., Tungsten Trioxide Nanostructures for Photoelectrochemical Water Splitting: Material Engineering and Charge Carrier Dynamic Manipulation. *Adv. Funct. Mater.* **2019**, 1809036.

(127). Kay, A.; Cesar, I.; Grätzel, M., New benchmark for water photooxidation by nanostructured α-Fe2O3 films. *J. Am. Chem. Soc.* **2006,** *128*, 15714-15721.

(128). Li, C.; Luo, Z.; Wang, T.; Gong, J., Surface, Bulk, and Interface: Rational Design of Hematite Architecture toward Efficient Photo-Electrochemical Water Splitting. *Adv. Mater.* **2018,** *30*, e1707502.

(129). Tilley, S. D.; Cornuz, M.; Sivula, K.; Gratzel, M., Light-induced water splitting with hematite: improved nanostructure and iridium oxide catalysis. *Angew. Chem. Int. Ed.* **2010,** *49*, 6405-6408.

(130). Warren, S. C.; Voitchovsky, K.; Dotan, H.; Leroy, C. M.; Cornuz, M.; Stellacci, F.; Hebert, C.; Rothschild, A.; Gratzel, M., Identifying champion nanostructures for solar water-splitting. *Nat. Mater.* **2013,** *12*, 842-9.

(131). Zhang, W.; Wu, F.; Li, J.; Yan, D.; Tao, J.; Ping, Y.; Liu, M., Unconventional Relation between Charge Transport and Photocurrent via Boosting Small Polaron Hopping for Photoelectrochemical Water Splitting. *ACS Energy Lett.* **2018**, 2232-2239.

(132). Qiu, W.; Xiao, S.; Ke, J.; Wang, Z.; Tang, S.; Zhang, K.; Qian, W.; Huang, Y.; Huang, D.; Tong, Y.; Yang, S., Freeing the Polarons to Facilitate Charge Transport in BiVO4 from Oxygen Vacancies with an Oxidative 2D Precursor. *Angew. Chem. Int. Ed.* **2019,** *58*, 19087-19095.

(133). Rettie, A. J.; Lee, H. C.; Marshall, L. G.; Lin, J. F.; Capan, C.; Lindemuth, J.; McCloy, J. S.; Zhou, J.; Bard, A. J.; Mullins, C. B., Combined charge carrier transport and photoelectrochemical characterization of BiVO4 single crystals: intrinsic behavior of a complex metal oxide. *J. Am. Chem. Soc.* **2013,** *135*, 11389-11396.

(134). Selim, S.; Pastor, E.; Garcia-Tecedor, M.; Morris, M. R.; Francas, L.; Sachs, M.; Moss, B.; Corby, S.; Mesa, C. A.; Gimenez, S.; Kafizas, A.; Bakulin, A. A.; Durrant, J. R., Impact of Oxygen Vacancy Occupancy on Charge Carrier Dynamics in BiVO4 Photoanodes. *J. Am. Chem. Soc.* **2019,** *141*, 18791−18798.

(135). Feng, S.; Wang, T.; Liu, B.; Hu, C.; Li, L.; Zhao, Z. J.; Gong, J., Enriched Surface Oxygen Vacancies of Photoanodes by Photoetching with Enhanced Charge Separation. *Angew. Chem. Int. Ed.* **2020,** *59*, 2044-2048.

(136). Kim, T. W.; Ping, Y.; Galli, G. A.; Choi, K. S., Simultaneous enhancements in photon absorption and charge transport of bismuth vanadate photoanodes for solar water splitting. *Nat. Commun.* **2015,** *6*, 8769-8779.

(137). Zhou, M.; Bao, J.; Xu, Y.; Zhang, J.; Xie, J.; Guan, M.; Wang, C.; Wen, L.; Lei, Y.; Xie, Y., Photoelectrodes based upon Mo: BiVO4 inverse opals for photoelectrochemical water splitting. *ACS Nano* **2014,** *8*, 7088-7098.

(138). Abdi, F. F.; Han, L.; Smets, A. H.; Zeman, M.; Dam, B.; van de Krol, R., Efficient solar water splitting by enhanced charge separation in a bismuth vanadate-silicon tandem photoelectrode. *Nat. Commun.* **2013,** *4*, 2195-2201.

(139). Wang, Z.; Mao, X.; Chen, P.; Xiao, M.; Monny, S. A.; Wang, S.; Konarova, M.; Du, A.; Wang, L., Understanding the Roles of Oxygen Vacancies in Hematite-Based Photoelectrochemical Processes. *Angew. Chem. Int. Ed.* **2019,** *58*, 1030-1034.

(140). Gao, S.; Gu, B.; Jiao, X.; Sun, Y.; Zu, X.; Yang, F.; Zhu, W.; Wang, C.; Feng, Z.; Ye, B.; Xie, Y., Highly Efficient and Exceptionally Durable CO2 Photoreduction to Methanol over Freestanding Defective Single-Unit-Cell Bismuth Vanadate Layers. *J. Am. Chem. Soc.* **2017,** *139*, 3438-3445.

(141). Zhang, Y.; Xu, Z.; Li, G.; Huang, X.; Hao, W.; Bi, Y., Direct Observation of Oxygen Vacancy Self-Healing on TiO2 Photocatalysts for Solar Water Splitting. *Angew. Chem. Int. Ed.* **2019,** *58*, 14229-14233.

(142). Wiktor, J.; Ambrosio, F.; Pasquarello, A., Role of Polarons in Water Splitting: The Case of BiVO4. *ACS Energy Lett.* **2018,** *3*, 1693-1697.

(143). Wang, G.; Ling, Y.; Wheeler, D. A.; George, K. E.; Horsley, K.; Heske, C.; Zhang, J. Z.; Li, Y., Facile synthesis of highly photoactive alpha-Fe(2)O(3)-based films for water oxidation. *Nano Lett.* **2011,** *11*, 3503-3509.

(144). Nair, V.; Perkins, C. L.; Lin, Q.; Law, M., Textured nanoporous Mo:BiVO4 photoanodes with high charge transport and charge transfer quantum efficiencies for oxygen evolution. *Energy Environ. Sci.* **2016,** *9*, 1412-1429.

(145). Kim, J. H.; Lee, J. S., Elaborately Modified BiVO4 Photoanodes for Solar Water Splitting. *Adv. Mater.* **2019,** *31*, e1806938.

(146). Ling, Y.; Wang, G.; Wheeler, D. A.; Zhang, J. Z.; Li, Y., Sn-doped hematite nanostructures for photoelectrochemical water splitting. *Nano Lett.* **2011,** *11*, 2119-2125.

(147). Cao, D.; Luo, W.; Feng, J.; Zhao, X.; Li, Z.; Zou, Z., Cathodic shift of onset potential for water oxidation on a Ti4+doped Fe2O3photoanode by suppressing the back reaction. *Energy Environ. Sci.* **2014,** *7*, 752-759.

(148). Franking, R.; Li, L.; Lukowski, M. A.; Meng, F.; Tan, Y.; Hamers, R. J.; Jin, S., Facile post-growth doping of nanostructured hematite photoanodes for enhanced photoelectrochemical water oxidation. *Energy Environ. Sci.* **2013,** *6*, 500-512.

(149). Jia, Y.; Jiang, K.; Wang, H.; Yao, X., The Role of Defect Sites in Nanomaterials for Electrocatalytic Energy Conversion. *Chem* **2019,** *5*, 1371-1397.

(150). Xie, C.; Yan, D.; Chen, W.; Zou, Y.; Chen, R.; Zang, S.; Wang, Y.; Yao, X.; Wang, S., Insight into the design of defect electrocatalysts: From electronic structure to adsorption energy. *Mater. Today* **2019,** *31*, 47-68.

(151). Wang, Y.; Han, P.; Lv, X.; Zhang, L.; Zheng, G., Defect and Interface Engineering for Aqueous Electrocatalytic CO2 Reduction. *Joule* **2018**.

(152). Chen, X.; Liu, L.; Yu, P. Y.; Mao, S. S., Increasing Solar Absorption for Photocatalysis with Black Hydrogenated Titanium Dioxide Nanocrystals. *Science* **2011,** *331*, 746-750.

(153). Wang, G.; Wang, H.; Ling, Y.; Tang, Y.; Yang, X.; Fitzmorris, R. C.; Wang, C.; Zhang, J. Z.; Li, Y., Hydrogen-treated TiO2 nanowire arrays for photoelectrochemical water splitting. *Nano Lett.* **2011,** *11*, 3026-3033.

(154). Zhang, B.; Wang, L.; Zhang, Y.; Ding, Y.; Bi, Y., Ultrathin FeOOH Nanolayers with Abundant Oxygen Vacancies on BiVO4 Photoanodes for Efficient Water Oxidation. *Angew. Chem. Int. Ed.* **2018,** *57*, 2248-2252.

(155). Zhang, Z.; Yates, J. T., Jr., Band bending in semiconductors: chemical and physical consequences at surfaces and interfaces. *Chem. Rev.* **2012,** *112*, 5520-51.

(156). Yang, H. G.; Sun, C. H.; Qiao, S. Z.; Zou, J.; Liu, G.; Smith, S. C.; Cheng, H. M.; Lu, G. Q., Anatase TiO2 single crystals with a large percentage of reactive facets. *Nature* **2008,** *453*, 638-41.

(157). Takata, T.; Jiang, J.; Sakata, Y.; Nakabayashi, M.; Shibata, N.; Nandal, V.; Seki, K.; Hisatomi, T.; Domen, K., Photocatalytic water splitting with a quantum efficiency of almost unity. *Nature* **2020,** *581*, 411-414.

(158). Li, D.; Liu, Y.; Shi, W.; Shao, C.; Wang, S.; Ding, C.; Liu, T.; Fan, F.; Shi, J.; Li, C., Crystallographic-Orientation-Dependent Charge Separation of BiVO4 for Solar Water Oxidation. *ACS Energy Lett.* **2019,** *4*, 825-831.

(159). Han, H. S.; Shin, S.; Kim, D. H.; Park, I. J.; Kim, J. S.; Huang, P.-S.; Lee, J.-K.; Cho, I. S.; Zheng, X., Boosting the solar water oxidation performance of a BiVO4 photoanode by crystallographic orientation control. *Energy Environ. Sci.* **2018**, *11*, 1299-1306.

(160). Liu, T.; Zhou, X.; Dupuis, M.; Li, C., The nature of photogenerated charge separation among different crystal facets of BiVO4 studied by density functional theory. *Phys. Chem. Chem. Phys.* **2015,** *17*, 23503-10.

(161). Xi, G.; Ye, J., Synthesis of bismuth vanadate nanoplates with exposed {001} facets and enhanced visible-light photocatalytic properties. *Chem. Commun.* **2010,** *46*, 1893-1895.

(162). Li, R.; Zhang, F.; Wang, D.; Yang, J.; Li, M.; Zhu, J.; Zhou, X.; Han, H.; Li, C., Spatial separation of photogenerated electrons and holes among {010} and {110} crystal facets of BiVO4. *Nat. Commun.* **2013,** *4*, 1432-1438.

(163). Chen, R.; Pang, S.; An, H.; Zhu, J.; Ye, S.; Gao, Y.; Fan, F.; Li, C., Charge separation via asymmetric illumination in photocatalytic Cu2O particles. *Nat. Energy* **2018,** *3*, 655-663.

(164). Chen, R.; Fan, F.; Dittrich, T.; Li, C., Imaging photogenerated charge carriers on surfaces and interfaces of photocatalysts with surface photovoltage microscopy. *Chem. Soc. Rev.* **2018,** *47*, 8238-8262.

(165). Zhu, J.; Pang, S.; Dittrich, T.; Gao, Y.; Nie, W.; Cui, J.; Chen, R.; An, H.; Fan, F.; Li, C., Visualizing the Nano Cocatalyst Aligned Electric Fields on Single Photocatalyst Particles. *Nano Lett.* **2017,** *17*, 6735-6741.

(166). Zhu, J.; Fan, F.; Chen, R.; An, H.; Feng, Z.; Li, C., Direct Imaging of Highly Anisotropic Photogenerated Charge Separations on Different Facets of a Single BiVO4 Photocatalyst. *Angew. Chem. Int. Ed.* **2015,** *54*, 9111-9114.

(167). Moniz, S. J. A.; Shevlin, S. A.; Martin, D. J.; Guo, Z.-X.; Tang, J., Visible-light driven heterojunction photocatalysts for water splitting – a critical review. *Energy Environ. Sci.* **2015,** *8*, 731-759.

(168). Grigioni, I.; Abdellah, M.; Corti, A.; Dozzi, M. V.; Hammarstrom, L.; Selli, E., Photoinduced Charge-Transfer Dynamics in WO3/BiVO4 Photoanodes Probed through Midinfrared Transient Absorption Spectroscopy. *J. Am. Chem. Soc.* **2018,** *140*, 14042-14045.

(169). Baek, J. H.; Kim, B. J.; Han, G. S.; Hwang, S. W.; Kim, D. R.; Cho, I. S.; Jung, H. S., BiVO4/WO3/SnO2 Double-Heterojunction Photoanode with Enhanced Charge Separation and Visible-Transparency for Bias-Free Solar Water-Splitting with a Perovskite Solar Cell. *ACS Appl. Mater. Interfaces* **2017,** *9*, 1479-1487.

(170). Zhang, X.; Wang, X.; Wang, D.; Ye, J., Conformal BiVO4-Layer/WO3-Nanoplate-Array Heterojunction Photoanode Modified with Cobalt Phosphate Cocatalyst for Significantly Enhanced Photoelectrochemical Performances. *ACS Appl. Mater. Interfaces* **2019,** *11*, 5623-5631.

(171). Su, J.; Guo, L.; Bao, N.; Grimes, C. A., Nanostructured WO3/BiVO4 heterojunction films for efficient photoelectrochemical water splitting. *Nano Lett.* **2011,** *11*, 1928-1933.

(172). Ma, M.; Kim, J. K.; Zhang, K.; Shi, X.; Kim, S. J.; Moon, J. H.; Park, J. H., Double-Deck Inverse Opal Photoanodes: Efficient Light Absorption and Charge Separation in Heterojunction. *Chem. Mater.* **2014,** *26*, 5592-5597.

(173). Rao, P. M.; Cai, L.; Liu, C.; Cho, I. S.; Lee, C. H.; Weisse, J. M.; Yang, P.; Zheng, X., Simultaneously efficient light absorption and charge separation in WO3/BiVO4 core/shell nanowire photoanode for photoelectrochemical water oxidation. *Nano Lett.* **2014,** *14*, 1099-1105.

(174). Li, A.; Wang, Z.; Yin, H.; Wang, S.; Yan, P.; Huang, B.; Wang, X.; Li, R.; Zong, X.; Han, H.; Li, C., Understanding the anatase-rutile phase junction in charge separation and transfer in a TiO2 electrode for photoelectrochemical water splitting. *Chem. Sci.* **2016,** *7*, 6076-6082.

(175). Wang, X.; Li, C., Roles of Phase Junction in Photocatalysis and Photoelectrocatalysis. *J. Phys. Chem. C* **2018,** *122*, 21083-21096.

(176). Li, P.; Zhou, Y.; Zhao, Z.; Xu, Q.; Wang, X.; Xiao, M.; Zou, Z., Hexahedron Prism-Anchored Octahedronal CeO2: Crystal Facet-Based Homojunction Promoting Efficient Solar Fuel Synthesis. *J. Am. Chem. Soc.* **2015,** *137*, 9547-9550.

(177). Wang, X.; Xu, Q.; Li, M.; Shen, S.; Wang, X.; Wang, Y.; Feng, Z.; Shi, J.; Han, H.; Li, C., Photocatalytic overall water splitting promoted by an alpha-beta phase junction on Ga2O3. *Angew. Chem. Int. Ed.* **2012,** *51*, 13089-13092.

(178). Luo, Z.; Wang, T.; Zhang, J.; Li, C.; Li, H.; Gong, J., Dendritic Hematite Nanoarray Photoanode Modified with a Conformal Titanium Dioxide Interlayer for Effective Charge Collection. *Angew. Chem. Int. Ed.* **2017,** *56*, 12878-12882.

(179). Zhong, M.; Hisatomi, T.; Kuang, Y.; Zhao, J.; Liu, M.; Iwase, A.; Jia, Q.; Nishiyama, H.; Minegishi, T.; Nakabayashi, M.; Shibata, N.; Niishiro, R.; Katayama, C.; Shibano, H.; Katayama, M.; Kudo, A.; Yamada, T.; Domen, K., Surface Modification of CoOx Loaded BiVO4 Photoanodes with Ultrathin p-Type NiO Layers for Improved Solar Water Oxidation. *J. Am. Chem. Soc.* **2015,** *137*, 5053-5060.

(180). Kenney, M. J.; Gong, M.; Li, Y.; Wu, J. Z.; Feng, J.; Lanza, M.; Dai, H., High-performance silicon photoanodes passivated with ultrathin nickel films for water oxidation. *Science* **2013,** *342*, 836-840.

(181). Yao, T.; Chen, R.; Li, J.; Han, J.; Qin, W.; Wang, H.; Shi, J.; Fan, F.; Li, C., Manipulating the Interfacial Energetics of n-type Silicon Photoanode for Efficient Water Oxidation. *J. Am. Chem. Soc.* **2016,** *138*, 13664-13672.

(182). Zandi, O.; Hamann, T. W., Enhanced Water Splitting Efficiency Through Selective Surface State Removal. *J. Phys. Chem. Lett.* **2014,** *5*, 1522-1526.

(183). Li, C.; Li, A.; Luo, Z.; Zhang, J.; Chang, X.; Huang, Z.; Wang, T.; Gong, J., Surviving High-Temperature Calcination: ZrO2 -Induced Hematite Nanotubes for Photoelectrochemical Water Oxidation. *Angew. Chem. Int. Ed.* **2017,** *56*, 4150-4155.

(184). Lee, H.; Yang, W.; Tan, J.; Oh, Y.; Park, J.; Moon, J., Cu-Doped NiOx as an Effective Hole-Selective Layer for a High-Performance Sb2Se3 Photocathode for Photoelectrochemical Water Splitting. *ACS Energy Lett.* **2019,** *4*, 995-1003.

(185). Yang, J.; Wang, D.; Han, H.; Li, C., Roles of cocatalysts in photocatalysis and photoelectrocatalysis. *Acc. Chem. Res.* **2013,** *46*, 1900-1909.

(186). Ye, H.; Park, H. S.; Bard, A. J., Screening of Electrocatalysts for Photoelectrochemical Water Oxidation on W-Doped BiVO4 Photocatalysts by Scanning Electrochemical Microscopy. *J. Phys. Chem. C* **2011,** *115*, 12464-12470.

(187). Zhang, J.; García-Rodríguez, R.; Cameron, P.; Eslava, S., Role of cobalt–iron(oxy)hydroxide (CoFeOx) as oxygen evolution catalyst on hematite photoanodes. *Energy Environ. Sci.* **2018,** *11*, 2972-2984.

(188). Zhong, D. K.; Cornuz, M.; Sivula, K.; Grätzel, M.; Gamelin, D. R., Photo-assisted electrodeposition of cobalt–phosphate (Co–Pi) catalyst on hematite photoanodes for solar water oxidation. *Energy Environ. Sci.* **2011,** *4*, 1759-1764.

(189). Kato, M.; Zhang, J. Z.; Paul, N.; Reisner, E., Protein film photoelectrochemistry of the water oxidation enzyme photosystem II. *Chem. Soc. Rev.* **2014,** *43*, 6485-6497.

(190). Nam, D. H.; Zhang, J. Z.; Andrei, V.; Kornienko, N.; Heidary, N.; Wagner, A.; Nakanishi, K.; Sokol, K. P.; Slater, B.; Zebger, I., Solar water splitting with a hydrogenase integrated in photoelectrochemical tandem cells. *Angew. Chem. Int. Ed.* **2018,** *57*, 10595-10599.

(191). Kanan, M. W.; Nocera, D. G., In situ formation of an oxygen-evolving catalyst in neutral water containing phosphate and Co2+. *Science* **2008,** *321*, 1072-1075.

(192). Zhong, D. K.; Sun, J.; Inumaru, H.; Gamelin, D. R., Solar water oxidation by composite catalyst/α-Fe2O3 photoanodes. *J. Am. Chem. Soc.* **2009,** *131*, 6086-6087.

(193). Zhong, D. K.; Gamelin, D. R., Photoelectrochemical water oxidation by cobalt catalyst ("Co−Pi")/α-Fe2O3 composite photoanodes: oxygen evolution and resolution of a kinetic bottleneck. *J. Am. Chem. Soc.* **2010,** *132*, 4202-4207.

(194). Shi, Y.; Yu, Y.; Yu, Y.; Huang, Y.; Zhao, B.; Zhang, B., Boosting Photoelectrochemical Water Oxidation Activity and Stability of Mo-Doped BiVO4 through the Uniform Assembly Coating of NiFe–Phenolic Networks. *ACS Energy Lett.* **2018,** *3*, 1648-1654.

(195). Zachaus, C.; Abdi, F. F.; Peter, L. M.; van de Krol, R., Photocurrent of BiVO4 is limited by surface recombination, not surface catalysis. *Chem. Sci.* **2017,** *8*, 3712-3719.

(196). Thorne, J. E.; Jang, J. W.; Liu, E. Y.; Wang, D., Understanding the origin of photoelectrode performance enhancement by probing surface kinetics. *Chem. Sci.* **2016,** *7*, 3347-3354.

(197). Gong, H.; Freudenberg, N.; Nie, M.; van de Krol, R.; Ellmer, K., BiVO4 photoanodes for water splitting with high injection efficiency, deposited by reactive magnetron co-sputtering. *AIP Adv.* **2016,** *6*, 045108.

Chapter 2. Bismuth Vanadate with Electrostatically Anchored 3D Carbon Nitride Nano-networks as Efficient Photoanodes for Water Oxidation

VIP **Very Important Paper**

Bismuth Vanadate with Electrostatically Anchored 3D Carbon Nitride Nano-networks as Efficient Photoanodes for Water Oxidation

Peng Luan,[a] Ying Zhang,[a] Xiaolong Zhang,[a] Zhijun Li,[b] Ragesh Prathapan,[a] Udo Bach,[c] and Jie Zhang*[a]

In this study, we report a photoanode consisting of a polymeric/inorganic nanojunction between novel nanostructured 3D C_3N_4 nano-networks and $BiVO_4$ substrate. This nanojunction is formed such that 3D C_3N_4 nano-networks with a positively charged surface are efficiently anchored on the $BiVO_4$ photoanode with a negatively charged surface. This electrostatic self-assembly can initiate and contribute to an intimate contact at the interfaces, leading to an enhanced photoelectrochemical activity and stability compared with that fabricated by non-electrostatic assembly. The C_3N_4 nano-network/$BiVO_4$ photoanode achieved a remarkable photocurrent density of 4.87 mA cm^{-2} for water oxidation at 1.23 V (vs. reversible hydrogen electrode) after depositing FeOOH/NiOOH as oxygen-evolution co-catalyst, which is among the highest photocurrent densities reported so far for $BiVO_4$-based photoanodes.

Introduction

With the consumption of fossil fuel, energy shortage becomes a significant problem for human society.[1–3] The photoelectrochemical (PEC) technique shows great potential in capturing, converting, and storing solar energy, especially by splitting water into hydrogen (H_2) and oxygen (O_2), providing a very attractive solution to the energy crisis.[4–8] Bismuth vanadate ($BiVO_4$), a typical n-type semiconductor, has been regarded as one of the most promising photoanode materials toward solar-driven water splitting, owing to its suitable band gap to absorb visible light, sufficiently positive valence band edge to drive water oxidation, and excellent stability in neutral and alkaline conditions.[5, 9, 10] However, it still suffers from high charge recombination and poor surface reaction kinetics, which results in a low photoconversion efficiency.[9, 11, 12]

To achieve a highly efficient $BiVO_4$ photoanode for water splitting, several strategies have been developed, for example, 1) introducing cocatalysts,[10, 13] 2) fabricating nanojunctions,[12, 14] 3) controlling nanostructures,[15,16] and 4) doping with heteroatoms.[17, 18] Among all these modification methods, formation of a nanojunction by rational design and fabrication is an effective way to decrease charge recombination, which is regarded as one of the main limiting factors in solar energy conversion.[9, 11, 19–21] Recent studies on constructing $BiVO_4$-based heterojunctions mostly focused on using inorganic semiconductor nanomaterials, such as WO_3, TiO_2, Co_3O_4, as the modifiers to improve the PEC performance of $BiVO_4$ substrates.[11, 21, 22] Graphitic carbon nitride (C_3N_4) is a conjugated and two-dimensional triazine-based polymer with p-conjugated planar layers like graphite.[23–26] It was widely studied in photocatalytic and electrocatalytic water splitting owing to its controllable band structure, flexible nanostructure, and high chemical stability.[27–31] By contrast, its application in PEC water splitting has been much less explored. Notably, Su et al. utilized an electrophoresis method to fabricate a nanocomposite of C_3N_4/reduced graphene oxide (rGO)/$BiVO_4$ with an enhanced PEC activity for water splitting.[32] Hou et al. fabricated a flexible photoanode of C_3N_4 nanosheets/WO_3 nanoarray by a hydrothermal and calcination process for PEC water oxidation.[33] Basu et al. reported a hybrid nanostructure of C_3N_4 nanosheets with embedded $CoSe_2$ on a silicon nanowire as photocathode for water reduction.[34] Despite all these progresses, the use of C_3N_4 for PEC applications is still limited, partially owing to of the following factors: 1) it is difficult to construct a compact heterojunction between C_3N_4 and substrates, resulting in low charge separation efficiency and poor stability[32, 35, 36] and 2) the nanostructure of C_3N_4 synthesized by electrophoresis, calcination, or hydrothermal methods is often amorphous or two-dimensional, providing fewer active sites for the oxygen evolution reaction (OER) than a three-dimensional network.[32, 33, 37]

[a] P. Luan, Y. Zhang, X. Zhang, R. Prathapan, Dr. J. Zhang
School of Chemistry
Monash University
Clayton, VIC 3800 (Australia)
E-mail: jie.zhang@monash.edu

[b] Dr. Z. Li
Ministry of Education Key Laboratory of Functional Inorganic Material
Chemistry
School of Chemistry and Materials Science
Heilongjiang University
Harbin 150080 (P. R. China)

[c] Prof. U. Bach
Department of Chemical Engineering
Monash University
Clayton, VIC 3800 (Australia)

Supporting Information and the ORCID identification number(s) for the author(s) of this article can be found under:
https://doi.org/10.1002/cssc.201801119.

An electrostatic self-assembly (ESA) strategy, utilizing electrostatic interactions between two nanomaterials with opposite surface charge properties (SCP), is widely applied in fabricating C_3N_4-based nanocomposites owing to the presence of -C-N- motifs in the repeating tri-s-triazine basic units, which are easily protonated to change their SCP without changing their nanostructure.[38–40] It is generally accepted that the pH of the isoelectric point of C_3N_4 and $BiVO_4$ is around 5.0 and 2.5, respectively.[41,42] Therefore, in principle, if the nanocomposite of $C_3N_4/BiVO_4$ is fabricated at pH 4, new chemical bonds may form after nanoscale $BiVO_4$ and C_3N_4 with opposite charges are brought into contact by the long-range electrostatic force, owing to the coordinating property of nitrogen motifs available in the defect-rich C_3N_4, which ensures the formation of an intimate contact between $BiVO_4$ and C_3N_4 to facilitate interfacial charge separation and transfer.

Herein, we report the design and fabrication of a polymeric/inorganic heterojunction of protonated 3D C_3N_4 nano-networks with $BiVO_4$ by an ESA method for efficient PEC water oxidation. The PEC activity and stability have been investigated to understand the effect of electrostatic interactions and C_3N_4 three-dimensional structure on photo-induced charge separation. The FeOOH/NiOOH oxygen evolution cocatalyst (OEC) is deposited to greatly improve the poor surface reaction kinetics of C_3N_4/$BiVO_4$ photoanode. A mechanism is proposed to explain the charge separation and transfer process in this novel heterojunction nanocomposite.

Results and Discussion

Two types of nanostructured C_3N_4 were synthesized by treating bulk C_3N_4 (BCN; Figure 1a) in the following ways: 1) 2D C_3N_4 nanosheets (CNNS) shown in Figure 1b were obtained from a further thermal exfoliation of BCN,[43] 2) 3D C_3N_4 nano-networks (CNNW) shown in Figure 1c and d were obtained from BCN in methanol solution containing H_2SO_4, in which protic methanol
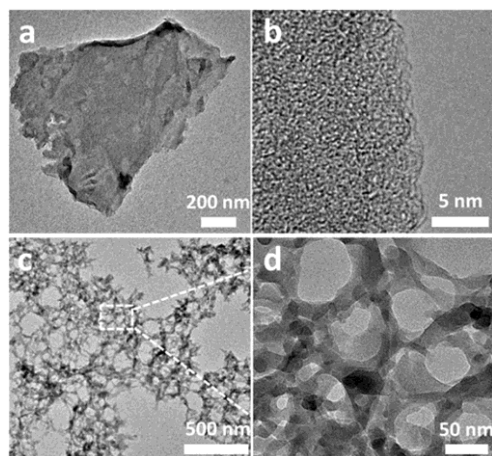
solvents could destroy the hydrogen bonds of BCN in the presence of H_2SO_4 and induce partial hydrolysis of BCN.[44] Afterwards, both CNNS and CNNW were protonated with HCl to introduce a positively charged surface. To quantify the SCP of CNNS and CNNW before and after protonation, zeta potential tests were conducted in deionized (DI) water. Figure 2 reveals
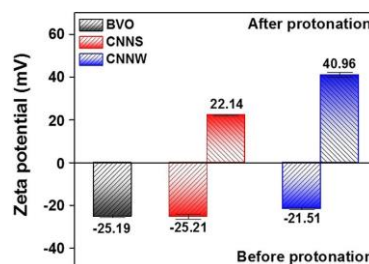

Figure 2. Zeta potential values of pristine BVO, protonated and unprotonated 2D CNNS, and 3D CNNW in deionized water.

that the pristine $BiVO_4$ (BVO), CNNW, and CNNS in DI water show negative SCPs as expected (-25.19, -21.51, and -25.21 mV, respectively). However, upon protonation, it is noticeable that both CNNW and CNNS exhibit positively charged surfaces with zeta potential values of 22.14 and 40.96 mV, respectively. Hence, polymeric/inorganic nanocomposites of CNNW/BVO and CNNS/BVO can be formed electrostatically by using BVO and protonated CNNW or CNNS.

To demonstrate the effectiveness of electrostatic anchoring of CNNW on BVO substrate, scanning electron microscopy (SEM) and transmission electron microscopy (TEM) images were taken from the fluorine-doped tin oxide (FTO) supported BVO before and after immersion in aqueous solutions containing protonated and unprotonated CNNW. The pristine BVO on the FTO substrate was obtained by conversion of the electrodeposited BiOI (Figure 3a and d) by using a procedure described in the Experimental Section and showed a lattice spacing of 0.31 nm corresponding to the (1 2 1) planes (Figure S1a in the Supporting Information).[10] Evidently, the surface of BVO was partly anchored by protonated CNNW through electrostatic interactions as a morphological change can be seen from Figure 3b and e. A high-resolution TEM image taken from the
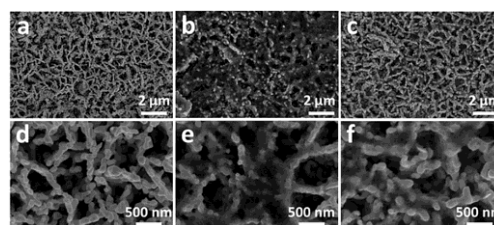

Figure 1. TEM images of (a) BCN, (b) 2D CNNS, (c) and (d) 3D CNNW.

Figure 3. SEM images of as-prepared (a, d) BVO, (b, e) BVO modified with protonated CNNW, (c, f) BVO modified with unprotonated CNNW.

sample peeled off from the FTO electrode confirms the formation of a uniformly and tightly packed CNNW/BVO nanocomposite as well as CNNS/BVO (Figure S1 b and c in the Supporting Information). In contrast, only a small amount of CNNW on the BVO surface was visualized when BVO was immersed in a solution containing pristine negatively charged CNNW (Figure 3 c and f and Figure S2 in the Supporting Information), illustrating the importance of SCP in the formation of a stable CNNW/BVO nanocomposite.

The crystal structures of CNNW, CNNS, and BVO were analyzed by powder X-ray diffraction (XRD). As presented in Figure S3 a (in the Supporting Information), BCN gives two typical diffraction peaks at 13.0° (1 0 0) and 27.5° (0 0 2), which are associated with in-plane tri-s-triazine motifs and periodic stacking of layers.[25] By contrast, the (0 0 2) peaks associated with CNNW and CNNS are significantly weakened, owing to the reduction in their layer thickness in comparison with BCN.[45] The decrease in (1 0 0) peak intensity for CNNW is attributed to its reduced long-range interplanar order, which is in good accordance with the TEM images (Figure 1 d).[29, 44] However, no significant XRD diffraction patterns associated with CNNW and CNNS were detected from CNNW/BVO and CNNS/BVO in Figure S3 b (in the Supporting Information), possibly because it is too weak to detect.

Fourier transformed infrared (FTIR) spectra (Figure 4 a) recorded for CNNS and CNNW show all typical vibration peaks resulted from the tri-s-triazine ring (800–1800 cm^{-1}) and -N-H- (3000–3400 cm^{-1}) vibrations, demonstrating that the exfoliation of BCN did not significantly change the primary framework of the tri-s-triazine structure.[44, 45] Moreover, these two typical vibration bands are also observed in the CNNW/BVO

and CNNS/BVO nanocomposites in addition to Bi—O and V—O vibration bands at wavelengths of less than 1000 nm (Figure 4 b).[46] In Figure S4 a and b (in the Supporting Information), X-ray photoelectron spectroscopy (XPS) surveys confirm the existence of Bi^{3+} and V^{5+} in monoclinic BVO.[47] Additionally, the peaks of C 1s and N 1s centered at the binding energies of 287.8 and 398.8 eV are associated with the sp^2 C—N bond in the aromatic rings and sp^2 in the triazine rings, respectively (Figure 4 c and d), hence confirming the presence of the tri-s-triazine nanostructure in CNNW/BVO.[45, 48] Based on the analysis of XPS and FTIR results, it is concluded that the nanocomposite of CNNW/BVO is successfully fabricated by the ESA method.

To understand the effects of C$_3$N$_4$ and its nanostructure on the PEC performance of the C$_3$N$_4$/BiVO$_4$ nanocomposites, the water oxidation photocurrent densities were determined with the pristine BVO, CNNW/BVO, unprotonated CNNW/BVO (UCNNW/BVO), and CNNS/BVO photoanodes (Figure 5 a). The CNNW/BVO anode exhibits a photocurrent density (J) of 2.24 mA cm^{-2} at 1.23 V (vs. reversible hydrogen electrode, RHE), which is much higher than that of the pristine BVO photoanode (1.30 mA cm^{-2} at 1.23 V vs. RHE). In contrast, the UCNNW/BVO photoanode with a much lower amount of C$_3$N$_4$ only produces a photocurrent of 1.33 mA cm^{-2} at 1.23 V (vs. RHE), which is very close to that of the pristine BVO photoanode, suggesting the important role of C$_3$N$_4$ in achieving high photoelectrochemical activity. Furthermore, the CNNW/BVO photoanode produces a higher photocurrent density than that of CNNS/BVO (1.57 mA cm^{-2} at 1.23 V vs. RHE) at the same applied bias, possibly owing to the increased interfacial area between 3D CNNW and the electrolyte solution providing more
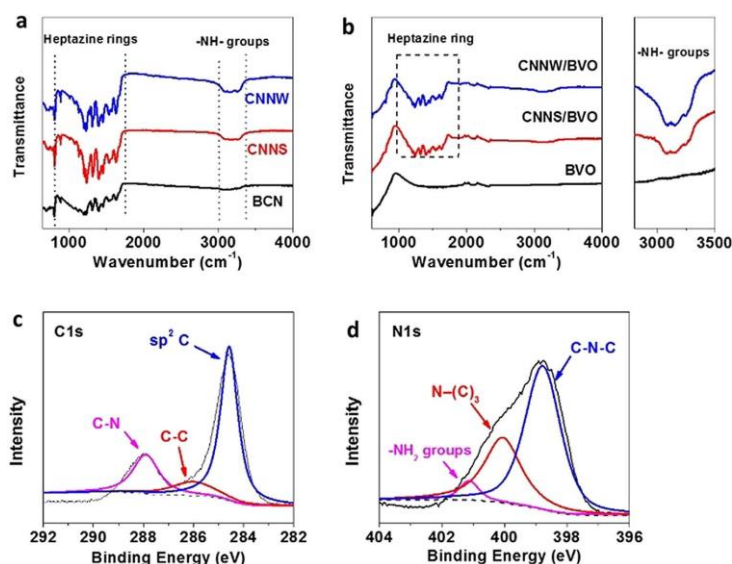
Figure 4. FTIR spectra of (a) BCN, CNNS, CNNW and (b) BVO, CNNS/BVO, CNNW/BVO; high-resolution XPS spectra of (c) C 1s and (d) N 1s in the nanocomposite of CNNW/BVO.
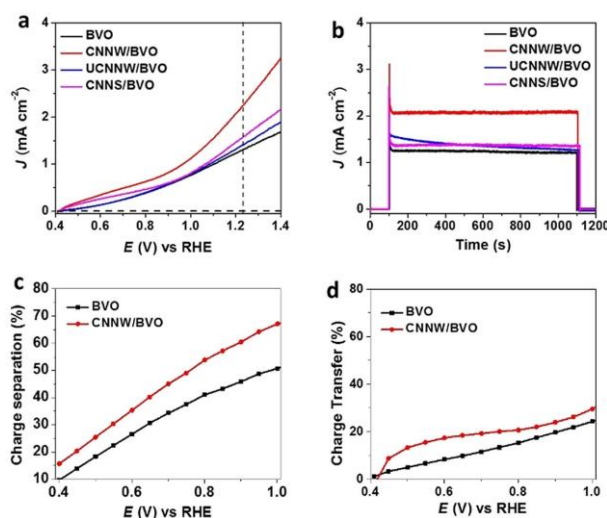
Figure 5. PEC performance of a CNNW/BVO nanocomposite modified electrode measured at the scan rate of 50 mV s^{-1} under AM 1.5 G irradiation. (a) J–V curves and (b) J–t curves at 1.23 V (vs. RHE) recorded in a 0.1 M KPi buffer solution. (c) Charge separation efficiency and (d) charge transfer efficiency determined and calculated by using the procedures described in the Supporting Information. The results obtained from other electrodes are also shown for comparison.

active sites for water oxidation than 2D CNNS. Naturally, the dark current of all photoanodes in the above-mentioned potential region are negligible.

To evaluate the PEC stability of the nanocomposites, J–t ($t=$ time) measurements were carried out at the applied potential bias of 1.23 V (vs. RHE) for 1000 s (Figure 5 b). It is clearly seen that both CNNS/BVO and CNNW/BVO exhibit excellent stabilities for water oxidation, indicating that ESA fabrication can form a stable and intimate contact between polymeric CNNW and inorganic BVO substrate. SEM images of the CNNW/BVO photoanode taken before and after the J–t measurement (Figure S5 a and b in the Supporting Information) show that the amount of CNNW anchored on BVO remains almost the same, confirming the effectiveness of the ESA fabrication method in obtaining a stable CNNW/BVO nanocomposite. To investigate the effect of the heterojunction on charge separation efficiency, the charge separation efficiencies (CSE) of BVO and CNNW/BVO were measured and calculated according to equations provided in the Supporting Information. As can be seen from Figure 5 c, CNNW/BVO shows a higher CSE than that of pristine BVO at all applied potential bias. A CSE value of 67.1% achieved at the applied potential bias of 1.0 V (vs. RHE) is 1.3 times higher than that of pristine BVO (50.7% at the same applied potential bias), suggesting that the presence of CNNW on the surface of BVO can effectively promote the charge separation. However, from Figure 5 d (details of the calculation are given in the Supporting Information), one can see that the charge transfer efficiency (CTE) of CNNW/BVO, which represents surface reaction conditions, is still under 30% at 1.0 V (vs. RHE), indicating slow surface OER kinetics.[11,47]

To make use of the surface-reaching holes as much as possible, FeOOH/NiOOH OEC is deposited on CNNW/BVO photoanodes to enhance the poor surface reaction kinetics. XPS spectra (Figure S9 in the Supporting Information) of a CNNW/BVO photoanode after deposition show typical peaks associated with Fe 2p and Ni 2p, indicating the successful introduction of FeOOH/NiOOH on the surface of CNNW/BVO nanocomposites. High angle annular dark field (HAADF)-STEM imaging and elemental mapping suggest that Fe and Ni elements are uniformly dispersed on the surface of CNNW/BVO nanocomposite (Figure S10 in the Supporting Information). In Figure 6 a, it is shown that the onset potentials of both BVO–FeOOH/NiOOH (BVO-FN) and CNNW/BVO–FeOOH/NiOOH (CNNW/BVO-FN) are reduced by around 200 mV, compared with those of BVO and CNNW/BVO. Significantly, CNNW/BVO-NF achieves a remarkable photocurrent density of as high as 4.87 mA cm^{-2} for water oxidation at 1.23 V (vs. RHE). This photocurrent value is about 1.3, 2.2, and 3.8 times compared with those of BVO-FN, CNNW/BVO, and BVO, respectively, indicating a more effective charge separation and transfer in the CNNW/BVO-FN nanocomposite. A summary of PEC activity of C$_3$N$_4$-modified BiVO$_4$ photoanodes for PEC water oxidation is given in Table S1 (in the Supporting Information), and is compared with other BiVO$_4$-based single photoanodes for water oxidation in Table S2 (in the Supporting Information). As shown in Figure 6 b, CNNW/BVO-FN and BVO-FN reach CTE values of 87.82% and 76.86% at 1.0 V (vs. RHE), which are much higher than those of CNNW/BVO (26.58%) and BVO (21.87%) at the same applied potential bias.

The applied bias photon-to-current efficiency (ABPE), which reveals solar-to-hydrogen efficiencies at different applied potential biases, determined by using the procedures described in Supporting Information, is presented in Figure 6 c. The ABPE reaches 1.52% and 1.05% at 0.7 V (vs. RHE) for CNNW/BVO-FN and BVO-FN, respectively. In contrast, much lower values of 0.29% and 0.18%, respectively, were obtained from CNNW/BVO and pristine BVO at a significantly more positive potential of 0.9 V (vs. RHE), suggesting the important role of FN in achieving high PEC efficiency. In addition, incident photon-to-current conversion efficiency (IPCE) is applied to reveal the photoresponse at different wavelengths. The results in Figure 6 d show that the separate introduction of CNNW/BVO heterojunctions and FeOOH/NiOOH cocatalyst increases the IPCE of pristine BVO at 370 nm and at 1.23 V (vs. RHE) from 14.9% to 42.2% and 72.0%, respectively, whereas the highest IPCE of 79.6% was achieved with CNNW/BVO-FN.

To gain a deeper insight into the interfacial charge-transfer behavior, electrochemical impedance spectroscopy (EIS) measurements were carried out under light illumination at the applied potential bias of 0.7 V (vs. RHE). In the Nyquist graph (Figure 6 e), the nanocomposite of CNNW/BVO shows a smaller semicircle radius compared with pristine BVO, which represents a more efficient charge separation.[47,49] Furthermore,
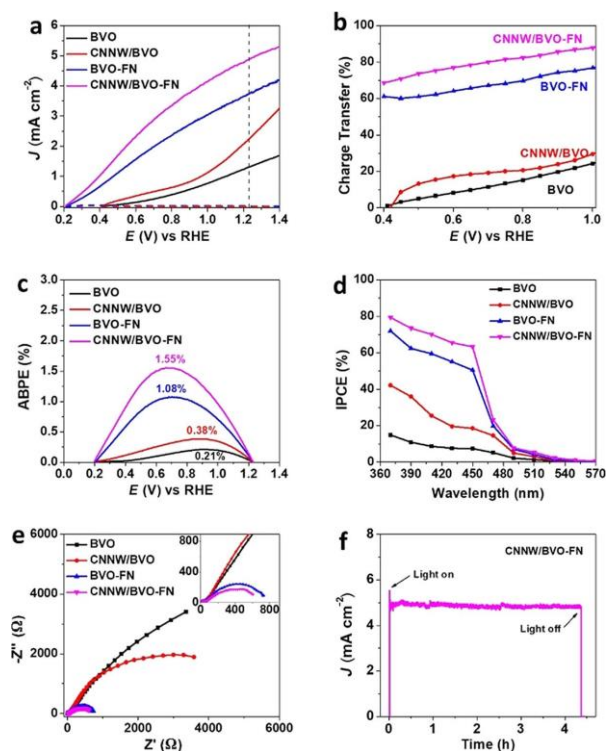
Figure 6. PEC performance of a CNNW/BVO-NF nanocomposite modified electrode measured under AM 1.5 G irradiation. (a) J–V curves, (b) charge transfer efficiency, (c) ABPE, (d) IPCE spectra at incident wavelength range from 370 to 570 nm at 1.23 V (vs. RHE), (e) EIS Nyquist plots collected at 0.7 V (vs. RHE), (f) J–t curves at 1.23 V (vs. RHE). The results obtained from other electrodes are also shown for comparison.

CNNW/BVO-FN exhibits the smallest semicircle radius among all photoanodes, suggesting a fastest interfacial charge transfer in the CNNW/BVO-FN heterojunction, which is consistent with the photocurrent and CTE results.[50] The operational stability of CNNW/BVO-FN was also evaluated at 1.23 V (vs. RHE). As presented in Figure 6 f, the CNNW/BVO-FN exhibits a stable

Figure 7. Schematic illustration of (a) comparison of charge separation in the nanocomposites of CNNS/BVO and CNNW/BVO and (b) efficient charge separation and surface reaction in CNNW/BVO-FN under illumination.

photoactivity with a decayed photocurrent of only 2.65 %, from 4.90 mA cm⁻² when the light is on to 4.77 mA cm⁻² before the light is switched off on a timescale of over 4 h.

The band structure of BCN, CNNS, and CNNW is estimated by measurement of diffuse reflectance spectral (DRS) and Mott–Schottky plots (Figure S11 in the Supporting Information) and the calculation results are summarized in Table S3 (in the Supporting Information). The band gap of BCN increases as it is exfoliated to 2D CNNS and 3D CNNW owing to quantum confinement effects. Based on all the results and analysis, a reaction scheme is proposed in Figure 7 to illustrate the charge separation and transfer in nanocomposite of CNNW/BVO-FN. Based on this scheme, it is postulated that CNNW/BVO with an increased solid–liquid junction area compared with CNNS/BVO (Figure 7 a) can provide more active sites for photoinduced holes for water oxidation, and the NiOOH/FeOOH cocatalyst can efficiently enhance the surface reaction kinetics (Figure 7 b), resulting in a highly efficient photoanode for water oxidation.

Conclusions

We successfully designed and fabricated a polymeric/inorganic nanojunction between C₃N₄ nano-networks (CNNW) and BiVO₄ (BVO) by the electrostatic self-assembly method. The intimate contact between the two materials promotes photoinduced charge separation and the 3D CNNW nanostructure increases the solid–liquid junction area, simultaneously contributing to an enhanced photoelectrochemical (PEC) activity toward water oxidation. The resulting CNNW/BVO–FeOOH/NiOOH photoanode with greatly improved surface reaction kinetics exhibits a significant photocurrent density of 4.87 mA cm⁻² at 1.23 V and applied bias photon-to-current efficiency of 1.55 % at 0.7 V (vs. RHE), which is among the highest values reported so far for BVO-based photoanodes. This work is likely to inspire the further development of new polymeric/inorganic nanojunctions for solar water splitting with superior performance.

Experimental Section

Materials

All the chemicals were purchased from Sigma–Aldrich and used without any further purification.

Preparation of BiVO₄ photoanodes

The BiVO₄ photoanode was prepared by a two-step process by using a modified version of Kim and Choi's method.[10] First, Bi(NO₃)₃ (2 mmol) was dissolved in KI solution (50 mL, 0.4 M). After its pH was adjusted to 1.7 by adding HNO₃, the solution was mixed with absolute ethanol (20 mL) containing *p*-benzoquinone
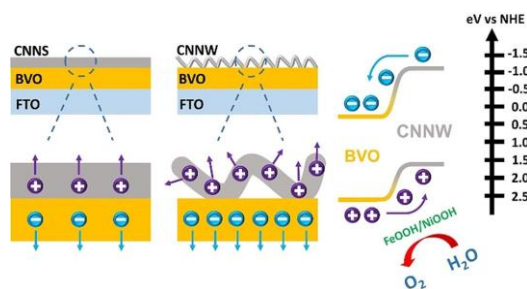
93

(4.6 mmol). After stirring for 20 min, electrodeposition of BiOI was carried out in a typical three-electrode setup by using a FTO substrate (3×1 cm²) as the working electrode (WE), a platinum wire as the counter electrode (CE), and Ag/AgCl (4 M KCl) as the reference electrode (RE). The electrodeposition was conducted at -0.1 V versus Ag/AgCl for 200 s. Afterwards, the BiOI-modified FTO electrode was rinsed with ethanol and dried in a nitrogen flow. Second, dimethyl sulfoxide (DMSO, 0.2 mL) solution containing 0.2 M vanadyl acetylacetonate was introduced dropwise onto the BiOI surface (1 cm $\times$ 1 cm), and then annealed in a furnace at 450 °C for 2 h under air. The as-prepared electrode was soaked in 1 M NaOH solution under gentle stirring to remove excess V_2O_5. The resulting $BiVO_4$ was rinsed with deionized (DI) water.

Preparation of 3D CNNWs

First, BCN was obtained by thermal condensation of dicyandiamide at 550 °C for 4 h in a furnace with a temperature ramp of 2.3 °C min^{-1}. BCN (0.5 g) was dissolved in H_2SO_4 (10 mL) and kept stirring for 2 h at 90 °C to obtain a light-yellow solution. The as-obtained solution (10 mL) was added dropwise into methanol (50 mL) and then kept stirring for 2 h at room temperature, allowing BCN to hydrolyze to form a 3D nanostructured CNNW. After that, the solution was centrifuged at 15 000 rpm for 10 min and the precipitate was collected and washed with CH_3OH for several times to remove the residual H_2SO_4. Then, the precipitate was redispersed in CH_3OH and sonicated for 30 min.

Preparation of 2D carbon nitride nanosheets

The 2D C_3N_4 nanosheets were prepared by thermal exfoliation of bulk C_3N_4 and sonication.[43] Briefly, bulk C_3N_4 was obtained by thermal condensation of melamine at 520 °C for 4 h with a ramp rate of 5 °C min^{-1}, and followed with further exfoliation by thermal treatment at 550 °C for 3 h with a ramp rate of 5 °C min^{-1}. Then, C_3N_4 nanosheets (50 mg) were dispersed in H_2O (100 mL) and sonicated for 6 h at about 20 °C. The final product was centrifuged and dried under vacuum at 60 °C for 6 h.

Preparation of CNNW/BVO photoanodes

The CNNW/BVO photoanode was prepared by an electrostatic self-assembly method. First, the as-obtained CNNW was protonated in an aqueous 4 M HCl solution (50 mL) and kept stirring for 4 h. After that, the protonated CNNW was washed with DI water several times to remove the excess HCl. Secondly, the BVO photoanode was immersed in an aqueous solution containing 10 mg mL^{-1} protonated CNNW for 4 h, taken out from the solution, rinsed with DI water, dried in air flow, and then heated in a furnace to 120 °C from room temperature with a temperature ramp of 2 °C min^{-1}. The UCNNW/BVO and CNNS/BVO photoanodes were prepared by using the same procedure.

Preparation of BVO-NF and CNNW/BVO-NF photoanodes

The NiOOH/FeOOH OEC was introduced by using a photo-assisted electrodeposition method.[47] In brief, the FeOOH was first photoelectrodeposited on BVO and CN/BVO in 0.1 M $FeSO_4$ solution at the potential bias of 0.25 V vs. Ag/AgCl with total charge 45 mC cm^{-2}. Subsequently, the NiOOH was photoelectrodeposited on BVO–FeOOH and CNNW/BVO–FeOOH in 0.1 M $NiSO_4$ solution (pH 6.8) at the potential bias of 0.11 V vs. Ag/AgCl with total

charge 22 mC cm^{-2}. At last, electrodeposition was conducted without illumination at the bias of 1.2 V vs. Ag/AgCl in 0.1 M $NiSO_4$ solution for 1 min to fully cover the photoanode.

Characterization

XRD data were collected with a Bruker D2 PHASER powder diffractometer (CuK$_\alpha$ radiation, $\lambda = 0.15406$ nm). Transmission electron microscopic (TEM) images were collected with a FEI Tecnai G2 T20 TWIN TEM instrument. Aberration-corrected high-angle annular dark-field scanning transmission electron microscopy (HAADF-STEM) images and energy-dispersive X-ray spectra (EDS) were acquired with a FEI Tecnai G2 F20 S-TWIN FEGTEM instrument operated at 200 kV. Scanning electron microscopic (SEM) images and EDS were recorded with a FEI Nova NanoSEM 450 FEG SEM instrument equipped with Bruker Quantax 400 X-ray analysis system. The zeta potential was measured by phase analysis light scattering (PALS) with a dynamic light scattering system (DLS, NanoBrook Omni, Brookhaven Corporation), which measured the electrophoretic mobility of each charged nanoparticle to calculate the zeta potential values. X-ray photoelectron spectroscopy (XPS) was performed with a Kratos-AXIS ULTRA DLD apparatus with Al (Mono) X-ray source to gain further insight into the surface composition and elemental chemical state of the samples. The FTIR spectra of the samples were collected with a Cary 630 FTIR spectrometer (Agilent Technologies).

Photoelectrochemical and electrochemical measurements

PEC and electrochemical measurements were both conducted at 25 ± 2 °C by using an AUTOLAB electrochemical workstation (PGSTAT100) in a three-electrode PEC cell (K040-S Tianjin lda Ltd.) with a photoanode as the working electrode, Ag/AgCl (4 M KCl) as the reference electrode, and a Pt wire as the counter electrode. The illuminated areas of photoanodes were 0.25 cm². Potassium phosphate (KPi, 0.1 M) buffer solution (pH 7) was used as the electrolyte and purged with nitrogen for 30 min to remove oxygen before every test. During the PEC measurements, the simulated solar light, generated by using from a 300 W Xeon lamp (Microsolar300 Beijing Perfectlight Technology Co., Ltd.) with an AM 1.5 G filter, was passed through the insulating side of the FTO substrate. The power density of the incident light was calibrated to 100 mW cm^{-2} (one-sun illumination) at the surface of the FTO substrate by using a light meter (PECSI01 Bunkoukeiki). Photocurrent measurement was collected at a scan rate of 50 mV s^{-1} in 0.1 M KPi buffer (pH 7). Electrochemical impedance spectroscopy (EIS) was carried out in the frequency range 10^{-2}–10^5 Hz with an AC voltage amplitude of 10 mV at a bias voltage of 0.6 V (vs. RHE), by using a CHI 760E electrochemical workstation (CH Instruments, Austin, Texas, USA). Incident photon-to-electron conversion efficiency (IPCE) was measured by using an AUTOLAB electrochemical workstation at a bias voltage of 1.23 V (vs. RHE) combined with simulated solar light passed through a mono-wavelength filter from 570 to 370 nm at an interval of 20 nm (Newport 10BPF10 FILTER, BANDPASS). Mott–Schottky measurements were carried out from -0.5 to 1.0 V vs. Ag/AgCl with 50 mV increments, a frequency of 1 kHz, and an amplitude of 10 mV in the dark.

Acknowledgements

Conflict of interest

The authors declare no conflict of interest.

[1] M. G. Walter, E. L. Warren, J. R. McKone, S. W. Boettcher, Q. Mi, E. A. Santori, N. S. Lewis, *Chem. Rev.* **2010**, *110*, 6446–6473.

[2] M. Grätzel, *Nature* **2001**, *414*, 338–344.

[3] K. Sivula, *J. Phys. Chem. Lett.* **2013**, *4*, 1624–1633.

[4] C. Jiang, S. J. A. Moniz, A. Wang, T. Zhang, J. Tang, *Chem. Soc. Rev.* **2017**, *46*, 4645–4660.

[5] Z. Li, W. Luo, M. Zhang, J. Feng, Z. Zou, *Energy Environ. Sci.* **2013**, *6*, 347–370.

[6] J. Yang, D. Wang, H. Han, C. Li, *Acc. Chem. Res.* **2013**, *46*, 1900–1909.

[7] P. Chakthranont, T. R. Hellstern, J. M. McEnaney, T. F. Jaramillo, *Adv. Energy Mater.* **2017**, *7*, 1701515.

[8] Y. Qiu, W. Liu, W. Chen, W. Chen, G. Zhou, P.-C. Hsu, R. Zhang, Z. Liang, S. Fan, Y. Zhang, Y. Cui, *Sci. Adv.* **2016**, *2*, e1501764.

[9] Y. Park, K. J. McDonald, K. S. Choi, *Chem. Soc. Rev.* **2013**, *42*, 2321–2337.

[10] T. W. Kim, K.-S. Choi, *Science* **2014**, *343*, 990–994.

[11] X. Chang, T. Wang, P. Zhang, J. Zhang, A. Li, J. Gong, *J. Am. Chem. Soc.* **2015**, *137*, 8356–8359.

[12] M. Zhong, T. Hisatomi, Y. Kuang, J. Zhao, M. Liu, A. Iwase, Q. Jia, H. Nishiyama, T. Minegishi, T. Nakabayashi, N. Shibata, R. Niishiro, C. Katayama, H. Shibano, M. Katayama, A. Kudo, T. Yamada, K. Domen, *J. Am. Chem. Soc.* **2015**, *137*, 5053–5060.

[13] F. S. Hegner, I. Herraiz-Cardona, D. Cardenas-Morcoso, N. R. López, J.-R. N. Galán-Mascarós, S. Gimenez, *ACS Appl. Mater. Interfaces* **2017**, *9*, 37671–37681.

[14] X. Shi, I. Y. Choi, K. Zhang, J. Kwon, D. Y. Kim, J. K. Lee, S. H. Oh, J. K. Kim, J. H. Park, *Nat. Commun.* **2014**, *5*, 4775–4782.

[15] M. Zhou, J. Bao, Y. Xu, J. Zhang, J. Xie, M. Guan, C. Wang, L. Wen, Y. Lei, Y. Xie, *ACS Nano* **2014**, *8*, 7088–7098.

[16] Y. Zhou, L. Zhang, L. Lin, B. R. Wygant, Y. Liu, Y. Zhu, Y. Zheng, C. B. Mullins, Y. Zhao, X. Zhang, G. Yu, *Nano Lett.* **2017**, *17*, 8012–8017.

[17] J. H. Kim, Y. Jo, J. H. Kim, J. W. Jang, H. J. Kang, Y. H. Lee, D. S. Kim, Y. Jun, J. S. Lee, *ACS Nano* **2015**, *9*, 11820–11829.

[18] T. W. Kim, Y. Ping, G. A. Galli, K. S. Choi, *Nat. Commun.* **2015**, *6*, 8769–8779.

[19] M. T. Mayer, Y. Lin, G. Yuan, D. Wang, *Acc. Chem. Res.* **2013**, *46*, 1558–1566.

[20] P. Luan, M. Xie, D. Liu, X. Fu, L. Jing, *Sci. Rep.* **2014**, *4*, 6180–6186.

[21] P. M. Rao, L. Cai, C. Liu, I. S. Cho, C. H. Lee, J. M. Weisse, P. Yang, X. Zheng, *Nano Lett.* **2014**, *14*, 1099–1105.

[22] M. Xie, X. Fu, L. Jing, P. Luan, Y. Feng, H. Fu, *Adv. Energy Mater.* **2014**, *4*, 1300995.

[23] W. J. Ong, L. L. Tan, Y. H. Ng, S. T. Yong, S. P. Chai, *Chem. Rev.* **2016**, *116*, 7159–7329.

[24] Y. Wang, X. Wang, M. Antonietti, *Angew. Chem. Int. Ed.* **2012**, *51*, 68–89; *Angew. Chem.* **2012**, *124*, 70–92.

[25] X. Wang, K. Maeda, A. Thomas, K. Takanabe, G. Xin, J. M. Carlsson, K. Domen, M. Antonietti, *Nat. Mater.* **2009**, *8*, 76–80.

[26] Y. Zheng, L. Lin, B. Wang, X. Wang, *Angew. Chem. Int. Ed.* **2015**, *54*, 12868–12884; *Angew. Chem.* **2015**, *127*, 13060–13077.

[27] G. Zhang, G. Li, Z. A. Lan, L. Lin, A. Savateev, T. Heil, S. Zafeiratos, X. Wang, M. Antonietti, *Angew. Chem. Int. Ed.* **2017**, *56*, 13445–13449; *Angew. Chem.* **2017**, *129*, 13630–13634.

[28] J. Ran, T. Y. Ma, G. Gao, X.-W. Du, S. Z. Qiao, *Energy Environ. Sci.* **2015**, *8*, 3708–3717.

[29] Q. Han, B. Wang, J. Gao, Z. Cheng, Y. Zhao, Z. Zhang, L. Qu, *ACS Nano* **2016**, *10*, 2745–2751.

[30] S. Cao, J. Low, J. Yu, M. Jaroniec, *Adv. Mater.* **2015**, *27*, 2150–2176.

[31] Y. Zheng, J. Liu, J. Liang, M. Jaroniec, S. Z. Qiao, *Energy Environ. Sci.* **2012**, *5*, 6717–6731.

[32] J. Su, Z. Bai, B. Huang, X. Quan, G. Chen, *Nano Energy* **2016**, *24*, 148–157.

[33] Y. Hou, F. Zuo, A. P. Dagg, J. Liu, P. Feng, *Adv. Mater.* **2014**, *26*, 5043–5049.

[34] M. Basu, Z. W. Zhang, C. J. Chen, T. H. Lu, S. F. Hu, R. S. Liu, *ACS Appl. Mater. Interfaces* **2016**, *8*, 26690–26696.

[35] Q. Ruan, W. Luo, J. Xie, Y. Wang, X. Liu, Z. Bai, C. J. Carmalt, J. Tang, *Angew. Chem. Int. Ed.* **2017**, *56*, 8221–8225; *Angew. Chem.* **2017**, *129*, 8333–8337.

[36] J. Xu, M. Shalom, *ACS Appl. Mater. Interfaces* **2016**, *8*, 13058–13063.

[37] C. Feng, Z. Wang, Y. Ma, Y. Zhang, L. Wang, Y. Bi, *Appl. Catal. B* **2017**, *205*, 19–23.

[38] W.-J. Ong, L.-L. Tan, S.-P. Chai, S.-T. Yong, A. R. Mohamed, *Nano Energy* **2015**, *13*, 757–770.

[39] T. Y. Ma, S. Dai, M. Jaroniec, S. Z. Qiao, *Angew. Chem. Int. Ed.* **2014**, *53*, 7281–7285; *Angew. Chem.* **2014**, *126*, 7409–7413.

[40] L. Shi, T. Wang, H. Zhang, K. Chang, J. Ye, *Adv. Funct. Mater.* **2015**, *25*, 5360–5367.

[41] Y. Wang, W. Wang, H. Mao, Y. Lu, J. Lu, J. Huang, Z. Ye, B. Lu, *ACS Appl. Mater. Interfaces* **2014**, *6*, 12698–13706.

[42] B. Zhu, P. Xia, W. Ho, J. Yu, *Appl. Surf. Sci.* **2015**, *344*, 188–195.

[43] H. Zhao, H. Yu, X. Quan, S. Chen, Y. Zhang, H. Zhao, H. Wang, *Appl. Catal. B* **2014**, *152–153*, 46–50.

[44] Z. Zhou, Y. Shen, Y. Li, A. Liu, S. Liu, Y. Zhang, *ACS Nano* **2015**, *9*, 12480–12487.

[45] S. Yang, Y. Gong, J. Zhang, L. Zhan, L. Ma, Z. Fang, R. Vajtai, X. Wang, P. M. Ajayan, *Adv. Mater.* **2013**, *25*, 2452–2456.

[46] B. Zhang, G. Dong, L. Wang, Y. Zhang, Y. Ding, Y. Bi, *Catal. Sci. Technol.* **2017**, *7*, 4971–4976.

[47] K.-H. Ye, Z. Wang, J. Gu, S. Xiao, Y. Yuan, Y. Zhu, Y. Zhang, W. Mai, S. Yang, *Energy Environ. Sci.* **2017**, *10*, 772–779.

[48] P. Niu, L. Zhang, G. Liu, H.-M. Cheng, *Adv. Funct. Mater.* **2012**, *22*, 4763–4770.

[49] X. Shi, L. Cai, M. Ma, X. Zheng, J. H. Park, *ChemSusChem* **2015**, *8*, 3192–3203.

[50] Y. Hou, Z. Wen, S. Cui, X. Feng, J. Chen, *Nano Lett.* **2016**, *16*, 2268–2277.

95

Supporting Information

Bismuth Vanadate with Electrostatically Anchored 3D Carbon Nitride Nano-networks as Efficient Photoanodes for Water Oxidation

Peng Luan,[a] Ying Zhang,[a] Xiaolong Zhang,[a] Zhijun Li,[b] Ragesh Prathapan,[a] Udo Bach,[c] and Jie Zhang*[a]

Equations used in this work:[1]

1. The potential *vs.* Ag/AgCl can be converted to potential *vs.* RHE scale with the Nernst equation:

$$E_{RHE} = E_{Ag/AgCl} + E^0_{Ag/AgCl} + 0.059 \times \text{pH}$$

$E^0_{Ag/AgCl}$ = 0.197 V *vs.* NHE

2. Calculation of applied bias photon-to-current efficiency (ABPE):

$$ABPE = \frac{J_{PEC} \times (1.23 - V_{app})}{P_{light}}$$

J_{PEC} (mA·cm^{-2}) is the measured photocurrent density, V_{app} (V) is the applied external potential *vs.* RHE and P_{light} (100mW·cm^{-2}) is the power density of the illumination.

3. Calculation of light harvesting efficiency (LHE):

$$LHE = 1 - 10^{-A_\lambda}$$

A_λ is absorbance at a wavelength of λ (nm).

4. Calculation of incident-photon-to-current conversion efficiency (IPCE):

$$IPCE = \frac{J_\lambda \times 1240}{\lambda \times P_\lambda}$$

J_λ (mA·cm^{-2}) is the photocurrent density measured under monochromatic illumination at λ, P_λ (mW·cm^{-2}) is the power intensity of the incident monochromatic light at wavelength λ. The value of *1240* (V·nm) is calculated from the equation of hc/e, where e is the charge of one electron (1.6 × 10^{-19} C), h is Planck's constant (6.63 × 10^{-34} J·s), and c is the speed of light (3 × 10^8 m·s^{-1}).

5. Calculation of absorbed photon-to-current conversion efficiency (APCE):

$$APCE = \frac{IPCE}{LHE}$$

6. Calculation of maximum photocurrent density (J_{max}):

J_{max} (mA·cm^{-2}) is obtained by integrating IPCE with AM 1.5. Briefly, the standard solar spectral irradiance (ASTMG-173-03) is converted to the solar energy spectrum in terms of number of photons (s^{-1}·m^{-2}·nm^{-1}) *vs.* λ (nm), then the number of photons above the photo-active range between λ_1 (nm) and λ_2 (nm) is selected to calculate its maximum photocurrent density. In this work, $\lambda_1 = 300$ nm and $\lambda_2 = 600$ nm were selected as the photo-active range.

7. Calculation of absorption photocurrent density (J_{abs}):

$$J_{abs} = J_{max} \times LHE$$

J_{abs} (mA·cm^{-2}) is the photocurrent density converted from photon absorption rate assuming 100% APCE.

8. Calculation of charge separation efficiency ($\eta_{separation}$):

$$\eta_{separation} = \frac{J_{scavenger}}{J_{abs}}$$

$J_{scavenger}$ is the measured photocurrent density in 0.5 M Na$_2$SO$_3$ as an added hole scavenger in KPi buffer solution (pH = 7) to minimize surface charge recombination.

9. Calculation of surface charge transfer efficiency ($\eta_{transfer}$):

$$\eta_{transfer} = \frac{J_{PEC}}{J_{scavenger}}$$

$J_{scavenger}$ (mA·cm^{-2}) and J_{PEC} (mA·cm^{-2}) are the measured photocurrent density in 0.1 M

KPi buffer with and without 0.5 M Na_2SO_3 as an added hole scavenger.

Figure S1. TEM images of a) pristine BVO, nanocomposites of b) CNNW/BVO, and c) CNNS/BVO.
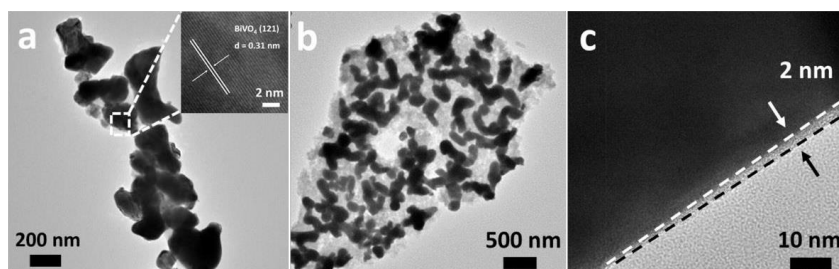
Figure S2. Large-scaled SEM image of BVO immersed in unprotonated CNNW aqueous solution.
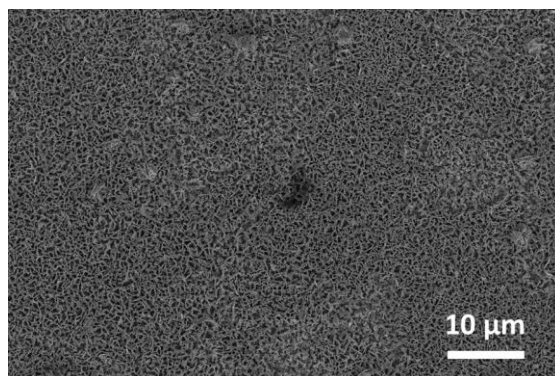
Figure S3. XRD patterns of a) BCN, CNNS and CNNW, b) BVO, CNNS/BVO and CNNW/BVO.
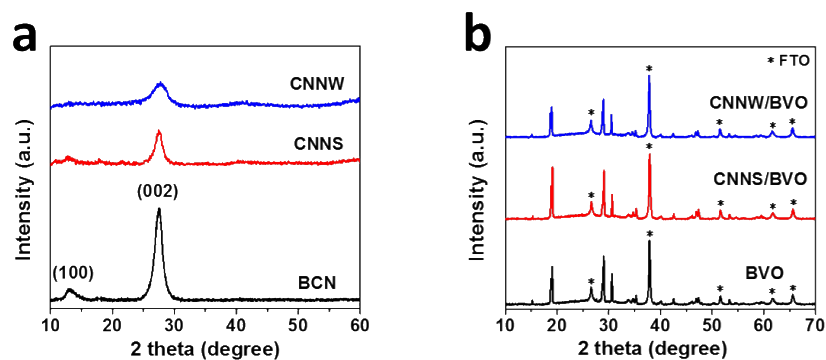
Figure S4. High-resolution XPS spectra of Bi4f and V2p.
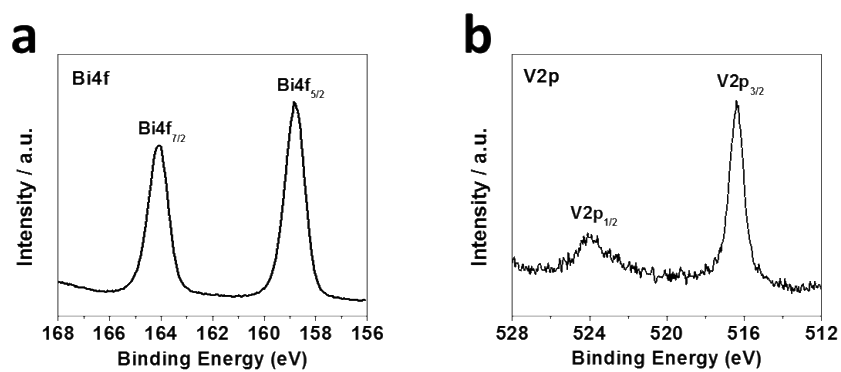
Figure S5. SEM images of CNNW/BVO nanocomposites a) before and b) after *J-t* measurement.
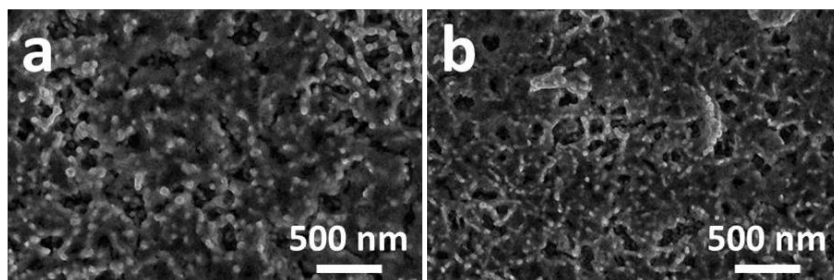
Figure S6. *J-V* curves in KPi buffer with 0.5 M Na₂SO₃ as an added hole scavenger.
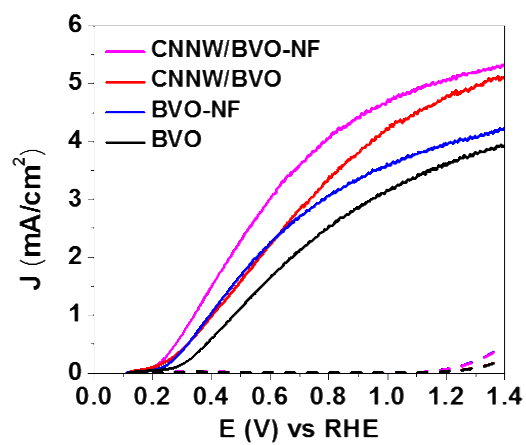
Figure S7. a) Uv-Vis absorption spectra and b) Light harvesting efficiency (LHE) of BVO, CNNS/BVO and CNNW/BVO.
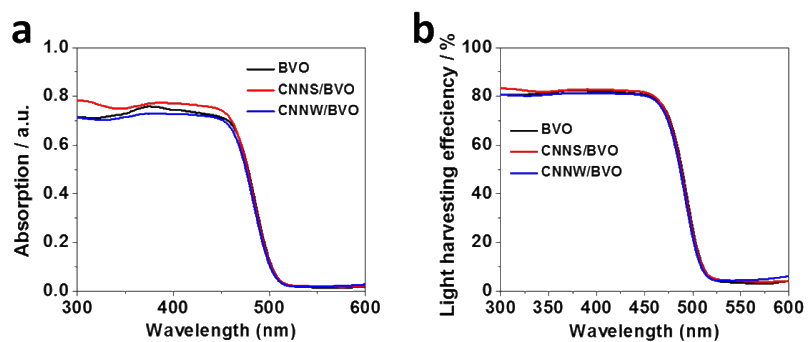
Figure S8. Spectra of the solar irradiance of AM 1.5G (ASTM G173-03) and J_{abs} of BVO and CNNW/BVO integrated from solar irradiance and LHE.
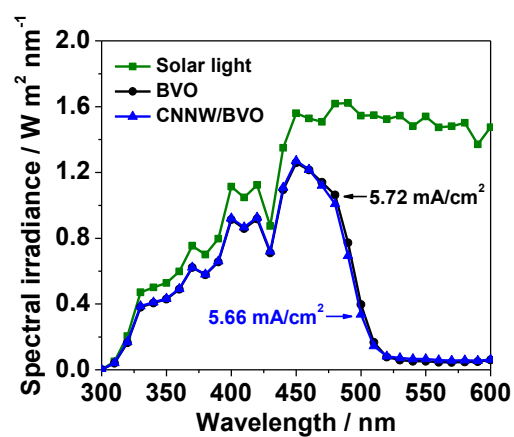
Figure S9. XPS spectra of Fe2p and Ni2p for CNNW/BVO-FN.
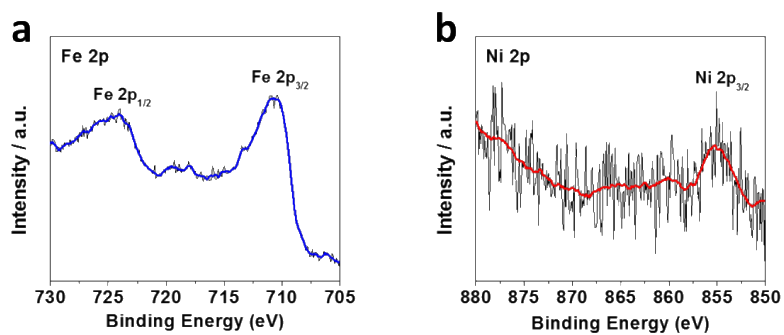
Figure S10. HAADF-STEM image and elemental mapping of CNNW/BVO-FN.
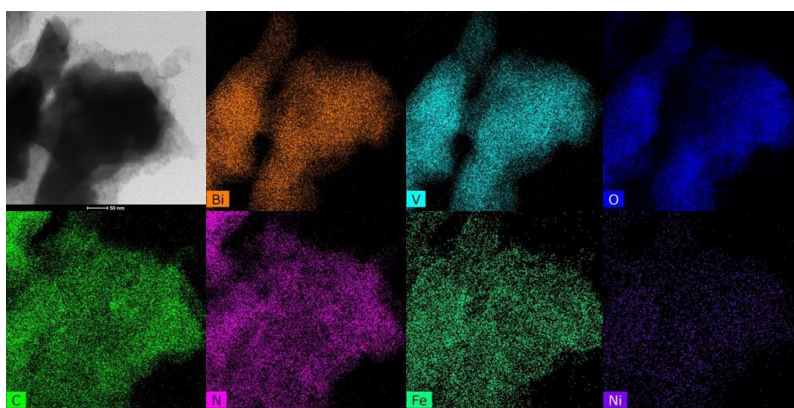
Table S1. Comparison of C_3N_4-modified $BiVO_4$ photoanodes toward PEC water oxidation:

Photoanode	Cocatalyst	Photocurrent density at 1.23V *vs.* RHE	Light	Fabrication method	Ref.
Nanoporous BVO/RGO/C₃N₄ Nanosheets	Co-Pi	3.4 mA/cm²	AM 1.5G	Electrophoresis	[2]
Nanoporous BVO/C₃N₄ Nanosheets	N/A	3.12 mA/cm²	> 420 nm	Calcination	[3]
BVO/C₃N₄	N/A	0.7 mA/cm²	> 420 nm	Calcination	[4]
BVO/C₃N₄ Nanosheets	N/A	0.44 mA/cm²	> 420 nm	Electrospinning	[5]
Nanoporous BVO/C₃N₄ Nano-networks	**NiOOH/FeOOH**	**4.87 mA/cm²**	**AM 1.5G**	**Electrostatic self-assembly**	**Our work**

Table S2. Comparison of the performance of $BiVO_4$-based photoanodes toward PEC water oxidation under AM 1.5G:

Photoanode	Cocatalyst	Photocurrent density	IPCE *vs.* RHE	Ref.
Nanoporous BiVO₄	NiOOH/FeOOH	2.73 mA/cm² at 0.6 V	60% at 420 nm at 0.6 V	[6]
Nanoporous BiVO₄/Carbon QDs	NiOOH/FeOOH	5.99 mA/cm² at 1.23 V	85% at 420 nm at 0.6 V	[7]
BiVO₄	NiOOH/NiO/CoOx	3.5 mA/cm² at 1.23 V	N/A	[8]
Nanoporous BiVO₄/Co₃O₄	N/A	2.71 mA/cm² at 1.23 V	50% at 1.23 V	[9]
Nanoporous N-doped BiVO₄	NiOOH/FeOOH	3.47 mA/cm² at 0.6 V	~ 64% at 400 nm at 0.6V	[10]
Helical WO₃/Mo, W-codoped BiVO₄	NiOOH/FeOOH	5.35 mA/cm² at 1.23 V	> 90% at 450 nm at 1.23V	[11]
WO₃/BiVO₄ Core/Shell Nanowire	Ni:FeOOH	4.5 mA/cm² at 1.23 V	N/A	[12]
Core-shell WO3/BiVO₄ nanorods	CoPi	6.72 mA/cm² at 1.23 V	>90% at 300-516 nm at 1.0V	[13]
Nanoworm transparent BiVO₄	NiOOH/FeOOH-Bi	3.2 mA/cm² at 1.23 V	N/A	[14]
Mo-doped Macro-Mesoporous BiVO₄	N/A	2.0 mA/cm² at 1.6 V⁽ᵃ⁾	40% at 350-400 nm at 1.0 V	[15]
WO₃/BiVO₄ Nanoporous Sphere Arrays	NiOOH/FeOOH	5.5 mA/cm² at 1.23 V	N/A	[16]
Mo:BiVO₄/Ni/Sn	NiFe mixture	~ 2.5 mA/cm² at 0.6 V	N/A	[17]
Gradient W-doped BiVO₄	CoPi	3 mA/cm² at 1.23 V	N/A	[18]
Electrochemically Treated BiVO₄	CoBi	3.2 mA/cm² at 1.23 V	76% at 340 nm at 0.7 V	[19]
H, Mo-codoped BiVO₄	CoPi	4.8 mA/cm² at 1.23 V	~ 95% at ~ 370 nm at 1.23 V	[20]
Layered-by-Layered WO₃/BiVO₄	N/A	2.78 mA/cm² at 1.2 V⁽ᵇ⁾	~ 40% at ~ 420 nm at 0.7 V	[21]
Nanocone Pt/Mo:BiVO₄	NiOOH/FeOOH	5.82 mA/cm² at 1.23 V	75% at 460 nm	[22]
Nanoporous BiVO₄/C₃N₄ Nano-networks	**NiOOH/FeOOH**	**4.87 mA/cm² at 1.23V**	**79.6% at 360 nm**	**Our work**

*All the potentials are with respect to RHE except (a) and (b) which are with respect to Ag/AgCl.

Figure S11. a) DRS, b) Bandgap value calculated from the $(\alpha h\nu)^{1/2}$ versus hν plots, and c) Mott-Schottky plots.
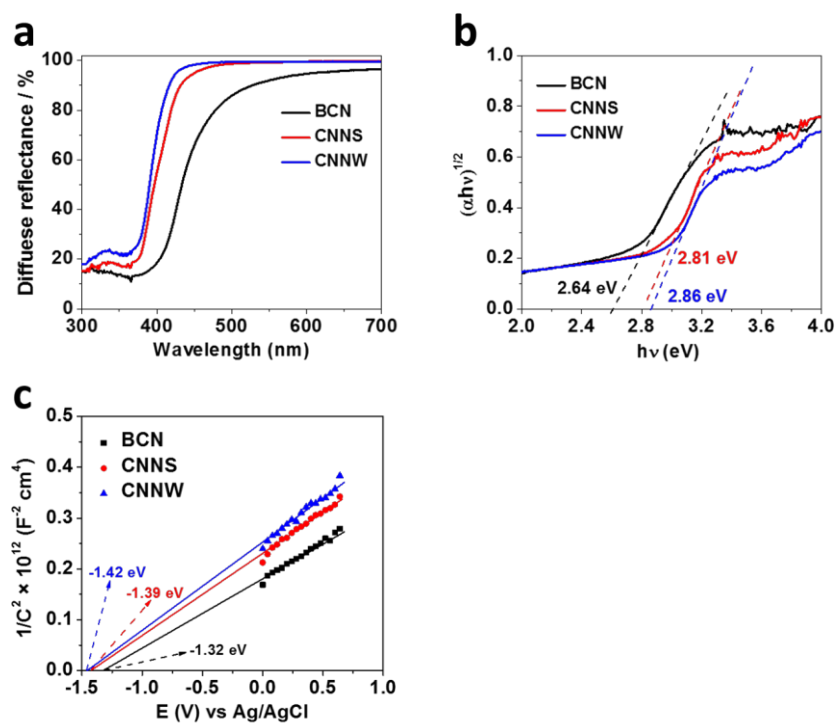

Table S3. The energy band structure of BCN, CNNS, and CNNW.

vs. NHE	BCN	CNNS	CNNW
CB position (eV)	-1.12	-1.19	-1.22
VB position (eV)	1.52	1.62	1.64
Bandgap (eV)	2.64	2.81	2.86

References

[1] X. Shi, L. Cai, M. Ma, X. Zheng, J. H. Park, *ChemSusChem*. **2015**, *8*, 3192-3203.

[2] J. Su, Z. Bai, B. Huang, X. Quan, G. Chen, *Nano Energy*. **2016**, *24*, 148-157.

[3] C. Feng, Z. Wang, Y. Ma, Y. Zhang, L. Wang, Y. Bi, *Appl. Cata. B: Environ.* **2017**, *205*, 19-23.

[4] B. Zhang, S. Y. Zhao, H. H. Wang, T. J. Zhao, Y. X. Liu, L. B. Lv, X. Wei, X. H. Li, J. S. Chen, *Chem. Commun.* **2017**, *53*, 10544-10547.

[5] Y. Wang, J. Sun, J. Li, X. Zhao, *Langmuir*. **2017**, *33*, 4694-4701.

[6] T. W. Kim, K. S. Choi, *Science*. **2014**, *343*, 990-994.

[7] K.-H. Ye, Z. Wang, J. Gu, S. Xiao, Y. Yuan, Y. Zhu, Y. Zhang, W. Mai, S. Yang, *Energy Environ. Sci.* **2017**, *10*, 772-779.

[8] M. Zhong, T. Hisatomi, Y. Kuang, J. Zhao, M. Liu, A. Iwase, Q. Jia, H. Nishiyama, T. Minegishi, M. Nakabayashi, N. Shibata, R. Niishiro, C. Katayama, H. Shibano, M. Katayama, A. Kudo, T. Yamada, K. Domen, *J. Am. Chem. Soc.* **2015**, *137*, 5053-5060.

[9] X. Chang, T. Wang, P. Zhang, J. Zhang, A. Li, J. Gong, *J. Am. Chem. Soc.* **2015**, *137*, 8356-8359.

[10] T. W. Kim, Y. Ping, G. A. Galli, K. S. Choi, *Nat. Commun.* **2015**, *6*, 8769-8779.

[11] X. Shi, I. Y. Choi, K. Zhang, J. Kwon, D. Y. Kim, J. K. Lee, S. H. Oh, J. K. Kim, J. H. Park, *Nat. Commun.* **2014**, *5*, 4775-4782.

[12] L. Cai, J. Zhao, H. Li, J. Park, I. S. Cho, H. S. Han, X. Zheng, *ACS Energy Lett.* **2016**, *1*, 624-632.

[13] Y. Pihosh, I. Turkevych, K. Mawatari, J. Uemura, Y. Kazoe, S. Kosar, K. Makita, T. Sugaya, T. Matsui, D. Fujita, M. Tosa, M. Kondo, T. Kitamori, *Sci. Rep.* **2015**, *5*, 11141.

[14] Y. Kuang, Q. Jia, H. Nishiyama, T. Yamada, A. Kudo, K. Domen, *Adv. Energy Mater.* **2016**, *6*, 1501645.

[15] M. Zhou, J. Bao, Y. Xu, J. Zhang, J. Xie, M. Guan, C. Wang, L. Wen, Y. Lei, Y. Xie, *ACS Nano*. **2014**, *8*, 7088-7098.

[16] Y. Zhou, L. Zhang, L. Lin, B. R. Wygant, Y. Liu, Y. Zhu, Y. Zheng, C. B. Mullins, Y. Zhao, X. Zhang, G. Yu, *Nano Lett.* **2017**, *17*, 8012-8017.

[17] Y. Kuang, Q. Jia, G. Ma, T. Hisatomi, T. Minegishi, H. Nishiyama, M. Nakabayashi, N. Shibata, T. Yamada, A. Kudo, K. Domen, *Nat. Energy*. **2016**, *2*, 16191-16200.

[18] F. F. Abdi, L. Han, A. H. Smets, M. Zeman, B. Dam, R. van de Krol, *Nat. Commun.* **2013**, *4*, 2195-

2202.

[19] S. Wang, P. Chen, J. H. Yun, Y. Hu, L. Wang, *Angew. Chem. Int. Ed.* **2017**, *56*, 8500-8504.

[20] J. H. Kim, Y. Jo, J. H. Kim, J. W. Jang, H. J. Kang, Y. H. Lee, D. S. Kim, Y. Jun, J. S. Lee, *ACS Nano*. **2015**, *9*, 11820-11829.

[21] S. J. Hong, S. Lee, J. S. Jang, J. S. Lee, *Energy Environ. Sci.* **2011**, *4*, 1781-1787.

[22] Y. Qiu, W. Liu, W. Chen, W. Chen, G. Zhou, P.-C. Hsu, R. Zhang, Z. Liang, S. Fan, Y. Zhang, Y. Cui, *Sci. Adv.* **2016**, *2*, e1501764.

Chapter 3. Dual Quantum Dot-Decorated Bismuth Vanadate Photoanodes for Highly Efficient Solar Water Oxidation

Dual Quantum Dot-Decorated Bismuth Vanadate Photoanodes for Highly Efficient Solar Water Oxidation

Peng Luan,[a] Xiaolong Zhang,[a] Ying Zhang,[a] Zhijun Li,[c] Udo Bach,[b] and Jie Zhang*[a]

Photo-induced charge separation and photon absorption play important roles in determining the performance of the photo-electrocatalytic water splitting process. In this work, we utilize dual quantum dots (QDs), consisting of $BiVO_4$ and carbon, to fabricate a hybrid homojunction-based $BiVO_4$ photoanode for efficient and stable solar water oxidation. Formation of homojunctions, by decorating as-prepared $BiVO_4$ substrate with $BiVO_4$ QDs, enhances the charge separation efficiency by 1.3 times. This enhancement originates from lattice match, which benefits charge transfer across the interface. Furthermore, the use of carbon QDs as a stable photosensitizer effectively extends the photon absorption limit from 520 nm to over 700 nm, yielding an incident photon-to-electron conversion efficiency of 6.0%, even at 600 nm at 1.23 V versus RHE. Finally, a remarkable photocurrent density of 6.1 mAcm^{-2} at 1.23 V was recorded after depositing FeOOH/NiOOH as cocatalysts, thereby, reaching 82% of the theoretical efficiency for $BiVO_4$.

Introduction

To meet the increasing energy demands and address the severe environmental issues in this century, traditional fossil fuels should be substituted by clean and renewable energy. Utilizing photoelectrochemical (PEC) technique to directly convert solar energy to hydrogen (H_2) fuel is regarded as a promising way to achieve the goal of building a sustainable society.[1–3] Solar-to-hydrogen (STH) efficiency of PEC water splitting is predominantly determined by the properties of photoelectrode, especially photoanode which performs the rate-determining oxygen evolution reaction (OER). Hence, developing an energy efficient photoanode is indispensable.[4,5] Monoclinic bismuth vanadate ($BiVO_4$), an n-type semiconductor, is widely studied in PEC water oxidation and solar cell tandem devices because of its suitable band gap for visible light absorption (generally < 520 nm), proper valence band location to drive the OER, and excellent stability in alkaline environment.[5–8] However, its charge separation (both on surface and in bulk)

and photon absorption range (only partial visible region) still need to be optimized to achieve a higher STH efficiency.[9–11]

Designing and fabricating a junction between two semiconductors with different band alignments to form an interfacial electric field is widely employed to promote the photo-induced charge separation.[12,13] A homojunction is an interface between two similar semiconductor materials.[14–16] The continuity of band bonding associated with a homojunction can effectively facilitate charge transfer across the interface.[15,17] Generally, research is focused on atom doping to tune the electronic band positions. For example, Abdi et al. reported a concentration gradient of tungsten doping in $BiVO_4$ film, thereby creating a distributed n$^+$-n homojunction to enhance the solar water oxidation.[14] Li et al. fabricated a homojunction-based photoanode consisting of metallic Mg-doped Fe_2O_3/nonmetallic P-doped Fe_2O_3 nanorods to eliminate lattice mismatching and enhance charge separation.[17] The band gap is greatly dependent on the size owing to quantum confinement effects. Hence, decreasing the size down to nanoscale by nano-engineering provides a feasibility to tune the band position (both conduction and valence bands).[18] Nanoparticles of this type are also called quantum dots (QDs). Furthermore, smaller sized QDs facilitate the migration of photo-induced charge carriers to the surface owing to the short diffusion distance.[19] Consequently, it is expected that a homojunction consisting of $BiVO_4$ QDs (BQDs) and $BiVO_4$ can promote the photo-induced charge separation.

Besides photo-induced charge separation, photon absorption is another significant factor influencing the PEC performance.[11,20] Generally, photosensitizers such as CdS/CdTe QDs, layered black phosphorous, and ruthenium/rhenium-based dye are employed in photocatalysis, photoelectrocatalysis, and solar cells to broaden photon-absorption range.[20–23] However, they are either toxic or unstable for practical applica-

[a] P. Luan, X. Zhang, Y. Zhang, Dr. J. Zhang
School of Chemistry
Monash University
Clayton, VIC 3800 (Australia)
E-mail: jie.zhang@monash.edu

[b] Prof. U. Bach
Department of Chemical Engineering
Monash University
Clayton, VIC 3800 (Australia)

[c] Dr. Z. Li
Ministry of Education Key Laboratory of Functional Inorganic Material Chemistry
School of Chemistry and Materials Science
Heilongjiang University
Harbin 150080 (P. R. China)

Supporting Information and the ORCID identification number(s) for the author(s) of this article can be found under:
https://doi.org/10.1002/cssc.201900230.

110

tions. Carbon QDs (CQDs), consisting of amorphous carbon and nanocrystalline regions of sp^2-hybridized graphitic carbon, exhibit excellent optical and charge-transport properties as well as high stability, non-toxicity, and low cost.[11,24] Therefore, these superior physico-chemical properties make CQDs promising as a broad spectrum light harvester.

Herein, we report the design and fabrication of a hybrid homojunction-based photoanode consisting of dual QDs (BQDs and CQDs) on a $BiVO_4$ substrate for highly efficient solar water oxidation. Significantly, the construction of lattice matched homojunction between BQDs and as-prepared $BiVO_4$ substrate is beneficial for promoting photo-induced charge separation. Furthermore, CQDs are used as photosensitizers to widen the photon-absorption range from partial (up to 540 nm) to full-visible (up to 700 nm) region. After the deposition of FeOOH/NiOOH as the oxygen-evolution cocatalyst (OEC), a remarkable photocurrent density of 6.1 mA cm^{-2} could be achieved at 1.23 V (vs. RHE) under AM 1.5G illumination.

Results and Discussion

The X-ray diffraction (XRD) spectra of pristine $BiVO_4$ (BVO), BQD-decorated $BiVO_4$ (B/BVO), CQD-decorated $BiVO_4$ (C/BVO), and dual QDs-decorated $BiVO_4$ (CB/BVO) are shown in Figure 1 a. Typical peaks of monoclinic BVO are observed in BVO, B/BVO, C/BVO, and CB/BVO. The peak intensities of B/BVO and CB/BVO are slightly higher than that of pristine BVO owing to the thermal treatment resulting in a higher crystallinity of BVO. The surface composition and chemical states of BVO and B/BVO were further analyzed by XPS. In Figure S1 a and b (see the Supporting Information), the peaks corresponding to Bi 4f (centered at 158.7 and 164.0 eV) and V 2p (centered at 516.4 and 524.1 eV) orbitals are ascribed to the Bi^{3+} and V^{5+} species in the monoclinic BVO, respectively.[25]

The scanning electron microscopy (SEM) images of BVO, B/BVO, C/BVO, and CB/BVO show that the cross-linked microstructure of the BVO substrate remains unchanged under all

synthesis conditions (Figure S2 a–c). However, the QDs were too small to be observed even under the highest magnification (Figure S2 d–l). Figure 1 b–d depicts the transmission electron microscopy (TEM) and high-resolution TEM (HRTEM) images of BVO, B/BVO, and CB/BVO as well as their crystal lattice information. No well-defined nanoscale surface feature was observed on the pristine BVO (Figures 1 b and S3 a). By contrast, Figures 1 c and S3 b show 8 nm-sized BQDs homogeneously distributed on the surface of BVO substrate after a successive adsorption of Bi^{3+} and VO_3^- followed by thermal annealing. Importantly, BQDs show a lattice spacing of 0.31 nm corresponding to (1 2 1) lattice plane, which matches well with that of the as-prepared BVO substrate.[10,26] Thereafter, CQD photosensitizers with the characteristic binding energy (Figure S4 a) and a size of 5–8 nm (Figure S4 b) were introduced to the surface of B/BVO to enhance the photon absorption. As observed from Figure 1 d, the BQDs and CQDs display a lattice spacing of 0.31 nm and 0.21 nm corresponding to (1 2 1) and (1 0 0) facets, respectively,[27,28] and are co-decorated on the surface of the BVO substrate. To further confirm the role of CQDs on effectively broadening the photon absorption range, UV/Vis absorption spectra were acquired and the related light harvesting efficiency (LHE) were estimated based on Equation (S2), as shown in Figure S5. It is observed that the photon absorption range can be extended from 520 nm for pristine BVO and B/BVO to more than 700 nm by decorating with CQDs (CB/BVO), indicating a significant role of CQDs in photosensitizing.

To evaluate the effect of homojunction on bulk charge separation, photocurrent density was measured in an electrolyte solution containing a sacrificial reagent (Na_2SO_3), in which surface charge recombination is negligible because of the fast kinetics of sulphite oxidation.[7,29] As shown in Figure 2 a, B/BVO exhibits a larger photocurrent density than pristine BVO, which originates from the enhanced bulk charge separation in the presence of the homojunction. The detailed charge-separation efficiency (η_{CSE}) is calculated based on the photocurrent density measured in Na_2SO_3 ($J_{scavenger}$) and the maximum photocurrent density (J_{max}) integrated from the number of absorbed photons in solar light (Figure S6) by using Equations (S3) and (S4).[10] In Figure 2 b, B/BVO shows a gradual increase in CSE as the applied potential increases from 0.4 to 1.0 V (vs. RHE, and the same elsewhere unless otherwise stated) and presents an average of 1.3 time enhanced CSE in this potential region compared to pristine BVO, reaching 92% at an applied bias of 1.0 V.

To accurately estimate the photo-induced charge separation onset wavelength, photocurrents associated with the photo-oxidation of SO_3^{2-} at the applied bias of 1.23 V were measured as a function of wavelength to calculate the incident photon-to-electron conversion efficiency (IPCE) according to Equation S5.[30] In Figure 2 c, IPCE values of 2.8% and 1.3% were achieved at 700 nm for CB/BVO and C/BVO, respectively, which gradually increased to 15% and 9.0% at 520 nm; whereas, negligible values were observed for pristine B/BVO and BVO in this
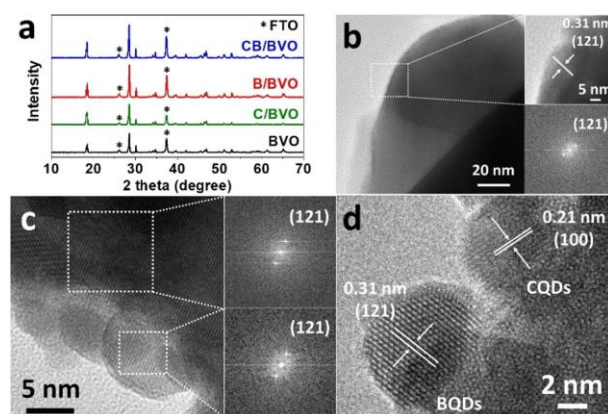
Figure 1. (a) XRD patterns of BVO, B/BVO, C/BVO, and CB/BVO. TEM, HRTEM, and related FFT images of (b) BVO and (c) B/BVO. d) HRTEM image of CB/BVO.
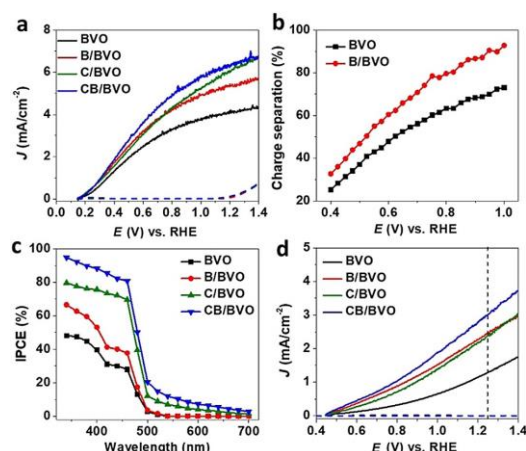
Figure 2. PEC measurements of pristine BVO, B/BVO, and CB/BVO under AM 1.5G irradiation in sodium borate buffer (0.05 M ;pH 9.3) with or without Na_2SO_3 (0.1 M) as a hole scavenger. (a) J–V curves measured in sodium borate buffer with Na_2SO_3, (b) charge separation efficiency, (c) IPCE recorded at incident wavelength ranging from 340 to 700 nm at an applied bias of 1.23 V versus RHE in sodium borate with Na_2SO_3, and (d) J–V curves measured in sodium borate without Na_2SO_3.

range, implying that photo-induced charge separation can be triggered even by photons with energy levels as low as 700 nm. Subsequently, the photocurrent density measurements of BVO, B/BVO, C/BVO, and CB/BVO were performed in the same electrolyte solution in the absence of a sacrificial reagent. As shown in Figure 2 d, CB/BVO produced the highest photocurrent density of 3.0 mA cm^{-2} at 1.23 V under one-sun illumination, which is 2.4, 1.2, and 1.2 times higher than BVO, C/BVO, and B/BVO, respectively. This improvement resulted from the enhanced photon absorption by CQDs and improved charge separation by BQDs. However, this value is still far below the photocurrent density measured in the presence of Na_2SO_3 (6.3 mA cm^{-2} at 1.23 V), suggesting a poor surface reaction kinetics of water on CB/BVO photoanode.

To minimize the surface hole–electron pair recombination and accelerate the surface reaction kinetics, FeOOH/NiOOH OEC was deposited on the CB/BVO photoanode.[6,31–33] In Figure S7, XPS results confirm the coexistence of Fe^{3+} (peaks located at binding energies of 710.8 and 724.3 eV) and Ni^{3+} (peaks located at binding energies of 852.6 and 870.8 eV) presumably in the form of FeOOH/NiOOH.[11,34] The high-angle annular dark-field scanning transmission electron microscopy (HAADF-STEM) mapping images show a uniform distribution of FeOOH/NiOOH on the surface of CB/BVO (Figure S8). Afterwards, the detailed PEC performance and efficiency of CB/BVO-FeOOH/NiOOH (CB/BVO-NF) was evaluated. As shown in Figure 3 a, CB/BVO-NF displays a maximum photocurrent density of 6.1 mA cm^{-2} at 1.23 V, which is close to the value obtained in the presence of Na_2SO_3, indicating a highly efficient charge transfer on the surface. The obtained photocurrent density value is comparable to that reported for the state-of-the-art

$BiVO_4$-based photoanodes (Table S1). This result is further confirmed by the calculated η_{CTE}, shown in Figure 3 b [based on the $J_{scavenger}$, shown in Figure S9 and Equation (S6)]. CB/BVO-NF reaches a η_{CTE} of 80%, which is much higher than CB/BVO (34%), B/BVO (31%), C/BVO (27%), and BVO (14%) at 1.0 V. Electrochemical impedance spectroscopy (EIS) measurements were performed in dark and under illumination to study the interfacial charge-transfer behavior (Figure S10). In the Nyquist diagram, the radius of each semicircle is associated with the charge-transfer process at the corresponding interface of photoanode/electrolyte.[35,36] The smallest radius observed for CB/BVO-NF correlates with the lowest charge-transfer resistance, indicating a faster charge transfer on the surface of CB/BVO-NF compared to CB/BVO, B/BVO, C/BVO, and BVO owing to the presence of the FeOOH/NiOOH cocatalyt.[37]

The PEC efficiency is increased as well, owing to the excellent surface charge transfer after depositing with FeOOH/NiOOH OEC. Firstly, applied bias photon-to-current efficiency (ABPE), which indicates STH efficiency at different applied potential bias (Equation S7), reaches 1.7% at 0.72 V for CB/BVO-NF; whereas, it is less than 0.5% for CB/BVO, B/BVO, and BVO (Figure 3 c). The IPCE value of CB/BVO-NF reaches 90% at 340 nm and an applied bias of 1.23 V, which is significantly higher than those of CB/BVO, B/BVO, and BVO (Figure 3 d). Notably, an IPCE value of 3.1% produced from CB/BVO even at 600 nm and an applied bias of 1.23 V is attributed to the effective photosensitization by CQDs. CB/BVO-NF exhibits an even larger IPCE value of 6.0% owing to the optimization of the surface reaction kinetics. By contrast, the IPCE values are negligibly small for B/BVO and BVO at a wavelength of 500 nm. To evaluate the operational stability of CB/BVO-NF photoanode for solar water oxidation, J–t curve and the related amount of gas production were evaluated in a single compartment airtight PEC cell under one sun illumination. Under an applied bias of 1.23 V, CB/BVO-NF exhibits an average photocurrent density of around 6.0 mA cm^{-2} for 10 h, demonstrating an excellent PEC activity and stability of this hybrid homojunction-based BVO photoanode (Figure 3 e). As shown in Figure 3 f, the amount of H_2 produced is 848 μmol cm^{-2} after 6 h reaction, with a faradaic efficiency of above 90%. The faradaic efficiency for O_2 evolution over this period is slightly smaller owing to the configuration of the PEC cell. O_2 generated from the photoanode was partially reduced at the Pt counter electrode in this single compartment cell, as also reported previously.[38,39]

To investigate the charge separation and transfer in this hybrid homojunction-based CB/BVO-NF photoanode, free-standing BQDs with a similar size were prepared to estimate the electronic band position of BQD at the photoanode (Figure S11 and Table S2).[19] It is seen that the band gap increases from 2.49 to 2.61 eV upon decreasing the size from bulk down to nanoscale owing to the quantum confinement effect.[18,19] Based on all the above results and analyses, a reaction scheme is proposed in Figure 4 to illustrate the charge separation and transfer in the CB/BVO-NF photoanode. The presence of homojunctions between BQDs and BVO substrate successfully promotes photo-induced charge separation, in which photo-induced holes are transferred to the surface, whereas the photo-

112
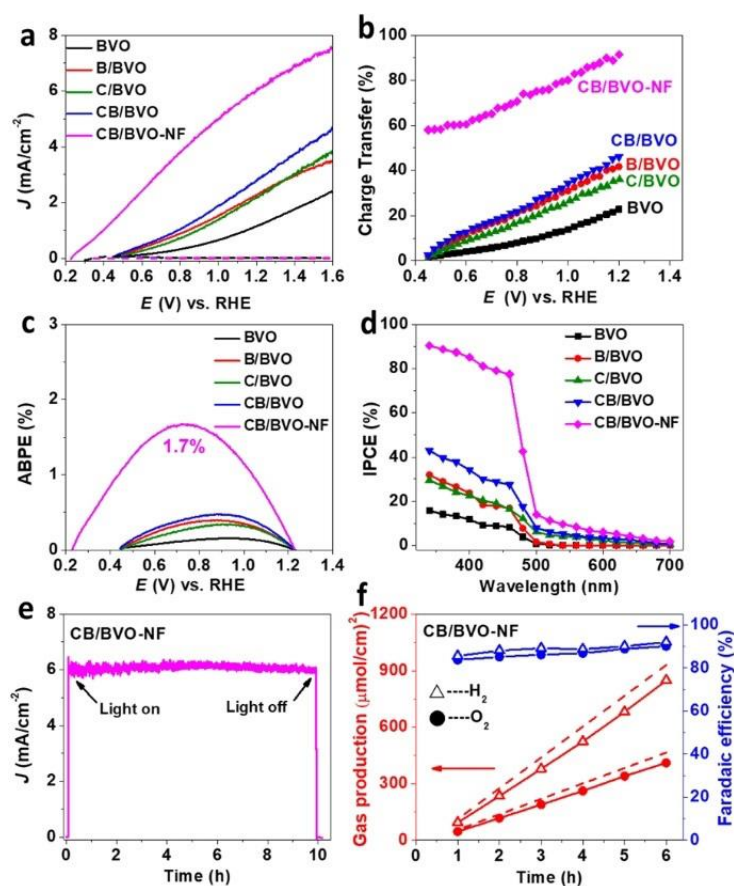
Figure 3. PEC performance of BVO, B/BVO, CB/BVO, and CB/BVO-NF measured in sodium borate buffer (0.05 м ;pH 9.3) under AM 1.5G irradiation. (a) *J–V* curves, (b) charge transfer efficiency, (c) ABPE, (d) IPCE at incident wavelength ranging from 340 to 700 nm at an applied bias of 1.23 V versus RHE, (e) *J–t* curves, and (f) oxygen and hydrogen production of CB/BVO-NF at an applied bias of 1.23 V versus RHE.
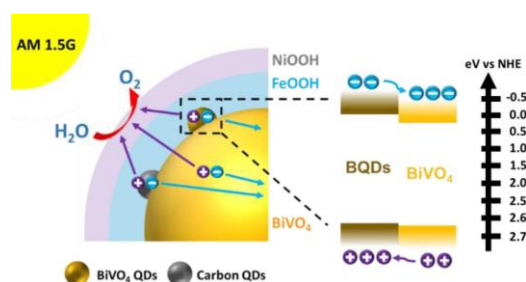
Figure 4. Proposed mechanism for water oxidation on CB/BVO-NF photoanode and energy-related charge transfer diagram.

induced electrons are transported to the counter electrode. In addition, more photons in the wavelength range of 520 to 700 nm can be absorbed to create extra electron–hole pairs owing to photosensitization by CQDs. Finally, the photo-excited holes from CQDs, BQDs, and the BVO substrate are effectively transferred to the photoelectrode/electrolyte interface and oxidize water to O_2, catalyzed by the layered FeOOH/NiOOH OEC.

Conclusions

We have successfully designed and fabricated a dual QD-decorated BiVO₄ as a homojunction-based photoanode for highly efficient and stable solar water oxidation. The resulting CB/BVO-NF photoanode with optimal surface reaction kinetics exhibits a remarkable photocurrent density of 6.1 mA cm⁻² at 1.23 V. This enhanced PEC performance is attributed to the improved charge separation by the BQD-decorated homojunctions and enhanced photon absorption by the CQDs photosensitizers. This material and structural design, based on homojunction strategy, presents a great feasibility for fabricating

photoanodes with excellent activity and stability for solar water oxidation.

Experimental Section

Preparation of BiVO₄ (BVO) photoanodes

BiVO₄ photoanode was prepared by a two-step process by modifying Kim and Choi's method.[6] Firstly, Bi(NO₃)₃ (2 mmol) was dissolved in a KI solution (50 mL; 0.4 M). The pH was adjusted to 1.7 by adding concentrated HNO₃, and the solution was mixed with absolute ethanol (20 mL) containing *p*-benzoquinone (4.6 mmol). After stirring for 20 min, electrodeposition of BiOI was performed in a typical three-electrode setup using an FTO substrate (2× 1 cm²) as the working electrode, a platinum wire as the counter electrode, and Ag/AgCl (4 M KCl) as the reference electrode. The electrodeposition was conducted at −0.1 V versus Ag/AgCl for 200 s. Afterwards, the BiOI-modified FTO electrode was rinsed with ethanol and dried under nitrogen flow. Secondly, dimethyl sulfoxide solution (0.2 mL) containing vanadyl acetylacetonate (0.2 M; VO(acac)₂) was added dropwise onto the BiOI surface (1×1 cm²), and then annealed in air at 450 °C for 2 h. The as-prepared electrode was soaked in NaOH solution (1 M) under gentle stirring to remove excess V₂O₅. The resulting BiVO₄ was rinsed with DI water.

Preparation of BQD-decorated BVO photoanodes

BQDs were deposited onto the as-prepared BVO photoanode by a modified method involving successive ionic layer absorption and reaction.[40] Firstly, BVO photoanode was dipped in ethylene glycol (20 mL) containing Bi(NO₃)₃·5H₂O (1 mmol) for 60 s and then rinsed with DI water and dried under N₂ flow. Secondly, this BVO photoanode was dipped in DI water (20 mL) containing NH₄VO₃ (1 mmol; adjusted to pH 4 with 1 M HNO₃) for 60 s and then rinsed with DI water and dried under N₂ flow. These two dipping processes were alternated and repeated 10 times. Finally, the obtained sample was annealed in air at 400 °C for 1 h.

Preparation of CQDs

CQDs were synthesized using a simple pyrolysis method reported in literature.[41] Typically, sucrose (0.375 g) was dissolved in deionized water (15 mL) at room temperature with continuous stirring for 10 min. The as-prepared solution was subsequently transferred into a 20 mL Teflon-lined stainless-steel autoclave and kept at 180 °C for 5 h. After cooling to room temperature, the obtained products were collected and washed with DI water and ethanol, and dried at 80 °C for 8 h.

Preparation of CQD-decorated BVO photoanodes

To create a hydrophilic surface on the BVO photoanode for effective adsorption of CQDs from an aqueous solution, BVO photoanode was immersed in a borate buffer solution (1.0 M; pH 9.3) containing Na₂SO₃ (0.2 M), and the potential was swept between 0.25 and 0.45 V versus Ag/AgCl under 1 sun illumination followed by rinsing with DI water and drying under an air stream. This process could result in a hydrophilic surface without damaging the photoanode. After this treatment, the BVO photoanode was immersed in CQs solution for 6 h and dried at 80 °C for 6 h.

Preparation of CQD-decorated B/BVO photoanodes

The process is the same as preparation of C/BVO, by using B/BVO as the photoanode immersed in CQDs solution.

Preparation of NiOOH/FeOOH cocatalyst on CB/BVO photoanodes

The NiOOH/FeOOH OEC was prepared using a photo-assisted electrodeposition method with a light intensity of 5 mW cm⁻² at the FTO surface by a neutral-density filter. In brief, photo-assisted electrodeposition of FeOOH was performed on BVO in FeSO₄ solution (50 mM) at a bias of 0.18 V versus Ag/AgCl with a total charge of approximately 25 mC cm⁻². Subsequently, photo-assisted electrodeposition of NiOOH was performed on BVO-FeOOH in NiSO₄ solution (50 mM) at a bias of 0.08 V versus Ag/AgCl with a total charge of approximately 10 mC cm⁻².

Preparation of free-standing quantum-sized BiVO₄

Free-standing quantum sized BiVO₄ was prepared according to a previous report.[42] Sodium oleate (1.3 mmol) and Bi(NO₃)₃·5H₂O (0.4 mmol) were successively added to distilled water (20 mL). An aqueous solution (20 mL) containing Na₃VO₄·12H₂O (0.4 mmol) was then injected into the above solution. After vigorously stirring for 2 h, the mixture was transferred to an autoclave and kept at 100 °C for 12 h. After cooling down to room temperature, the obtained sample was collected by centrifugation, and washed with n-hexane and absolute ethanol.

Characterization

XRD data were collected with a Bruker D8 Eco powder diffractometer (CuKα radiation, λ = 0.15406 nm). TEM images were collected on a FEI Tecnai G2 T20 TWIN TEM instrument. HAADF-STEM images and energy-dispersive X-ray spectra (EDS) were acquired with a FEI Tecnai G2 F20 S-TWIN FEGTEM instrument operated at 200 kV. XPS was performed with a Kratos-AXIS ULTRA DLD apparatus with Al (Mono) X-ray source, to gain further insight into the surface composition and elemental chemical state of the samples.

Photoelectrochemical and electrochemical measurements

Photoelectrochemical and electrochemical measurements were conducted at 25 ± 2 °C using an AUTOLAB electrochemical workstation (PGSTAT100) in a three-electrode PEC cell (K040-S Tianjin Ida Ltd.) with photoanode as the working (0.15 cm²), Ag/AgCl (4 M KCl) as reference and Pt wire as the counter electrode, respectively. A sodium borate (0.05 M) buffer solution (pH 9.3) with or without Na₂SO₃ (0.1 M) as a hole scavenger was used as the electrolyte and purged with N₂ for 30 min to remove oxygen before test. During the PEC measurements, the simulated solar light was generated from a 300 W Xenon lamp (Microsolar300 Beijing Perfectlight Technology Co., Ltd.) equipped with an AM 1.5G filter and passed through the insulating side of the FTO substrate. The power density of the incident light was calibrated to 100 mW cm⁻² (one sun illumination) at the surface of the FTO substrate using a light meter (PECSI01 Bunkoukeiki). Photocurrent measurement was performed at a scan rate of 50 mV s⁻¹ in borate buffer (0.05 M; pH 9.3). EIS measurement was performed in the frequency range of 10⁻¹– 10⁵ Hz with an AC voltage amplitude of 10 mV at a bias voltage of 0.6 V versus RHE, using a CHI 760E electrochemical workstation

114

Acknowledgements

Conflict of interest

The authors declare no conflict of interest.

[1] M. G. Walter, E. L. Warren, J. R. McKone, S. W. Boettcher, Q. Mi, E. A. Santori, N. S. Lewis, *Chem. Rev.* **2010**, *110*, 6446–6473.
[2] S. Ye, C. Ding, R. Chen, F. Fan, P. Fu, H. Yin, X. Wang, Z. Wang, P. Du, C. Li, *J. Am. Chem. Soc.* **2018**, *140*, 3250–3256.
[3] K. Sivula, R. van de Krol, *Nat. Rev. Mater.* **2016**, *1*, 15010.
[4] J. Tang, J. R. Durrant, D. R. Klug, *J. Am. Chem. Soc.* **2008**, *130*, 13885–13891.
[5] Y. Kuang, Q. Jia, G. Ma, T. Hisatomi, T. Minegishi, H. Nishiyama, M. Nakabayashi, N. Shibata, T. Yamada, A. Kudo, K. Domen, *Nat. Energy* **2016**, *2*, 16191.
[6] T. W. Kim, K.-S. Choi, *Science* **2014**, *343*, 990–994.
[7] J. H. Kim, Y. Jo, J. H. Kim, J. W. Jang, H. J. Kang, Y. H. Lee, D. S. Kim, Y. Jun, J. S. Lee, *ACS Nano* **2015**, *9*, 11820–11829.
[8] P. Chakthranont, T. R. Hellstern, J. M. McEnaney, T. F. Jaramillo, *Adv. Energy Mater.* **2017**, *7*, 1701515.
[9] P. M. Rao, L. Cai, C. Liu, I. S. Cho, C. H. Lee, J. M. Weisse, P. Yang, X. Zheng, *Nano Lett.* **2014**, *14*, 1099–1105.
[10] X. Chang, T. Wang, P. Zhang, J. Zhang, A. Li, J. Gong, *J. Am. Chem. Soc.* **2015**, *137*, 8356–8359.
[11] K.-H. Ye, Z. Wang, J. Gu, S. Xiao, Y. Yuan, Y. Zhu, Y. Zhang, W. Mai, S. Yang, *Energy Environ. Sci.* **2017**, *10*, 772–779.
[12] M. T. Mayer, Y. Lin, G. Yuan, D. Wang, *Acc. Chem. Res.* **2013**, *46*, 1558–1566.
[13] P. Luan, Y. Zhang, X. Zhang, Z. Li, R. Prathapan, U. Bach, J. Zhang, *ChemSusChem* **2018**, *11*, 2510–2516.
[14] F. F. Abdi, L. Han, A. H. Smets, M. Zeman, B. Dam, R. van de Krol, *Nat. Commun.* **2013**, *4*, 2195.
[15] P. Li, Y. Zhou, Z. Zhao, Q. Xu, X. Wang, M. Xiao, Z. Zou, *J. Am. Chem. Soc.* **2015**, *137*, 9547–9550.
[16] X. Chen, L. Liu, P. Y. Yu, S. S. Mao, *Science* **2011**, *331*, 746–750.
[17] F. Li, J. Li, F. Li, L. Gao, X. Long, Y. Hu, C. Wang, S. Wei, J. Jin, J. Ma, *J. Mater. Chem. A* **2018**, *6*, 13412–13418.
[18] Y. Yan, J. Chen, N. Li, J. Tian, K. Li, J. Jiang, J. Liu, Q. Tian, P. Chen, *ACS Nano* **2018**, *12*, 3523–3532.
[19] S. Sun, W. Wang, D. Li, L. Zhang, D. Jiang, *ACS Catal.* **2014**, *4*, 3498–3503.
[20] M. Zhu, S. Kim, L. Mao, M. Fujitsuka, J. Zhang, X. Wang, T. Majima, *J. Am. Chem. Soc.* **2017**, *139*, 13234–13242.
[21] G. Sahara, H. Kumagai, K. Maeda, N. Kaeffer, V. Artero, M. Higashi, R. Abe, O. Ishitani, *J. Am. Chem. Soc.* **2016**, *138*, 14152–14158.
[22] W. Zhang, Y. Wu, H. W. Bahng, Y. Cao, C. Yi, Y. Saygili, J. Luo, Y. Liu, L. Kavan, J.-E. Moser, A. Hagfeldt, H. Tian, S. M. Zakeeruddin, W.-H. Zhu, M. Grätzel, *Energy Environ. Sci.* **2018**, *11*, 1779–1787.
[23] G. Wang, X. Yang, F. Qian, J. Z. Zhang, Y. Li, *Nano Lett.* **2010**, *10*, 1088–1092.
[24] B. C. Martindale, G. A. Hutton, C. A. Caputo, E. Reisner, *J. Am. Chem. Soc.* **2015**, *137*, 6018–6025.
[25] C. Lv, G. Chen, X. Zhou, C. Zhang, Z. Wang, B. Zhao, D. Li, *ACS Appl. Mater. Interfaces* **2017**, *9*, 23748–23755.
[26] S. S. Patil, M. G. Mali, M. A. Hassan, D. R. Patil, S. S. Kolekar, S. W. Ryu, *Sci. Rep.* **2017**, *7*, 8404.
[27] L. Pan, S. Sun, L. Zhang, K. Jiang, H. Lin, *Nanoscale* **2016**, *8*, 17350–17356.
[28] H. Ding, H.-M. Xiong, *RSC Adv.* **2015**, *5*, 66528–66533.
[29] S. Wang, P. Chen, Y. Bai, J. H. Yun, G. Liu, L. Wang, *Adv. Mater.* **2018**, *30*, 1800486.
[30] J. H. Kim, J. W. Jang, Y. H. Jo, F. F. Abdi, Y. H. Lee, R. van de Krol, J. S. Lee, *Nat. Commun.* **2016**, *7*, 13380.
[31] L. Yu, H. Zhou, J. Sun, F. Qin, F. Yu, J. Bao, Y. Yu, S. Chen, Z. Ren, *Energy Environ. Sci.* **2017**, *10*, 1820–1827.
[32] M. Gong, Y. Li, H. Wang, Y. Liang, J. Z. Wu, J. Zhou, J. Wang, T. Regier, F. Wei, H. Dai, *J. Am. Chem. Soc.* **2013**, *135*, 8452–8455.
[33] A. Wu, Y. Xie, H. Ma, C. Tian, Y. Gu, H. Yan, X. Zhang, G. Yang, H. Fu, *Nano Energy* **2018**, *44*, 353–363.
[34] Y. Shi, Y. Yu, Y. Yu, Y. Huang, B. Zhao, B. Zhang, *ACS Energy Lett.* **2018**, *3*, 1648–1654.
[35] Y. Hou, F. Zuo, A. Dagg, P. Feng, *Nano Lett.* **2012**, *12*, 6464–6473.
[36] Y. Zhou, L. Zhang, L. Lin, B. R. Wygant, Y. Liu, Y. Zhu, Y. Zheng, C. B. Mullins, Y. Zhao, X. Zhang, G. Yu, *Nano Lett.* **2017**, *17*, 8012–8017.
[37] P. Peerakiatkhajohn, J. H. Yun, H. Chen, M. Lyu, T. Butburee, L. Wang, *Adv. Mater.* **2016**, *28*, 6405–6410.
[38] Y. Pihosh, I. Turkevych, K. Mawatari, J. Uemura, Y. Kazoe, S. Kosar, K. Makita, T. Sugaya, T. Matsui, D. Fujita, M. Tosa, M. Kondo, T. Kitamori, *Sci. Rep.* **2015**, *5*, 11141.
[39] J. Su, Z. Bai, B. Huang, X. Quan, G. Chen, *Nano Energy* **2016**, *24*, 148–157.
[40] F. Huang, J. Hou, Q. Zhang, Y. Wang, R. C. Massé, S. Peng, H. Wang, J. Liu, G. Cao, *Nano Energy* **2016**, *26*, 114–122.
[41] B. Long, Y. Huang, H. Li, F. Zhao, Z. Rui, Z. Liu, Y. Tong, H. Ji, *Ind. Eng. Chem. Res.* **2015**, *54*, 12788–12794.
[42] Y. Sun, Y. Xie, C. Wu, S. Zhang, S. Jiang, *Nano Res.* **2010**, *3*, 620–631.

Supporting Information

Dual Quantum Dot-Decorated Bismuth Vanadate Photoanodes for Highly Efficient Solar Water Oxidation

Peng Luan,[a] Xiaolong Zhang,[a] Ying Zhang,[a] Zhijun Li,[c] Udo Bach,[b] and Jie Zhang*[a]

cssc_201900230_sm_miscellaneous_information.pdf

Equations used in this work:

1. The potential *vs.* Ag/AgCl ($E_{Ag/AgCl}$) is converted to the potential *vs.* RHE (E_{RHE}) using the following equation: [1, 2]

$$E_{RHE} = E_{Ag/AgCl} + 0.059 \times \text{pH} + 0.197 \qquad (S1)$$

2. Calculation of light harvesting efficiency (LHE):

$$LHE = 1 - 10^{-A_\lambda} \qquad (S2)$$

A_λ is absorbance at a wavelength of λ (nm).

3. Calculation of maximum photocurrent density (J_{max}):

J_{max} (mA·cm^{-2}) is the maximum photocurrent density under AM 1.5G irradiation. Briefly, the standard solar spectral irradiance (ASTMG-173-03) is converted to the solar energy spectrum in terms of number of photons (s^{-1}·m^{-2}·nm^{-1}) *vs.* λ (nm), then the number of photons in the photo-active range between λ_1 (nm) and λ_2 (nm) is selected to calculate its maximum photocurrent density. In this work, $\lambda_1 = 300$ nm and $\lambda_2 = 700$ nm were selected as the photo-active range.

4. Calculation of absorption photocurrent density (J_{abs}):

$$J_{abs} = J_{max} \times LHE \qquad (S3)$$

J_{abs} (mA·cm^{-2}) is the photocurrent density converted from photon absorption rate assuming 100% APCE.

5. Calculation of charge separation efficiency (η_{CSE}):

$$\eta_{CSE} = \frac{J_{scavenger}}{J_{abs}} \qquad (S4)$$

$J_{scavenger}$ is the measured photocurrent density in a 0.05 M sodium borate buffer solution (pH = 9.3) with 0.1 M Na_2SO_3 as a hole scavenger.

6. Calculation of incident-photon-to-current conversion efficiency (IPCE):

$$IPCE = \frac{J_\lambda \times 1240}{\lambda \times P_\lambda} \qquad (S5)$$

J_λ (mA·cm^{-2}) is the photocurrent density measured under monochromatic illumination at λ; P_λ (mW·cm^{-2}) is the power intensity of the incident monochromatic light at wavelength λ; the value of *1240* (V·nm) is calculated from the equation of hc/e, where e is the charge of one electron (1.6×10^{-19} C); h is Planck's constant (6.63×10^{-34} J·s) and c is the speed of light (3×10^8 m·s^{-1}).

7. Calculation of surface charge transfer efficiency (η_{CTE}):

$$\eta_{CTE} = \frac{J_{PEC}}{J_{scavenger}} \qquad (S6)$$

$J_{scavenger}$ (mA·cm^{-2}) and J_{PEC} (mA·cm^{-2}) are the measured photocurrent density in a 0.05 M sodium borate buffer solution (pH = 9.3) with and without 0.1 M Na_2SO_3.
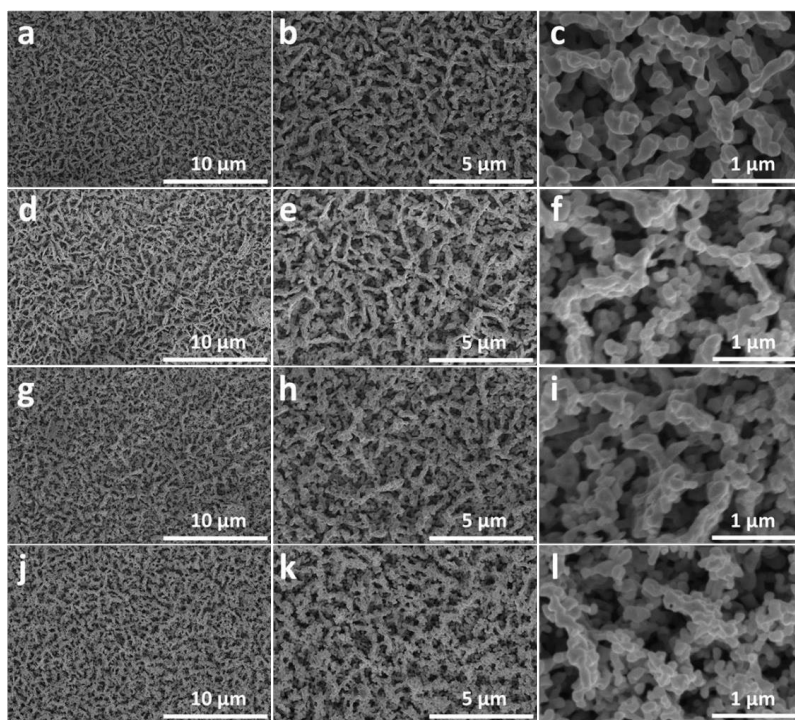
8. Calculation of applied bias photon-to-current efficiency (ABPE):

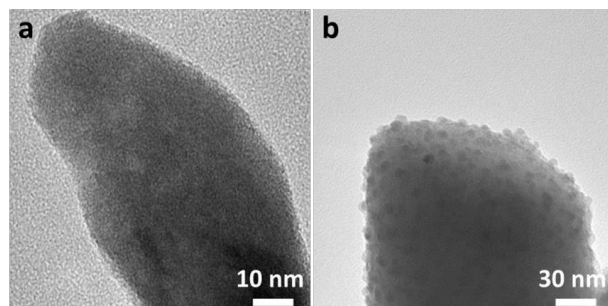$$ABPE = \frac{J_{PEC} \times (1.23 - V_{app})}{P_{light}} \qquad (S7)$$

J_{PEC} (mA·cm^{-2}) is the measured photocurrent density; V_{app} (V) is the applied external potential *vs*. RHE and P_{light} (100mW·cm^{-2}) is the power density of the illumination.
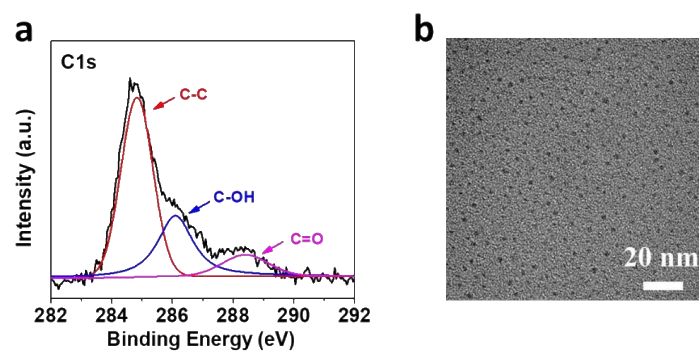
118
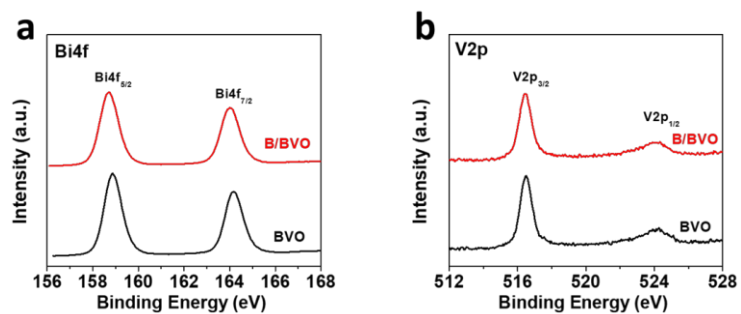
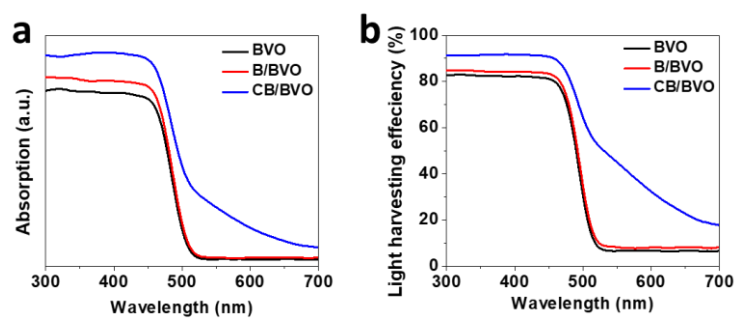**Figure S1.** High-resolution XPS spectra of (a) Bi4f; (b) V2p.

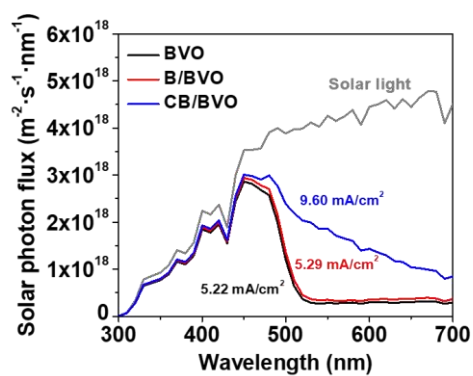**Figure S2.** SEM images of (a-c) BVO, (d-f) B/BVO, (g-i) C/BVO and (j-l) CB/BVO.

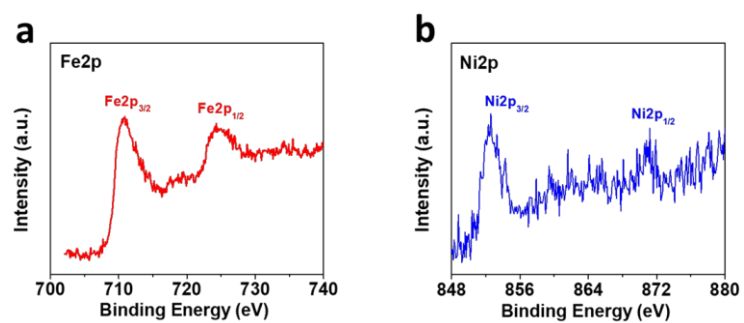**Figure S3.** TEM images of (a) pristine BVO and (b) B/BVO.

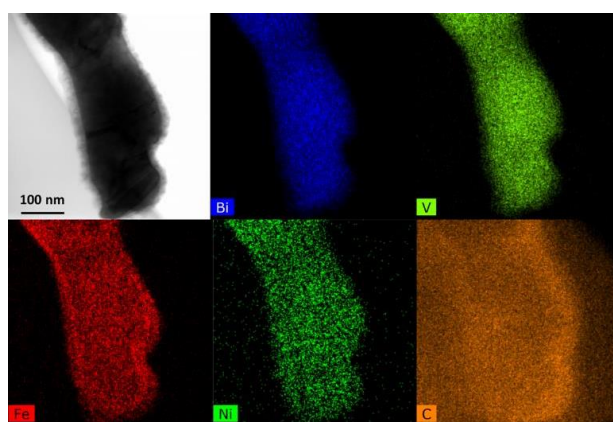**Figure S4.** XPS spectra (a) C1s and (b) TEM image of CQDs.

Figure S5. (a) UV-Vis absorption spectra and (b) LHE of BVO, B/BVO and CB/BVO.

Figure S6. Spectra of the solar irradiance of AM 1.5G (ASTM G173-03) and J_{abs} of BVO, B/BVO and CB/BVO integrated from solar irradiance and LHE.
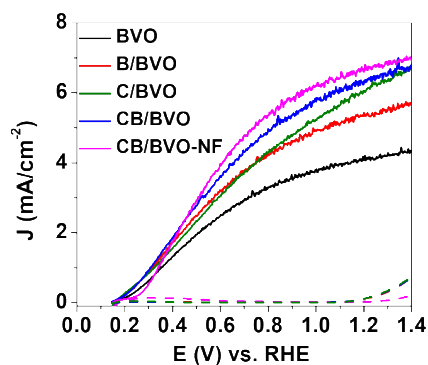
Figure S7. High-resolution XPS spectra of (a) Fe2p and (b) Ni2p.
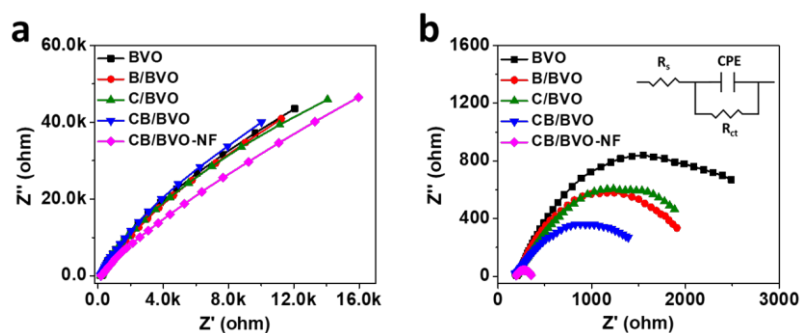

Figure S8. HAADF-STEM image and elemental mapping of CB/BVO-NF.

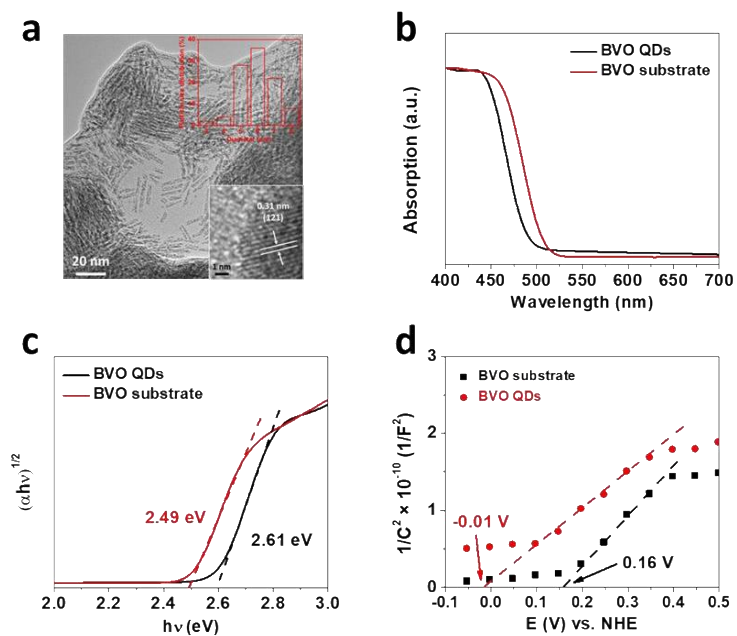**Figure S9.** *J-V* curves of BVO, B/BVO, C/BVO, CB/BVO and CB/BVO-NF under AM 1.5G irradiation in 0.05 M sodium borate buffer (pH = 9.3) with 0.1 M Na_2SO_3 as a hole scavenger.

Figure S10. EIS Nyquist plots collected at 0.7 V *vs*. RHE in (a) dark and (b) under illumination. (R_s is series resistance, R_{ct} is surface charge transfer resistance, and CPE is constant-phase elements).

Figure S11. Structural and optical characterization of free-standing quantum-sized BiVO₄. (a) TEM image, and HR-TEM and Particle size distribution as the insert; (b) UV-Vis absorption spectra; (c) Tauc plots of $(\alpha h\nu)^2$ *vs.* $h\nu$ and (d) Mott-Schottky plots.

Table S1. Comparison of the performance of BiVO$_4$-based photoanodes for PEC water oxidation under AM 1.5G:

Photoanode	Cocatalyst	Photocurrent density	IPCE *vs.* RHE	Ref.
Nanoporous BiVO$_4$	NiOOH/FeOOH	2.73 mA/cm^2 at 0.6 V	60% at 420 nm at 0.6 V	[3]
Nanoporous BiVO$_4$/Carbon QDs	NiOOH/FeOOH	5.99 mA/cm^2 at 1.23 V	85% at 420 nm at 0.6 V	[4]
BiVO$_4$	NiOOH/NiO/CoOx	3.5 mA/cm^2 at 1.23 V	N/A	[5]
Nanoporous BiVO$_4$/Co$_3$O$_4$	N/A	2.71 mA/cm^2 at 1.23 V	50% at 1.23 V	[6]
Helical WO$_3$/Mo, W-codoped BiVO$_4$	NiOOH/FeOOH	5.35 mA/cm^2 at 1.23 V	> 90% at 450 nm at 1.23V	[7]
WO$_3$/BiVO$_4$ Core/Shell Nanowire	Ni:FeOOH	4.5 mA/cm^2 at 1.23 V	N/A	[8]
Core-shell WO$_3$/BiVO$_4$ nanorods	CoPi	6.72 mA/cm^2 at 1.23 V	>90% between 300-516 nm at 1.0 V	[9]
Dual O$_{vancacy}$-enriched BiVO$_4$	NiOOH/FeOOH	5.87 mA/cm^2 at 1.23 V	N/A	[10]
WO$_3$/BiVO$_4$ Nanoporous Sphere Arrays	NiOOH/FeOOH	5.5 mA/cm^2 at 1.23 V	N/A	[11]
H, Mo-codoped BiVO$_4$	CoPi	4.8 mA/cm^2 at 1.23 V	~ 95% at ~ 370 nm at 1.23 V	[12]
Exposed (001) facets BiVO$_4$	CoPi	6.1 mA/cm^2 at 1.23 V	74 % at 350 nm at 1.23 V	[13]
Nanocone Pt/Mo:BiVO$_4$	NiOOH/FeOOH	5.82 mA/cm^2 at 1.23 V	75% at 460 nm at 1.23 V	[14]
3D C$_3$N$_4$ Nano-networks/BiVO$_4$	NiOOH/FeOOH	4.87 mA/cm^2 at 1.23 V	79.6% at 360 nm at 1.23 V	[15]
Mo-doped BiVO$_4$	NiFe-Phenolic Networks	5.1 mA/cm^2 at 1.23 V	95% between 365-475 nm at 1.23 V	[16]
CQDs&BQDs/BiVO$_4$	**NiOOH/FeOOH**	**6.12 mA/cm^2 at 1.23V**	**91 % at 340 nm at 1.23 V**	**Our work**

Table S2. Band position of BVO QDs and BVO substrate *vs.* NHE.

	Conduction band (eV)	Valence band (eV)	Bandgap (eV)
BVO QDs	-0.01	2.60	2.61
BVO substrate	0.16	2.65	2.49

Reference

[1] G. V. Govindaraju, G. P. Wheeler, D. Lee, K.-S. Choi, *Chem. Mater.* **2016**, *29*, 355-370.

[2] X. Shi, L. Cai, M. Ma, X. Zheng, J. H. Park, *ChemSusChem*. **2015**, *8*, 3192-3203.

[3] T. W. Kim, K. S. Choi, *Science*. **2014**, *343*, 990-994.

[4] K.-H. Ye, Z. Wang, J. Gu, S. Xiao, Y. Yuan, Y. Zhu, Y. Zhang, W. Mai, S. Yang, *Energy Environ. Sci.* **2017**, *10*, 772-779.

[5] M. Zhong, T. Hisatomi, Y. Kuang, J. Zhao, M. Liu, A. Iwase, Q. Jia, H. Nishiyama, T. Minegishi, M. Nakabayashi, N. Shibata, R. Niishiro, C. Katayama, H. Shibano, M. Katayama, A. Kudo, T. Yamada, K. Domen, *J. Am. Chem. Soc.* **2015**, *137*, 5053-5060.

[6] X. Chang, T. Wang, P. Zhang, J. Zhang, A. Li, J. Gong, *J. Am. Chem. Soc.* **2015**, *137*, 8356-8359.

[7] X. Shi, I. Y. Choi, K. Zhang, J. Kwon, D. Y. Kim, J. K. Lee, S. H. Oh, J. K. Kim, J. H. Park, *Nat. Commun.* **2014**, *5*, 4775-4782.

[8] L. Cai, J. Zhao, H. Li, J. Park, I. S. Cho, H. S. Han, X. Zheng, *ACS Energy Lett.* **2016**, *1*, 624-632.

[9] Y. Pihosh, I. Turkevych, K. Mawatari, J. Uemura, Y. Kazoe, S. Kosar, K. Makita, T. Sugaya, T. Matsui, D. Fujita, M. Tosa, M. Kondo, T. Kitamori, *Sci. Rep.* **2015**, *5*, 11141.

[10] S. Wang, P. Chen, Y. Bai, J. H. Yun, G. Liu, L. Wang, *Adv. Mater.* **2018**, *30*, e1800486.

[11] Y. Zhou, L. Zhang, L. Lin, B. R. Wygant, Y. Liu, Y. Zhu, Y. Zheng, C. B. Mullins, Y. Zhao, X. Zhang, G. Yu, *Nano Lett.* **2017**, *17*, 8012-8017.

[12] J. H. Kim, Y. Jo, J. H. Kim, J. W. Jang, H. J. Kang, Y. H. Lee, D. S. Kim, Y. Jun, J. S. Lee, *ACS Nano*. **2015**, *9*, 11820-11829.

[13] H. S. Han, S. Shin, D. H. Kim, I. J. Park, J. S. Kim, P.-S. Huang, J.-K. Lee, I. S. Cho, X. Zheng, *Energy Environ. Sci.* **2018**, *11*, 1299-1306.

[14] Y. Qiu, W. Liu, W. Chen, W. Chen, G. Zhou, P.-C. Hsu, R. Zhang, Z. Liang, S. Fan, Y. Zhang, Y. Cui, *Sci. Adv.* **2016**, *2*, e1501764.

[15] P. Luan, Y. Zhang, X. Zhang, Z. Li, R. Prathapan, U. Bach, J. Zhang, *ChemSusChem.* **2018**, *11*, 2510-2516.

[16] Y. Shi, Y. Yu, Y. Yu, Y. Huang, B. Zhao, B. Zhang, *ACS Energy Lett.* **2018**, *3*, 1648-1654.

Chapter 4. Unique Layer-Doping-Induced Regulation of Charge Behavior in Metal-Free Carbon Nitride Photoanodes for Enhanced Performance

Unique Layer-Doping-Induced Regulation of Charge Behavior in Metal-Free Carbon Nitride Photoanodes for Enhanced Performance

Peng Luan,[a] Qingqiang Meng,[b] Jing Wu,[c] Qinye Li,[e] Xiaolong Zhang,[a] Ying Zhang,[a] Luke A. O'Dell,[d] Sonia R. Raga,[e] Jennifer Pringle,[d] James C. Griffith,[g] Chenghua Sun,[f] Udo Bach,[e] and Jie Zhang*[a]

Photoinduced charge carrier behavior is critical in determining photoelectrocatalytic activity. In this study, a unique layer-doped metal-free polymeric carbon nitride (C_3N_4) photoanode is fabricated by using one-pot thermal vapor deposition. With this method, a photoanode consisting of a phosphorus-doped top layer, boron-doped middle layer, and pristine C_3N_4 bottom layer, was formed as a result of the difference in thermal polymerization kinetics associated with the boron-containing H_3BO_3–melamine complex and the phosphorus-containing H_3PO_4–dicyandiamide complex. This layer-doping fabrication strategy effectively contributes to the formation of dual junctions that optimizing charge carrier behavior. The ternary-layer C_3N_4 photoanode exhibits significantly enhanced photoelectrochemical water oxidation activity compared to pristine C_3N_4, with a record photocurrent density of $150 \pm 10 \, \mu A \, cm^{-2}$ at 1.23 V vs. RHE. This layer-doping strategy provides an effective means for design and fabrication of photoelectrodes for solar water oxidation.

Introduction

Photoelectrochemical (PEC) water splitting utilizing semiconductor photoelectrodes as both the light absorber and the energy converter is one of the most promising pathways to artificial photosynthesis.[1] Since the first report of TiO_2 for PEC water splitting, metal-based semiconductors such as $BiVO_4$, Fe_2O_3, Cu(In,Ga)Se$_2$, and Cu_2O have been widely investigated as photoanodes or photocathodes for solar water splitting.[2] Recently, metal-free polymeric carbon nitride (C_3N_4), consisting of earth-abundant elements with superior layered nanostructure and favorable electronic band position, is considered a promising photocatalyst for overall water splitting.[3] However, its application in photoelectrocatalysis is still less reported, mainly owing to poor photoinduced charge carrier behavior in film-based photoelectrodes, resulting in high bulk charge recombination and consequently low PEC activity.[4]

Rational design and fabrication strategies, such as heterostructure construction, single-atom coordination, and surface modification, have been widely applied to boost the photoactivity of C_3N_4.[4a, 5] Generally, doping with heteroatoms, such as phosphorus, boron, and sulfur, can effectively tune the electronic band position by forming localized states and hence improve charge transport properties.[6] Significantly, the change in electronic band position (usually elevating valence band position) from the bulk material not only enhances the photon absorption, but also constructs a junction to form a built-in electrical field at the interface, thus promoting photoinduced charge separation and transfer.[4c,7] For example, Abdi et al. fabricated a gradient W-doped $BiVO_4$ to create a distributed n^+–n homojunction.[7] This multiple built-in electric field resulted from layered doping fabrication efficiently promotes bulk charge separation efficiency up to 80%. More relevant to the topic of this study, Ruan et al. reported a gradient B-doping fabrication of a C_3N_4 photoanode to construct a binary-layer junction of B-doped C_3N_4 layer and bulk pristine C_3N_4 layer that enabled faster bulk charge transfer and mitigated charge recombination, achieving a tenfold enhancement in

[a] P. Luan, X. Zhang, Y. Zhang, Prof. J. Zhang
School of Chemistry, Monash University
Clayton, VIC 3800 (Australia)
E-mail: jie.zhang@monash.edu

[b] Q. Meng
MIIT Key Laboratory of Critical Materials Technology for New Energy Conversion and Storage, School of Chemistry and Chemical Engineering
Harbin Institute of Technology, Harbin, 150001 (P. R. China)

[c] J. Wu
State Key Laboratory of Urban Water Resource and Environment
Harbin Institute of Technology, Harbin, 150001 (P. R. China)

[d] Dr. L. A. O'Dell, Prof. J. Pringle
Institute for Frontier Materials, Deakin University
Waurn Ponds, VIC 3216 (Australia)

[e] Q. Li, S. R. Raga, Prof. U. Bach
Department of Chemical Engineering
Monash University, Clayton, VIC 3800 (Australia)

[f] Prof. C. Sun
Department of Chemistry and Biotechnology and Center for Translational Atomaterials
Swinburne University of Technology, Hawthorn, VIC 3122 (Australia)

[g] J. C. Griffith
Monash X-ray Platform, Monash University
Wellington Road, Clayton, VIC 3800 (Australia)

Supporting Information and the ORCID identification number(s) for the author(s) of this article can be found under:
https://doi.org/10.1002/cssc.201902967.

photocurrent in comparison with the pristine bulk C_3N_4 photoanode.[4c]

Herein, we report a unique layer-doped C_3N_4 photoanode composed of ternary layers, that is, P-doped top layer, B-doped middle layer, and pristine C_3N_4 bottom layer, that significantly enhances the photocurrent density of the pristine C_3N_4 photoanode by nearly 9 times. Detailed investigation reveals that this enhancement originates synergistically from heteroatom doping and junction formation, which effectively regulate the charge carrier lifetime, density, and diffusion length to promote photoinduced charge separation and transfer.

Results and Discussion

Based on the aforementioned prior reports, we hypothesized that multiple layer doping strategy may further enhance the PEC performance of C_3N_4. To test this hypothesis, density functional theory (DFT) calculations were first undertaken taken to investigate the charge behavior of layer-doped C_3N_4 (CN), composed of ternary layers, with a P-doped C_3N_4 (PCN) top layer, B-doped C_3N_4 (BCN) middle layer, and pristine CN bottom layer. The calculated electrostatic potential along the *c*-axis (Figure 1a) clearly shows that the work function gradually decreases from pristine CN to BCN and PCN layers, which is beneficial for charge transfer from bulk to surface. Such a change is essentially determined by the dopants, as indicated by the calculated profiles of local density of states (LDOS; Figure 1b). A major change is that the edges of valence bands were slightly increased by B and P doping, so photoinduced holes transferred from inner layers can be trapped by these states and become involved in surface water oxidation. Furthermore, these layers have the same lattice structures and similar electronics, which can minimize the interfacial resistance but promote charge separation owing to the special separation of frontier orbitals (HOMO and LUMO; Figure 1c). In addition, B and P doping can create new states around the Fermi level, which can serve as the source to fill the holes generated by photoexcitation, leaving active holes at the surface layers.

Encouraged by the positive outcome of the above analysis, the layer-doped CN photoanode was fabricated based on the difference in thermal polymerization routes of melamine (Mel)

and dicyandiamide (DCDA; see the Supporting Information, Scheme S1). It is proposed that NH_2-containing DCDA and Mel molecules can strongly interact with H_3PO_4 and H_3BO_3, respectively, through hydrogen-bonding interactions in water, thus forming P-containing DCDA (P-DCDA) and B-containing Mel (B-Mel) complexes.[6b] These different thermal polymerization routes of P-DCDA and B-Mel with different kinetics can result in a B- and P-layer-doped CN photoanode. During the fabrication process, B-Mel was thermally vaporized and deposited on the fluorine-doped tin oxide (FTO) substrate and first polymerized to give a B-doped Mel-derived CN layer (Scheme 1), followed by polymerization of the P-DCDA complex to give a P-doped DCDA-derived CN layer. The bottom pristine Mel-derived CN layer formed on the FTO substrate because the poly-
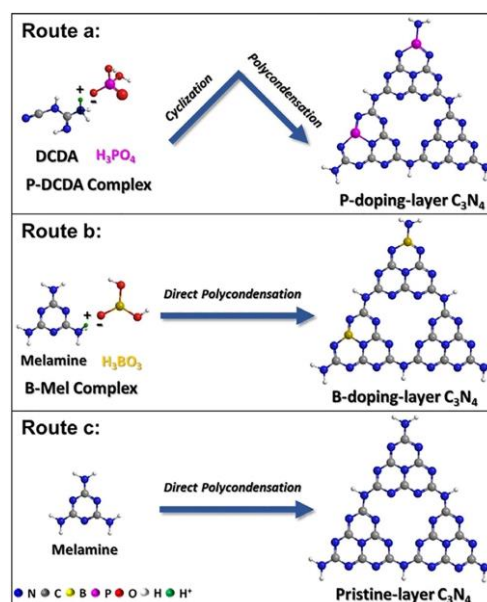
Scheme 1. Polymerization routes: Route a) P-DCDA complex to PCN; route b) B-Mel complex to BCN; route c) melamine to pristine CN.
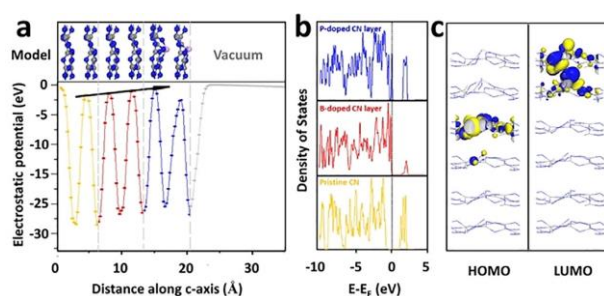

Figure 1. a) Electrostatic potential along the *c*-axis in different doping layers and related models. b) Local density of states (LDOS) and c) electron density distribution for HOMO and LUMO in different doping layers.

merization process is faster than the heteroatom doping process.[4c] Further details of the thermal deposition procedures (Scheme S2) and film thickness optimization (Figures S1 and S2) are provided in the Supporting Information.

The chemical structures of CN, B-doped CN (BCN), P-doped CN (PCN) and P/B layer-doped CN (PBCN) were first characterized by X-ray diffraction (XRD) and Fourier-transform infrared (FTIR) spectroscopy. Typically, the two diffraction peaks at 27.9° and 13.0° indexed for (002) and (100) in the XRD spectrum correspond, respectively, to interlayer stacking of conjugated aromatic rings and repeated in-plane heptazine motifs in CN (Figure S3a).[3a] The serial stretching

vibrations between 850 and 1730 cm^{-1} in the FTIR spectrum represent the repeating units of heptazine ring while an obvious peak at 803 cm^{-1} are attributed to the out-of-plane bending vibration of heptazine rings overlapped with that of -B-N- or -P-N- (Figure S3 b).[4d,8] The intrinsic conjugated framework structure of polymeric CN was found to be preserved after doping with P and B. Scanning electron microscopy (SEM) images show that the surfaces of the CN, BCN, PCN, and PBCN films were relatively smooth and compact. The cross-section view of the films shows that the thickness is about 1 μm (Figure S4). The high-angle annular dark-field scanning transmission electron microscopy (HAADF-STEM) image and elemental mapping indicate the presence of both B and P in PBCN (Figure S5).

To reveal the elemental distributions of P and B in the PBCN photoanode, the depth profiles and concentration were determined by using X-ray photoelectron spectroscopy (XPS; Figure 2 a,b). The intensity of the P2p peak associated with the -P—N bond at about 133.6 eV gradually decreases as a function of the depth. Detailed analysis suggests that the amount of P decreases from 0.87% (surface) to 0.18% (100 nm depth), implying that the thickness of the P-doped CN layer is about 100 nm.[6b,9] In contrast, the B1s peak associated with the B—N bond centered at about 191.8 eV is negligibly small on the surface and at a depth of 50 nm, but shows a rapid increase after a depth of 100 nm and reaches its highest amount of 1.42% at 200 nm, demonstrating that the B-doped CN layer is mainly present beyond a depth of 100 nm.[10] However, P and B were not absolutely separated from each other, as a tiny amount of P was detected in the BCN layer and vice versa (Table S1 and Figure S6). Solid-state NMR spectroscopy was undertaken to reveal further structural details of PBCN (Figure 2 c,d). Two peaks associated with ^{11}B were detected at −5.8 and 15.1 ppm, suggesting the presence of two different binding sites for B atoms in the heptazine-based frameworks, corresponding to substitution of the bay and corner C sites with B atoms (Figure 2 c).[10] For the ^{31}P spectrum (Figure 2 d), three peaks are observed at 0.8, −9.1, and −21.6 ppm. Among them, the peaks at −9.1 and −21.6 ppm are attributed to the substitution of the bay and corner C sites by P atoms.[6c,9] The additional peak at 0.8 ppm is attributed to residual PO$_4^{3-}$, since this chemical shift is very close to the ^{31}P chemical shift of the reference sample NH$_4$H$_2$PO$_4$ (Figure S7). XPS C1s spectra associated with C=C, C—O, and N—C≡N are essentially identical for PBCN and CN, because the chemical environments of C atoms in these materials are similar (Figure 2 e).[11] Furthermore, in the XPS N1s spectra (Figure 2 f), the main peak at 398.2 eV and two smaller ones at higher energies of 400.1 and 401.0 eV were characteristically associated with C—N≡C, N—(C)$_3$ and —NH$_2$ groups, respectively, which is again consistent with those found in pristine CN.[8] The additional N1s peak at 399.2 eV is thought to originate from B or P substitution of C, since substitution of C atoms with less electronegative B or P atoms would introduce a positive shift of the binding energy for N. Based on all the above evidence, we conclude that B and P atoms were incorporated into the conjugated frameworks with a unique layered distribution of B/P in the film.
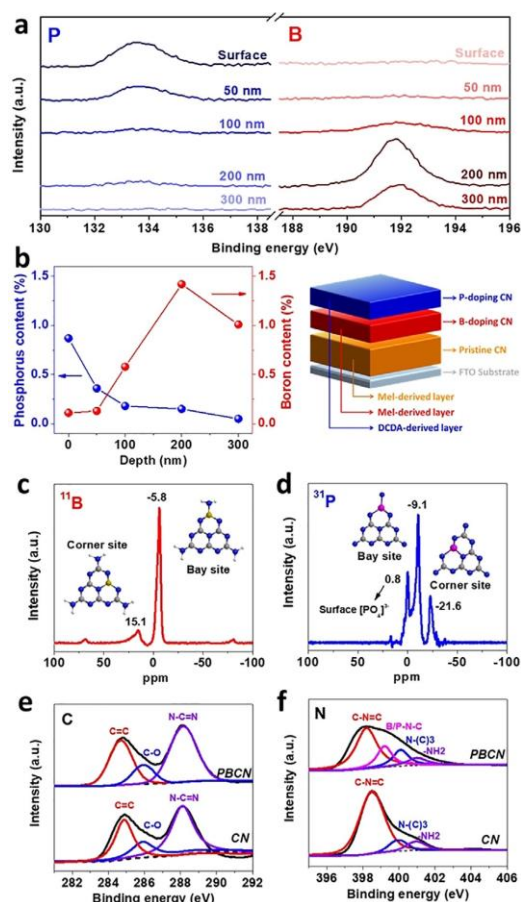
Figure 2. Structural characterization of PBCN: a) XPS depth profile; b) elemental distribution of P and B. c,d) Solid-state MAS NMR spectra of ^{11}B (c) and ^{31}P (d). e,f) XPS spectra of CN and PBCN for C1s (e) and N1s (f).

PEC activities associated with this unique layer-doped material were evaluated in 0.1 M Na$_2$SO$_4$ electrolyte under AM 1.5G illumination. PBCN exhibits a significantly enhanced PEC water oxidation performance compared to the pristine CN (Figure 3 a), with a record photocurrent density of 150± 10 μA cm^{-2} at 1.23 V vs. reversible hydrogen electrode (RHE) with optimal amounts of B and P (Figure S8), which is 1.4, 1.7, and 8.9 times higher than those of PCN, BCN, and pristine CN, respectively. This value is also considerably higher than those obtained for state-of-the-art CN-based photoanodes (Table S2). This layer-doping strategy therefore provides a promising way to fabricate metal-free polymer photoanodes for solar water splitting. However, this value is still significantly lower than those for metal oxide-based photoanodes.[2e,12] Further research is needed to improve the photocurrent density.

To reveal the origin of the enhanced PEC water oxidation performance associated with PBCN, the bulk charge separation
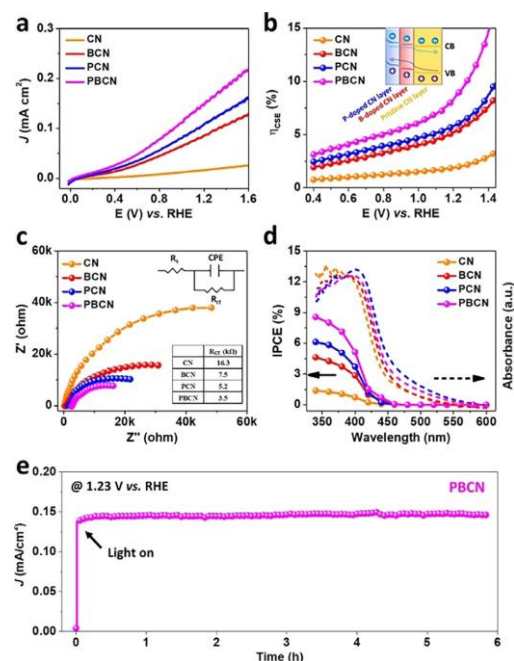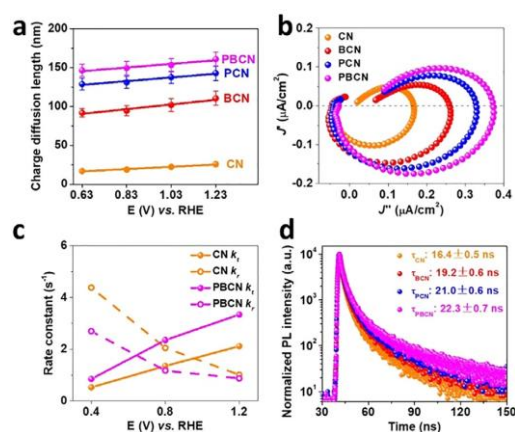
Figure 3. PEC performances of CN, BCN, PCN and PBCN: a) J–V measurement. b) Charge separation efficiency (ηCSE) and schematic illustration of photoinduced charge separation and transfer in PBCN as inset. c) EIS Nyquist plots (insets are the equivalent circuit and estimated resistance values). d) IPCE values (solid line) and absorbance (dashed line). e) J–t measurement.

sion efficiency (IPCE) was applied to reveal the photoactive range in solar light (Figure 3d).[14] The photo-active range starts from around 460 nm, which is consistent with the absorbance of PBCN, PCN, BCN and CN. A slight redshift of PBCN, PCN, and BCN compared to pristine CN results from the formation of a new dopant energy level that leads to a narrowed band gap. The IPCE value of PBCN is 8.6% at 340 nm at 1.23 V vs. RHE, which is higher than those for PCN (6.1%), BCN (4.6%), and CN (1.4%). Significantly, PBCN shows a superior operational stability for over 5 h at 1.23 V vs. RHE under illumination of AM 1.5G (Figure 3e), indicating no obvious decomposition of PBCN photoanode itself and strong adhesion of PBCN on FTO substrate.

Photoinduced charge carrier behaviors were also investigated. Generally, charge carrier diffusion length plays an important role in the competition between the diffusive transport and recombination in a photoelectrode, which can be experimentally estimated by absorption coefficient (Figure S13) and IPCE values determined from the frontside/backside illumination (Figure S14).[14,15] Doping of either P or B into the conjugated frameworks can significantly elongate hole diffusion lengths, owing to the improved electronic structure (Figure 4a). Notably, PBCN shows the largest charge carrier length of 161 ± 9 nm, compared to those of 143 ± 8 nm (PCN), 110 ± 4 nm (BCN) and 26 ± 3 nm (CN) at 1.23 V vs. RHE, indicating that elemental doping in the conjugated frameworks and the formation of built-in electrical field on each interfacial junction synergistically drives charge carrier migration, thus promoting photoinduced charge separation and transfer. Intensity-modulated photocurrent spectroscopy (IMPS; Figure 4b) was employed to reveal charge transfer from the bulk to the surface (hole extraction) since the accumulation of energetic holes on the photoanode surface is always regarded as the key driving force of the oxygen evolution reaction.[16] It is accepted that charge transport in bulk corresponds to the high-frequency

efficiencies (η_{CSE}) of doped CN and pristine CN were further compared (Figure 3b). To calculate η_{CSE} [see Equations (S5) and (S6)], the light-harvesting efficiency (LHE) was estimated by integrating absorbance (Figure S9), $J_{scavenger}$ was estimated based on the photocurrent density obtained in the presence of 0.1 M Na$_2$SO$_3$ as the hole scavenger (Figure S10a) and the absorption photocurrent density (J_{max}) was obtained from the integration of LHE and solar light spectrum (Figure S10b). Bulk η_{CSE} shows an obvious increase from 1.3% for CN to 9.0% for PBCN at 1.23 V vs. RHE upon layer-doping with P and B, which is attributed to the built-in electric field on the interface of junction according to the electronic band structures (Table S3) determined from the XPS valence band spectra (Figure S11) and Tauc plots (Figure S12) consistent with the theoretical prediction (Figure 1). The changed conduction band (CB) and gradually elevating valence band (VB) positions can effectively drive charge separation and transfer (Figure 3b, inset).

To estimate the charge transfer properties, the Nyquist plots of electrochemical impedance spectroscopy (EIS) were collected under illumination at 1.23 V vs. RHE (Figure 3c). PBCN shows the smallest charge transfer resistance (3.5 kΩ), compared to PCN (5.2 kΩ), BCN (7.5 kΩ), and CN (16.3 kΩ), suggesting an effective charge shuttling at the photoanode/electrolyte interface and charge transfer at the bulk interfacial junction.[13] Simultaneously, incident photon-to-current conver-

Figure 4. a) Photoinduced charge diffusion at wavelength of 400 nm at different applied biases. b) IMPS plots collected at 0.6 V vs. RHE under excitation of 430 ± 10 nm. c) Rate constants k_t and k_r at different potentials under excitation of 430 ± 10 nm. d) Charge carrier lifetime.

semicircle (below dashed line), whereas surface interfacial charge transfer is related to the low-frequency semicircle (above dashed line). The hole transfer in bulk was gradually promoted from CN, BCN, PCN, to PBCN, implying the layer-doping-induced dual built-in electric field favors hole transfer from the bulk to the surface, where surface-reaching holes can either oxidize water or recombine with electrons.[4c, 16b]

To obtain further quantitative insights, the first-order rate constant for charge transfer (k_t) and charge recombination (k_r) derived from the IMPS plots of CN and PBCN (Figure S15) were calculated (see the Supporting Information for details). The results obtained are shown in Figure 4c for comparison. For PBCN, the value of k_t reached 3.3 s^{-1}, whereas that of k_r declined to 0.9 s^{-1} on increasing the applied potential, which are 1.6 times higher and 1.2 times lower than those for CN, respectively, suggesting that layer-doping fabrication enables more efficient charge transfer in bulk. The lifetime of charge carriers is another important factor that affects PEC performance, which can be estimated based on the time-resolved photoluminescence (PL) decay data (Table S4). The lifetime of charge carriers is effectively prolonged from 16.6 ± 0.5 ns (CN), 19.2 ± 0.6 ns (BCN), 21.0 ± 0.6 ns (PCN) to 22.3 ± 0.7 ns (PBCN), elucidating reduced electron–hole recombination in the bulk (Figure 4d), which is well consistent with the results of charge diffusion length and IMPS.[4a]

Conclusions

In summary, we have designed and constructed a unique P/B-layer-doped metal-free CN photoanode for significantly enhanced solar water oxidation. The layered doping induces the formation of dual junctions composed of ternary layers, effectively regulating and optimizing charge behaviors, including charge carrier lifetime, density, and diffusion length. The resulting layer-doped PBCN photoanode exhibits a record photocurrent density of 150 ± 10 $\mu A\,cm^{-2}$ and a charge separation efficiency of 9.0% at 1.23 V vs. RHE. It is anticipated that this work will provide a promising path for the design and fabrication of high-efficiency metal-free photoelectrodes for solar water splitting.

Experimental Section

Preparation of phosphorus-containing dicyandiamide complex precursor (P-DCDA)

DCDA (500 mg) and phosphorous acid (H_3PO_4; 5 wt%) were dissolved in deionized (DI) water (20 mL) and stirred for 2 h to form a homogeneous solution. The solvent was then removed from this solution by evaporation at 70 °C and the resulting complex crystal was ground into powder.

Preparation of boron-containing melamine complex precursor (B-Mel)

Melamine (500 mg) and boric acid (H_3BO_3; 5 wt%) were dissolved in DI water (50 mL) and stirred for 2 h to form a homogeneous solution. The solvent was then removed from this solution by evapo-

ration at 70 °C and the resulting complex crystal was ground into powder.

Preparation of phosphorus/boron layer-doped g-C$_3$N$_4$ photoanode (PBCN)

B-Mel (25 mg) and P-DCDA (25 mg) complex precursors were mixed and dissolved in a porcelain boat with DI water (2 mL), followed by sonication for 1 min to disperse homogenously. After being dried and crystallized at 70 °C for 2 h, the precursor was adhered to the inner wall of the porcelain boat. Finally, the adhered precursor was thermally vaporized and deposited on an FTO substrate in a preheated furnace at 600 °C for 20 min and subsequently cooled in air to room temperature. The processes for preparing PCN and BCN are the same as that for PBCN except using 50 mg of P-DCDA or B-Mel as the only precursor. The process for preparing pristine CN is the same as PBCN but with 25 mg pristine melamine and 25 mg pristine DCDA as the precursors.

Characterization

X-ray Diffraction (XRD) data were collected with a Bruker D8 Eco powder diffractometer (Cu$_{K\alpha}$ radiation, $\lambda = 0.15406$ nm). FTIR spectra of the samples were collected with a Cary 630 FTIR spectrometer (Agilent Technologies). X-ray photoelectron spectroscopy (XPS) was performed with a Kratos-AXIS ULTRA DLD apparatus using Al X-ray source to gain the insight into surface composition and Ar^{n+} gas cluster ion source sputtering was employed to obtain element distribution depth profiles. Scanning electron microscopy (SEM) was carried out with a FEI Magellan 400 XHR FEGSEM Instrument. High-angle annular dark-field scanning transmission electron microscopy (HAADF-STEM) and energy-dispersive X-ray spectroscopy were carried out with a FEI Tecnai G2 F20 S-TWIN FEGTEM instrument operated at 200 kV. The photoluminescence and fluorescence decay spectroscopies were carried out on a FLUOROMAX-4C-TCSPC. ^{11}B and ^{31}P solid-state NMR spectra were acquired on a Bruker Avance III 500 MHz wide-bore spectrometer with a Bruker 4 mm HX MAS NMR probe and a sample spinning rate of 12 kHz.

PEC and electrochemical measurements

PEC and electrochemical measurements were both conducted at 25 ± 2 °C by using an AUTOLAB electrochemical workstation (PGSTAT100) in a three-electrode PEC cell (K040-S Tianjin Ida Ltd.) with photoanode (0.2 cm^2) working, Ag/AgCl (4 M KCl) reference, and Pt wire counter electrodes. A 0.1 M Na$_2$SO$_4$ solution (pH 6.5) was used as the electrolyte and purged with N$_2$ for 20 min to remove oxygen before testing. During the PEC measurements, the simulated solar light, generated from a 300 W Xeon lamp (Microsolar300 Beijing Perfectlight Technology Co. Ltd.) with an AM 1.5G filter, passed through the insulating side of the FTO substrate. The power density of the incident light was calibrated to 100 mW cm^{-2} (one-sun illumination) at the surface of the FTO substrate using a light meter (PECSI01 Bunkoukeiki). Photocurrent measurements were collected at a scan rate of 50 mV s^{-1}. Electrochemical impedance spectroscopy (EIS) was carried out under illumination at a bias voltage of 0.6 V (vs. RHE) in a frequency range of 10^{-1}–10^5 Hz with an AC voltage amplitude of 10 mV. Incident photon-to-electron conversion efficiency (IPCE) was measured at a bias voltage of 1.23 V vs. RHE combined with simulated solar light pass through a mono-wavelength filter (Newport 10BPF10 Filter, Bandpass) from 600 nm to 340 nm at an interval of 20 nm. Mott–Schottky measure-

ments were carried out in dark from −1.5 to 1.0 V (vs. Ag/AgCl) with 10 mV increments at a frequency of 1, 2, and 3 kHz and an amplitude of 10 mV. Intensity modulated photocurrent spectroscopy (IMPS) was recorded with a Zahner Zehniumm potentiostat equipped with a frequency response analyzer module and a monochromated LED light source of 430 ± 10 nm. The cell was connected in a three-electrode configuration and the IMPS spectrum was collected at 0.65 V vs. RHE. The DC bias illumination was adjusted to be 200 mW cm^{-2}, and the light AC sinusoidal perturbation was set to 15.5% of the DC light intensity (± 31 W m^{-2}). The frequency range recorded was from 10 kHz to 0.1 Hz.

DFT calculations

Theoretical calculations were performed under spin-polarized density functional theory calculations based on the generalized gradient approximation,[17] together with PBE functional[18] and double numerical polarized basis, as embedded in DMol3 package.[19] To consider the layer–layer interaction, van der Waals correction was carried out by using the Tkatchenko–Scheffler scheme.[20] Along the stacking direction, six C_3N_4 layers were employed, with two layers for each component (undoped, B-doped, and P-doped C_3N_4). Owing to the large size of the supercell, k-space is sampled with a grid of $3 \times 3 \times 1$. For all calculations, geometries were fully relaxed without any fixed atoms until the force converged to 0.05 eV Å^{-1} and energy to 10^{-4} eV. Frontier orbitals (HOMO and LUMO) were calculated based on optimized structures at gamma point.

Conflict of interest

The authors declare no conflict of interest.

[1] a) M. G. Walter, E. L. Warren, J. R. McKone, S. W. Boettcher, Q. Mi, E. A. Santori, N. S. Lewis, *Chem. Rev.* **2010**, *110*, 6446–6473; b) K. Sivula, R. van de Krol, *Nat. Rev. Mater.* **2016**, *1*, 15010–15026; c) Z. Li, W. Luo, M. Zhang, J. Feng, Z. Zou, *Energy Environ. Sci.* **2013**, *6*, 347–370; d) K. Sivula, F. Le Formal, M. Gratzel, *ChemSusChem* **2011**, *4*, 432–449.

[2] a) P. Luan, J. Zhang, *ChemElectroChem* **2019**, *6*, 3227–3243; b) C. Li, Z. Luo, T. Wang, J. Gong, *Adv. Mater.* **2018**, *30*, 1707502; c) M. Chen, Y. Liu, C. Li, A. Li, X. Chang, W. Liu, Y. Sun, T. Wang, J. Gong, *Energy Environ. Sci.* **2018**, *11*, 2025–2034; d) L. Pan, J. H. Kim, M. T. Mayer, M.-K. Son, A. Ummadisingu, J. S. Lee, A. Hagfeldt, J. Luo, M. Grätzel, *Nat. Catal.* **2018**, *1*, 412–420; e) T. Yao, X. An, H. Han, J. Q. Chen, C. Li, *Adv. Energy Mater.* **2018**, *8*, 1800210.

[3] a) X. Wang, K. Maeda, A. Thomas, K. Takanabe, G. Xin, J. M. Carlsson, K. Domen, M. Antonietti, *Nat. Mater.* **2009**, *8*, 76–80; b) W. J. Ong, L. L. Tan, Y. H. Ng, S. T. Yong, S. P. Chai, *Chem. Rev.* **2016**, *116*, 7159–7329; c) S. Cao, J. Low, J. Yu, M. Jaroniec, *Adv. Mater.* **2015**, *27*, 2150–2176; d) H. Wang, X. Zhang, Y. Xie, *Mater. Today* **2019**, *23*, 72–86.

[4] a) W. Che, W. Cheng, T. Yao, F. Tang, W. Liu, H. Su, Y. Huang, Q. Liu, J. Liu, F. Hu, Z. Pan, Z. Sun, S. Wei, *J. Am. Chem. Soc.* **2017**, *139*, 3021–3026; b) Y. Hou, Z. Wen, S. Cui, X. Feng, J. Chen, *Nano Lett.* **2016**, *16*, 2268–2277; c) Q. Ruan, W. Luo, J. Xie, Y. Wang, X. Liu, Z. Bai, C. J. Carmalt, J. Tang, *Angew. Chem. Int. Ed.* **2017**, *56*, 8221–8225; *Angew. Chem.* **2017**, *129*, 8333–8337; d) G. Peng, M. Volokh, J. Tzadikov, J. Sun, M. Shalom, *Adv. Energy Mater.* **2018**, *8*, 1800566; e) G. Peng, J. Albero, H. Garcia, M. Shalom, *Angew. Chem. Int. Ed.* **2018**, *57*, 15807–15811; *Angew. Chem.* **2018**, *130*, 16033–16037.

[5] a) W. Liu, L. Cao, W. Cheng, Y. Cao, X. Liu, W. Zhang, X. Mou, L. Jin, X. Zheng, W. Che, Q. Liu, T. Yao, S. Wei, *Angew. Chem. Int. Ed.* **2017**, *56*, 9312–9317; *Angew. Chem.* **2017**, *129*, 9440–9445; b) L. Jing, W. Zhou, G. Tian, H. Fu, *Chem. Soc. Rev.* **2013**, *42*, 9509–9549.

[6] a) J. Xu, S. Cao, T. Brenner, X. Yang, J. Yu, M. Antonietti, M. Shalom, *Adv. Funct. Mater.* **2015**, *25*, 6265–6271; b) J. Ran, T. Y. Ma, G. Gao, X.-W. Du, S. Z. Qiao, *Energy Environ. Sci.* **2015**, *8*, 3708–3717; c) F. Raziq, Y. Qu, M. Humayun, A. Zada, H. Yu, L. Jing, *Appl. Catal. B* **2017**, *201*, 486–494; d) G. Liu, P. Niu, C. Sun, S. C. Smith, Z. Chen, G. Q. Lu, H.-M. Cheng, *J. Am. Chem. Soc.* **2010**, *132*, 11642–11648.

[7] F. F. Abdi, L. Han, A. H. Smets, M. Zeman, B. Dam, R. van de Krol, *Nat. Commun.* **2013**, *4*, 2195–2201.

[8] S. Yang, Y. Gong, J. Zhang, L. Zhan, L. Ma, Z. Fang, R. Vajtai, X. Wang, P. M. Ajayan, *Adv. Mater.* **2013**, *25*, 2452–2456.

[9] Y. Zhang, T. Mori, J. Ye, M. Antonietti, *J. Am. Chem. Soc.* **2010**, *132*, 6294–6295.

[10] Y. Wang, H. Li, J. Yao, X. Wang, M. Antonietti, *Chem. Sci.* **2011**, *2*, 446–450.

[11] S. Guo, Z. Deng, M. Li, B. Jiang, C. Tian, Q. Pan, H. Fu, *Angew. Chem. Int. Ed.* **2016**, *55*, 1830–1834; *Angew. Chem.* **2016**, *128*, 1862–1866.

[12] Y. Yang, S. Niu, D. Han, T. Liu, G. Wang, Y. Li, *Adv. Energy Mater.* **2017**, *7*, 1700555.

[13] Y. Hou, Z. Wen, S. Cui, X. Guo, J. Chen, *Adv. Mater.* **2013**, *25*, 6291–6297.

[14] J. H. Kim, Y. Jo, J. H. Kim, J. W. Jang, H. J. Kang, Y. H. Lee, D. S. Kim, Y. Jun, J. S. Lee, *ACS Nano* **2015**, *9*, 11820–11829.

[15] a) W. H. Leng, P. R. F. Barnes, M. Juozapavicius, B. C. O'Regan, J. R. Durrant, *J. Phys. Chem. Lett.* **2010**, *1*, 967–972; b) J. Halme, G. Boschloo, A. Hagfeldt, P. Lund, *J. Phys. Chem. C* **2008**, *112*, 5623–5637.

[16] a) J. E. Thorne, J. W. Jang, E. Y. Liu, D. Wang, *Chem. Sci.* **2016**, *7*, 3347–3354; b) D. Klotz, D. S. Ellis, H. Dotan, A. Rothschild, *Phys. Chem. Chem. Phys.* **2016**, *18*, 23438–23457.

[17] W. Kohn, L. J. Sham, *Phys. Rev.* **1965**, *140*, A1133.

[18] B. Hammer, L. B. Hansen, J. K. Nørskov, *Phys. Rev. B* **1999**, *59*, 7413.

[19] a) B. Delley, *J. Chem. Phys.* **1990**, *92*, 508–517; b) B. Delley, *J. Chem. Phys.* **2000**, *113*, 7756–7764.

[20] A. Tkatchenko, M. Scheffler, *Phys. Rev. Lett.* **2009**, *102*, 073005.

135

Supporting Information

Unique Layer-Doping-Induced Regulation of Charge Behavior in Metal-Free Carbon Nitride Photoanodes for Enhanced Performance

Peng Luan,[a] Qingqiang Meng,[b] Jing Wu,[c] Qinye Li,[e] Xiaolong Zhang,[a] Ying Zhang,[a] Luke A. O'Dell,[d] Sonia R. Raga,[e] Jennifer Pringle,[d] James C. Griffith,[g] Chenghua Sun,[f] Udo Bach,[e] and Jie Zhang*[a]

cssc_201902967_sm_miscellaneous_information.pdf

Unique Layer-Doping-Induced Regulation of Charge Behaviour in Metal-Free Carbon Nitride Photoanodes for Enhanced Performance

Peng Luan,[a] Qingqiang Meng,[b] Jing Wu,[c] Qinye Li,[e] Xiaolong Zhang,[a] Ying Zhang,[a] Luke A. O'Dell,[d] Sonia R. Raga,[e] Jennifer Pringle,[d] James C. Griffith,[g] Chenghua Sun,[f] Udo Bach[e] and Jie Zhang*[a]

a School of Chemistry, Monash University, Clayton, VIC 3800, Australia.

b MIIT Key Laboratory of Critical Materials Technology for New Energy Conversion and Storage, School of Chemistry and Chemical Engineering, Harbin Institute of Technology, Harbin, PR China.

c State Key Laboratory of Urban Water Resource and Environment, Harbin Institute of Technology, Harbin, PR China.

d Department of Chemical Engineering, Monash University, Clayton, VIC 3800, Australia.

e Institute for Frontier Materials, Deakin University, Waurn Ponds, VIC 3216, Australia.

f Department of Chemistry and Biotechnology, Faculty of Science, Engineering & Technology, Swinburne University of Technology, Hawthorn, VIC 3122, Australia.

g Monash X-ray Platform, Monash University, Clayton, VIC 3800, Australia

Equations used in this work:[1]

1. Conversion of the Ag/AgCl potential scale to the RHE potential scale:

$$E_{RHE} = E_{Ag/AgCl} + 0.059 \times \text{pH} + 0.197 \qquad (Eq.S1)$$

2. Calculation of incident-photon-to-current conversion efficiency (IPCE):

$$IPCE = \frac{J_\lambda \times 1240}{\lambda \times P_\lambda} \qquad (Eq.S2)$$

Where J_λ (mA·cm^{-2}) is the photocurrent density measured under monochromatic illumination at λ, P_λ (mW·cm^{-2}) is the power intensity of the incident monochromatic light at wavelength λ, the value of *1240* (V·nm) is calculated from the equation of hc/e, where e is the charge of one electron (1.6×10^{-19} C); h is Planck's constant (6.63×10^{-34} J·s) and c is the speed of light (3×10^8 m·s^{-1}).

3. Calculation of light harvesting efficiency (LHE):

$$LHE = 1 - 10^{-A_\lambda} \qquad (Eq.S3)$$

Where A_λ is the absorbance at a given wavelength.

4. Calculation of maximum photocurrent density (J_{max}):

J_{max} (mA·cm^{-2}) is the maximum photocurrent density under AM 1.5G irradiation. Briefly, the standard solar spectral irradiance (ASTMG-173-03) is converted to the solar energy spectrum in terms of number of photons (s^{-1}·m^{-2}·nm^{-1}) *vs.* λ (nm), then the number of photons in the photo-active range between λ_1 (nm) and λ_2 (nm) is selected to calculate its maximum photocurrent density. In this work, $\lambda_1 = 300$ nm and $\lambda_2 = 460$ nm were selected as the photo-

active range according to the IPCE results.

$$J_{max} = e \times \int_{\lambda_2}^{\lambda_1} \frac{P_\lambda \times \lambda}{h \times c} \qquad (Eq.\,S4)$$

5. Calculation of absorption photocurrent density (J_{abs}):

$$J_{abs} = J_{max} \times LHE \qquad (Eq.\,S5)$$

Where J_{abs} (mA·cm^{-2}) is the photocurrent density converted from photon absorption rate

assuming 100% APCE.

6. Calculation of charge separation efficiency (η_{CSE}):

$$\eta_{CSE} = \frac{J_{scavenger}}{J_{abs}} \qquad (Eq.\,S6)$$

Where $J_{scavenger}$ is the measured photocurrent density in a 0.1 M Na$_2$SO$_4$ with 0.1 M Na$_2$SO$_3$ as

the hole scavenger.

7. Calculation of absorption coefficient (α):

$$\alpha = \frac{-ln(10^{-A})}{d} \qquad (Eq.\,S7)$$

Where d is thickness of the photoanode film (μm).

8. Calculation of hole diffusion length (L):

$$\frac{IPCE_{front}(\lambda, d)}{IPCE_{back}(\lambda, d)} = \frac{\sinh\left(\frac{d}{L}\right) + L\alpha(\lambda)\cosh\left(\frac{d}{L}\right) - L\alpha(\lambda)e^{\alpha(\lambda)d}}{\sinh\left(\frac{d}{L}\right) - L\alpha(\lambda)\cosh\left(\frac{d}{L}\right) + L\alpha(\lambda)e^{-\alpha(\lambda)d}} \times e^{-\alpha(\lambda)d} \quad (Eq.\,S8)$$

Where α is the absorption coefficient, d is thickness of the photoanode film, IPCE$_{front}$ and

IPCE$_{back}$ are measured at 400 nm at 0.63, 0.83, 1.03, 1.23 V *vs.* RHE respectively.

9. Calculation of charge carrier lifetime (τ_{ave}):

$$\tau_{ave} = \frac{A_1\tau_1^2 + A_2\tau_2^2 + A_3\tau_3^2}{A_1\tau_1 + A_2\tau_2 + A_3\tau_3} \qquad (Eq.\,S9)$$

10. Calculation of first order constant rate of charge transfer (k_t) and charge recombination (k_r):

$$\frac{k_t}{k_t + k_r} = \frac{LHI}{HFI} \qquad (Eq.\,S10)$$

$$\omega_{max} = k_t + k_r \qquad (Eq.\,S11)$$

Where LFI is the low frequency intercept with the real axis, HFI is the high frequency intercept with the real axis, and ω_{max} is extracted from Ima $J'(\omega)$ in the IMPS spectrum.

Scheme S1. The polymerization routes for (a) Mel-derived CN and (b) DCDA-derived CN. Mel-derived CN can be formed via a fast one-step thermal polycondensation process from triazine-based Mel molecule. By contrast, DCDA-derived CN is formed in a much slower rate via a two-step process, which involves an initial cyclization of chain-based DCDA molecule to triazine-based Mel molecule followed by polycondensation to form polymeric CN.
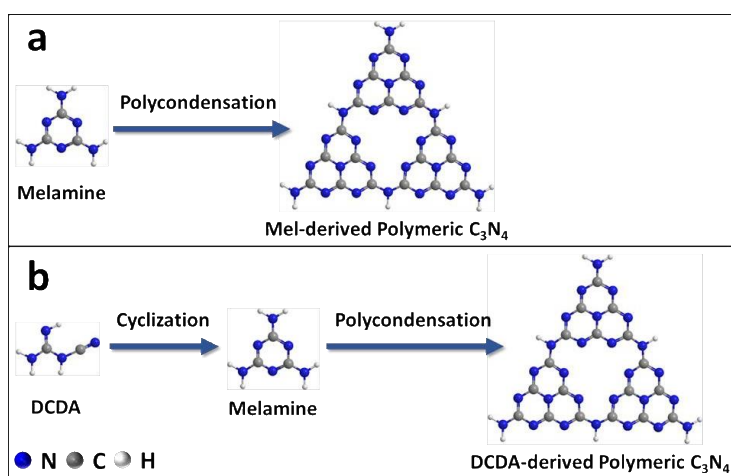
**Scheme S2.** Illustration of one-step thermal vapor deposition of CN-based film on FTO.
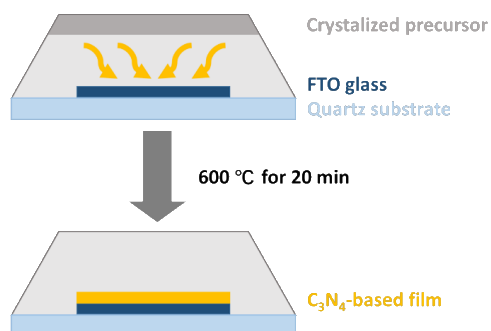
Figure S1. Cross-section SEM images of CN film with different thermal vapor deposition time. (a) 10, (b) 15, (c) 20 and (d) 25 min.
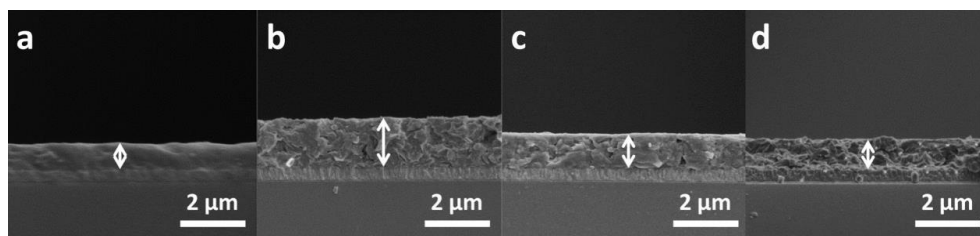
Figure S2. The influence of deposition time on the thickness of CN and its photocurrent density collected at 1.23 V vs. RHE. The photoanode with the CN film thickness of 1 μm presented the highest photocurrent density. Generally, thicker film leads to a lower PEC performance probably due to a longer charge transfer distance across the film while thinner film may result in a negative effect on the PEC performance since the light absorption becomes less efficient.
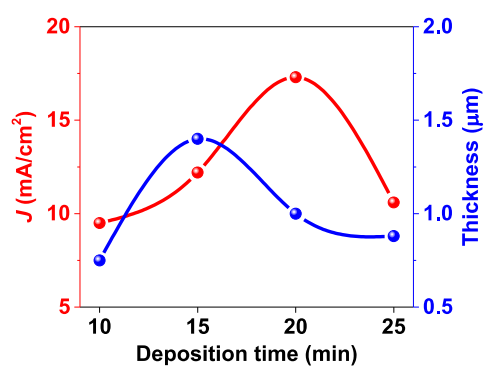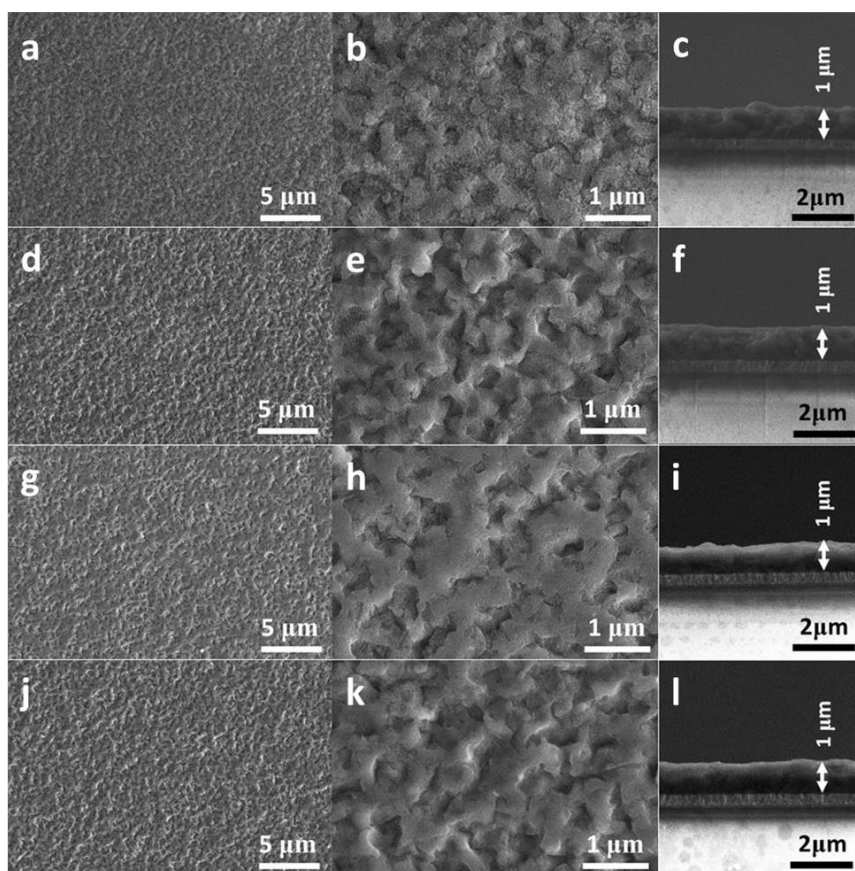
Figure S3. (a) XRD patterns and (b) FITR spectra of CN, BCN, PCN and PBCN.
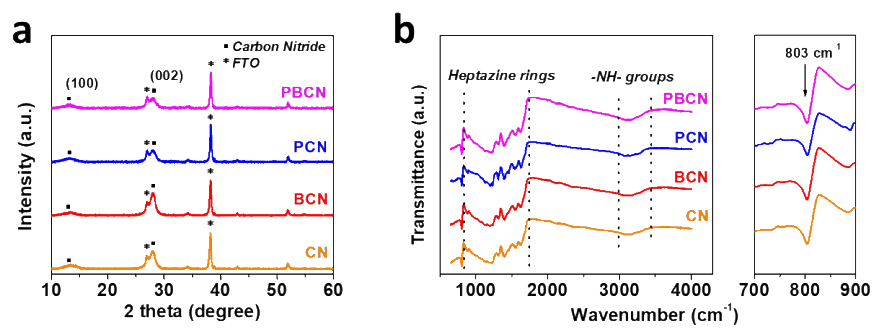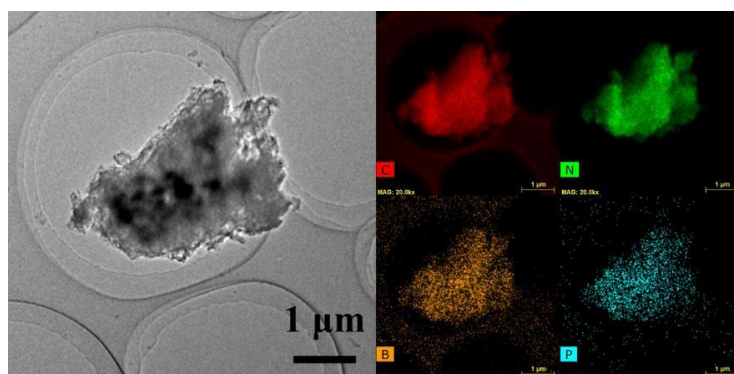
Figure S4. SEM top and cross section images of (a-c) CN, (d-f) BCN, PCN and (j-l) PBCN. The SEM top view images demonstrate that all films were uniformly deposited on the surface of the FTO substrate while the side-view images show that the thickness is around 1 μm for CN, BCN, PCN and PBCN films.

Figure S5. TEM image and elemental mapping of PBCN.

Figure S6. XPS spectra of PBCN (a) B1s at surface and 50 nm depth and (b) P2p at 200 and 300 nm depth. Due to the different polymerization routes, the elemental P and B are mainly distributed on the surface (0.87 %) and 100 nm from the surface (1.42 %), respectively, although tiny amount of B (0.11 %) and P (0.15 %) are found throughout the film.
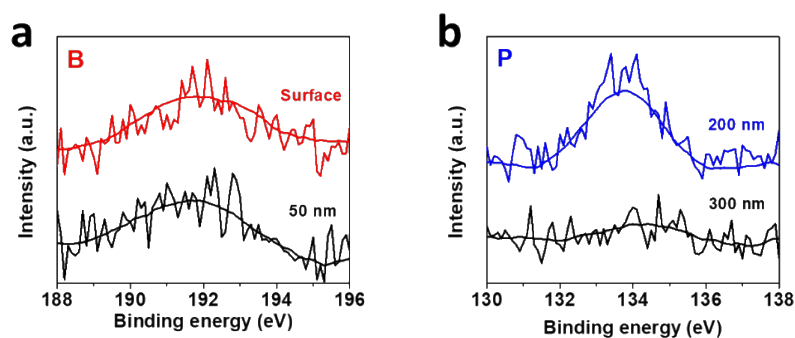
Figure S7. Solid-state NMR of ^{31}P reference $NH_4H_2PO_4$
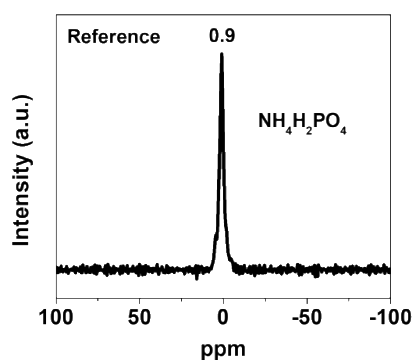
Figure S8. Photocurrent density of (a) BCN and (b) PCN with different amount (1., 3, 5 and 7 %) of boron and phosphorus dopants.
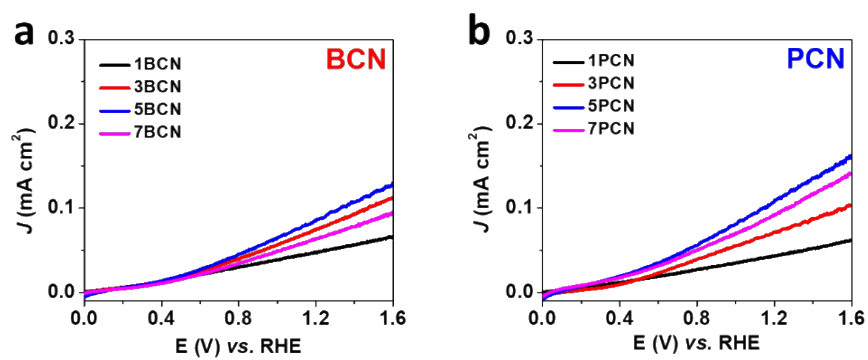
Figure S9. Absorbance and related LHE of CN, BCN, PCN and PBCN.
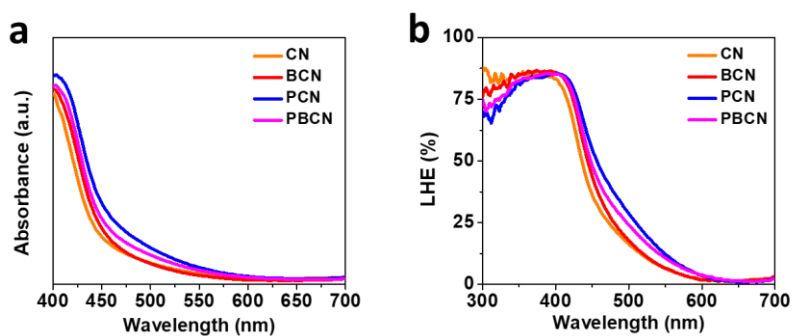
Figure S10. (a) Photocurrent density measured in 0.1 Na₂SO₄ electrolyte containing 0.1 M Na₂SO₃ as a hole scavenger and (b) J_{abs} in the photoactive range from 300 to 460 nm of CN, BCN, PCN and PBCN.
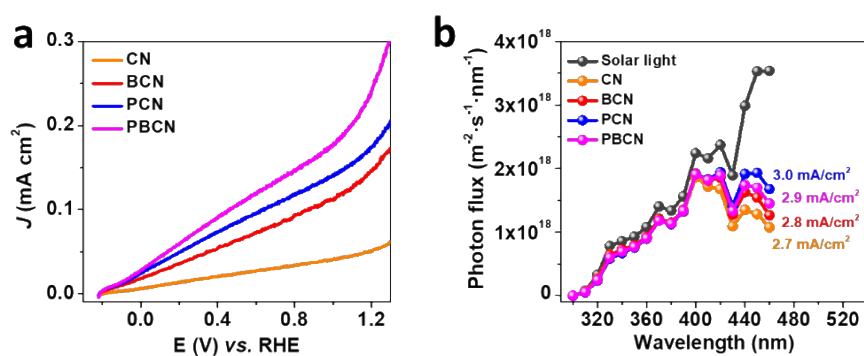
Figure S11. Valence-band XPS spectra of CN, BCN and PCN *vs.* NHE.
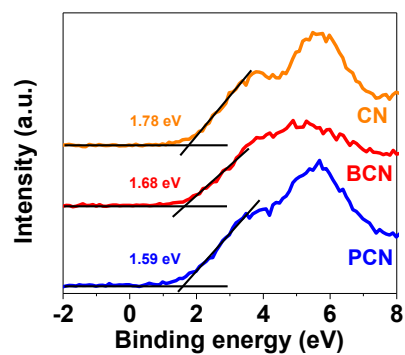
Figure S12. Tauc plots of (αhν) *vs.* hν of CN, BCN, PCN and PBCN.
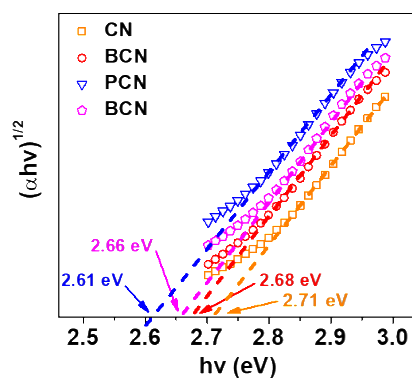
Figure S13. Absorption coefficient of CN, BCN, PCN and PBCN.

CN	2.13
BCN	2.19
PCN	2.34
PBCN	2.23
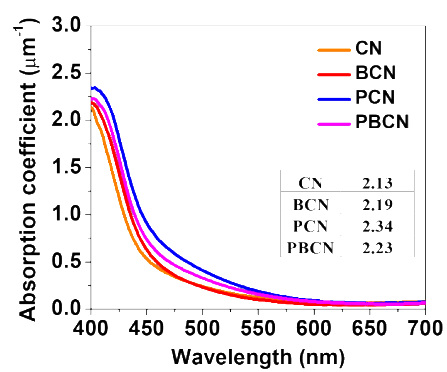
Figure S14. IPCE values of (a) CN, (b) BCN, (c) PCN and (d) PBCN measured from 400 nm illumination through FTO side (IPCE$_{back}$), film side (IPCE$_{front}$) and related ratio of IPCE$_{front}$/IPCE$_{back}$ at the applied potential of 0.63, 0.83, 1.03, 1.23 V *vs.* RHE, respectively.
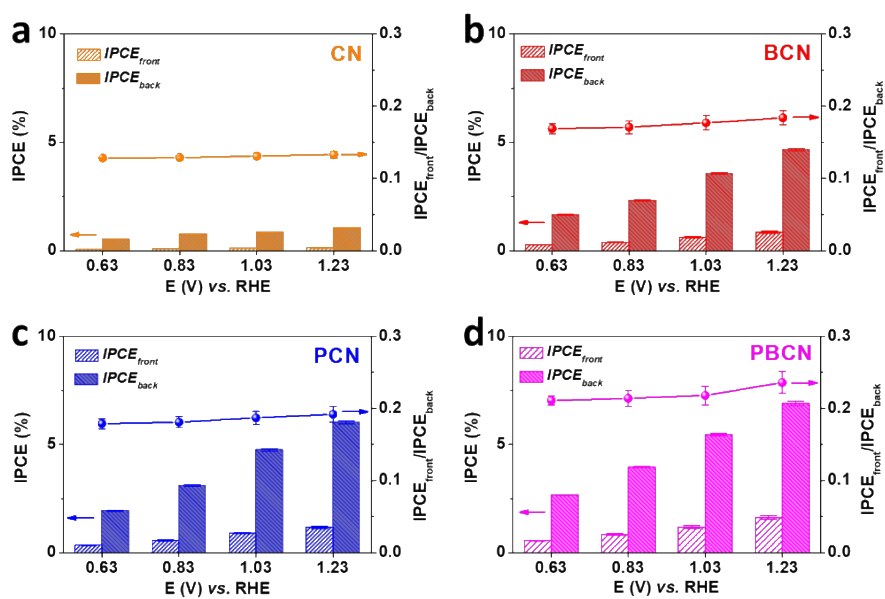
Figure S15. IMPS plots of (a) CN and (b) PBCN at 0.4, 0.8 and 1.0 V *vs.* RHE.
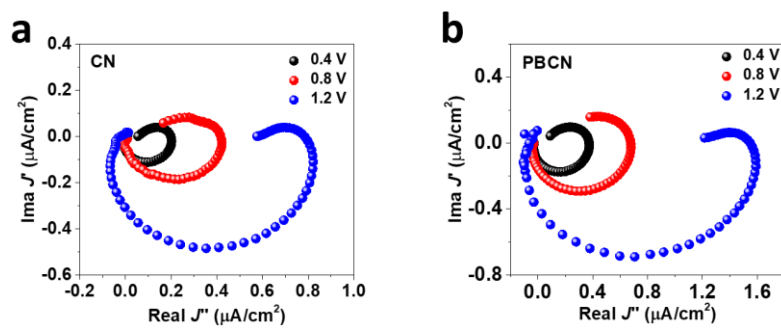
Table S1. The contents of boron and phosphorus in different depth of PBCN.

	Surface	50 nm	100 nm	200 nm	300 nm
Phosphorus (%)	0.87	0.36	0.18	0.15	0.05
Boron (%)	0.11	0.13	0.58	1.42	1.01

Table S2. Summary of PEC performance of CN-based photoanodes.

Photoanode	Photocurrent density ($\mu A/cm^2$) at 1.23 V *vs.* RHE	IPCE (%)	Ref.
C_3N_4	63	6.6 at 350 nm	[2]
C_3N_4/r-GO	75	5.3 at 400 nm	[3]
Textured C_3N_4	30.2	NA	[4]
Nickel-C_3N_4	69.8	> 2 at 400 nm	[5]
Boron-doped C_3N_4	103.2	10 at 400 nm	[6]
S-Supported C_3N_4	100	16 at 340 nm	[7]
Closely-packed C_3N_4	116	8.5 at 400 nm	[8]
Phosphorylated C_3N_4	120	8 at 460 nm	[9]
Vertically Aligned Porous C_3N_4	120.5	~ 15 at 360 nm	[10]
P/B-layer-doping C_3N_4	**150 ± 10**	**8.6 at 340 nm**	**This work**

Table S3. Conduction band (CB) and valence band (VB) edge *vs.* NHE of CN, BCN and PCN derived from the XPS valence band spectra and Tauc plots, respectively.

	CB edge (eV)	VB edge (eV)	Band gap (eV)
CN	-0.93	1.78	2.71
BCN	-0.99	1.69	2.68
PCN	-1.02	1.59	2.61

Table S4. Kinetic analysis of emission decay of CN, BCN, PCN and PBCN.

	τ_1 (ns)	τ_2 (ns)	τ_3 (ns)	τ_{ave} (ns)
CN	3.71 ± 0.08	0.69 ± 0.02	23.4 ± 0.7	16.4 ± 0.5
	41.6 %	43.6 %	14.8 %	
BCN	4.09 ± 0.08	0.68 ± 0.02	25.2 ± 0.7	19.2 ± 0.6
	42.0 %	37.7 %	20.3 %	
PCN	4.37 ± 0.09	0.73 ± 0.03	27.2 ± 0.8	21.0 ± 0.6
	45.0 %	33.1 %	21.9 %	
PBCN	4.67 ± 0.10	0.82 ± 0.04	28.5 ± 0.9	22.3 ± 0.7
	44.4 %	31.6 %	24.0 %	
	44.4 %	31.6 %	24.0 %	

Reference

[1]   a) X. Shi, L. Cai, M. Ma, X. Zheng, J. H. Park, *ChemSusChem* **2015**, *8*, 3192-3203; b) J. Halme, G. Boschloo, A. Hagfeldt, P. Lund, *J. Phys. Chem. C* **2008**, *112*, 5623-5637; c) G. V. Govindaraju, G. P. Wheeler, D. Lee, K.-S. Choi, *Chem. Mater.* **2016**, *29*, 355-370; d) K.-H. Ye, Z. Wang, J. Gu, S. Xiao, Y. Yuan, Y. Zhu, Y. Zhang, W. Mai, S. Yang, *Energy Environ. Sci.* **2017**, *10*, 772-779; e) D. Klotz, D. S. Ellis, H. Dotan, A. Rothschild, *Phys. Chem. Chem. Phys.* **2016**, *18*, 23438-23457.

[2]   X. Lv, M. Cao, W. Shi, M. Wang, Y. Shen, *Carbon* **2017**, *117*, 343-350.

[3]   G. Peng, M. Volokh, J. Tzadikov, J. Sun, M. Shalom, *Adv. Energy Mater.* **2018**, *8*, 1800566.

[4]   J. Liu, H. Wang, Z. P. Chen, H. Moehwald, S. Fiechter, R. van de Krol, L. Wen, L. Jiang, M. Antonietti, *Adv. Mater.* **2015**, *27*, 712-718.

[5]   W. Zhang, J. Albero, L. Xi, K. M. Lange, H. Garcia, X. Wang, M. Shalom, *ACS Appl. Mater. Interfaces* **2017**, *9*, 32667-32677.

[6]   Q. Ruan, W. Luo, J. Xie, Y. Wang, X. Liu, Z. Bai, C. J. Carmalt, J. Tang, *Angew. Chem. Int. Ed.* **2017**, *56*, 8221-8225.

[7]   Y. Fang, X. Li, X. Wang, *ACS Catal.* **2018**, *8*, 8774-8780.

[8]   G. Peng, J. Albero, H. Garcia, M. Shalom, *Angew. Chem. Int. Ed.* **2018**, *57*, 15807-15811.

[9]   Y. Fang, X. Li, X. Wang, *ChemSusChem* **2019**, *12*, 2605-2608.

[10]   B. Guo, L. Tian, W. Xie, A. Batool, G. Xie, Q. Xiang, S. U. Jan, R. Boddula, J. R. Gong, *Nano Lett.* **2018**, *18*, 5954-5960.

Chapter 5. Polymeric Carbon Nitride Photoanodes Decorated with Atomically Dispersed Ruthenium Cocatalysts for Efficient Solar Water Oxidation

Abstract

Solar water splitting offers a promising means for low-cost and renewable hydrogen generation. Elaborately designing photoelectrodes that favors for both bulk and surface charge behavior critically determines photoelectrochemical performance. Previous progress was mainly made to optimize metal-based semiconducting photoelectrodes and nanoscale cocatalysts, whereas comparatively little effort has been expended in metal-free polymer photoelectrodes and atomic-scale cocatalysts. Here we report a high-efficiency, low-cost and easy-processed 2D/2D photoanode of supramolecular-derived carbon nitride/reduced graphene oxide (C_3N_4/RGO) with atomically dispersed ruthenium species as cocatalysts for efficient solar water oxidation. Significantly, the conductive RGO play as effective scaffolds that obviously elongates the holes diffusion length, while the propensity of surface-reaching holes was strikingly promoted for water-oxidation chemistry by designing atomically dispersed ruthenium cocatalysts. With these efforts, a record-high photocurrent density of 1.0 mA/cm^2 at 1.23 V *vs.* RHE under AM 1.5G was achieved in an alkaline electrolyte, enabling photoelectrochemical performance of polymeric C_3N_4-based photoanodes from micro- to milli-ampere scale.

Introduction

Photoelectrochemical (PEC) water splitting offers the ability to directly convert energy from the largest renewable source, the Sun, to stored chemical energy in the form of molecular hydrogen (H_2).[1-3] Designing advanced photoelectrodes that benefits for bulk and surface charge carriers utilization is one of the most direct and effective approaches to enhance solar energy conversion efficiency.[4] In a recent decade, a class of metal-based semiconductors and nanoscale electrocatalysts are employed and investigated as photoelectrodes and cocatalysts, respectively, for solar water splitting.[5-9] By contrast, the developments of low-cost metal-free polymeric photoelectrodes and atomic-scale cocatalysts still remain a challenge, which is mainly plagued by intrinsically low conductivity and poor surface kinetics of polymer-based films.[4, 10]

Graphitic carbon nitride (C_3N_4), a tri-triazine-based conjugated polymer, is becoming a very promising material in solar energy conversion, arisen from its appealing electronic band structure, superior layered nanostructure, high physicochemical stability and earth-abundant nature.[11-12] However, compared to its photocatalysis in a suspension system,[12] the film-based PEC applications are not yet widely reported due to the aforementioned limitations as well as the difficulties in fabricating stable and uniform film.[10] These drawbacks always result in relatively low bulk and surface charge carriers utilization, and thereby making the photocurrent density at as low as a micro-ampere level.[13-15] Self-assembly supramolecular cyanuric acid-melamine (CM) complex is a promising precursor candidate for thermal polymerization to C_3N_4, which also enables a feasible process with other materials, such as conductive reduced graphene oxide (RGO) for enhancing bulk charge diffusion length.[16-17]

Besides the intrinsic optimization of charge behavior in bulk, there always exists long-standing interest in designing cocatalysts on the surface to improve reaction kinetics by potentially providing active sites, lowering the activation energies and trapping charge carriers.[18-20] In principle, higher PEC selectivity and activity can be achieved via rational molecular engineering of homogeneous

cocatalysts (*e.g.* molecular catalysts) immobilized on photoelectrodes, resulting from well-defined coordination geometry, active center and ligands.[21-22] However, it is greatly hindered by poor stability due to weak chemical bonding to photoelectrodes, and high sensitivity to pH and temperature. In comparison, heterogeneous cocatalysts (*e.g.* layered double hydroxides) can exhibit long-term stability and recyclability.[23-24] However, it should be well in consistence with photoelectrode semiconductors in terms of compatible lattice and electronic structures (Fermi levels), enabling efficient charge transfer across semiconductor-cocatalyst and cocatalyst-electrolyte interface.[8, 20] Additionally, only a limited proportion of active centers are exposed and involved in solar water splitting reaction, leading to a low atom-utilization efficiency.

Single-atom catalysts (SACs) with maximum atom-utilization efficiency and unique electronic properties exhibit a great opportunity in bridging the merits of homogeneous and heterogeneous catalysis.[25-27] Two-dimensional (2D) C_3N_4 is regarded as one of the most ideal supports to confine and coordinate the single atoms, attributed to the explicit sp^2 N atoms with lone pair electrons as donors, and tri-s-triazine structural motif with large N-coordinating cavities as binding pockets.[26, 28] These advantageous features can effectively and strongly stabilize single metal atoms those have unsaturated *d* orbits. Ruthenium (Ru)-based catalysts are extensively investigated in electrocatalytic water oxidation, which is mainly linked to its flexible redox state originated from frequent adsorption/desorption of oxygenated species.[29-31] As a result, it is given a great rationality and feasibility to fabricate an atomically dispersed Ru-based species as cocatalysts on polymeric C_3N_4 support.

Toward these goals, we employed an easy-processed blade coating method to fabricate a polymeric 2D/2D C_3N_4/RGO (GCN) photoanode with atomically dispersed ruthenium species as cocatalysts for efficient solar water oxidation. The resulting RuOP-GCN has reached a photocurrent density of as high as 1.0 mA/cm^2 at 1.23 V *vs.* RHE, which is even comparable with conventional metal-based semiconducting photoanodes. This work is notable in simultaneously demonstrating that polymeric

C3N4 can be a promising candidate for photoelectrodes, and cocatalysts can be precisely designed at atomic scale for solar water oxidation.

Results
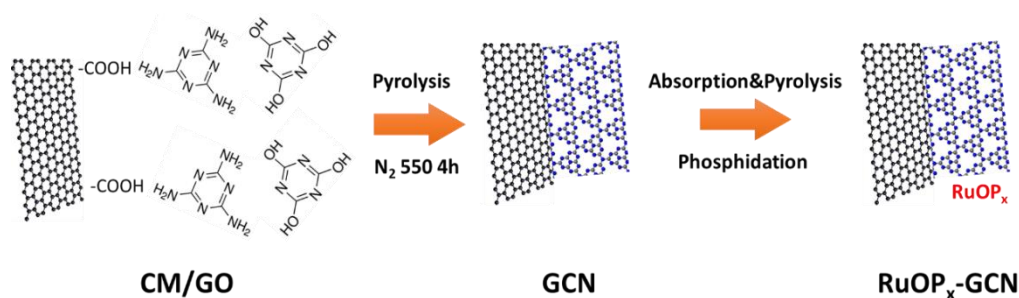
Scheme 1. Schematic illustration of the synthesis of RuOP-GCN.

Synthesis and characterization of RuOP-GCN photoanodes.

The typical fabrication procedure of RuOP-GCN photoanodes is illustrated in **Scheme 1**, including the precursor preparation and photoanode fabrication. The supramolecular cyanuric acid-melamine/graphene oxides (CM/GO) complex was first synthesized based on acid-base interaction and non-covalent hydrogen bonding.[16, 32] In detail, GO featuring abundant functional −COOH groups was first chemically bonded with melamine via acid-base interaction. Afterwards, supramolecular CM was formed on GO surface through cross connection of adjacent melamine and cyanuric acid molecule by hydrogen bonding and layered stack in a perpendicular direction to the triazines by π-π interaction.[33-34] Specifically, new peaks in X-ray diffraction patterns (XRD) for supramolecular CM crystal compared to melamine and cyanuric acid were originated from new hydrogen bonding-mediated arrangement (**Supplementary Fig. 1a**), where the in-plane pattern of CM at 10.5, 11.5, and 21.5° were indexed to (100), (110), and (200) of the in-planar packing, respectively, and a well-defined lamellar stacking peak of (002) was observed at 27.6° corresponding to a sheet-like structure.[35] Additionally, Fourier-transform infrared (FTIR) spectroscopy reveals that the C=O peak

of cyanuric acid at 1691 cm^{-1} is split into two peaks at 1657 cm^{-1} and 1731 cm^{-1}, while the vibration peak of the triazine ring in melamine is shifted from 807 cm^{-1} to 761 cm^{-1} (**Supplementary Fig. 1b**), demonstrating the establishment of supramolecular assembly.[33]
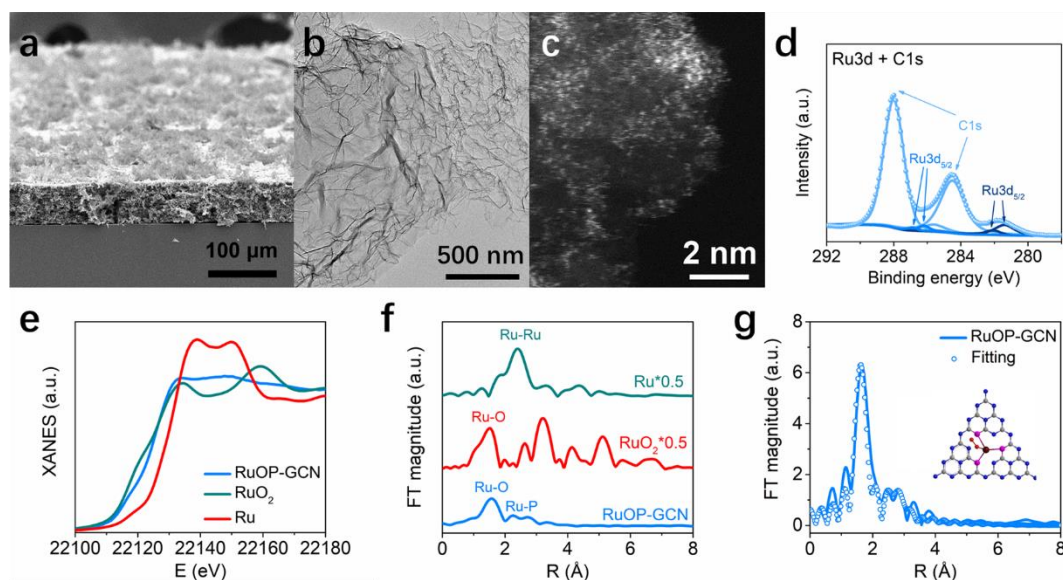
Fig. 1 Characterizations of RuOP-GCN. a, SEM image. **b**, TEM image. **c**, HAADF-STEM image. **d**, XPS spectra of Ru 3d and C 1s. **e**, Ru K-edge XANES spectra. **f**, FT-EXAFS spectra of RuOP-GCN, RuO$_2$ and Ru metal. **g**, FT-EXAFS fitting for RuOP-GCN.

The porous GCN photoanode was then obtained after the doctor blading method and thermal polymerization in nitrogen, in which the film thickness ranging from 5 ~ 75 μm could be controlled by placing different tape layers (**Supplementary Fig 2**). To introduce atomically dispersed ruthenium cocatalysts, the GCN photoanode was vertically immersed in ruthenium red (Cl$_6$H$_{42}$N$_{14}$O$_2$Ru$_3$) aqueous solution under slow stirring condition to absorb Ru-containing species via a strong electrostatic interaction.[36] Consequently, RuOP-GCN photoanode was obtained via a pyrolysis process and phosphidation treatment. The scanning electron microscopy (SEM) image of RuOP-GCN (**Fig. 1a**) gives a similar porous structure with a thickness of about 40 μm as well as the morphology of GCN (**Supplementary Fig 2h and 2i**) and CN (**Supplementary Fig 3**) films. The transmission

electron microscopy (TEM) image (**Fig. 1b**) reveals that no aggregation of Ru nanoparticles are formed on GCN surface. This is also confirmed by comparing XRD patterns (**Supplementary Fig 4a**) and FTIR spectra (**Supplementary Fig 4b**) of CN, GCN and RuOP-GCN, where only typical diffraction peaks and stretching vibrations are observed for conjugated polymeric CN. Furtherly, aberration-corrected high-angle annular dark-field scanning TEM (HAADF-STEM) image gives high-contrast and well-defined Ru atoms on GCN (**Fig. 1c**), suggesting a homogeneous atomic dispersion of Ru on GCN.

X-ray photoelectron spectroscopy (XPS) was applied to investigate oxidation state and chemical composition. As given in **Supplementary Fig 5a and 5b**, all characteristic binding energies of C 1s and N 1s are essentially identical for intrinsic conjugated framework structure of polymeric CN.[34, 37] Moreover, for RuOP-GCN, it is observed Ru-O bonding at 131.0 eV (**Supplementary Fig 5c**) and Ru-P was observed in Significantly, new peaks of RuOP-GCN at 281.4 eV in **Fig 1d** associated with Ru $3d_{5/2}$ indicates a positive Ru binding energy than metallic Ru (279.8 eV), suggesting a positive oxidation states of single Ru atoms in O and P coordination environments and no metallic Ru-Ru bonding in RuOP-GCN.[38] To further investigate the structure of Co species at the atomic level, X-ray absorption fine structure (XAFS) measurements were carried out. From **Fig. 2e**, it is given the Ru K-edge X-ray absorption near-edge structure (XANES) spectra of RuOP-GCN, RuO_2 and metallic Ru. According to the absorption edge of RuOP-GCN in **Fig. 2e**, the Ru atom valence is situated between Ru^0 and Ru^{4+}. The Fourier transforms of extended X-ray absorption fine structure (EXAFS) spectra are plotted in **Fig. 2f** to probe the local environment of Ru. The main peak at ~ 2.4 Å is associated with the Ru-Ru interaction in metallic Ru. For RuOP-GCN, the main peak at ~ 1.6 Å corresponds to the scattering interaction between Ru and O comparing with RuO_2, and an additional small peak appearing at ~ 2.2 Å can be ascribed to Ru-P bond, which is consistent with the fact that the length of metal-P bond is longer than metal-O bond. Meanwhile, the fitting curve shown in **Fig. 2g** indicates that the Ru atom is spatially coordinated by three P atoms and two O atoms in the RuOP-GCN.
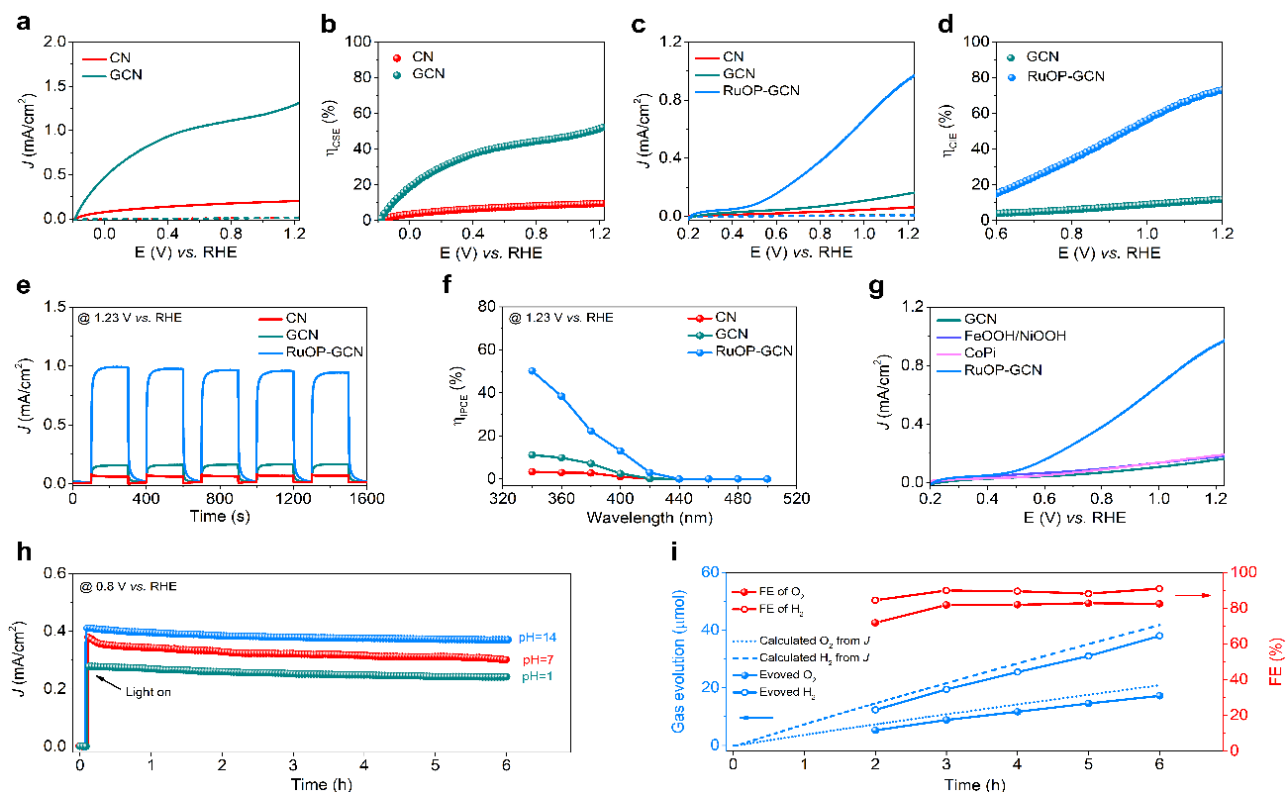
Fig. 2 PEC performance of CN, GCN, and RuOP-GCN. a, J-E curve of CN and GCN measured in the 1 M NaOH aqueous electrolyte with TEOA as hole scavenger. **b,** η_{CSE} of CN and GCN. **c,** J-E curve of CN, GCN and RuOP-GCN measured in the 1 M NaOH aqueous electrolyte. **d,** η_{CSE} of GCN and RuOP-GCN. **e,** Transient photocurrent density measured at the applied bias of 1.23 V. **f,** η_{IPCE}. **g,** J-E curve of RuOP-GCN, bulk NiOOH/FeOOH and CoPi cocatalysts on GCN. **h,** J-t curve. **i,** Faradaic efficiency and O_2/H_2 hydrogen production.

PEC performance evaluation

PEC performance was first examined in the presence of triethanolamine (TEOA) served as the hole scavenger. The oxidation process of TEOA is thermodynamically and kinetically more facile than that of water, which can enable the investigation of PEC properties of GCN independent from surface kinetics of water-oxidation chemistry. The optimized correlation between thickness of GCN films and ratio of GO/CM (mg/mmol) were given in **Supplementary Fig. 6 and 7**, showing that the best-performance GCN photoanode with the thickness of 40 μm (balanced the charge transfer distance and

light absorption) and ratio of 3 reached a photocurrent density of 1.3 mA/cm^2 at 1.23 V *vs.* RHE

(applied bias is versus reversible hydrogen electrode elsewhere unless stated). In **Fig. 2a**, it is given

a rapid increase of photocurrent density in the potential window of $-0.2 < E < 0.5$ V with an excellent

fill factor, contributing to a photocurrent density of 1.0 mA/cm^2 at an applied bias as low as around

0.5 V. Incident photon-to-current conversion efficiency (η_{IPCE}) of GCN measured in TEOA reached

a value of nearly 80 % and revealed an onset wavelength of IPCE around 430 nm (**Supplementary**

Fig. 8), which is in well accordance with the UV-Vis absorbance and bandgap Tauc plots

(**Supplementary Fig. 9**). Calculated from theoretical absorption photocurrent density (J_{abs}) based on

light harvesting efficiency (η_{LHE}) and simulated solar spectrum (**Supplementary Fig. 10**), an obvious

enhancement in charge separation efficiency (η_{CSE}) of GCN was presented over 50 % at 1.23 V

compared to that of pristine CN (**Fig. 2b**), which is essentially resulted from the improvement of

charge transport property by coupling the conductive RGOs.

However, PEC performance of CN and GCN in water oxidation is considerably lower than that in the

electrolyte with TEOA (**Fig. 2c**), indicating that the majority of surface-reaching holes were lost to

surface recombination due to poor surface catalytic nature for water-oxidation chemistry. To promote

the water oxidation kinetics, the active atomically dispersed ruthenium cocatalysts were designed and

fabricated as aforementioned. The amount of RuOP cocatalysts were optimized by controlling the

absorption of ruthenium red in aqueous solution in order to maximize the photocurrent generation

(**Supplementary Fig. 11**). It is obviously seen that, in **Fig. 2c**, the markedly enhanced PEC

performance of RuOP-GCN for water oxidation was achieved compared to that of GCN and pristine

CN, with a record photocurrent density of 1.0 mA/cm^2 at 1.23 V (a summary of CN-based photoanode

for PEC water oxidation in **Supplementary Table 1**), which is attributed to an improved surface

reaction kinetics. This significant enhancement is originated from atomically dispersed ruthenium

species rather than single component of P or Ru species (**Supplementary Fig. 12**). The surface charge

injection efficiency (η_{CIE}) of RuOP-GCN from photoanode into electrolyte was significantly

enhanced from 15 to nearly 75 % in the potential window, leading to a suppressed surface charge recombination, while GCN exhibited a constant CIE lower than 15 %. Under the applied bias of 1.23 V, transient photocurrent density of RuOP-GCN exhibited a good switching behavior under illumination and in dark (**Fig. 2e**). It is notably that no spikes were observed in the transient photocurrent curves upon illumination for RuOP-GCN, demonstrating an efficient photo-induced hole extraction at the photoanode/electrolyte interface.[39] Meanwhile, in **Fig. 2f**, IPCE of RuOP-GCN showed an impressive value of 50.1 % at 340 nm compared to GCN (11.2 %) and CN (3.4 %).

To compare the performance of atomically dispersed ruthenium cocatalysts with bulk counterparts, two typical bulk water-oxidation cocatalysts of iron-nickel oxyhydroxide (FeOOH/NiOOH) and cobalt phosphate (CoPi) were selected and electrodeposited on GCN photoanodes. In **Fig. 2g**, almost no enhanced photocurrent density was observed by introducing bulk FeOOH/NiOOH and CoPi cocatalysts. This may originate from low interfacial charge transfer between polymeric CN and bulk FeOOH/NiOOH and CoPi cocatalysts due to the incompatible lattice and electronic structures, which results in a high photoanodes/cocatalysts interfacial charge recombination.[8] The long-term operational activity and stability of RuOP-GCN was evaluated and compared in acid, neutral and alkaline electrolytes, respectively, at 0.8 V. As seen in **Fig 2h**, no obvious decays were observed in PEC measurement over 6 hours in all pH, demonstrating a high durability and pH-resistance of RuOP-GCN. Additionally, O_2 and H_2 gases were quantified in **Fig 2i**. The total amounts of O_2 and H_2 were 17.2 and 38.1 µmol after a 6-hour test, which were close to the calculated amounts from measured photocurrent density with about 90 % Faradaic efficiency.
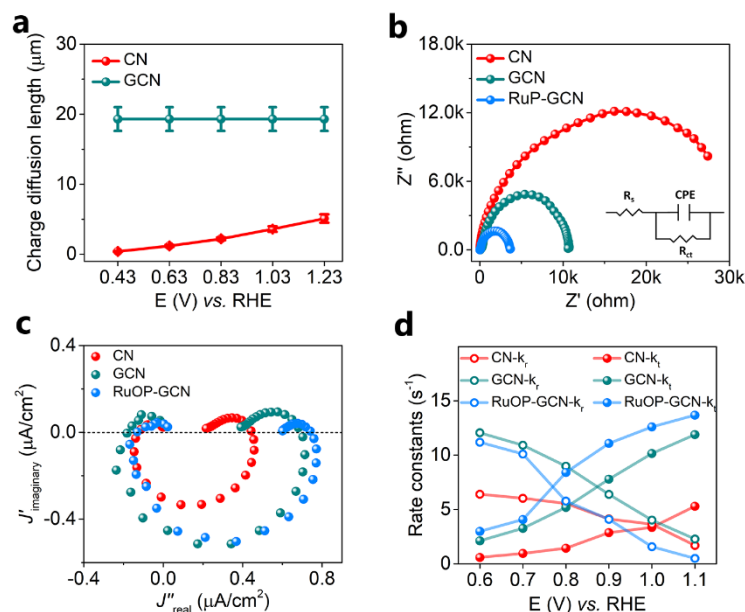
Fig. 3 Mechanistic insights into charge behavior of CN, GCN, and RuOP-GCN. a, Photoinduced charge diffusion at wavelength of 400 nm at different applied biases. **b**, EIS Nyquist plots collected at 1.23 V. **c**, IMPS plots collected at 1.23 V under excitation of 385 ± 10 nm. **d**, Rate constants k_t and k_r at different applied biases under excitation of 385 ± 10 nm.

Mechanistic insights into charge behavior

Charge diffusion length (L) can be a useful parameter for the quantitative description of competition between bulk charge carriers diffusive transport and recombination in a photoelectrode.[37, 40] Therefore, in order to quantify the enhancement in charge transport by coupling conductive RGO, L was calculated based on the comparison of IPCE values of illumination from front and back in **Supplementary Fig. 13**.[41] It is observed that L was significantly prolonged from less than 5 μm (CN) to nearly 20 μm (GCN) (**Fig. 3a**). This result clearly states that the photo-induced charge transport in bulk was remarkably promoted by coupling highly conductive reduced GOs. To estimate the surface charge transfer, the Nyquist plots of electrochemical impedance spectroscopy (EIS) were collected under illumination at 1.23 V in **Fig. 3b**. Clearly, the smallest arc radium was observed for RuOP-GCN as compared to those of GCN and CN, demonstrating a fast charge transfer and suppressed

photo-induced charge recombiantion at the interface photoanode/electrolyte via fabricating atomically dispersed ruthenium cocatalysts.

Intensity-modulated photocurrent spectroscopy (IMPS) was employed to reveal charge behavior in terms of transport in bulk and surface reaction properties. It is accepted that bulk charge transport corresponds to the high-frequency semicircle, whereas surface interfacial charge transfer is related to the low-frequency semicircle.[13, 42-43] As presented in **Fig. 3c**, the high-frequency capacitance-impedance arc (below dashed line) of both RuOP-GCN and GCN were obviously increased compared to the pristine CN, illustrating that improved bulk charge transport effectively enables more photo-induced holes flux arriving at the surface for both RuOP-GCN and GCN via the conductive RGO. More importantly, a decreased low-frequency capacitance-impedance arc (above dashed line) was observed for RuOP-GCN in comparison with GCN, which is demonstrated that atomically dispersed ruthenium cocatalysts successfully suppress surface charge recombination and facilitate surface-reaching holes transfer from photoanode to electrolyte.

Generally, kinetics of charge carriers can be represented by the first order rate constant of surface charge recombination (k_r) and interfacial charge transfer (k_t) derived from IMPS plots data (**Supplementary Fig. 14**).[37, 42] In principle, larger k_r describes a faster charge recombination on the photoanode surface. It is observed that k_r was gradually decreased with an increased applied potential as expected for an ideal photoanode/electrolyte interface in all samples (**Fig. 3d**), because the continuous applied potential drop contributes to an enhanced band bending so that photo-induced charge recombination on the surface is suppressed. Moreover, k_t is defined to describe the interfacial charge transfer between photoanode and electrolyte, that is, surface reaction of photo-induced holes with water. As seen in **Fig. 3d**, k_t of GCN was obviously larger than pristine CN in the potential window, indicating more photo-induced holes reached to the surface to oxidize water via coupling conductive RGO as scaffolds. Significantly, k_t of RuOP-GCN was apparently larger than GCN over 0.7 V, which demonstrates a faster surface reaction rate of photo-induced holes with water as a result

of fabrication of atomically dispersed ruthenium species as cocatalysts. In order to indicate the efficiency of photoanodes, the ratio of k_t/k_r values were plotted in **Supplementary Fig. 15**. In higher applied potential range, the value of k_t/k_r of RuOP-GCN became sharply increased with over five-times larger at 1.1 V, which furtherly indicates a faster interfacial charge transfer on the photoanode/electrolyte interface.

Discussion

In summary, we have fabricated atomically dispersed ruthenium cocatalysts on polymeric GCN photoanode for efficient solar water oxidation. The well-defined atomically dispersed ruthenium cocatalysts simultaneously improve the surface kinetics of water-oxidation catalysis and facilitate charge transfer from GCN to active RuOP sites, enabling a record high photocurrent density of 1.0 mA/cm^2 at 1.23 V under AM 1.5G illumination. This work opens an alternative way for developing highly efficient cocatalysts for solar water splitting.

Methods

Preparation of supramolecular CM complex. 1 mmol CA and Mel was fully dissolved in 10 mL water with stirring for 30 min at 60 °C, respectively. Then mix two homogeneous solution at the same temperature with another stirring 6 hours to assemble supramolecular CM complex. Consequently, it was collected by filtration and dried at 60 °C overnight.

Preparation of GO. GO was first synthesized from natural graphite using the method reported by Hummers *et al*. Furtherly, as-synthesized GO is treated using Li's *et al* method to increase its quality and dispersion.[44]

Preparation of CN photoanode. 100 mg supramolecular CM powder was first blended thoroughly in 100 μL ethylene glycol to form a homogeneous paste. Then the CM paste was cast onto fluorine-doped tin oxide (FTO) via a blade coating method, followed by dried on a hotplate. Afterwards, the film was put into an enclosed quartz tube purged with N$_2$ for 30 min. Finally, thermal polymerization

was carried out at 550 °C for 4 h under N_2 atmosphere with an increasing rate of 5 °C/min to obtain the pristine CN photoanode. The obtained film was rinsed with water and dried under N_2 flow.

Preparation of GCN photoanode. Different amounts of GO (1 mg, 2 mg, 3 mg and 4 mg) were dispersed in 10 mL water with ultrasonication for 2 h. Afterwards, 1 mmol melamine was added into GO solution and kept stirring for 10 h at 60 °C to be fully dissolved. Subsequently, 10 mL aqueous solution containing homogeneously dispersed 1 mmol cyanuric acid was dropped into this solution and kept moderate stirring for 6 h at 60 °C to form composite of CM/GO, and then collected by filtration and dried at 60 °C overnight. The CM/GO paste was made using the same method as CM. After the thermal polymerization process, the CM/GO was converted into GCN. The obtained film was rinsed with water and dried under N_2 flow. Different layers of tapes are applied to change the thickness of GCN photoanodes. The obtained film was rinsed with water and dried under N_2 flow.

Preparation of RuOP-GCN photoanode. GCN film was vertically immersed in 1.0 mg/mL ruthenium red aqueous solution for 0.5, 1, 2, and 4 h respectively, to absorb the Ru species on the surface of GCN via strong electrostatic interaction. Then, thermal treatment was carried out at 400 °C for 2 h in argon (Ar) atmosphere with an increase of 2 °C/min (Ru-GCN). Afterwards, sodium hypophosphite (NaH_2PO_2) was used as the P source for phosphidation treatment. Typically, 20 mg NaH_2PO_2 and Ru-GCN film were placed in a small porcelain boat. Finally, thermal treatment was carried out at 350 °C for 2 h in Ar atmosphere with an increase of 5 °C/min. Upon phosphidation treatment, Ru-GCN was supposed to convert into $RuOP_x$-GCN. The obtained film was rinsed with water and dried under N_2 flow.

Preparation of Ru-GCN photoanode.

GCN film was vertically immersed in 1.0 mg/mL ruthenium red aqueous solution for 2 h to absorb the Ru species on the surface of GCN via strong electrostatic interaction. Then, thermal treatment was carried out at 400 °C for 2 h in Ar atmosphere with an increase of 2 °C/min. The obtained film was rinsed with water and dried under N_2 flow.

Preparation of P-GCN photoanode.

20 mg NaH_2PO_2 and GCN film were placed in a small porcelain boat. Thermal treatment was carried out at 350 °C for 2 h in Ar atmosphere with an increase of 5 °C/min. The obtained film was rinsed with water and dried under N_2 flow.

Characterization. X-ray Diffraction (XRD) data were collected with a Bruker D8 Eco powder diffractometer (Cu K_α radiation, $\lambda = 0.15406$ nm). The Fourier-transform infrared spectroscopy (FTIR) spectra of the samples were collected with a Cary 630 FTIR spectrometer (Agilent Technologies). X-ray photoelectron spectroscopy (XPS) was performed with a Kratos-AXIS ULTRA DLD apparatus using Al X-ray source. Scanning electron microscopic (SEM) images were obtained with a FEI Magellan 400 XHR FEGSEM Instrument. High-angle annular dark-field scanning transmission electron microscopic (HAADF-STEM) images and energy-dispersive X-ray spectra were acquired with a FEI Tecnai G2 F20 S-TWIN FEGTEM instrument operated at 200 kV. The photoluminescent and fluorescence decay spectra were carried out on the FLUOROMAX-4C-TCSPC.

Optical properties. The UV-Vis absorption spectra were measured using UV-Vis spectrophotometer (PG, UH-4150) at room temperature. For the calculation of light harvesting efficiency (η_{LHE}):

$$\eta_{LHE} = 1 - 10^{-A_\lambda}$$

Where A_λ is the absorbance at a given wavelength. For the calculation of light absorption coefficient (α):

$$\alpha = \frac{-ln(10^{-A})}{d}$$

Where d is thickness of the photoanode film (μm).

PEC and electrochemical tests. PEC and electrochemical tests were both conducted at 25 ± 2 °C using a CHI-760E electrochemical workstation in a three-electrode PEC cell with photoanode (0.12 cm²) working, Ag/AgCl (4M KCl) reference, and Pt wire counter electrodes. A 1 M NaOH solution (pH = 13.6) was used as the electrolyte and purged with N_2 for 30 min to remove O_2 before every test. The recorded potentials *vs.* Ag/AgCl were converted to reversible hydrogen electrode (RHE) using the Nernstian equation below:

$$E_{RHE} = E_{Ag/AgCl} + 0.059 \times \text{pH} + 0.197$$

During the PEC measurements, the simulated solar light, generated from a 300 W Xeon lamp (Microsolar300 Beijing Perfectlight Technology Co. Ltd.) with an AM 1.5G filter, passed through the insulating side of the FTO substrate (back-side illumination). The power density of the incident light was calibrated to 100 mW/cm² (one-sun illumination) at the surface of the FTO substrate using a light meter (PECSI01 Bunkoukeiki). Photocurrent density measurement was collected at a scan rate of 50 mV/s. Incident photon-to-electron conversion efficiency (IPCE) was measured at an applied bias of 1.23 V combined with simulated solar light pass through mono-wavelength filter (Newport 10BPF10 Bandpass Filter) from 600 nm to 340 nm at an interval of 20 nm:

$$\eta_{IPCE} = \frac{J_\lambda \times 1240}{\lambda \times P_\lambda}$$

Where J_λ (mA·cm⁻²) is the photocurrent density measured under monochromatic illumination at λ, P_λ (mW·cm⁻²) is the power intensity of the incident monochromatic light at wavelength λ.

J_{max} is the calculation of maximum photocurrent density under AM 1.5G irradiation. Briefly, the standard solar spectral irradiance (ASTMG-173-03) is converted to the solar energy spectrum in terms of number of photons (s⁻¹·m⁻²·nm⁻¹) *vs.* λ (nm), then the number of photons in the photo-active range

between λ_1 (nm) and λ_2 (nm) is selected to calculate its maximum photocurrent density. In this work, $\lambda_1 = 300$ nm and $\lambda_2 = 460$ nm were selected as the photo-active range according to the IPCE results:

$$J_{max} = e \times \int_{\lambda_2}^{\lambda_1} \frac{P_\lambda \times \lambda}{h \times c}$$

Where e is the charge of one electron (1.6×10^{-19} C), h is Planck's constant (6.63×10^{-34} J·s) and c is the speed of light (3×10^8 m/s). For the calculation of absorption photocurrent density (J_{abs}):

$$J_{abs} = J_{max} \times \eta_{LHE}$$

Where J_{abs} (mA/cm^2) is the photocurrent density converted from photon absorption rate assuming 100% absorbed photon-to-current conversion efficiency (η_{APCE}). For the calculation of charge separation efficiency (η_{CSE}):

$$\eta_{CSE} = \frac{J_{scavenger}}{J_{abs}}$$

Where $J_{scavenger}$ is the measured photocurrent density in a 1 M NaOH with TEOA as the hole scavenger. For the calculation of charge injection efficiency (η_{CIE}), photocurrent density was measured in 1 M NaOH aqueous electrolyte containing TEOA as the hole scavenger with volume ratio of 1:10.

$$\eta_{CIE} = \frac{J}{J_{scavenger}}$$

Where $J_{scavenger}$ and J are the measured photocurrent density in a 1 M NaOH with and without TEOA.

Electrochemical impedance spectroscopy (EIS) was carried out under illumination at an applied bias of 1.23 V in a frequency range of 10^{-1}-10^5 Hz with an AC voltage amplitude of 10 mV. Intensity modulated photocurrent spectroscopy (IMPS) was recorded with a Zahner Zehniumm potentiostat equipped with a frequency response analyzer module and a monochromated LED light source of 385 ± 10 nm. The cell was connected in a three-electrode configuration and the IMPS spectra was collected at 1.23 V. The DC bias illumination was adjusted to be 50 mW/cm^2, and the light AC sinusoidal perturbation was set to 15.5% of the DC light intensity (± 13 W/m^2), the frequency range was recorded from 10^5 to 10^{-1} Hz. For the calculation of first order constant rate of charge transfer (k_t) and charge recombination (k_r):

$$\frac{k_t}{k_t + k_r} = \frac{LHI}{HFI}$$

$$\omega_{max} = k_t + k_r$$

Where LFI is the low frequency intercept with the real axis, HFI is the high frequency intercept with the real axis, and ω_{max} is extracted from Ima $J'(\omega)$ in the IMPS spectrum.

The hole diffusion length (L) was evaluated based on the results of IPCE values from front and back illumination at different applied bias:

$$\frac{IPCE_{front}(\lambda, d)}{IPCE_{back}(\lambda, d)} = \frac{\sinh\left(\frac{d}{L}\right) + L\alpha(\lambda)\cosh\left(\frac{d}{L}\right) - L\alpha(\lambda)e^{\alpha(\lambda)d}}{\sinh\left(\frac{d}{L}\right) - L\alpha(\lambda)\cosh\left(\frac{d}{L}\right) + L\alpha(\lambda)e^{-\alpha(\lambda)d}} \times e^{-\alpha(\lambda)d}$$

Where d is thickness of the photoanode film (μm), IPCE$_{front}$ and IPCE$_{back}$ are measured at 400 nm at 0.63, 0.83, 1.03, 1.23 V *vs.* RHE respectively.

Product analysis. The H_2 gas was detected using a gas chromatograph-mass spectrometer (Shimazu, GCMS-QP2010 Ultra) equipped with a ShinCarbon ST packed column (Restek) and a secondary electron detector. He (99.9997%) was used as the carrier gas. The amount of H_2 and O_2 evolution was determined by sampling 100 μl of gas from the headspace of the CE compartment using a gas-tight syringe every 1 h. The Faradaic efficiency was calculated by dividing the amount of gas detected by the theoretical amount of gas calculated on the basis of the total charge passed, using the following equation:

$$\eta_{FE} = \frac{A \times n_{gas} \times F}{C} \times 100\%$$

Where F is the Faraday constant (96485.33 C/mol), n_{gas} is the amount of O_2 or H_2 (mol), A is the number of electrons transfer to produce one O_2 or H_2 molecule, and C is the total charge passed through photoanode.

Reference

(1).   Walter, M. G.; Warren, E. L.; McKone, J. R.; Boettcher, S. W.; Mi, Q.; Santori, E. A.; Lewis, N. S., Solar water splitting cells. *Chem. Rev.* **2010,** *110*, 6446-6473.

(2).   Grätzel, M., Photoelectrochemical Cells. *Nature* **2001,** *414*, 338-344.

(3).   Kim, J. H.; Hansora, D.; Sharma, P.; Jang, J. W.; Lee, J. S., Toward practical solar hydrogen production - an artificial photosynthetic leaf-to-farm challenge. *Chem. Soc. Rev.* **2019,** *48*, 1908-1971.

(4).   Sivula, K.; van de Krol, R., Semiconducting materials for photoelectrochemical energy conversion. *Nat. Rev. Mater.* **2016,** *1*, 15010-15026.

(5).   Luan, P.; Zhang, J., Stepping towards Solar Water Splitting: Recent Progress in Bismuth Vanadate Photoanodes. *ChemElectroChem* **2019,** *6*, 3227-3243.

(6).   Yao, T.; An, X.; Han, H.; Chen, J. Q.; Li, C., Photoelectrocatalytic Materials for Solar Water Splitting. *Adv. Energy Mater.* **2018,** *8*, 1800210.

(7). Seo, J.; Nishiyama, H.; Yamada, T.; Domen, K., Visible-Light-Responsive Photoanodes for Highly Active, Stable Water Oxidation. *Angew. Chem. Int. Ed.* **2018,** *57*, 8396-8415.

(8). Yang, J.; Wang, D.; Han, H.; Li, C., Roles of cocatalysts in photocatalysis and photoelectrocatalysis. *Acc. Chem. Res.* **2013,** *46*, 1900-1909.

(9). Laskowski, F. A. L.; Nellist, M. R.; Qiu, J.; Boettcher, S. W., Metal Oxide/(oxy)hydroxide Overlayers as Hole Collectors and Oxygen-Evolution Catalysts on Water-Splitting Photoanodes. *J. Am. Chem. Soc.* **2019,** *141*, 1394-1405.

(10). Volokh, M.; Peng, G.; Barrio, J.; Shalom, M., Carbon Nitride Materials for Water Splitting Photoelectrochemical Cells. *Angew. Chem. Int. Ed.* **2019,** *58*, 6138-6151.

(11). Wang, X.; Maeda, K.; Thomas, A.; Takanabe, K.; Xin, G.; Carlsson, J. M.; Domen, K.; Antonietti, M., A metal-free polymeric photocatalyst for hydrogen production from water under visible light. *Nat. Mater.* **2009,** *8*, 76-80.

(12). Ong, W. J.; Tan, L. L.; Ng, Y. H.; Yong, S. T.; Chai, S. P., Graphitic Carbon Nitride (g-C3N4)-Based Photocatalysts for Artificial Photosynthesis and Environmental Remediation: Are We a Step Closer To Achieving Sustainability? *Chem. Rev.* **2016,** *116*, 7159-7329.

(13). Ruan, Q.; Luo, W.; Xie, J.; Wang, Y.; Liu, X.; Bai, Z.; Carmalt, C. J.; Tang, J., A Nanojunction Polymer Photoelectrode for Efficient Charge Transport and Separation. *Angew. Chem. Int. Ed.* **2017,** *56*, 8221-8225.

(14). Peng, G.; Albero, J.; Garcia, H.; Shalom, M., A Water-Splitting Carbon Nitride Photoelectrochemical Cell with Efficient Charge Separation and Remarkably Low Onset Potential. *Angew. Chem. Int. Ed.* **2018,** *57*, 15807-15811.

(15). Karjule, N.; Barrio, J.; Xing, L.; Volokh, M.; Shalom, M., Highly Efficient Polymeric Carbon Nitride Photoanode with Excellent Electron Diffusion Length and Hole Extraction Properties. *Nano Lett.* **2020,** *20*, 4618-4624.

(16).   Prior, T. J.; Armstrong, J. A.; Benoit, D. M.; Marshall, K. L., The structure of the melamine–cyanuric acid co-crystal. *CrystEngComm* **2013,** *15*, 5838-5843.

(17).   Peng, G.; Volokh, M.; Tzadikov, J.; Sun, J.; Shalom, M., Carbon Nitride/Reduced Graphene Oxide Film with Enhanced Electron Diffusion Length: An Efficient Photo-Electrochemical Cell for Hydrogen Generation. *Adv. Energy Mater.* **2018,** *8*, 1800566.

(18).   Zhang, P.; Wang, T.; Gong, J., Current Mechanistic Understanding of Surface Reactions over Water-Splitting Photocatalysts. *Chem* **2018,** *4*, 223-245.

(19).   Kuang, Y.; Yamada, T.; Domen, K., Surface and Interface Engineering for Photoelectrochemical Water Oxidation. *Joule* **2017,** *1*, 290-305.

(20).   Nellist, M. R.; Laskowski, F. A.; Lin, F.; Mills, T. J.; Boettcher, S. W., Semiconductor-Electrocatalyst Interfaces: Theory, Experiment, and Applications in Photoelectrochemical Water Splitting. *Acc. Chem. Res.* **2016,** *49*, 733-40.

(21).   Matheu, R.; Moreno-Hernandez, I. A.; Sala, X.; Gray, H. B.; Brunschwig, B. S.; Llobet, A.; Lewis, N. S., Photoelectrochemical Behavior of a Molecular Ru-Based Water-Oxidation Catalyst Bound to TiO2-Protected Si Photoanodes. *J. Am. Chem. Soc.* **2017,** *139*, 11345-11348.

(22).   Creissen, C. E.; Warnan, J.; Antón-García, D.; Farré, Y.; Odobel, F.; Reisner, E., Inverse Opal CuCrO2 Photocathodes for H2 Production Using Organic Dyes and a Molecular Ni Catalyst. *ACS Catal.* **2019,** *9*, 9530-9538.

(23).   Kim, T. W.; Choi, K.-S., Nanoporous BiVO4 photoanodes with dual-layer oxygen evolution catalysts for solar water splitting. *Science* **2014,** *343*, 990-994.

(24).   Kuang, Y.; Jia, Q.; Ma, G.; Hisatomi, T.; Minegishi, T.; Nishiyama, H.; Nakabayashi, M.; Shibata, N.; Yamada, T.; Kudo, A.; Domen, K., Ultrastable low-bias water splitting photoanodes via photocorrosion inhibition and in situ catalyst regeneration. *Nat. Energy* **2016,** *2*, 16191-16200.

(25).   Cui, X.; Li, W.; Ryabchuk, P.; Junge, K.; Beller, M., Bridging homogeneous and heterogeneous catalysis by heterogeneous single-metal-site catalysts. *Nat. Catal.* **2018,** *1*, 385-397.

(26).   Wang, A.; Li, J.; Zhang, T., Heterogeneous single-atom catalysis. *Nat. Rev. Chem.* **2018,** *2*, 65-81.

(27).   Chen, Y.; Ji, S.; Chen, C.; Peng, Q.; Wang, D.; Li, Y., Single-Atom Catalysts: Synthetic Strategies and Electrochemical Applications. *Joule* **2018,** *2*, 1242-1264.

(28).   Chen, Z.; Mitchell, S.; Vorobyeva, E.; Leary, R. K.; Hauert, R.; Furnival, T.; Ramasse, Q. M.; Thomas, J. M.; Midgley, P. A.; Dontsova, D.; Antonietti, M.; Pogodin, S.; López, N.; Pérez-Ramírez, J., Stabilization of Single Metal Atoms on Graphitic Carbon Nitride. *Adv. Funct. Mater.* **2017,** *27*, 1605785.

(29).   Stoerzinger, K. A.; Rao, R. R.; Wang, X. R.; Hong, W. T.; Rouleau, C. M.; Shao-Horn, Y., The Role of Ru Redox in pH-Dependent Oxygen Evolution on Rutile Ruthenium Dioxide Surfaces. *Chem* **2017,** *2*, 668-675.

(30).   Yao, Y.; Hu, S.; Chen, W.; Huang, Z.-Q.; Wei, W.; Yao, T.; Liu, R.; Zang, K.; Wang, X.; Wu, G.; Yuan, W.; Yuan, T.; Zhu, B.; Liu, W.; Li, Z.; He, D.; Xue, Z.; Wang, Y.; Zheng, X.; Dong, J.; Chang, C.-R.; Chen, Y.; Hong, X.; Luo, J.; Wei, S.; Li, W.-X.; Strasser, P.; Wu, Y.; Li, Y., Engineering the electronic structure of single atom Ru sites via compressive strain boosts acidic water oxidation electrocatalysis. *Nat. Catal.* **2019,** *2*, 304-313.

(31).   Mao, J.; He, C. T.; Pei, J.; Chen, W.; He, D.; He, Y.; Zhuang, Z.; Chen, C.; Peng, Q.; Wang, D.; Li, Y., Accelerating water dissociation kinetics by isolating cobalt atoms into ruthenium lattice. *Nat. Commun.* **2018,** *9*, 4958-4965.

(32).   Ma, T. Y.; Ran, J.; Dai, S.; Jaroniec, M.; Qiao, S. Z., Phosphorus-doped graphitic carbon nitrides grown in situ on carbon-fiber paper: flexible and reversible oxygen electrodes. *Angew. Chem. Int. Ed.* **2015,** *54*, 4646-4650.

(33).   Shalom, M.; Inal, S.; Fettkenhauer, C.; Neher, D.; Antonietti, M., Improving carbon nitride photocatalysis by supramolecular preorganization of monomers. *J. Am. Chem. Soc.* **2013,** *135*, 7118-7121.

(34).   Guo, S.; Deng, Z.; Li, M.; Jiang, B.; Tian, C.; Pan, Q.; Fu, H., Phosphorus-Doped Carbon Nitride Tubes with a Layered Micro-nanostructure for Enhanced Visible-Light Photocatalytic Hydrogen Evolution. *Angew. Chem. Int. Ed.* **2016,** *55*, 1830-4.

(35).   Xiao, Y.; Tian, G.; Li, W.; Xie, Y.; Jiang, B.; Tian, C.; Zhao, D.; Fu, H., Molecule Self-Assembly Synthesis of Porous Few-Layer Carbon Nitride for Highly Efficient Photoredox Catalysis. *J. Am. Chem. Soc.* **2019,** *141*, 2508-2515.

(36).   Luan, P.; Zhang, Y.; Zhang, X.; Li, Z.; Prathapan, R.; Bach, U.; Zhang, J., Bismuth Vanadate with Electrostatically Anchored 3D Carbon Nitride Nano-networks as Efficient Photoanodes for Water Oxidation. *ChemSusChem* **2018,** *11*, 2510-2516.

(37).   Luan, P.; Meng, Q.; Wu, J.; Li, Q.; Zhang, X.; Zhang, Y.; O'Dell, L. A.; Raga, S. R.; Pringle, J.; Griffith, J. C.; Sun, C.; Bach, U.; Zhang, J., Unique Layer-Doping-Induced Regulation of Charge Behavior in Metal-Free Carbon Nitride Photoanodes for Enhanced Performance. *ChemSusChem* **2020,** *13*, 328-333.

(38).   Balcerzak, J.; Redzynia, W.; Tyczkowski, J., In-situ XPS analysis of oxidized and reduced plasma deposited ruthenium-based thin catalytic films. *Appl. Surf. Sci.* **2017,** *426*, 852-855.

(39).   Zhong, D. K.; Cornuz, M.; Sivula, K.; Grätzel, M.; Gamelin, D. R., Photo-assisted electrodeposition of cobalt–phosphate (Co–Pi) catalyst on hematite photoanodes for solar water oxidation. *Energy Environ. Sci.* **2011,** *4*, 1759-1764.

(40).   Noda, Y.; Merschjann, C.; Tarabek, J.; Amsalem, P.; Koch, N.; Bojdys, M. J., Directional Charge Transport in Layered Two-Dimensional Triazine-Based Graphitic Carbon Nitride. *Angew. Chem. Int. Ed.* **2019,** *58*.

(41).   Leng, W. H.; Barnes, P. R. F.; Juozapavicius, M.; O'Regan, B. C.; Durrant, J. R., Electron Diffusion Length in Mesoporous Nanocrystalline TiO2 Photoelectrodes during Water Oxidation. *J. Phys. Chem. Lett.* **2010,** *1*, 967-972.

(42).   Thorne, J. E.; Jang, J. W.; Liu, E. Y.; Wang, D., Understanding the origin of photoelectrode performance enhancement by probing surface kinetics. *Chem. Sci.* **2016,** *7*, 3347-3354.

(43).   Klotz, D.; Ellis, D. S.; Dotan, H.; Rothschild, A., Empirical in operando analysis of the charge carrier dynamics in hematite photoanodes by PEIS, IMPS and IMVS. *Phys. Chem. Chem. Phys.* **2016,** *18*, 23438-23457.

(44).   Li, D.; Muller, M. B.; Gilje, S.; Kaner, R. B.; Wallace, G. G., Processable aqueous dispersions of graphene nanosheets. *Nat. Nanotechnol.* **2008,** *3*, 101-105.

Supporting Information
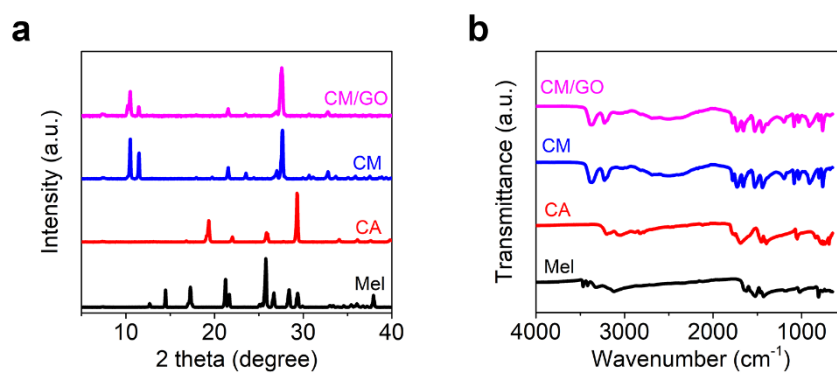
Supplementary Figure 1. (a) XRD patterns and (b) FTIR spectra of melamine (Mel), cyanuric acid (CA), supramolecular cyanuric acid-melamine (CM) and cyanuric acid-melamine/graphene oxide (CM/GO).
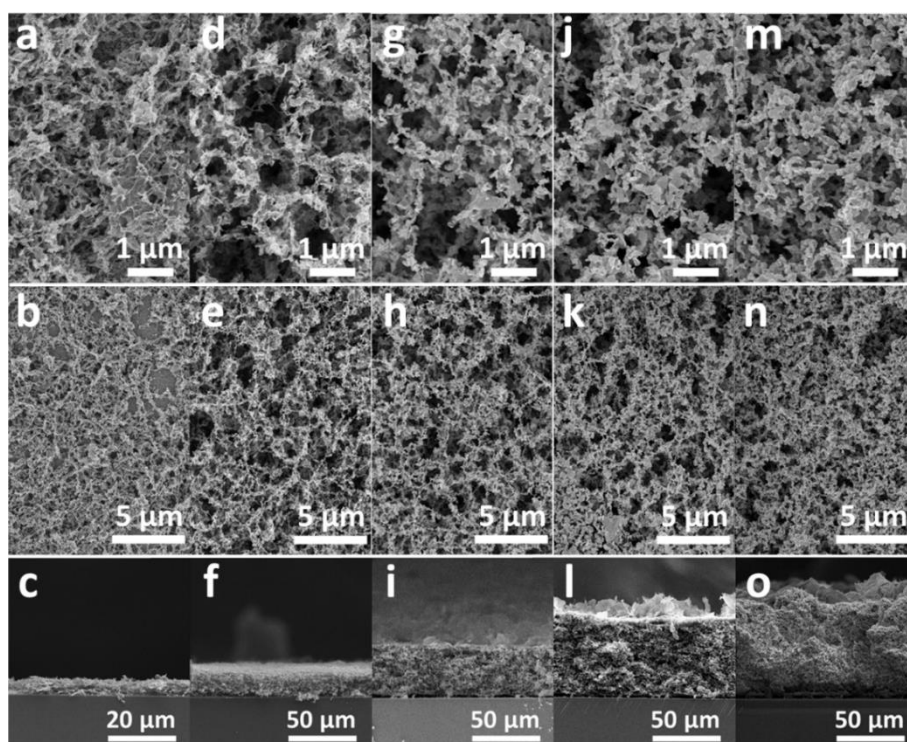
Supplementary Figure 2. SEM images of GCN photoanodes from top and side view using different Scotch tape layers blade with (a-c) one layer, (d-f) two layers, (g-i) three layers, (j-l) four layers, and (m-o) five layers.
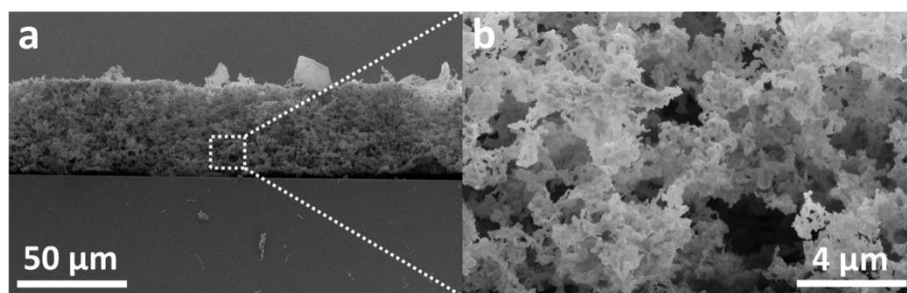
Supplementary Figure 3. SEM images of CN photoanode from side view using Scotch tape with three layers.
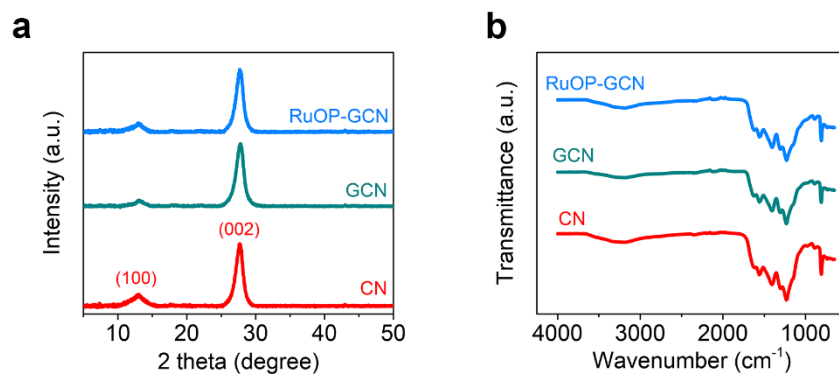
Supplementary Figure 4. (a) XRD patterns and (b) FTIR spectra of CN, GCN and RuOP-GCN.

Typically, the two diffraction peaks at 27.7 and 13.0 indexed for (002) and (100) in the XRD spectrum correspond, respectively, to interlayer stacking of conjugated aromatic rings and repeated in-plane heptazine motifs in CN. The serial stretching vibrations of 850 to 1730 cm^{-1} and 3000 to 3400 cm^{-1} in the FTIR spectrum represent the repeating units of heptazine ring and −NH$_2$ groups, respectively.
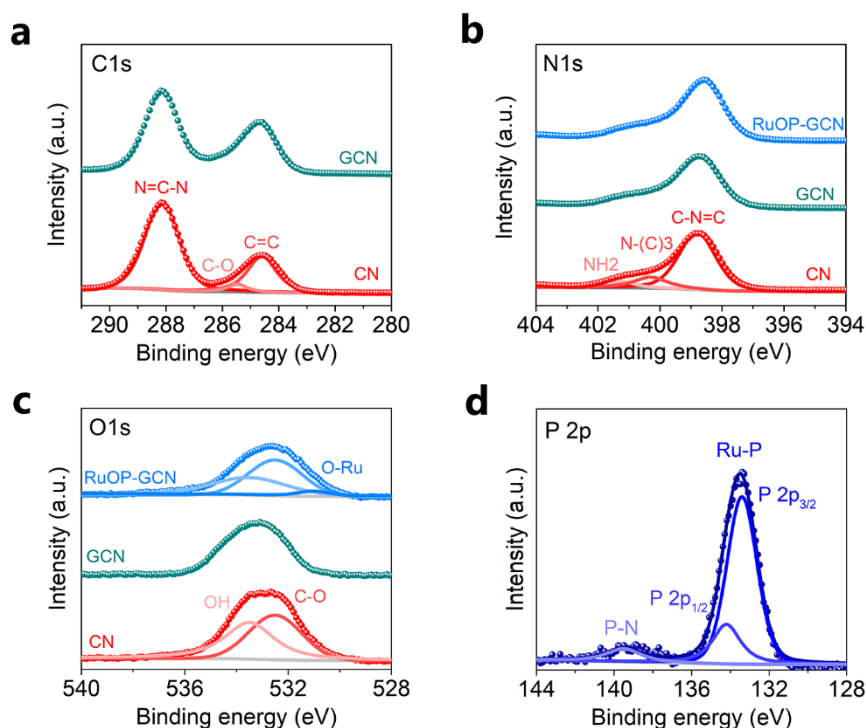
Supplementary Figure 5. XPS spectra of (a) C 1s, (b) N 1s, (c) O 1s of CN, GCN and RuOP-GCN, and (d) P 2p of RuOP-GCN.

XPS C 1s spectra associated with C=C, C−O, and N−C=N are essentially identical for polymeric CN, while in N 1s spectra, the main peak at 398.2 eV and two smaller ones at higher energies of 400.1 and 401.0 eV are characteristically corresponded to C−N=C, N−(C)$_3$ and −NH$_2$ groups, respectively. Because there is a very strong overlap between the Ru 3d and C 1s regions, C 1s of RuOP-GCN is not presented here.

In O 1s spectra, two typical peaks at 532.5 and 533.5 eV are associated with C-O and O-H bonds for all the samples. Significantly, the Ru-O bonding was observed in RuOP-GCN, which demonstrate the center Ru atoms are coordinated with O atoms. Furtherly, in P 2p spectra, the 133.4 eV peak can be attributed to Ru-P bonds, while the 139.5 eV peak is characteristic of P-N coordination.
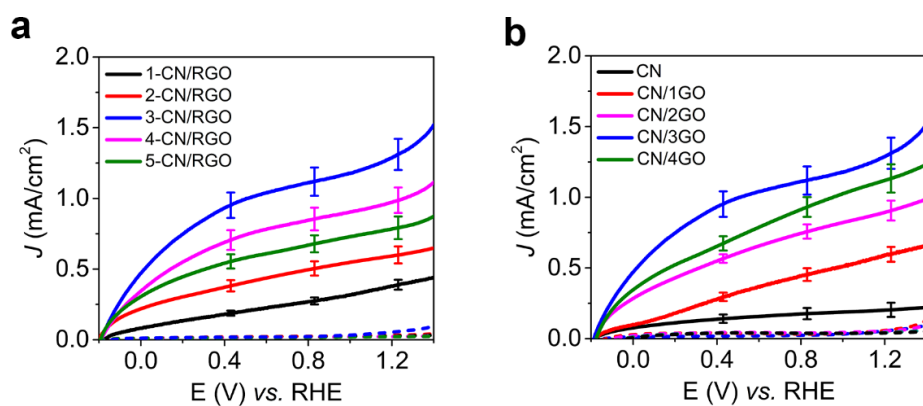
Supplementary Figure 6. *J*-E curves of GCN with (a) different layers and (b) ratios of CN (mmol) to GO (mg) measured in in 1 M NaOH aqueous electrolyte with triethanolamine (TEOA) as the hole scavenger.
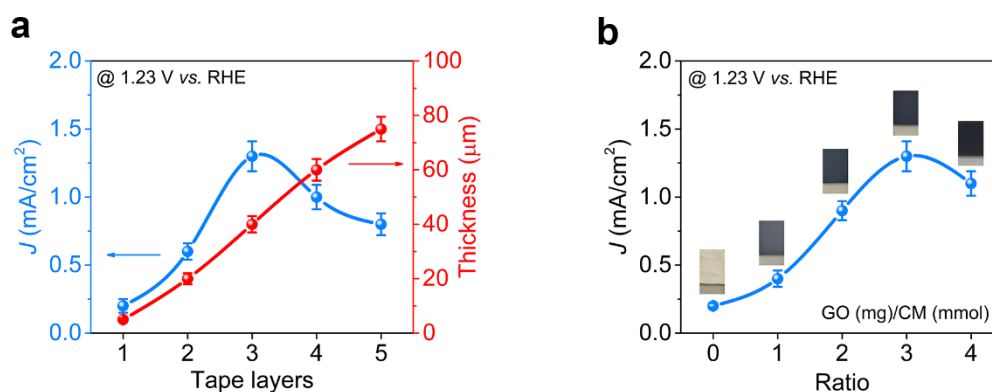
Supplementary Figure 7. Photocurrent density measured in TEOA of (a) GCN photoanodes with respect to different thickness, and (b) Different ratios of GO (mg) to CM (mmol) from 0 to 4.

Generally, thicker film leads to a lower PEC performance probably due to a longer charge transfer distance across the film while thinner film may result in a negative effect on the PEC performance since the light absorption becomes less efficient. As increasing the ratio of GO (mg) to supramolecular CM (mmol), the color of films obviously changed from the light yellow to black.
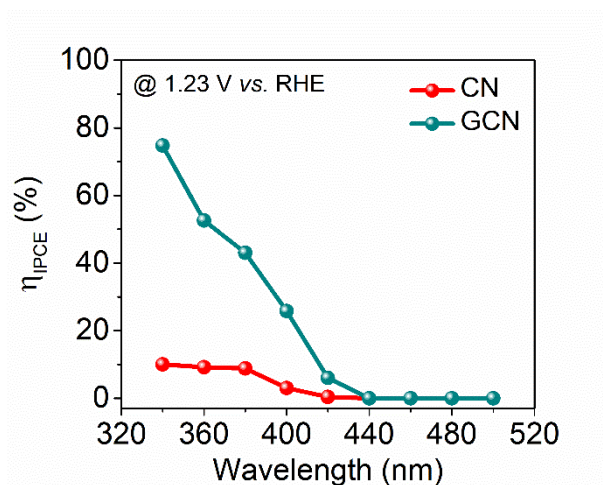
Supplementary Figure 8. η_{IPCE} of CN and GCN measured in 1 M NaOH aqueous electrolyte with TEOA as the hole scavenger.
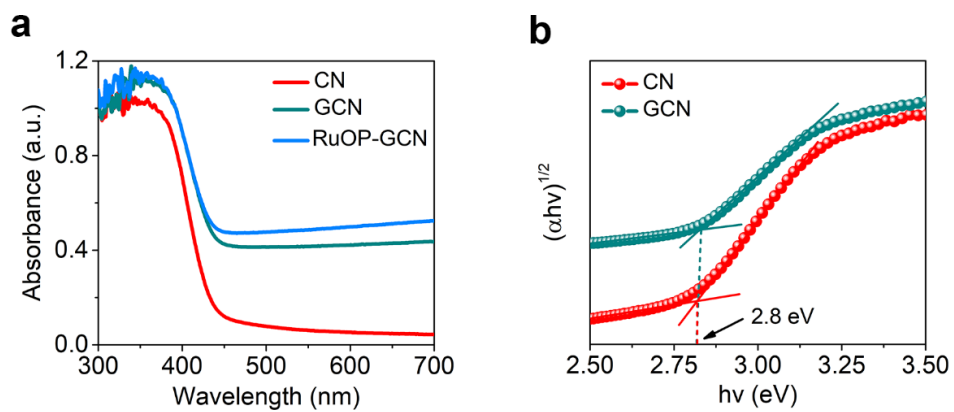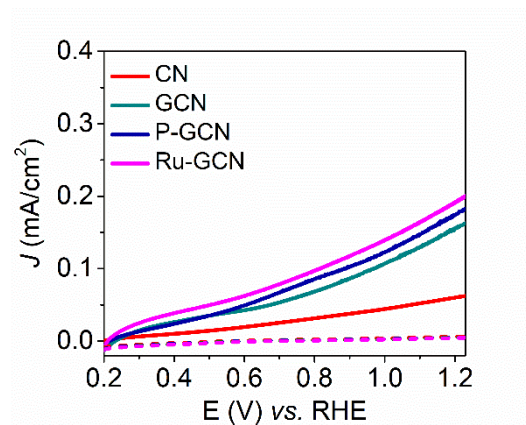
Supplementary Figure 9. Optical property of (a) UV-Vis absorbance, and (b) calculated Tauc plots.
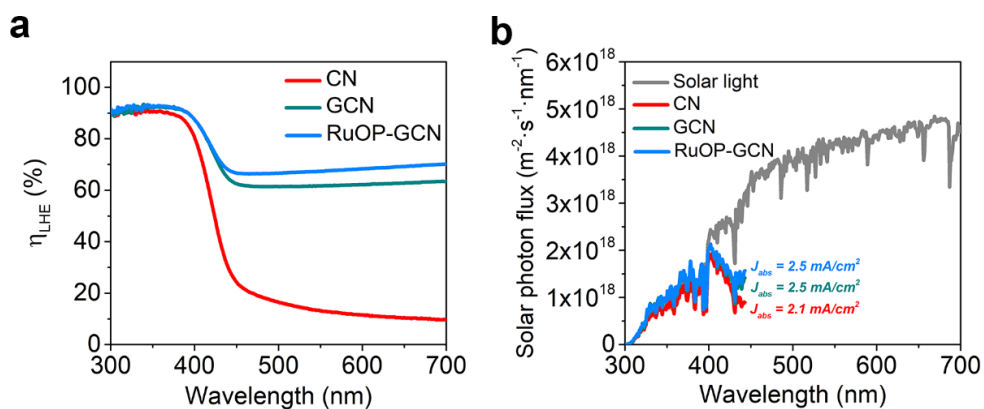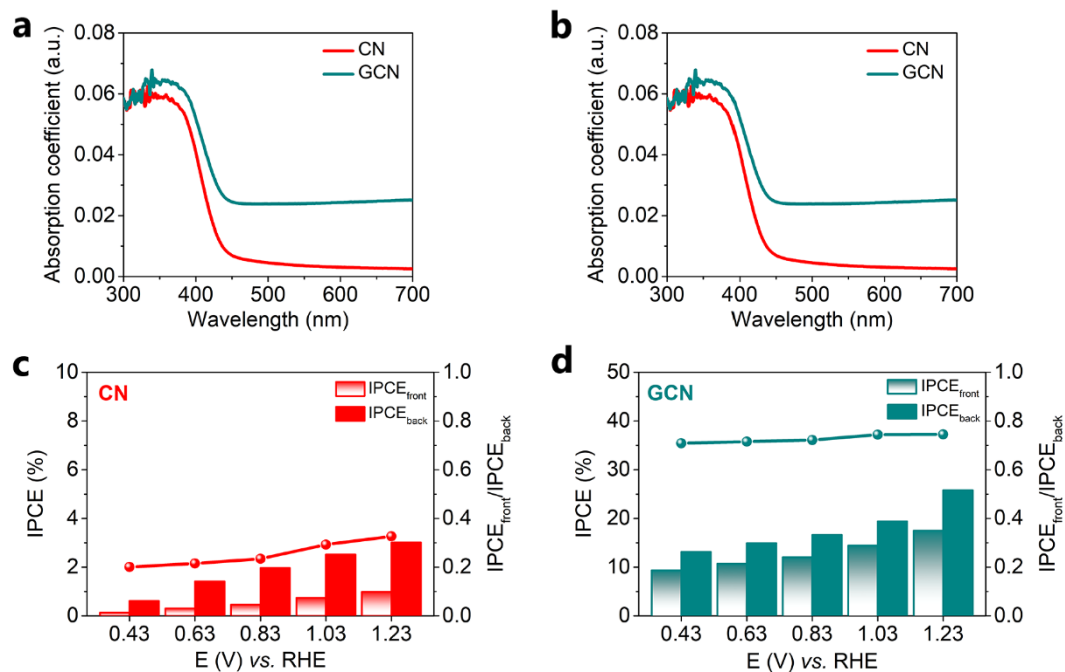
Supplementary Figure 10. (a) Calculated light harvesting efficiency (η_{LHE}), and (b) Spectra of AM 1.5G (ASTM G173-03) solar irradiance and η_{LHE}-weighted spectra from 300 to 430 nm. The J_{abs} given for each curve was calculated from integration of the corresponding spectrum.
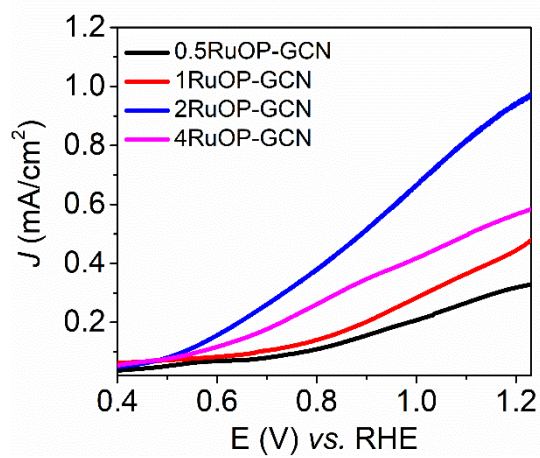
Supplementary Figure 11. *J*-E curve of RuOP-GCN, 0.5, 1, 2 and 4 represent the time dipping in

the ruthenium red aqueous solution.

Supplementary Figure 12. *J*-E curve of CN, GCN, P-GCN and Ru-GCN.

Supplementary Figure 13. Optical property of (a) absorbance and (b) absorption coefficient of CN and GCN, IPCE values at different applied bias measured from the front and back illumination and corresponding calculated ratio of (c) CN and (d) GCN.
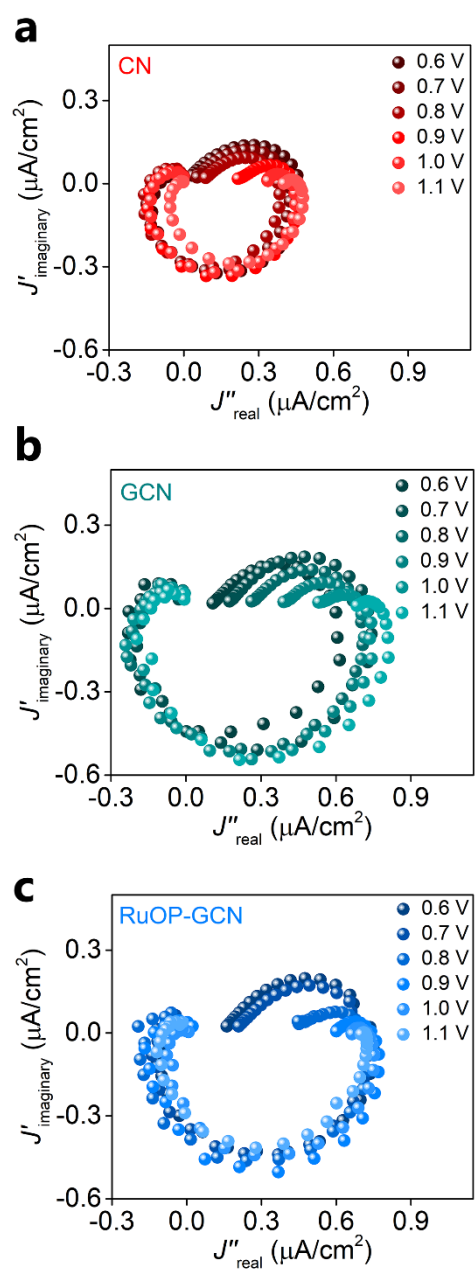
Supplementary Figure 14. For the identification of the rate constants k_t and k_r from an IMPS spectrum of CN, GCN and RuOP-GCN.
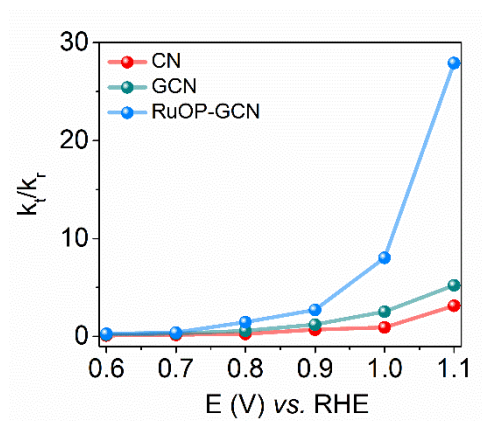
Supplementary Figure 15. The ratio of k_t/k_r of CN, GCN and RuOP-GCN.

Supplementary Table 1. Summary of PEC water oxidation performance of CN-based photoanodes recorded at 1.23 V *vs.* RHE under AM 1.5 illumination.

Photoanode	J (μA/cm^2)	IPCE (%)	Ref.
C_3N_4	63	6.6 at 350 nm	[1]
C_3N_4/RGO	75	5.3 at 400 nm	[2]
Boron-doped C_3N_4	103.2	10 at 400 nm	[3]
S-supported C_3N_4	100	16 at 340 nm	[4]
Close-packed C_3N_4	116	8.5 at 400 nm	[5]
Phosphorylated C_3N_4	120	8 at 460 nm	[6]
Vertically aligned porous C_3N_4	120.5	~ 15 at 360 nm	[7]
Crystal-facet C_3N_4	228.2	23.1 at 380 nm	[8]
Phosphorus/Boron-layer-doped C_3N_4	150 ± 10	8.6 at 340 nm	[9]
Tight-packed C_3N_4/RGO	270	17.1 at 380 nm	[10]
RuOP-GCN	**1.0 mA/cm^2**	**50.2 at 340 nm**	**This work**

Supplementary Table 2. Kinetic analysis of emission decay of CN, GCN and RuP-GCN.

	τ_1 (ns)	τ_2 (ns)	τ_3 (ns)	τ_{ave} (ns)
CN	6.6	47.3	1.4	26.4
	41.7%	21.8%	36.5%	
GCN	4.2	26.3	0.7	27.1
	45.6%	19.9%	34.5%	
RuP-GCN	7.8	44.3	1.5	32. 9
	45.1%	29.9%	25%	

Reference

(1). Lv, X.; Cao, M.; Shi, W.; Wang, M.; Shen, Y., A new strategy of preparing uniform graphitic carbon nitride films for photoelectrochemical application. *Carbon* **2017,** *117*, 343-350.

(2). Peng, G.; Volokh, M.; Tzadikov, J.; Sun, J.; Shalom, M., Carbon Nitride/Reduced Graphene Oxide Film with Enhanced Electron Diffusion Length: An Efficient Photo-Electrochemical Cell for Hydrogen Generation. *Adv. Energy Mater.* **2018,** *8*, 1800566.

(3). Ruan, Q.; Luo, W.; Xie, J.; Wang, Y.; Liu, X.; Bai, Z.; Carmalt, C. J.; Tang, J., A Nanojunction Polymer Photoelectrode for Efficient Charge Transport and Separation. *Angew. Chem. Int. Ed.* **2017,** *56*, 8221-8225.

(4). Fang, Y.; Li, X.; Wang, X., Synthesis of Polymeric Carbon Nitride Films with Adhesive Interfaces for Solar Water Splitting Devices. *ACS Catal.* **2018,** *8*, 8774-8780.

(5). Peng, G.; Albero, J.; Garcia, H.; Shalom, M., A Water-Splitting Carbon Nitride Photoelectrochemical Cell with Efficient Charge Separation and Remarkably Low Onset Potential. *Angew. Chem. Int. Ed.* **2018,** *57*, 15807-15811.

(6). Fang, Y.; Li, X.; Wang, X., Phosphorylation of Polymeric Carbon Nitride Photoanodes with Increased Surface Valence Electrons for Solar Water Splitting. *ChemSusChem* **2019,** *12*, 2605-2608.

(7). Guo, B.; Tian, L.; Xie, W.; Batool, A.; Xie, G.; Xiang, Q.; Jan, S. U.; Boddula, R.; Gong, J. R., Vertically Aligned Porous Organic Semiconductor Nanorod Array Photoanodes for Efficient Charge Utilization. *Nano Lett.* **2018,** *18*, 5954-5960.

(8). Xiong, W.; Chen, S.; Huang, M.; Wang, Z.; Lu, Z.; Zhang, R. Q., Crystal-Face Tailored Graphitic Carbon Nitride Films for High-Performance Photoelectrochemical Cells. *ChemSusChem* **2018,** *11*, 2497-2501.

(9). Luan, P.; Meng, Q.; Wu, J.; Li, Q.; Zhang, X.; Zhang, Y.; O'Dell, L. A.; Raga, S. R.; Pringle, J.; Griffith, J. C.; Sun, C.; Bach, U.; Zhang, J., Unique Layer-Doping-Induced Regulation of Charge

Behavior in Metal-Free Carbon Nitride Photoanodes for Enhanced Performance. *ChemSusChem* **2020,** *13*, 328-333.

(10).   Karjule, N.; Barrio, J.; Xing, L.; Volokh, M.; Shalom, M., Highly Efficient Polymeric Carbon Nitride Photoanode with Excellent Electron Diffusion Length and Hole Extraction Properties. *Nano Lett.* **2020,** *20*, 4618-4624.

Chapter 6. Summary and outlook

By mimicking natural photosynthesis, solar water splitting for H_2 production has been widely and intensively investigated for nearly 50 years since Fujishima and Honda's first report. It is quite clear that the ultimate goal of solar water splitting is to fabricate highly efficient and self-powered PEC cells to realize leaf-to-farm application. As a result, design and fabrication of efficient photoelectrode materials with favored photo-induced charge behavior is highly significant in improving the overall PEC performance. In this Thesis, I focused on the design and synthesis of photoanode materials to regulate photo-induced charge behavior in bulk and on surface. The main findings include:

1. Utilizing an electrostatic strategy to fabricate a $C_3N_4/BiVO_4$ photoanode for solar water oxidation. The effective heterojunction can promote bulk charge separation of $BiVO_4$ and 3D nano-networks C_3N_4 provides a larger surface area for solar water oxidation reaction

2. A homojunction of QDs $BiVO_4/BiVO_4$ photoanode was prepared by an *in situ* growth method. Compared to the heterojunction system, charge transfer is more efficient due to lattice matching in the homojunction system.

3. A unique phosphorus and boron layered doping C_3N_4 photoanode was fabricated by thermal vapor deposition, based on the different polymerization pathways of melamine and dicyandiamide precursors. Efficient triple layers of $P-C_3N_4/B-C_3N_4/C_3N_4$ was formed and successfully promote the bulk charge separation by the internal electrical field.

4. An atomically dispersed cocatalyst of RuOP was fabricated on the C_3N_4/rGO photoanode, where the surface charge injection efficiency was obviously improved with a photocurrent density of as high as 1.0 mA/cm^2 at 1.23 *vs.* RHE at AM 1.5G. More important, the decreased charge recombination at the photoelectrode/cocatalyst interface contributes to the enhanced PEC performance as atomically dispersed ruthenium cocatalyst are integrated into C_3N_4.

Based on the conclusion in the thesis, photo-induced charge behavior plays a vital role in the final resulting solar energy conversion efficiency, which can be precisely tuned both in bulk and on surface as forementioned. Towards the future commercial mass production, the front-illustration photoanodes

side must be composed of multi-junction or layer to optimize bulk energetics, light absorption range, and charge behavior favoring for holes migration to the surface for water oxidation reaction. The Chapter 2, 3 and 4 tells an efficient strategy of junction fabrication in hetero and homo type by using electrostatic self-assembly and in situ growth of BiVO4-based photoanodes. Moreover, surface reaction kinetics must be boosted by incorporating efficient cocatalysts. Considering the interfacial photoelectrode/cocatalyst charge recombination and cocatalyst stability, the Chapter 5 tells a novel strategy by designing and fabricating atomic scale cocatalysts. By incorporating the active sites into the photoelectrodes, the interfacial photoelectrode/cocatalyst charge transfer can be significantly facilitated and instability originated from loss of nanoscale cocatalysts can be maximized eliminated. As a result, both of two strategies in the thesis provide ideas for the future commercialization of PEC water splitting.
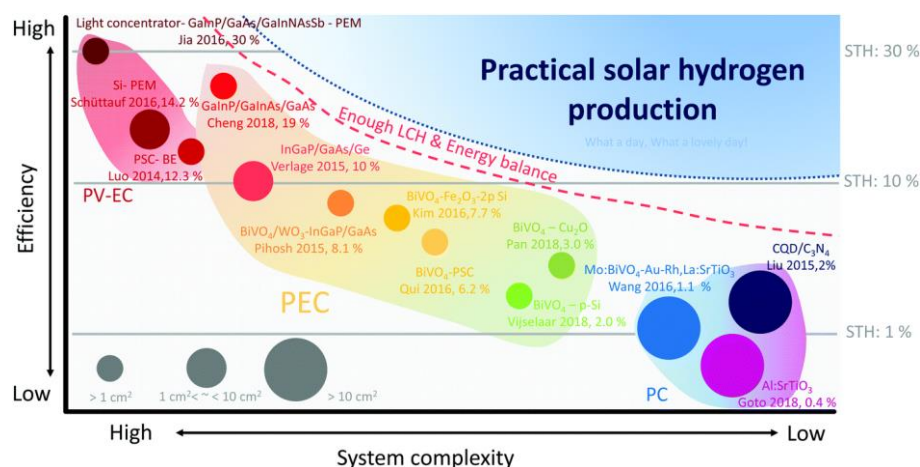
Figure 38. Technological map showing various photon-driven water splitting approaches for solar energy conversion and specific experimental demonstrations. Presentation format followed that of Kazuhiro Sayama and Yugo Miseki with permission. Copyright (2014) National Institute of Advanced Industrial Science and Technology.

Despite various strategies are employed to develop new photoelectrode materials, understand new photophysical and photochemical charge behaviour, and manufacture advanced cells in the past decade, η_{STH} based on PEC and PEC-PV tandem cells is still under 10%, which is much lower than

PV-electrolyzer system. A technology map presented in **Figure 38** shows efficiency *vs.* system complexity. It is obviously seen that intrinsically stable metal oxide-based materials have low efficiencies and low complexity, while PV-grade materials exhibit high efficiencies, but a higher complexity and hence a higher cost. It is suggested that material developments have to go in parallel with the scale up and demonstration projects for practical applications.

In order to compete with the high technology readiness level PV-electrolyzer system technologically and commercially, several key points need to be considered for future improvements. First, advanced manufacturing processes should be developed to produce commercial-size photoelectrodes. The illumination area of emerging high-efficiency photoelectrodes operated and recorded in laboratories are always quite small (usually less than 1.0 cm^2). To produce large sized photoelectrodes for commercial applications, more efforts should be taken to the development of scalable techniques with easily accessible and processable materials, using conventional fabrication techniques (such as spin-coating and chemical vapor deposition) and burgeoning nanotechnology fabrication processes (such as 3D printing and atomic layer deposition). Second, long-term operational stability under solar illumination is another crucial factor in practical applications. Poor stability of photoelectrodes mainly originates from the direct contact or proximity between the light-absorbing materials and corrosive electrolytes. Specifically, nanoscale materials suffer from instability or even decomposition during the reaction due to their high surface energy. Finally, the projected cost of tandem cells, including the cost for raw materials, manufacturing of photoelectrodes, and cell assembly processes, must be competitive in order to be deployable at the energy-market scale. The ultimate target for using the PEC device to produce clean hydrogen energy is the massive production of photoelectrodes with a STH efficiency of at least 10 %, a lifetime of at least 10 years and a cost of less than US\$ 100/m^2, which is challenging but still achievable.